PγXSiS

Portable Gamma/X-ray Silicon Spectrometer

SENIOR DESIGN I

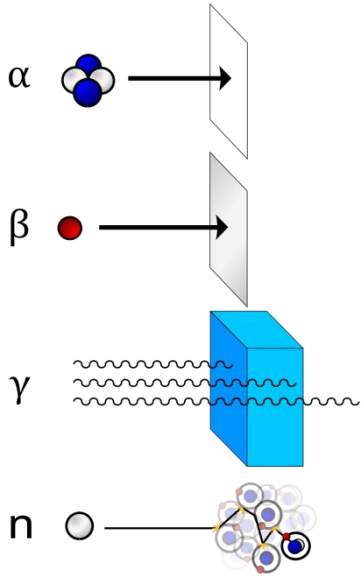

Group 9:
JOHNNY KLARENBEEK
DEAN SULLIVAN
DAVID VALENTINE
AMAN KATARIA

TABLE OF CONTENTS

1.0 INTRODUCTION 1

1.1 NARRATIVE 1
1.1.a Executive Summary 1
1.1.b Motivation 2
1.2 PROJECT SPECIFICATIONS 3
1.2.a Hardware Specifications 4
1.2.b Software Specifications 5

2.0 RESEARCH 6

2.1. RADIATION AND SPECTROSCOPY 6
2.1.a Radiation Characteristics 6
2.1.b Radiation Test Sources 6
2.1.c Spectroscopy Considerations 7
2.1.d Silicon Properties 8
2.1.e Direct Interaction of Radiation with Silicon 9
2.1.f Indirect Interaction of Radiation with Silicon 12
2.2 SEMICONDUCTOR DETECTORS 14
2.2.a Detector Technologies 14
2.2.a.i PN Photodiode 14
2.2.a.ii P-i-N Photodiode 15
2.2.a.iii Photodiode Processing Considerations 15
2.2.b Theory of Operation for Direct Detection 16
2.2.b.i Probability of Interaction 16
2.2.b.ii Quantum Efficiency and Responsivity 17
2.2.b.iii Induced Charge 19
2.2.b.iv Induced Photocurrent 19
2.2.b.v Junction Capacitance and Depletion Voltage 21
2.2.b.vi Detector Noise 22
2.2.b.vii Temperature Effects 24
2.2.c Performance Characteristics 25
2.2.c.i Dark Current 25
2.2.c.ii Response Time and Shaping Time 25
2.2.c.iii Equivalent Noise Charge 26
2.2.c.iv Noise Equivalent Power 28
2.2.c.v Detectivity 28
2.2.c.vi Resolution (FWHM) 29
2.3 SCINTILLATOR CONSIDERATIONS 30
2.3.a Indirect Interaction Theory of Operation 30
2.3.b Scintillator Technologies 31
2.3.c Performance Characteristics 32
2.3.c.i Light Yield 32
2.3.c.ii Scintillator Noise 32
2.3.c.iii Resolution (FWHM) 33
2.4 AMPLIFIERS 33
2.4.a Preamplifer 33
2.4.a.i Charge Integrating Preamplifiers 33
2.4.a.ii Noise Analysis 36

2.4.a.iii JFET Buffer Stage 39
2.4.a.iv Stability 40
2.4.b Pulse Shaping 42
2.4.b.i Differentiator 43
2.4.b.ii Integrator 44
2.4.b.iii Circuit Topology 45
2.4.b.iv Pulse Processing & Equivalent Noise Charge 47
2.5 DIGITAL HARDWARE 49
2.5.a Microcontrollers 49
2.5.b Flash Memory 50
2.5.b.i Speed 50
2.5.b.ii Capacity 50
2.5.c LCD Technologies / Interface 51
2.5.d Touch Technologies 53
2.6 POWER MANAGEMENT 55
2.6.a Component Power Requirements 55
2.6.a.i Detector Bias 56
2.6.a.ii Amplifiers 57
2.6.a.iii Microcontroller 58
2.6.a.iv Thermoelectric Cooler 58
2.6.a.v Digital Peripherals 59
2.6.b Battery Management 60
2.6.b.i Battery Technologies 61
2.5.b.ii Charge Controller 64
2.6.c Voltage Regulators 68
2.6.c.i Linear Regulator 69
2.6.c.ii Switch-Mode Regulators 72
2.6.d Sensor Cooling 75
2.6.d.i Thermoelectric Cooler 76
2.6.d.ii Driver Circuitry 81

3.0 PROOF OF CONCEPT 82

3.1 PROTOTYPE TEST GOALS 82
3.2 DESIGN 83
3.2.a Preamplifier Design 84
3.2.b Pulse Shaper Design 85
3.3 SIMULATION / EXPERIMENT RESULTS 88
3.3.a General Device Response 88
3.3.b Device Geometry 90
3.4 DISCUSSION 93

4.0 DESIGN 94

4.1 DETECTOR DESIGN 94
4.1.a Direct Detector Performance Characteristics 94
4.1.b Direct Detector Package 98
4.1.c Direct Detector Shielding 98
4.1.d Scintillator Performance Characteristics 99
4.1.e Indirect Detector Performance Characteristics 99
4.1.f Indirect Detector Package 100
4.1.g Scintillator Mounting/Indirect Detector Shielding 101
4.2 CHARGE AMPLIFIER 102

4.2.a Schematic....102
4.2.b JFET Buffered Implementation....105
4.3 PULSE SHAPING....107
4.4 DIGITAL HARDWARE....111
4.4.a MCU....111
4.4.b Power Control....113
4.4.c Peripheral Connections....115
4.4.d Signal Conditioning....117
SECTION 4.5 POWER MANAGEMENT....119
4.5.a Battery....120
4.5.b Charge Control....121
4.5.c Regulation....122
4.5.d Sensor Cooling....125
4.6 SOFTWARE....127
4.6.a Program Overview....127
4.6.b Classes and Methods....129
4.6.c Multi-channel Analyzer....134
4.6.c.i Digital Filtering....135
4.7 PARTS AQUISITION/BOM....139

5.0 TEST PLAN....141

5.1 POWER MANAGEMENT....141
5.2 DETECTOR....142
5.3 PULSE SHAPER....143
5.4 DIGITAL HARDWARE....144
5.4.a MCU....144
5.4.b Power Control....144
5.4.c LCD / SD Card / Touch Screen....145
5.4.d Signal Conditioning and Acquisition....146
5.5 SENSOR COOLING....147
5.6 SOFTWARE....147
5.7 FULL ASSEMBLY....149

6.0 ADMINISTRATIVE....150

6.1 MILESTONE DISCUSSION....150
6.2 BUDGET & FINANCE....151

APPENDIX....152

I. REFERENCES....152
II. PERMISSIONS....156

1.0 INTRODUCTION

1.1 NARRATIVE

1.1.a Executive Summary

Gamma spectroscopy is an important analytical tool used daily in the applied fields of nuclear science and technology. It is the quantitative study of the energy spectra of gamma-ray emitting radionuclides. Gamma spectroscopy is used primarily in the nuclear laboratory, geochemistry, astrophysics, nuclear safety, and in quality control of raw materials manufacturing.

Most radioisotopes that emit gamma rays emit rays of different energies and intensities. A gamma ray spectrometer can record these emissions and plot them on a histogram of energy levels (most commonly measured in the kilo to mega electron volt (keV to MeV) range. Since every different radioisotope has a unique signature gamma ray emission, this gamma energy spectrum can be analyzed to determine the type of gamma emitting radioisotopes present.

This paper will document the research, design, prototyping, and final build of a low power solid state gamma ray detector capable of analyzing gamma ray emissions in the range of 50keV to a few MeV. The lower end of the spectroscopy range is typically used in the area of X-ray fluorescence (x-ray spectroscopy), an important tool used in materials production quality control, elemental and chemical analysis, geochemistry, forensic science, and archaeology. The range extending from a few hundred keV to several MeV encompasses the usual nuclear proliferation suspects such as U-235 and Pu-239. It is important to design a device which is capable of resolving gamma ray energies in a large range to maximize applications of the device.

The gamma spectrometer will operate through the use of a semiconductor detector (photodiode or PIN diode) to absorb radiation. A major challenge in the design of a solid state detector is to obtain a good signal to noise ratio and high energy resolution. A low noise shielded multi stage amplifier design will be required to achieve good resolution. Additionally, the device's sensor and amplifier will actively cooled by a stack of thermoelectric coolers as most noise in the system will be temperature dependent. Because solid state detection of gamma radiation produces a very small amount of charge on the semiconductor, a well designed amplifier is crucial for the success of the project. The spectrometer will have a digital interface accessible through a color LCD screen with touch panel or tactile button input. Software features will include capturing and plotting gamma ray emissions on an energy histogram as well as some auxiliary functions such as basic gamma dosimetry. The user will be able to save and load data from plots onto external data storage. The detector will be portable (battery powered) and light weight. See figure 1.1.a.i for a high level overview of device operation.

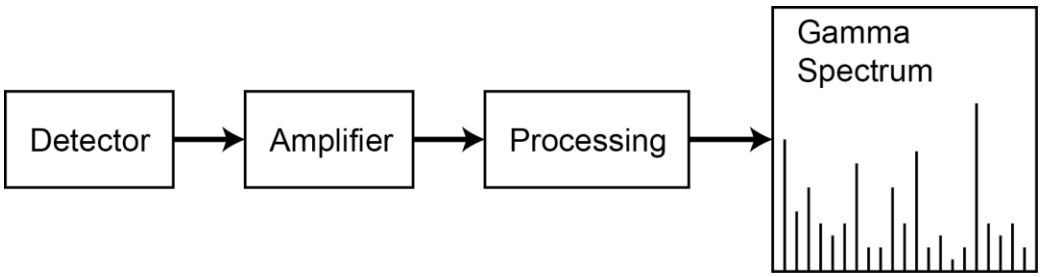

Figure 1.1.a.i: Gamma spectrometer device overview.

In contrast to the operation of a Geiger counter (which only resolves the detection rate of gamma rays) the spectrometer will measure the energy of an incident gamma ray by measuring the proportional charge generated in the photodiode detector. This requires an ultra-low noise charge amplifier and pulse shaping amplifier with careful shielding and circuit layout.

1.1.b Motivation

While gamma spectroscopy is a tool that has been available for decades, it is primarily performed with scintillation counters or liquid cooled germanium detectors. Scintillation counters employ a material that exhibits luminescence when excited by high energy photons. This is similar to how UV dyes fluoresce under a blacklight. By measuring the intensity of a flash of light produced from an incident gamma ray the energy of the gamma ray can be determined. Scintillation counters typically require expensive photomultiplier tubes and a dedicated high voltage power supply or sensitive photodiodes and a low noise amplifier. Additionally, the spectral resolution of scintillation counters is generally poor, and the response of the detector is limited by the crystal material and dimensions. Different crystal materials have to be used depending on the measurement range of interest.

Germanium detectors are semiconductor devices that directly capture the energy from incident gamma rays to produce free electron-hole pairs. They operate in a similar manner to our proposed silicon based detector. While the energy resolution of germanium detectors is vastly superior to that of scintillation counters, they require special cryogenic equipment to cool them to low temperatures. This is due to the low energy band gap of germanium, which results in too much electrical noise from thermal electrons crossing the band gap. In addition, germanium detectors are extremely expensive to produce, as they require high purity crystals (so called high purity germanium detectors) and often have a depletion region with a thickness of several centimeters. Our gamma spectrometer will feature a low cost general purpose silicon photodiode operated in a similar fashion to the germanium detector. Silicon has better noise performance than germanium and is widely available in photodiodes.

Our motivation behind this project is to produce a low cost, accessible portable gamma spectrometer which will operate in a broad range of energies. The gamma spectrometer market is currently dominated by either scintillation detectors (reasonably affordable) or specialty germanium based detectors (extremely expensive). While silicon based detectors are still actively being researched, not many commercial devices utilize them for the purpose of spectroscopy. This research can be utilized to produce a low cost, high performance detector. The project idea is also appealing due to the variety of scientific and technological disciplines involved, such as nuclear physics, low noise analog amplifier and filter design, digital electronics, power systems, control systems, and digital signal processing. We hope to gain valuable experience in all of these disciplines from this project.

1.2 PROJECT SPECIFICATIONS

The primary specification of the project is to be able to accurately quantify gamma ray emissions from radioactive sources over a wide energy range through the use of a silicon detector. Accuracy and the energy range of operation is further defined in table 1.2.a.i and table 1.2.b.i below, as well as other device specific requirements such as power consumption. A detailed high level flowchart showing interconnections of each subsystem of the device is provided in figure 1.2.1.i.

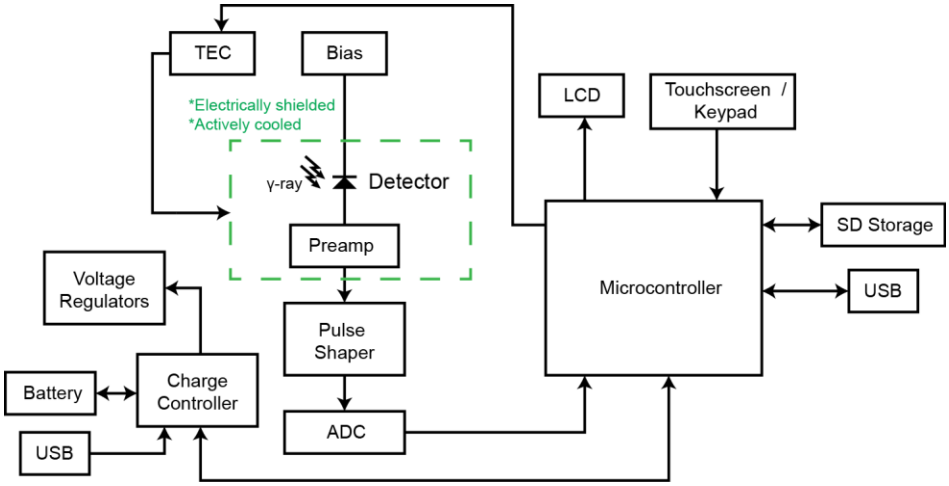

Figure 1.2.1.i: Flowchart of gamma spectrometer subsystems. Note: connections from voltage regulators to other systems are applied.

1.2.a Hardware Specifications

Hardware Requirement	Description
1	The gamma spectrometer will be a portable battery powered device with low power consumption, drawing no more than 3 watts.
2	An integrated battery will provide power for all device hardware. This battery will be rechargeable via a provided USB connector.
3	Device will have a battery life of at least four hours of continuous use without thermoelectric cooler. Two hours of continuous use with thermoelectric cooler.
4	Device will have an integrated color LCD screen with software GUI to provide all software functionality.
5	Device will include peripherals for user input such as keypad or touch screen to control software functionality.
6	Device will provide both graphical (LCD) and audio feedback (buzzer) during gamma spectroscopy measurement.
7	Device will utilize a semiconductor detector to capture energy from individual gamma rays for energy measurement.
8	Device will amplify semiconductor response through a preamplifier circuit and pulse shaping circuit prior to digitization of signal.
9	Device will be able to detect and measure gamma radiation in the energy range of 10 keV to 5 MeV.
10	Device will be able to distinguish between different energy levels in the entire range of measurement with lowest full width half maximum (FWHM) resolution as possible.
11	Device will provide peripherals for actively cooling the semiconductor detector and preamplifier circuitry to a temperature of -20C to reduce noise and increase resolution through a thermoelectric cooler.
12	Device will include microcontroller flash storage and peripherals for external SD card storage to store obtained spectroscopy data.
13	Device will include USB peripheral for battery charging and access to SD storage device for retrieval of spectroscopy data.

Table 1.2.a.i: Detailed device hardware requirements.

1.2.b Software Specifications

Software Requirement	Description
1	Device will sample pulse heights from amplifier output signal and sort and store them in the form of pulse counts relative to measured amplitude.
2	Device will perform additional digital signal processing to reduce noise of measured gamma energy spectrum as well as identify likely energy peaks from data.
3	Processed gamma energy spectrum will be plotted on color LCD screen. User can zoom in on spectrum to view region of interest.
4	Device will include graphical user interface (GUI) with menus to provide configuration functionality, file management, and data storage / retrieval.
5	Device will optionally perform real-time dosimetry based on detection of incident gamma radiation and audibly and graphically warn user if user-defined limit is reached.
6	Device will include functionality for enabling / disabling thermoelectric cooler for increased device resolution and deceased noise.
7	Device will display battery management information, such as remaining battery capacity and voltage
8	Device will mount as removable storage when connected to a computer via USB connector. User will be able to copy and remove gamma spectrum data from external SD storage.

Table 1.2.b.i: Detailed device software requirement.

2.0 RESEARCH

2.1. RADIATION AND SPECTROSCOPY

2.1.a Radiation Characteristics

Ionizing radiation is carried by high energy particles that collide with atoms causing the atom to lose its bound electrons. Some typical forms of ionizing radiation are: alpha, beta, neutron, X and gamma.

Our device will measure Gamma and X-ray energies. We will be shielding our detector from visible light so that ionizing radiation will be the only form of interaction. The shielding will be chosen such that alpha and beta particles will be blocked. It requires very little to block alphas – paper will work - and although betas are slightly more penetrating they are easily shielded with a high density, conductive material such as aluminum. Neutron interaction may occur, but will only represent a small percentage of total interaction.

The gamma ray energies we will be measuring are the result of radioactive decay that occurs because the atomic structure of certain isotopic elements is inherently unstable, and in the process of breakdown the element characteristically transforms to a different state, thereby emitting an energetic ionizing particle. This transformation is unique to the isotope and produces characteristic emissions, which form the basis for spectroscopy.

An X-ray is a secondary radioactive emission process resulting from irradiation. When high energy radiation incident on matter expels a bound electron, the atomic structure of the medium is left unstable. A higher energy electron will fill the gap in the bond left vacant by the ejected electron and emit a photon with energy in the low keV range. This emitted photon is characteristic of the medium and can be used for identification, otherwise known as x-ray fluorescence.

2.1.b Radiation Test Sources

We will be using a model radiation standard source test kit (2000) and other decay elements for prototyping, calibration and final design checking. The characteristic decay scheme of the following elements will be used:

Source	Energy (keV)	Quantum Yield (%)
Co-57	14.41	87.69
	122.06	85.51
	136.47	12.30
Am-241	26.3446	21
	33.1963	21.3
	43.42	12.1
	59.5409	77.6
Cs-137	661.657	94.36

Table 2.1.b.i: Characteristic decay scheme of source kit

Source	Energy (*keV*)	Quantum Yield (%)
Cd-109	88.0336	100
Na-22	511	
	1274.537	99.94
Ba-133	53.1622	15
	79.6142	7.34
	80.9979	90.1
	276.3992	7.57
	302.8512	19.15
	356.0134	63.64
	383.8481	9.12

Table 2.1.b.i: Characteristic decay scheme of source kit (continued)

The unit μCi denotes the microcurie and 1 μCi = 3.7 x 10^4 decays per second. Detailed decay schemes, showing the dominant gamma energies and corresponding quantum yield are given in Appendix I.

2.1.c Spectroscopy Considerations

Collisions of gamma rays transfer energy via the photoelectric effect, Compton scattering and pair production. Each type of interaction produces an electron with energy proportional to that of the incident radiation and characteristic of the type of interaction. A photoelectron has energy directly proportional to the gamma ray and therefore has a monolithic energy distribution that is typically Gaussian in shape. A Compton electron typically has less energy than the incident gamma ray, which is determined by an angle of recoil that spans 180°. The distribution is typically flat over a range of energies and then displays a characteristic exponential edge. Pair production for direct detection will not be considered because it occurs at energies above 2 MeV, which is far outside our detectors response. However, for detection with a scintillator pair production decay will detectable and is typically displayed as a single/double peak. Other interactions will occur - such as bremsstrahlung – and not all of the interaction mechanisms mentioned occurs directly – such as collisions with the shielding and detector edges - so that the induced energy distribution is dissipated and the spectrum degraded. With this in mind, a general view of the radiation interaction process for direct detection is depicted in figure 2.1.c.i below.

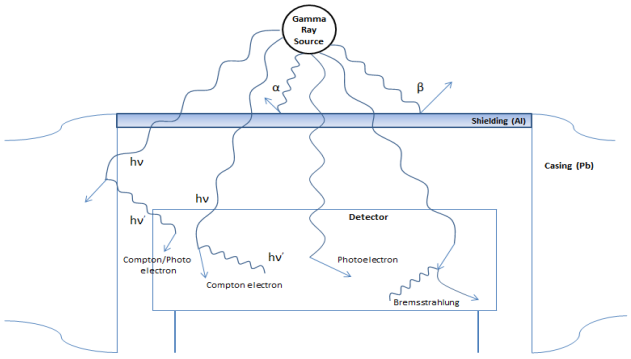

Figure 2.1.c.i: Schematic of characteristic direct interaction of radiation with matter for spectroscopy.

For indirect detection, the radiation interaction processes are the same, but instead are incident on a scintillator, which then produces photons via luminescence that are incident on the silicon detector. The process is displayed in figure 2.1.c.ii below.

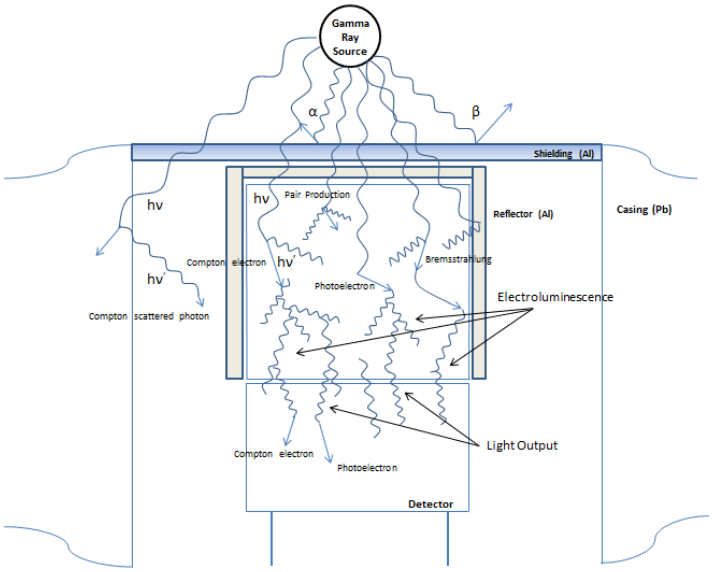

Figure 2.1.c.ii: Schematic of characteristic indirect interaction of radiation with matter for spectroscopy

2.1.d Silicon Properties

The physical properties of silicon govern its response to incident irradiation and induced electrical phenomena. Effective approximation and estimation of detector operation is therefore dependent on knowledge of these quantities. They are given in table 2.1.d.i below at room temperature and will be used as references in effective device design.

Physical Properties of Silicon (Si) at 300 K	
Atomic number	14
Atomic mass (amu)	28
Dielectric constant	11.8
Diffusion coefficient, electrons (cm^2/s)	36
Diffusion coefficient, holes ($cm^2/2$)	12
Intrinsic electron mobility (cm^2/Vs)	1500
Intrinsic hole mobility (cm^2/Vs)	600
Intrinsic carrier concentration (cm^{-3})	1.45×10^{10}
Band gap energy (eV)	1.12
Ionization energy (eV)	3.6
Density (g/cm^3)	2.33
Minority carrier lifetime (s)	$\leq 10^{-6}$

Table 2.1.d.i: Physical/electronic properties of Silicon

2.1.e Direct Interaction of Radiation with Silicon

Electromagnetic waves have a characteristic energy at a certain wavelength determined by the following relationship: $E(eV) = \frac{hc}{\lambda} = \frac{1240}{\lambda(nm)}$, where h is Plank's constant, and c is the speed of light in a vacuum. When an incident photon with energy E_{ph} exceeds the semiconductor bandgap energy E_g, then the energy of the photon will be absorbed in the semiconductor in the form of the photoelectric effect, Compton scattering or pair production. For silicon, E_g = 1.12 eV and therefore the cutoff wavelength for light-matter interaction is $\lambda_c(Si) \approx 1100$ nm. However, even for irradiation below the cutoff, not all of the photon energy above the semiconductor bandgap energy will be interactive. This is because light-matter interaction is partially determined by the penetration depth of the radiation into the semiconductor, which is given as the attenuation coefficient for a particularly energy/wavelength. Additionally, intrinsic semiconductor properties and processing defects will degrade the ideal response.

The dominant mechanisms of photon-EHP interaction for X and soft gamma rays are the photoelectric effect and Compton scattering. Both mechanisms are displayed in figure 2.1.e.i and figure 2.1.e.ii. As will be shown in section 2.2.C.ii, each interactions range of dominance is determined by the detector material and is probabilistically distributed over a characteristic energy range and depth.

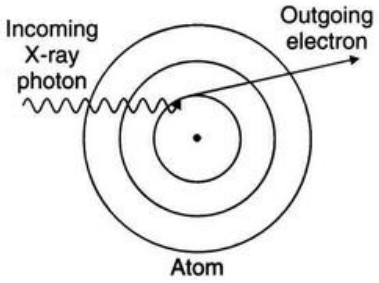

Figure 2.1.e.i: Photoelectric effect

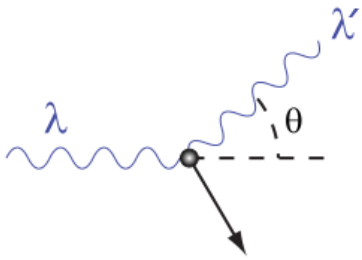

Figure 1.2.e.ii: Compton Scattering

The propagation of electromagnetic radiation through any medium exhibits a characteristic loss of power. The attenuation coefficient is a measure of this loss and is inversely proportional to the penetration depth. Properly, the penetration depth gives the distance travelled into a given material at which the incident radiation drops to 36% (1/e) of its initial intensity. Attenuation and probability of interaction type are related by the following expression: $\mu = \sigma\rho\frac{N_A}{A_r}$, where σ is the total probability of interaction, ρ is the detector density, A_r is the detector atomic mass and N_A is Avogadro's constant.

Because the attenuation coefficient and type of interaction are related for a given energy/wavelength, they are often shown together and the figure 2.1.e.iii below gives the attenuation as a function of energy and also displays the characteristic interaction mechanism over its dominant energy range for silicon. From the figure 2.1.e.iv, it can be seen that for low keV energies the photoelectric effect will be the dominant mechanism of interaction and for energies > 100 keV Compton scattering will dominate. It is also apparent that higher energy radiation will penetrate more deeply into the detector. Because of processing limitations, typical photodiode thicknesses are on the order of ~ 200 µm - 400µm.

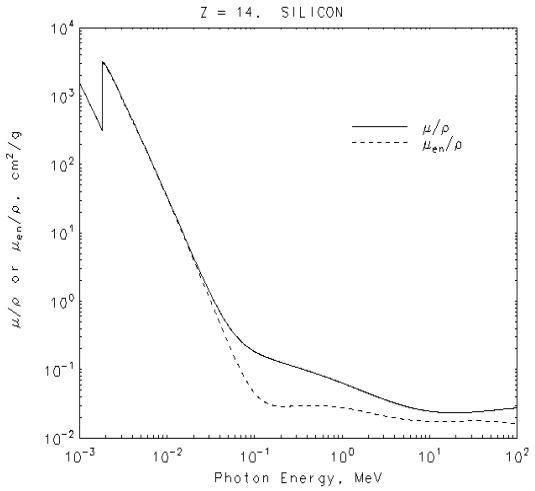

Figure 2.1.e.iii: Linear attenuation data for Silicon showing characteristic interaction mechanism dominance. *(Pending Permission)*

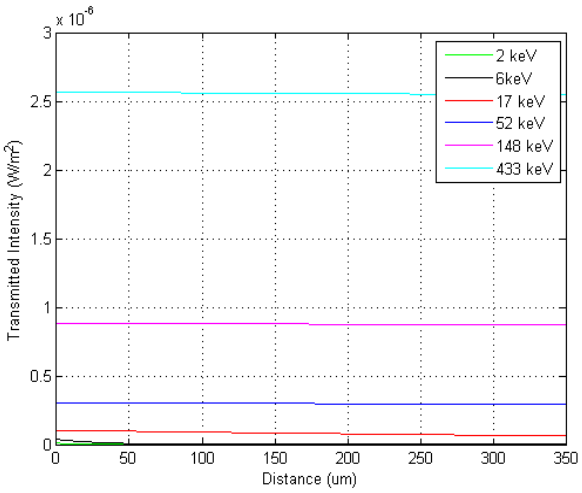

Figure 2.1.e.iv: Transmitted power through the detector

The attenuation coefficient is determined in order to estimate the amount of incident radiation absorbed by a material. From this characteristic absorption and a given E_{ph} with intensity I_o, the decay of intensity I_o at a distance x into the detector can be calculated via $I_t = I_o e^{-\mu x}$, where I_t is the intensity of radiation transmitted through the detector. From this, the energy absorbed by the detector can be found as an incident power minus the transmitted power. A distribution of incident discrete energies versus detector depth is shown above. It was assumed that the activity of the radiation was 1 µCi, so that the incident power is on the order of pW, which demonstrates that the energy transferred to the detector will be much larger than the ionization energy, thereby yielding a good probability of EHP generation. The ratio of I/I_o gives transmittance, which characterizes the amount of radiation that will pass through a medium. Ideally, for detection purposes, transmittance should be low so that the absorbance in the detector is high - $Abs = -\log T$. When absorbance is high there is a greater probability of useful interaction. Over the range of energies directly detectable via a silicon semiconductor detector and across typical detector thicknesses, the transmittance and absorbance are plotted in figure 2.1.e.v and figure 2.1.e.vi, respectively.

From figure 2.1.e.v it is apparent that at 433 keV the transmission through the detector is nearly unity, indicating that there is a low percent probability of interaction in the detector. The majority of absorption occurs below 150 keV, so that it becomes a rough estimation of the detectors upper limit. A more detailed analysis of percent probability for the given test sources will be applied later.

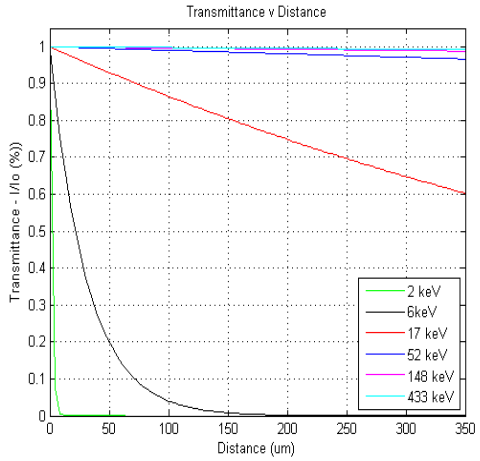

Figure 2.1.e.v: Fraction of optical power lost over detector distance

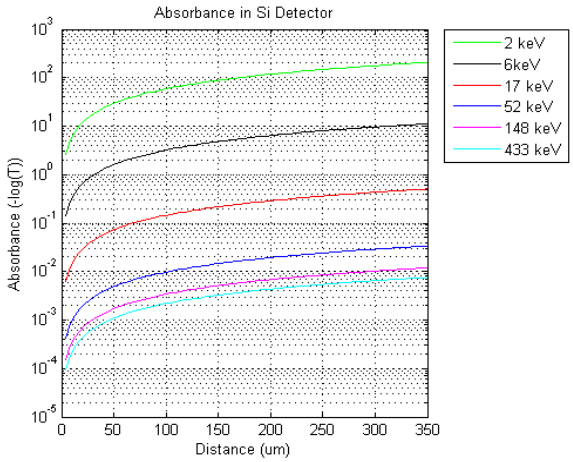

Figure 2.1.e.vi: Generation rate per photon flux over detector distance

For a p-i-n photodiode, the generation rate can be estimated as $G = \frac{\mu I_o}{E_{ph} A}$. Integration of the max photogenerated current over the intrinsic region of a p-i-n detector results in the generation rate of EHPs given by $G = \mu \varphi_o e^{-\mu x}$, where φ_o is the photon flux at the surface given by $I_o/(E_{ph}*A)$. Both instantiations of the generation rate are useful because they show the probable amount of generated EHPs per E_{ph} incident on the detector, if each absorbed photon produces an EHP. It also demonstrates detector area dependence, where decreasing A increases G. The generation rate is shown in the figure 2.1.e.vii below. The generation rate clearly jumps due to decreasing active area. This indicates that despite increased area for interaction, the generated rate will be small if the area is large. The noise analysis for a photodiode with both large and small area will ultimately determine detector choice because the photocurrent might be masked by noise if it is on the same order or less.

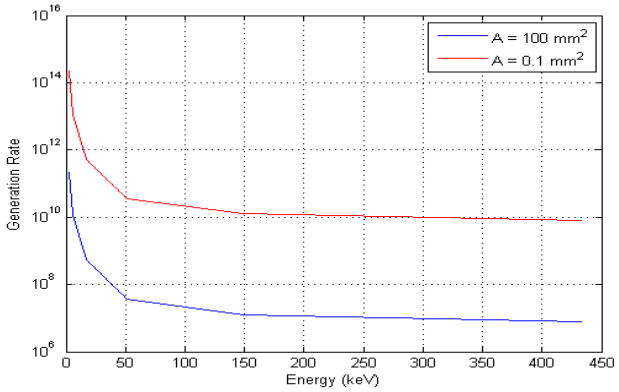

Figure 2.1.e.vii: Optical generation rate of electrons over a range of radiation energies

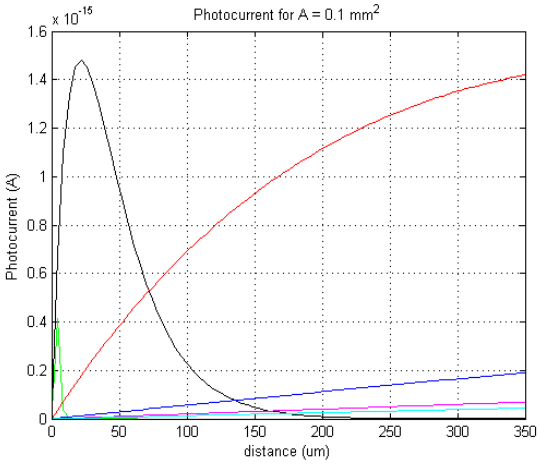

Figure 2.1.e.viii: Photocurrent versus distance for a 0.1 millimeter squared area

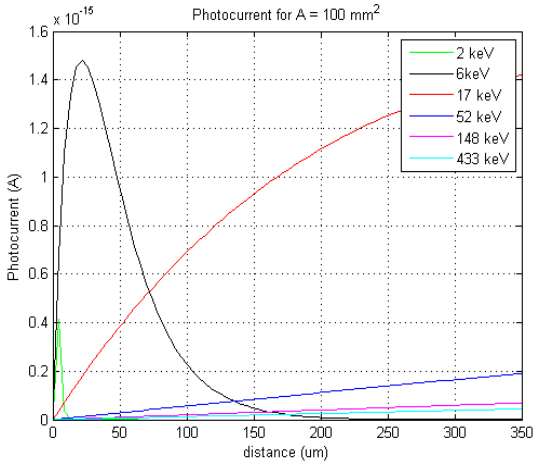

Figure2.1.e.viv: Photocurrent versus distance for a 100 millimeter squared area

The current produced by the interaction of gamma rays is proportional to the gamma ray energy and is transferred to the atom via the photoelectric effect or Compton scattering. When an ejected electron crosses the energy band gap into the conduction band, our device collects the induced charge via a high input impedance current-to-voltage operational amplifier. The figure clearly shows the effects of photon penetration into the detector on the generated current. As the position of photon-EHP interaction increases from the depletion region, the amount of generated electron-hole pairs that contributes to the current decreases. In fact, the photogenerated current approaches zero at the semiconductor surface, which is due to impurities and recombination centers. Processing a dead layer at the surface will yield better charge capture so the surface acts as a window, as well as doping with impurities with energies near the conduction and valence band. The figures can be correlated to the absorption and generation plot and demonstrates the proportional drop in induced charge over incident gamma ray wavelength as well as active area dependence. As the photon wavelength decreases, the magnitude of induced current does also. This provides the following general relationship, when λ is to the left of the visible spectrum, to guide our detector design considerations: $I_{gen} \propto \lambda \propto \frac{1}{E_{ph}}$. However, this is merely an approximation and a detailed analysis of the percent contribution of each detector region to the induced photocurrent for an ideal detector will follow later.

2.1.f Indirect Interaction of Radiation with Silicon

Indirect interaction of radiation with silicon occurs through the use of a scintillator, which operates as a bridge; radiation bombards the scintillator at one end and, through electroluminescence, photons exit the scintillator. Incident radiation upon a scintillator in the 100 keV to 5 MeV range is easily stopped because the scintillator is a high Z material (>80) and nearly completely insulating due to their wide band-gap energies.

Luminescence occurs through two mechanisms: fluorescence and phosphorescence. They both occur when incident radiation breaks a bound electron from the scintillator lattice and a higher energy electron fills it place. A photon is emitted in the process with energy in the visible range due to the decay energy characteristic of inorganic scintillator materials. They differ only in the magnitude of emitted energy, where fluorescence emits a photon of shorter wavelength and phosphorescence a longer wavelength.

The range of operation is based on the same optical principles as direct detection and is rated primarily by attenuation. Figure 2.1.f.i and figure 2.1.f.ii below shows the attenuation trends and probability of photoelectric, Compton and pair production for both inorganic and plastic scintillator materials. From both plots, it is apparent that detection of very high energy gamma rays is possible. Because the interaction probabilities are increased, pair production effects will have to be considered in spectral analysis above 1 MeV. However, the same principles governing photoelectric and Compton interactions for direct detection applies for indirect detection.

Pair production occurs when the energy of a photon is roughly two times larger than the resting mass of an electron, therefore putting a lower limit at ≈ 1.022 MeV.

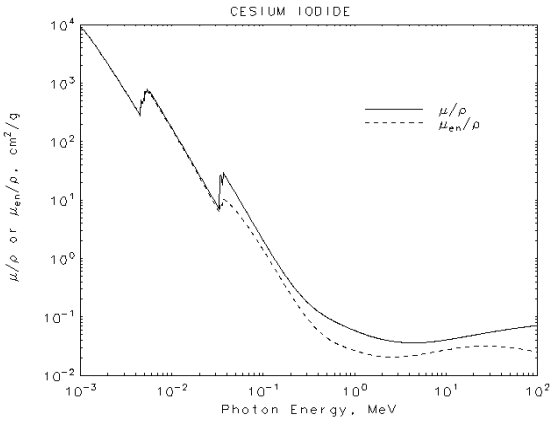

Figure 2.1.f.i: Inorganic Scintillator (CsI) linear attenuation plot
(Pending Permission)

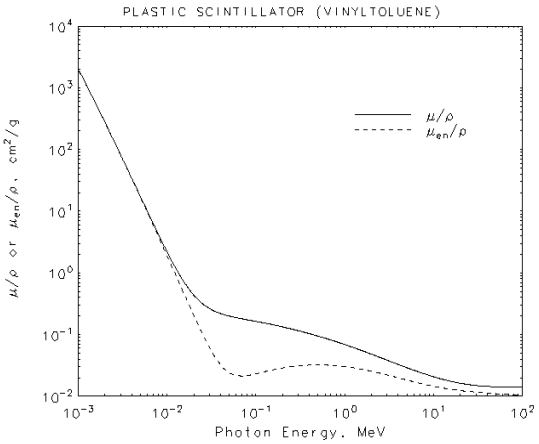

Figure 2.1.f.ii: Plastic Scintillator linear attenuation plot
(Pending Permission)

When an incident photon bombards an atom with this energy, an electron-positron pair can be generated. The probability of this occurring is roughly proportional to Z^2. When pair production does occur, the energy distribution is then determined by the fate of the electron and positron. The positron will eventually lose speed and annihilate with an electron, thereby producing two photons with $h\nu \approx 511$ keV. These photons might be registered by the detector and will display on the spectrum as a photopeak, characteristically displayed as a single/double escape peak. The electron will similarly contribute to the read-out. The interaction is displayed in the figure above.

–

Once incident radiation has passed through the scintillator, the detector interaction described in section *2.1.e* applies; however, because the scintillator outputs light photons, the probability of interaction and detection is greatly increased above that seen by direct detection for high energy gamma rays. Typical scintillator light output is in the 380nm 510nm range, and silicon is ideally suited for detection at these energies and all interaction is nearly photoelectric.

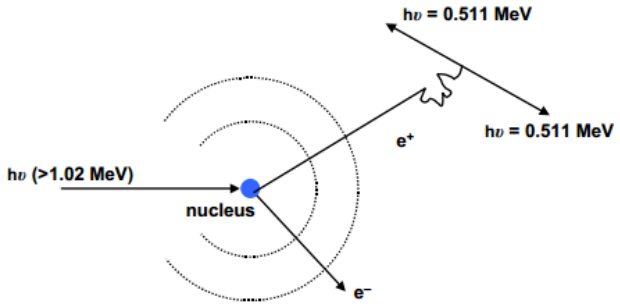

Figure 2.1.f.iii: Pair production interaction showing positron annihilation and subsequent dual 511 MeV photon generation.

2.2 SEMICONDUCTOR DETECTORS

2.2.a Detector Technologies

There are two types of technologies our project will use: a photodiode and a scintillator coupled to a photodiode. However, scintillator technology will be discussed in a later section.

A photodiode is a semiconductor sensor that enters non-equilibrium via the generation of excess carriers when illuminated by light or radiation. The resulting excess carrier concentration contributes to the forward current and is measured as a voltage in the photovoltaic mode when the photodiode is forward biased. When a reverse bias is applied, the reverse current is increased and is measured as a current in the photoconductive mode. Our device will be operated in the photoconductive mode. There are two classifications, by doping profile or construction that we will consider: PN photodiode and PIN photodiode

2.2.a.i PN Photodiode

The PN photodiode is characterized by increased surface area geometry, thicker wafer production, and an optimized doping profile to yield the best photo-response. The active area is large to increase interaction and is typically 2 mm^2 to 600 mm^2. The geometry is either planar or circular and the packages typically come with a quartz window because they are rated for visible/IR interaction, which will be removed to yield a greater probability of direct absorption in the detector. In other instances, epoxies are used as covers to block visible light. The doping concentration of a photodiode is designed in order to enhance its read-out. The contact layers are typically highly doped to reduce

resistivity and increase conductivity. Doped impurity ions with trapping centers near the conduction and valence bands are used over those with centers close to the middle of the band gap because the deeper the impurity energy, the more excitation is required to re-excite a trapped carrier. Hamamatsu photodiodes use selective diffusion of boron (B^-) to a thickness of approximately 1 µm because its impurity energy is 0.045 eV, so that it lies right next to the valence band. The profile is ideally p^+-*n*, with the *p* doped region at the surface and an *n* substrate because the induced current is dominated by drift mechanisms and *e* mobility » *h* mobility.

2.2.a.ii P-i-N Photodiode

A P-i-N photodiode is exemplified by its doping profile, where $i \equiv$ intrinsic. The intrinsic layer is doped epitaxially, meaning it is on the order of $\approx 10^{15}$ cm^{-3}. The intrinsic profile aids in fully depleting the space charge region with only a negligible applied bias compared to a normal photodiode. It also reduces any thermally generated current in the SCR because it is proportional to concentration. At the surface, the region is typically thin and highly doped in order to yield ideal ohmic contacts and reduce absorption. In most cases, the top layer is grown with a large band gap material (SiO_2) to create an effective window and eliminate absorption.

2.2.a.iii Photodiode Processing Considerations

Silicon photodiodes may be fabricated in a number of ways, each resulting in different characteristic optical responses. The main types are: diffused junction, and ion implanted.

Diffused junction diodes are fabricated by diffusing *n*-type impurities (group V elements) into a *p*-type bulk wafer. The concentrations and diffusion times are adjusted in order to accurately dope the detector to tenths of a micron. With this process, the surface layer becomes heavily doped *n*-type so that it is a n^+-*p* detector, which means the depletion layer extends primarily into the bulk *p* region. In so doing, the incident radiation has to pass through a relatively thick dead layer before entering the SCR. In addition, the diffusion process occurs at high temperatures (1000°C), thereby reducing carrier lifetime.

Ion-implanted diodes are formed by bombarding the detector with impurity ions and by controlling the ion energy, the concentration and depth can be regulated precisely. The process generates surface windows as small as several nanometers, reducing the dead layer and increasing interactive yield in the SCR. Because the process occurs at high energies, radiation damage occurs to the detector and it must go through an annealing processing (500°C) to recover. This similarly reduces charge mobility and increases noise effects, but much less so than in diffused junction diodes. The range of impurities energies is also much larger than diffused junction processes and allows design considerations, such as impurity energies close to the conduction/valence band, to be met.

2.2.b Theory of Operation for Direct Detection

What follows is a detailed analysis of the theory of operation for direct detection using a silicon photodiode. For indirect detection, the theory of operation still applies, but the details are rated as datasheet parameters.

2.2.b.i Probability of Interaction

The probability that an incident photon will be absorbed photoelectrically can be estimated using the following expression: $PE \propto \frac{Z^n}{(hv)^m}$, where Z is the atomic number and n and m are fitting parameters with 3 < n < 6 and 3 < m < 4. The parameters will be fitted using NIST data freely available online. The mechanism of scattering occurs directly when an incident photon collides with a bound electron. Some photon-EHP interaction will result from Compton scattering as well, which is an indirect energy transfer mechanism. The probability that an incident photon will collide with an electron resulting in Compton scattering is estimated by the following expression: $CS \propto \frac{Z}{E_{ph}}$. Because both the photoelectric effect and Compton scattering interactions can be approximated as a function of the atomic number, the atomic number can be used as a quick reference for design considerations. Figure 2.2.b.i.i depicts the following probability spectrum generated over the range of relevant photon energies for our detector. Also displayed are the total percent probabilities for different gamma ray sources, where T_{prob} = PE + CS. The dominant mechanism will be the photoelectric effect below 100 keV. And despite the high probability of interaction displayed at 5.9 keV for Fe^{55}, detection of the signal will be masked by noise inherent to the photodiode and front-end electronics. As will be shown, noise at the photodiode and trans- impedance op amp can be reduced with lowering the operational temperature. Design considerations regarding bias and capacitance can also reduce noise and yield a better signal at the low keV end.

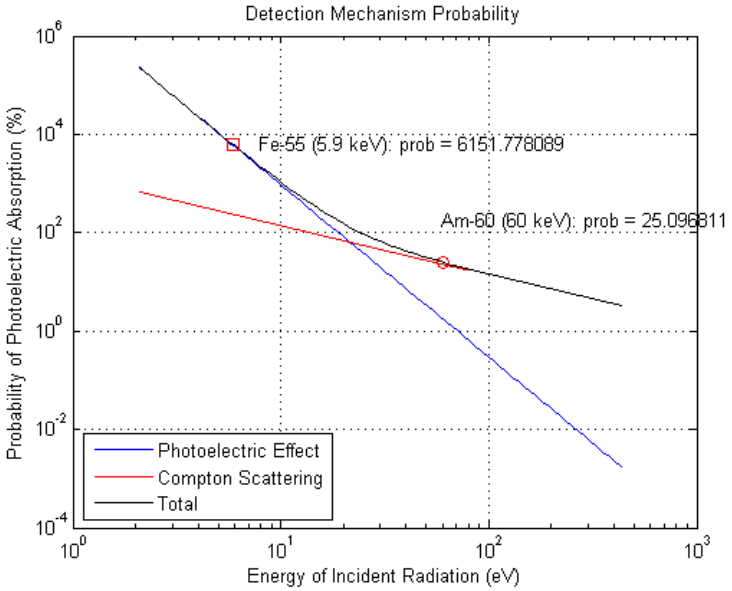

Figure 2.2.b.i.i: Detection Mechanism Probability as a function of irradiation wavelength

2.2.b.ii Quantum Efficiency and Responsivity

The spectral response is a measure of a semiconductor's sensitivity to incident radiation. This relationship is quantitatively evaluated by examining the quantum efficiency and responsivity of a given semiconductor over a range of irradiation.

Quantum efficiency is a measure of the generated charge carriers to the number of incident photons on the active semiconductor detector area, so that it is a quantity that shows the extent to which a given semiconductor responds to incident radiation. It can be given as a function of energy (eV) or wavelength (nm) and is evaluated as a percentage with increasing Q.E. representing improved radiation absorption and charge collection in the detector. That is, with increasing Q.E. the generated photocurrent increases as well. As the photocurrent increases above the leakage current and other noise effects, detection in the front-end stages of our design becomes easier to record. The expression for QE is given as: $QE = T(1 - e^{-\mu x})$, where T is the transmittance.

The responsivity of a given semiconductor detector is a materials property and is a measure of the devices sensitivity to ionizing radiation. It is an important parameter for detector design because it provides a measure of the photoconductive gain and is used to calculate the quantum efficiency. The expression relating the quantum efficiency to responsivity is given as:

$R = \frac{QE*g*\lambda(\mu m)}{1.24} = \frac{QE*g}{E_{ph}}$, where $g = \frac{\tau}{\tau_{tr}} \approx 1$ is the photodconductive gain for photodiodes. The photoconductive gain is given as the ratio of the carrier lifetime to the carrier transit time. This means that the gain is proportional to the carrier mobility and lifetime product as well as the applied bias. It is a figure of merit introduced along with responsivity curves because it is directly related to that particular detectors responsivity, so that if $\mu\tau$ increases so does *R*. In addition, the photoconductive gain can be characterized as the ratio of electronic flux to the incident photon flux, where each is perpendicular to one another. In other words, without an inherent gain mechanism (operating the device in avalanche breakdown) the photoconductive gain will always be approximately unity. The trade-off for this, however, is reduced noise which dominates design concerns for high-energy particle detection. Responsivity is characterized as the ratio of the photo-generated current produced in the detector (A) to the energy of the incident radiation (W). Incident radiation upon the semiconductor active area will have a characteristic energy (*hv*), which if greater than the semiconductor bandgap E_g, will be absorbed at a position in the semiconductor detector characteristic of its absorption length. If the incident radiation exceeds the ionization energy, then an EHP will be created with flow perpendicular to the photon flux. These two quantities will be equivalent if the diffusion length is sufficiently large and recombination at the surface is negligible. The normalized photo-generated current, given the designed detector conditions, with respect to the incident power yields the maximum detector responsivity. So, in order to increase responsivity it is necessary to maximize the diffusion length, decrease recombination, and reduce surface defects. Recombination centers and surface defects are process dependent and choice of manufacturer will be paramount. There are trusted companies working solely on photodiode detector production, such as Hamamatsu and Optodiode that will be considered first because of their experience. The diffusion length is a function of the diffusion coefficient and recombination lifetime. The diffusion

coefficient is proportionally a function of temperature and charge mobility, but charge mobility variations dominate. Because of mobility temperature dependence, keeping the temperature low and choosing a detector with a moderate doping profile will enhance the diffusion length response. Also, by choosing a detector with an appropriate doping profile to enhance the diffusivity, the recombination lifetime will be enhanced because it shows a similar dependence to carrier concentration. In order to decrease surface defects, a detector with a thinly grown passivated/dead layer at the surface must be chosen. Contact with the detector manufacturer will be required because this information is not typically given on a datasheet or the product webpage.

The figure 2.2.b.ii.i below shows quantum efficiency as a function of wavelength. QE was plotted over varying distances at constant attenuation corresponding to a unique energy. At lower energies, QE is greatest at the surface, and at higher energies QE peaks deep into the detector. This trend matches high energy penetration and absorbance plots because higher energy particles are more deeply penetrating. However, some interaction will occur towards the back of the detector because of silicon's stopping power. The QE versus wavelength demonstrates that QE peaks at different energies corresponding to penetration depth, which is expected. Both plots will aid in calibration for testing linearity and maximum spectral resolution. A responsivity plot is also shown as a function of wavelength over varying QEs and similarly demonstrates the small rate of generation at the surface for low energies. The plots only show general trends and are typically given as measured quantities. If possible these measurement will be performed, if not, the specific QE and R values at a given E_{ph} will be calculated and used for linearity estimation.

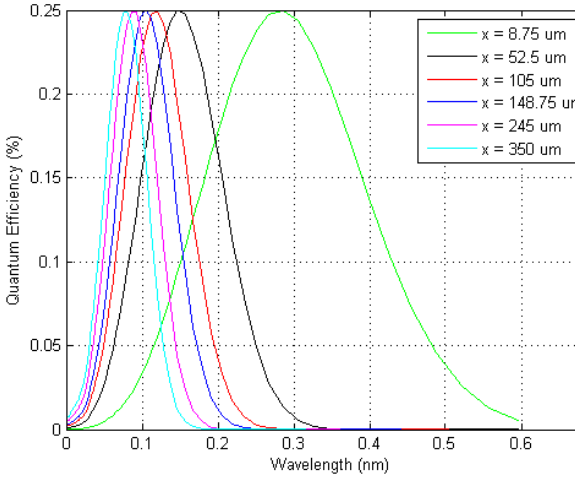

Figure 2.2.b.ii.i: Quantum Efficiency versus wavelength

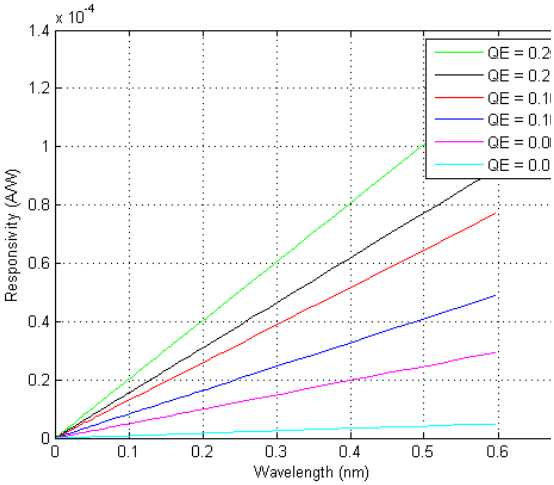

Figure 2.2.b.ii.ii: Responsivity versus wavelength at varying radiation energies

The responsivity is low for higher energies as expected, but the plot clearly demonstrates that despite generation deep into the detector the induced current will be small, which is primarily due to recombination in the bulk. The plot is linear with increasing energy and will act as a rubric for our matching our spectral response binning algorithm to incident energy.

2.2.b.iii Induced Charge

Characterization of the induced charge carriers over a range of energies that is the input to the trans-impedance op-amp is essential because it largely determines the limit to spectral resolution. It will be shown that as the number of induced charge carriers increases the percent resolution decreases, which is desired for a good spectrum readout. The estimated number of generated EHPs per E_{ph} is given in figure 2.2.b.iii.i

The induced charge for a given incident gamma decay is given by $Q_i = N_e q$, where $N_e = E_{ph}/\varepsilon_i$ and $\varepsilon_i(Si) = 3.6\ eV$. As the gamma energy increases, so does the induced charge. It is linearly rising with respect to ΔE_{ph} because it is a function of constant ionization energy. This characterization will be used in testing because it approximates the linearity of incident energy to input voltage as input to the trans-impedance op amp. This is because a small coupling capacitor is used at the input to the op amp so that the relationship Q = C/V can be applied when the pulse resembles a step function because all of the charge will be collected at the capacitor and transferred completely. The estimated charge per E_{ph} is given in figure 2.2.b.iii.ii.

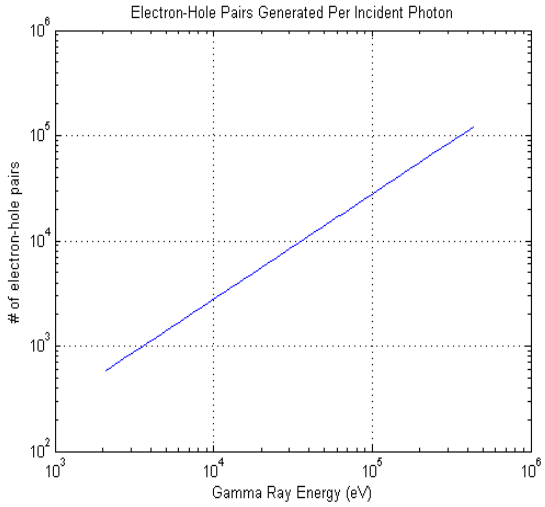

Figure 2.2.b.iii.i: Approximate induced EHPs in silicon over a range of radiation energies

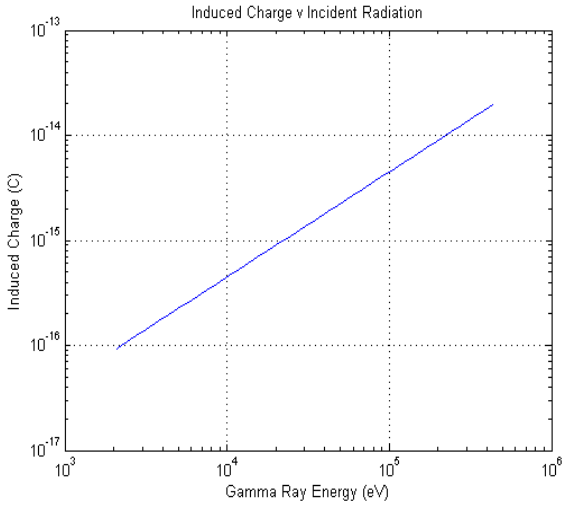

Figure 2.2.b.iii.ii: Approximate induced charge in silicon over a range of radiation energies

2.2.b.iv Induced Photocurrent

When a reverse bias is applied to a PN junction, the space charge region is depleted of excess carriers and a small reverse current flows through the device according to I_s (reverse saturation current), in the direction of the electric field. The capacitance of the diode is variable according to applied bias, and is reduced from its equilibrium or forward operation because the junction capacitance is inversely proportional to the space charge width as $C_j \propto {}^{1}/_{W_{SCR}}$. When illuminated by light/radiation, excess carriers are optically

generated and a photo-generated current is added to the total reverse current in parallel. Aschematic of the equivalent circuit and I-V curve is shown in the figure 2.2.b.iv.i. The diode current is due entirely to I_s because of the reverse bias. All normal device physics apply in the photoconductive regime and will be used to estimate induced charge, depleted supply bias, photogenerated current, capacitance, doping profile and dimensional quantities such as space charge width, and noise.

When excess minority carriers are induced in the space charge region, the large *E* field there sweeps the electrons towards the *n*-region and the holes towards the *p*-region, which creates a reverse drift current flowing from *n*-side to *p*-side. Similarly, minority carriers generated in the bulk will diffuse into the SCR and add to the drift current if the diffusion length is greater than the distance of generation from the SCR.

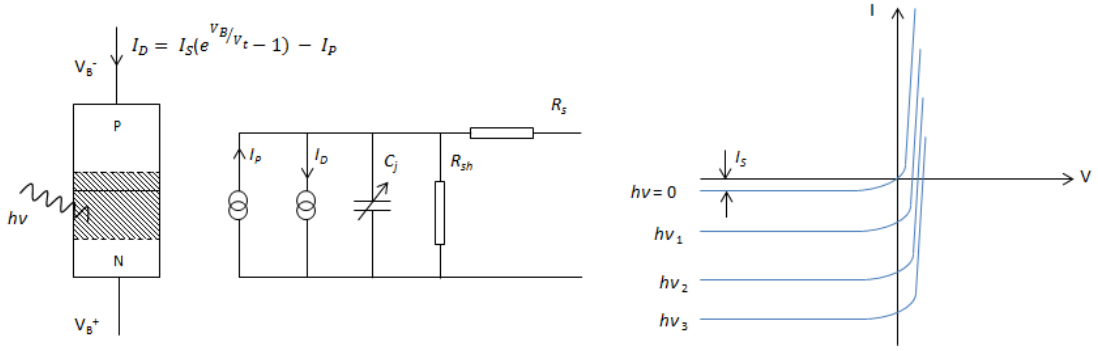

Figure 2.2.b.iv.i: From left to right → schematic of photoconduction, equivalent circuit, I-V curve

The total photo-generated current for a detector with a p-i-n geometry, which avoids simplifications to the generation-recombination mechanisms, detector efficiency and uniform current across the surface, bulk, and space charge region, is given below.

$$I = q\varphi_o \frac{E_{ph}}{\varepsilon_i}\left(\frac{L_a L_n}{L_a^2 + L_n^2}\left[\left(\coth\left(\frac{T_p}{L_n} + \frac{L_n}{L_a}\right)e^{-T_p/L_a}\right) - \frac{1}{\sinh\left(\frac{T_p}{L_a}\right)}\right] + e^{-T_p/L_a}\left(1 - e^{-W_{SCR}/L_a}\right)\right.$$
$$\left. + \frac{L_a L_n}{L_a^2 + L_n^2}\left[\left(\coth\left(\frac{T - W_{scr} - T_p}{L_n} - \frac{L_p}{L_a}\right)e^{-(W_{scr}-T_p)/L_a}\right) - \frac{e^{-T_p/L_a}}{\sinh\left(\frac{T - W_{scr} - T_p}{L_a}\right)}\right]\right)$$

where the first term represents the current in the p^+ region, the second term represents the current in the space charge/intrinsic region, and the third term represent the current in the *n* region. L_a is the absorption length of the penetrating photon and $T_{p/n}$ are the thicknesses of the *p* and *n* region. The derivation is based on the model shown in figure 2.2.b.iv.ii.

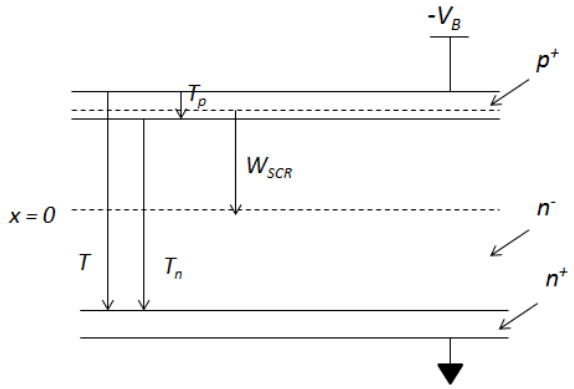

Figure 2.2.b.iv.ii: P-I-N geometry used for derivation of photo-generation in each region of the detector

The detector thicknesses will have to be extracted from C-V data because they are not given as figures on datasheets. The complete analysis will offer accurate accounting of collected charge and precise determination the MCA binning versus eV relationship.

Simplifications to this equation can be made once device geometry, fabrication processes and doping profile are known. For instance, for p-i-n photodiodes the surface is doped with a thin passivated layer that is transparent to incident gamma radiation and therefore induced current at the surface may be neglected. Also, the gamma energies we will be measuring will most likely be below 100 keV, so that the penetration depth will be into the space charge/bulk regions. The induced photocurrent in the bulk can then be evaluated via the continuity equation. For the present purposes, however, the induced current in the space region will be evaluated using the relationship provided by responsivity (A/W) as $I_{ph,scr} = \frac{q*QE*I_o}{E_{ph}}$, where I_o is the incident power and A is the active area of the detector. This is because the contribution to current from the surface and bulk can be considered negligible as an approximation for preliminary calibration and device characterization. A plot showing expected induced current is shown sin section 2.1.e It is on the order of femto-amperes, which is expected due to the previously plotted QE and responsivity curves. The current distribution width increases at increased distance into the detector because of generation at the estimated space charge region depths. Since the detected energies will be deeply penetrating, the induced surface current can be neglected. Lastly, the induced photocurrent in the bulk region can be approximated by $I_{ph,bulk} = \frac{q*QE*P}{E_{ph}}\left(\frac{\mu L_p}{1+\mu L_p}\right)(1-e^{-\mu x}) - \frac{qD_p p_{no}}{L_p}$. This will be evaluated for trans-impedance matching during the design section.

2.2.b.v Junction Capacitance and Depletion Voltage

The junction capacitance is essential in determining the time constant for pulse formation, equivalent noise charge, and open-loop gain stability (gain-peaking) when matched to the trans-impedance amplifier. It varies with applied bias, active area, and temperature; it is directly proportional to A and inversely proportional to V_A/W_{SCR}.

Junction capacitance is given as $C_j = A\sqrt{\frac{q\varepsilon_r}{2(V_{bi}-V_A)}\left(\frac{N_A N_D}{N_A+N_D}\right)}$. Design and control of these variables will be used for optimization of detector performance.

The depletion voltage is the applied reverse bias that completely depletes the space charge region. It will be necessary to determine in order to optimize gamma interaction in the SCR, because that is where generation of EHPs dominates and induced photocurrent is largest. It is given by $V_{scr} = \frac{qNW_{scr}^2}{\varepsilon_r}$.

2.2.b.vi Detector Noise

The total noise in a photodiode is due to the superposition of the thermal, generation-recombination, shot, and flicker noises. The dominant mechanism should be isolated and, if possible, reduced. To this end, the decay of Am-241 will be used as a model for estimation in detector choice later.

For a photodiode detector noise is a stationary, ergodic process and is quantitatively analyzed as the power spectrum via Fourier analysis of a characteristic autocorrelation function. This means that the average current noise is distributed over a frequency spectrum and its noise power over a band of positive frequencies, which can be expressed mathematically as $\overline{i_f^2} = \widetilde{S(f)}\Delta f$, where $\widetilde{S(f)}$ is the frequency spectrum and Δf is the detection bandwidth given by $1/2 * t_{int}$ and t_{int} is the integration time. Additionally, this allows the analysis of noise propagation via the noise equivalent circuit to proceed analogously to normal signal evaluation in a linear circuit. The noise is superimposed on the dark current in our detector and is a result of four types of characteristic noise responses: thermal (Johnson/Nyquist) noise, generation-recombination noise, shot noise, and flicker noise.

The thermal noise in our detector is given as $\overline{i_f^2} = \frac{4kT}{R}\tau$. This stems from consideration of the Boltzmann distribution function of an electron and relevant boundary conditions for analysis of the noise power spectrum, as well as the estimated contribution of an electron/hole to the current. The relevant parameter for device design is the resistance R. It is functionally equivalent to the shunt resistance and series resistance seen by the photogenerated current. Typically, the series resistance is small and shows negligible variability from that in the photoconductive mode because of the nearly ideal behavior of the generated current at the ohmic contacts and applied bias being in the reverse regime. However, as a voltage noise it is dependent on the junction capacitance and will be non-negligible. The shunt resistance is a strong function of temperature and materials and must be considered for proper device operation. Effectively, the shunt resistance will double for every 10℃ drop in temperature and, as is apparent from the equation given for thermal noise, the current noise will decrease with increasing shunt resistance. Therefore, operating our device at decreased temperatures will aid in decreasing the thermal noise contribution to the dark current. Additionally, R_{sh} is given on most datasheet so that it will be a figure of merit for detector selection.

Electron-hole pair generation is a random process, so that fluctuations in current are the result of the density of free carries in the detector via Fermi statistics. The resultant current fluctuation is generated due to a density fluctuation if the average velocity of free carriers is non-zero. So, generation-recombination noise presents itself only when the current is non-zero. In other words, G-R noise is due to an applied electric field or doping gradient in the semiconductor. The generation process can have several different physical origins: generation at an impurity site, band-to-band thermionic emission, or photon absorption. In each case, however, the creation time follows a Poisson distribution so that a similar analysis to thermal noise can be applied. Accordingly, the current fluctuation autocorrelation function becomes $S(\omega) = \langle \dot{N} \rangle \left(\frac{qV}{L}\right)^2 \langle \tau \rangle$ and the average current becomes $\langle I \rangle = -\frac{qV}{L}\langle \tau \rangle \langle \dot{N} \rangle$, where $\langle \dot{N} \rangle$ is the generation rate and $\langle \tau \rangle$ is the average lifetime. This yields the expression used for estimating the contribution of generation-recombination noise to the current as $\overline{i_f^2} = 2qgI\frac{\langle \tau^2 \rangle}{\langle \tau \rangle}$, where $g = \frac{v\langle \tau \rangle}{L} = \frac{\langle \tau \rangle}{\tau_{tr}}$ is the photoconductive gain and τ_{tr} is the carrier transit time across a recombination center. Since our device is photoconductive, the simplifying assumption that the radiative lifetime will be distributed via a Poisson process can be made, whereby $\langle \tau^2 \rangle = 2\langle \tau \rangle$ follows. Applying the previous relationship to the current noise gives $\overline{i_f^2} = 4qgI_o\tau$, so that G-R noise can be considered as a generation noise amplified by gain g and added to the recombination noise. So G-R contribution to the dark current will dominate when recombination is non-negligible. This occurs when the free carriers move slowly and when there are a large number of carrier interactions within the neutral region. Therefore, a large minority carrier lifetime and reduced resistivity will improve G-R noise contribution to the dark current, as well as a large space charge region to dominate interaction. Since both the carrier lifetime and resistivity are inversely proportional to the concentration, a low to moderately doped detector will counteract the applied voltage effects. Additionally, G-R noise is decreased when photoconductive gain is negligible, signifying why and an APD will not be considered for our device.

Shot noise (quantum noise) is a quantum phenomenon resulting from the statistical uncertainty in the photon – EHP process and random thermal G-R rate. Note that thermal G-R does not factor into the G-R noise because G-R noise is dominated by density fluctuations in an extrinsic semiconductor – applied voltage or concentration gradient. Shot noise effects are seen as RMS noise added to the photo-generated current given by $i_f^2 = 2qI_{ph}\tau$. Since an applied voltage will be used to improve other aspects of our detector response, the shot noise will be non-negligible in noise analysis. Improving the thermal response by operating the detector at decreased temperatures will be necessary to nullify its effects.

Flicker noise is due to process variations and intrinsic device defects and shows dependence on DC current and frequency variations. The expression describing these dependencies is given by $\overline{i_f^2} = \frac{2k\tau I_{DC}}{f}$ where the coefficient k is an empirical quantity that shows intra-device variation and f is the low frequency limit, which is typically < 100 Hz.

Ideally the flicker noise is a function of only $1/f$ and is reduced for high frequency applications.

The total current noise is then the sum of each individual noise component and is given by $\overline{i_n^2} = \frac{4kT}{R_{sh}}\tau + 4qI_o\tau + 2qI_{ph}\tau + \frac{k_f \tau I_{DC}}{f}$.

2.2.b.vii Temperature Effects

If the irradiation energy incident on a semiconductor detector exceeds the semiconductor bandgap energy such that it breaks a bound electron free, then the electron can contribute to the photogenerated current. However, for high energy photon interaction (above UV) that far exceeds E_g, there is an excess of absorbed energy. This excess energy effectively heats up the semiconductor via thermionic and phonon interactions and degrades device operation by affecting charge mobility (i.e., conductivity), band-gap energy, and intrinsic carrier concentration. The temperature dependence of the reverse saturation current and noise parameters are evaluated in their respective sections. In each case, the relevant expression can be found in most semiconductor texts, but we will be using *Device Electronics for Integrated Circuits*. They are given in table 2.2.b.vii.i below.

Temperature Dependent Parameters	
electron/hole mobility	$u_n = 88T_n^{-0.57} + \frac{1250T_n^{-2.33}}{1 + \left[\frac{N}{1.26 \times 10^{17} T_n^{2.4}}\right] 0.88T_n^{-0.146}}$ $u_p = 54.3T_n^{-0.57} + \frac{407T_n^{-2.33}}{1 + \left[\frac{N}{2.35 \times 10^{17} T_n^{2.4}}\right] 0.88T_n^{-0.146}}$ $T_n = {}^{T}/_{300}$ and N is the dopant concentration
intrinsic carrier concentration	$n_i = 3.87 \times 10^{16} T^{3/2} e^{-(.00702)/T}$
band-gap energy	$E_g = 1.166 - \frac{4.73 \cdot 10^{-4} T^2}{T + 636}$
diffusion coefficient	$D_n = u_n \frac{kT}{q}$ *and* $D_p = u_p \frac{kT}{q}$
Built-in voltage	$V_{bi} = \frac{kT}{q} ln \frac{N_A N_D}{n_i^2}$

Table 2.2.b.vii.i: Temperature dependence of reverse saturation current and noise parameters

2.2.c Performance Characteristics

The operation of the detector can be characterized by several distinct parameters that, in effect, determine the spectral output. These include the dark current, noise equivalent power, detectivity, equivalent noise charge, fano factor, and resolution/full-width half maximum.

2.2.c.i Dark Current

The dark current is a datasheet parameter equivalent to the leakage current/reverse saturation current of a p-n junction diode. For direct detection, the dark current must be evaluated and added to the equivalent circuit model for pulse collection and MCA linearity analysis because at room temperature it is of the same order of magnitude as the generated photocurrent.

The dark current is the amount of current that flows through the detector when it is non-operational. Since our device is operating at a reverse bias, the photodiode current given by $I_D = I_s\left(e^{qV_B/kT} - 1\right) = -I_s$. It is determined from device geometry and is a strong function of temperature. For both p-n and p-i-n photodiode geometries, the reverse saturation current is evaluated normally and it is only necessary to determine whether the bulk width is greater than or less than the diffusion length to fully characterize it. Since we will most likely choose a p-i-n configuration, the diffusion length will be much larger than the bulk width. This ensures reduced recombination in the quasi-neutral region and optimizes current collection. Therefore, the photodiode can be approximated as short-based and the reverse saturation current given as $I_s = qAn_i^2(\frac{D_n}{N_A W_p'} + \frac{D_p}{N_D W_n'})$, where $W_n' = W_n - W_{SCR} - x_p$ and $W_p' = W_p - W_{SCR} - x_n$. Because of the temperature dependence of quantities making up the dark current, it is highly temperature dependent. An empirical relationship for dark current is given from an estimated % increase in I_s per℃, which is typically 15%, resulting in $I_s = 10^{-15}T_f{}^{(T-25)}$. So, at -20℃ the dark current is ~10^{-18} A. From this it is apparent that the dark current can be reduced to a minimum if the detector is operated below 0℃ making it negligible at the signal output.

2.2.c.ii Response Time and Shaping Time

The response time of a photodiode is determined by three time constants: charge collection time, *RC* network rise-time, and the diffusion time. The charge collection time is the amount of time it takes for the applied E (E = V/d) field across the space charge region to sweep the photo-generated carriers to the quasi-neutral regions. Below a maximum applied field, the drift velocity of charge carriers due to E varies proportionally with carrier mobility, but saturates above E_{max}. The drift velocity can be approximated from the relationship shown in the table 2.2.c.ii.i on the next page, with the relevant parameters listed.

$$v_d = v_l \frac{E}{E_c}\left(\frac{1}{1+\left(E/E_c\right)^{\beta}}\right)^{1/\beta}$$

Electrons	Holes
$v_{l,e} = 1.53 \times 10^{9} T^{-0.87}$	$v_{l,h} = 1.62 \times 10^{8} T^{-0.52}$
$E_{c,e} = 1.01 T^{1.55}$	$E_{c,h} = 1.24 T^{1.68}$
$\beta_e = 2.57 \times 10^{-2} T^{0.66}$	$\beta_h = 0.46 T^{0.17}$

Table 2.2.c.ii.i: Drift velocity parameters and relationships

Using the relationship $t_{cc} = W_{SCR}/v_d$ yields the relevant parameter. The rise-time is found from the *RC* network comprised of the parallel combination of the junction and feedback capacitances, and the equivalent load resistance (parallel combination of the series and feedback resistances). It is expressed as $t_{RC} = 2.2 R_{eq} C_{eq}$. The diffusion time is equivalent to the excess carrier lifetime, which is the characteristic decay due to recombination of minority carriers in the quasi-neutral region in order to achieve thermal equilibrium. It is typically determined experimentally and is on average $t_{diff} \leq 10^{-6}\ s$. Combining these three results yields $t_{total} = \sqrt{t_{cc} + t_{RC} + t_{diff}}$.

The shaping time is determined by the equivalent RC network consisting of the charge preamplifier and detector. These will be determined independently of detector selection and then later adjusted for optimization during experimentation.

2.2.c.iii Equivalent Noise Charge

Applicability of silicon detectors is largely determined by the signal-to-noise ratio – as indicated by NEP and D*. From section 2.2.b.iv, the induced photocurrent is low ($\approx 10^{-16}$ A) and because we will be operating the device at roughly -20° C the dark current is negligible so that ideally the entirety of the signal will be due to I_{ph}.

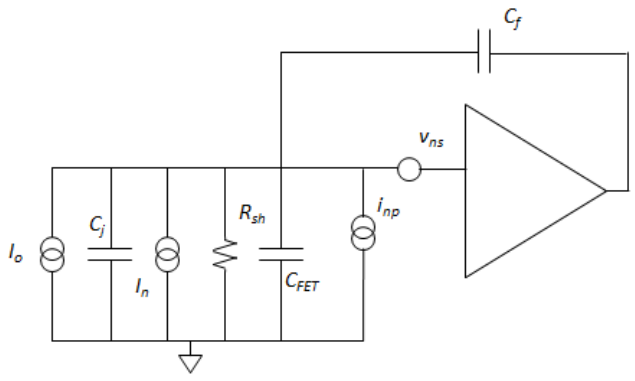

Figure 2.2.c.iii.i : Equivalent noise circuit model

This occurs despite the low ionization energy of silicon because for *p-n*/*p-i-n* photodiodes there is no internal amplification. The noise in the detector can be approximated as the equivalent noise charge, or the # of noise (RMS) electrons, as the noise due to the detector, the dark current, and the input FET of the charge preamplifier. The noise model is given by the figure 2.2.c.iii.i.

The noise due to the detector is given as $\overline{i_n^2} = \frac{4kT}{R_{sh}}\tau + 4qI_{ph}\tau + 2qI_{ph}\tau$. It is evident that any further reductions in noise are the result of reducing the integration time and temperature. The spectral voltage noise due to the series resistance is influenced by the junction capacitance when evaluating equivalent noise charge as Q = CV and also due to it forming an RC network with both the junction and feedback capacitance. It therefore must be included in the analysis and is given by $v_{nRs}^2 = 4kTR_s$. In addition, the noise due to the pre-amplifier is given by the series and parallel spectral noise densities of the op amp input gate, which will be a FET in order to reduce shot noise and allow fast switching speeds. The noise densities are made up of both $1/f$ and white noises. The series contribution can be found as the input voltage noise density at the flicker and flat-band frequencies, and the parallel contribution can be found as the input current noise density at the flicker frequency. They will therefore be op amp dependent and will be optimized during design.

The total ENC due to pulse shaping is found as the sum of squares of the spectral power as $ENC = \sqrt{\left(2qI_{ph}{}^2 + 2qI_o{}^2 + \frac{4kT^2}{R}\right)\tau + \left(4kTR_s{}^2 + v_n^2\right)\frac{C_{tot}^2}{\tau} + 4k_fC_{tot}^2}$, where C_{tot} is the FET and junction capacitance, k_f is the flicker coefficient, and τ is the shaping time. Veljko Radeka in "Detector Signal Process" provides an approximation to be used in place of the above equation, where some of the device parameters will be unknown until all parts are ordered, particularly the photodiode, which can be used instead.

It estimates the contribution as total voltage noise density due entirely to the FET and the current noise from the photodiode as predominately shot noise and is given as $ENC^2 = \frac{1}{2}e_n^2C_{in}^2\frac{A_1}{\tau} + \pi C_{in}^2k_fA_2 + qI_oA_3\tau$. The coefficient A1, A2, and A3 are weighting functions that characterized the shaping scheme. Table 2.2.c.ii.i is provided below.

Weighting Function	Series White A_1	Parallel White A_3	Series 1/f $A_{2(approx.)}$
Triangle	2	0.667	0.87
Semi-Gaussian	2.04	0.90	1.01
CR-RC	1.85	1.85	1.39
CR-RC^4	0.45	1.02	1.39
CR-RC^7	0.34	1.27	1.39
Trapezoidal	2	1.67	1.37

Table 2.2.c.iii.i: Coefficient weighting functions that characterize pulse shaping

The ENC is optimized when the current and voltage noise contributions are equal as displayed in the figure 2.2.c.ii.i below. This is determined by the integration time of the CR-RC shaper and will be evaluated in the corresponding pulse shaping section. Once found, the optimized equivalent noise charge is found by using the equality in the ENC equation given above.

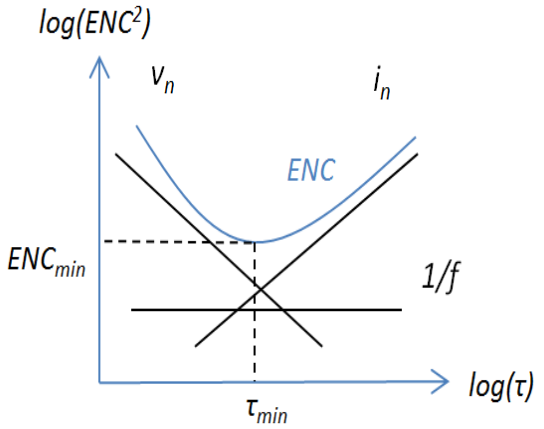

$$\tau_{opt} = \sqrt{\frac{C_{in}^2}{2}\left(\frac{e_n^2 A_1}{q I_o A_3}\right)}$$

Figure 2.2.c.iii.i: Depiction of optimization of equivalent noise charge

2.2.c.iv Noise Equivalent Power

The lower limit for detection of incident radiation for a photodiode is expressed as the incident power corresponding to a signal-to-noise ratio of 1. In other words, when the incident radiation produces a signal (photocurrent) equal to the generated noise, the noise equivalent power has been reached. This rates the device insofar as it allows one to determine the lowest amount of energy that is detectable above the noise threshold. For design concerns, the lower the NEP the better. This is easy to understand because as the NEP approaches zero, the current noise decreases and the signal increases, thereby achieving ideality. Also, because NEP is a function of detector noise it will be a function of the integral bandwidth, which is dependent on the device setup. That is, each measurement system has a unique integration time, so that the integration time of the detector signal will in large part determine the NEP and it will therefore change dramatically from device to device. Matching and optimization will have to occur after the shaping circuitry has been completed and then altered accordingly. As before, for indirect detection the NEP will be rated on the datasheet, and for direct detection it will need to be approximated. For both cases, $NEP = i_n/R$, where i_n is the total noise in the detector alone (or scintillator and detector) and R is the responsivity of the detector.

2.2.c.v Detectivity

The detectivity is defined as the inverse of the NEP and quantifies the minimum detectable power of incident radiation. It sets an upper limit to the detectors ability. Because the detection probability is related to the photodiode active area, the detectivity is often adjusted to become the specific detectivity D^* and is the ratio of the root of the detectors active area to the NEP. The higher the detectivity the better the photodiode is at detecting signals above the noise threshold.

Using the relationships provided for noise, and assuming that the detector is operating outside the range of influence for flicker noise, the current noise is given as $\overline{\imath_n^2} = \frac{4kT}{R}\tau + 4qI_o\tau + 2qI_{ph}\tau$. The induced photocurrent modeled in section 2.2.b.iv will be used along with the dark current equation to yield I_s.

2.2.c.vi Resolution (FWHM)

Given a characteristic radiation energy incident on a detector, the resulting energy distribution will differ depending on detector material. That is, if the same number of pulses are recorded in two distinct detectors the area under each distributed curve will be identical, but the widths different. This is because the widths reflect the amount of fluctuation in recorded pulses, which is limited by the resolving power of detector material, even though the incident energy is the same for both detectors. If the width of the energy distribution is small, then it begins to resemble a (dirac-delta) pulse. If the width of the energy distribution is large, then it begins to resemble a Gaussian (bell) curve. Ideally, a pulse is the desired spectral shape corresponding to a characteristic radioactive decay and the evaluation of a detector is largely determined by its ability to achieve this standard.

The resolution is a statistical quantity and can suffer from any number of fluctuations including: drift of detector operation characteristics, noise due to the detector and shaping electronics, and statistical noise. The first two have been discussed and will be regulated and controlled to achieve optimization. Statistical noise, however, represents a lower limit to resolution that cannot be controlled because it will always be present in the device. It is generated due to the discrete nature of the generated charge and therefore subject to random fluctuations from event to event. However, an estimate can be made as to the amount of statistical fluctuation assuming it occurs via a Poisson process and is given by the standard deviation in the number of generated charge carriers N as $\sqrt{N}$. Formally, the resolution of a detector is given by $Resolution = \frac{FWHM}{H_o}$, where FWHM (full width at half maximum) is the width of the distribution at half the maximum to the peak and H_o is the centroid of the peak. Using the Gaussian distribution function $G(H) = \frac{A}{\sigma\sqrt{2\pi}}\exp\left(\frac{(H-H_o)^2}{2\sigma^2}\right)$ the width parameter defines the FWHM as 2.35σ. As is apparent, the resolution is a dimensionless quantity and is typically given as a percentage, so that the smaller this quantity is the better the detector. This is because, assuming a low percent resolution, the detector can clearly distinguish between two peaks with decay energies close to one another.

The linearity of the detector has been shown above and because of this the approximation $H_o = kN$ can be made, where k is a proportionality constant. The standard deviation in the peak of the pulse height is then given by $\sigma = k\sqrt{N}$. Therefore, the resolution can be rewritten to give the Poisson lower limit as $Res_{limit} = \frac{2.35}{\sqrt{N}}$. From the previous expression, the lower limit to resolution is determined by the number of generated charge carriers and points to the trend that *Res* decreases as N increases. This is displayed graphically for the relevant energies for direct detection in figure 2.2.c.vi.i. Experimental detection resolution, however, varies from the theoretical evaluation given above and

indicates that the Poisson assumption is too simplistic. The Fano factor has been introduced to account for experimental variation and is defined as the ration of the observed variance in the number of generated charge carriers to the predicted Poisson variance. This alters the expression for resolution by $Res_{limit} = 2.35\sqrt{\frac{F}{N}}$. Typical values for the Fano factor for silicon are derived by using the following $F = \frac{E_x}{E_g}\left(\frac{\varepsilon_i}{E_g} - 1\right)$, where E_x is the excitation energy to generate a single EHP and is 0.037 eV for silicon. From this, the Fano factor for silicon is ≈ 0.08, which results in the variation to percent resolution shown in figure 2.2.c.vi.ii.

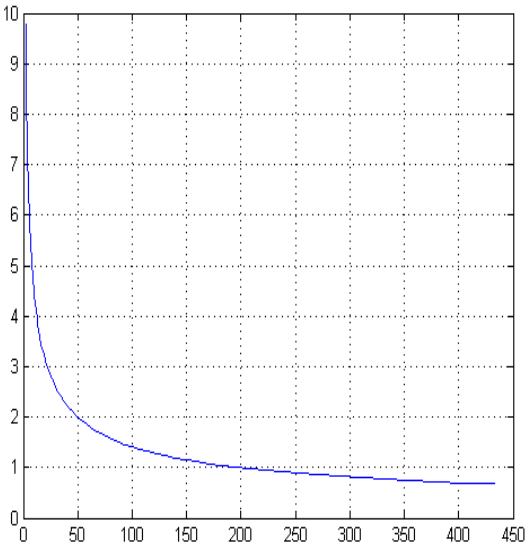

Figure 2.2.c.vi.i: Approximate expected resolution per energy

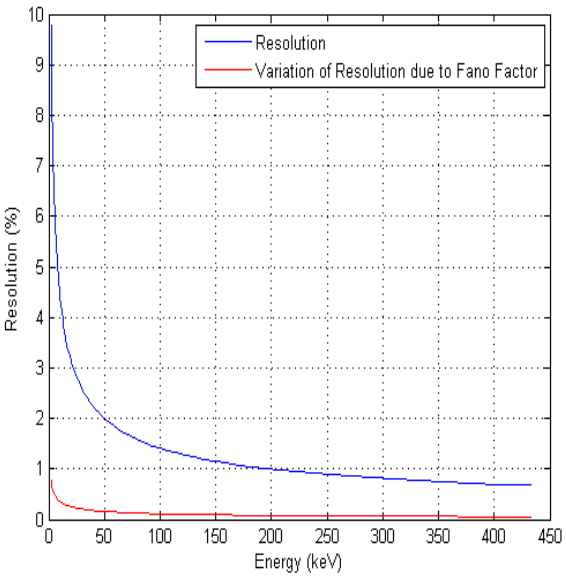

Figure 2.2.c.vi.ii: Approximate expected resolution per energy including variation due to Fano Factor

2.3 SCINTILLATOR CONSIDERATIONS

2.3.a Indirect Interaction Theory of Operation

A scintillator is a material which exhibits luminescence when excited by radiation, and it is the job of the photodiode to accurately detect this induced luminescence. The same semiconductor detector physics for direct detection apply. However, because visible light is produced by the scintillator, the stopping power of the detector is much greater – the transmittance is low - so that absorption and generation rate are very high and the induced photocurrent greatly improved. It also means that detector selection is greatly enhanced because they have been rated in the visible/IR spectrum. In other words, we do not have to estimate the range of operation and approximate the induced photocurrent as in the case of direct detection, and can use the accompanying datasheet for quantum efficiency and responsivity, as well as other performance parameters.

2.3.b Scintillator Technologies

Scintillators operate by transforming high energy radiation into photons by way of luminescence. The resultant light output has a characteristic wavelength and generates a characteristic numbers of photons/MeV, depending on scintillator material. Scintillator materials have a high Z and detection of higher energies – from 100 keV to 2 MeV - is greatly improved and varies with type: plastic, liquid, gas, and crystal(organic/inorganic). We will focus on selection of an inorganic crystal due to their availability and relatively inexpensive cost. There are also several other figures of merit listed along with scintillator material. It is the optimal coupling of these parameters with photodiode that will yield the best results.

The various figures of merit needed for accurate detection of gamma rays is high density for stopping power, small index of refraction, a rated wavelength of maximum emission for optimizing detector choice, a small decay time for high speed detection, large light-output response for greater probability of detection, and a scintillation pulse height data (relative to NaI(Tl)) for photocurrent estimation and binning calibration. Table 2.3.b.i below displays these properties for commonly used scintillators:

Scintillator	Density (g/cm^3)	Index Of Refraction	λ of Max Emmision(nm)	Decay Time (μs)	Pulse Height	Photons/MeV
Inorganic						
NaI	3.67	1.78	303	0.06	190	$4x10^4$
NaI(Tl)	3.67	1.85	410	0.25	100	38,000
CsI	4.51	1.80	310	0.01	6	$4x10^4$
CsI(Tl)	4.51	1.80	565	0.68 - 3.34	45	65,000
CsI(Na)	4.51	1.84	420	0.63	85	39,000
BGO	7.13	2.15	480	0.3	----	8,200
BaF_2	4.88	1.49	190/220/ 310	0.0006- 0.63	5/15	1,400 – 9,500
CeF_3	6.16	1.68	300/340	0.005- 0.020	5	4,400
PWO:Y	8.3	2.20	425/450	0.01- 0.03	----	----
LSO(Cs)/ LYSO(Cs)	7.4	1.82	420	0.04	----	25,000
Lil(Eu)	4.08	1.96	470	1.4	----	11,000
Plastic						
BC-408	1.032	1.58	425	.0021	64	7,500
RP-200	1.02	1.58	435	.0033	38	9,200

Table 2.3.b.i: Properties of commonly used scintillators

Plastic scintillators are much less expensive than inorganic ones and widely available. BGO is widely available and relatively inexpensive, but doesn't show much variation from plastic in photons/MeV. BGOs density is higher than plastics and therefore has greater stopping power. The relevant properties notwithstanding, we will ultimately be guided in our selection of scintillator by cost and availability.

2.3.c Performance Characteristics

The operation of the detector when coupled to a scintillator is similar to that for direct detection, but not the same. Three primary differences are: light yield, scintillator noise, and resolution/FWHM. The light yield gives a measure of photons/MeV incident on the detector and is integral in calculating the induced photocurrent, the total noise increases due to the scintillator and puts less theoretical strain on us because we can use the rated noise values given in the detector datasheet, and the resolution necessarily changes because the added noise changes and the interaction mechanisms in a scintillator are different.

2.3.c.i Light Yield

The ability of a scintillator to convert high energy radiation to light is characterized by its light yield, which is a measure of this capability. It is typically given as a figure in datasheet with units photons/MeV and is quantified by the average energy loss per scintillation photon and given as the quantum efficiency $QE_{sci} = E_{em}N_{pH}/E_{pH}$, where E_{em} is the energy of emitted photons and N_{ph} is the number of photons emitted due to E_{ph}. This relates to the light output by way of $L_{out} = QE_{sci}/E_{em}$. The light output and λ of maximum emission of max emission are given as figures of merit on datasheets, and from these quantities it is possible to calculate both QE_{sci} and N_{ph}.

The light yield is dissipated by two inherent effects. The first is due to temperature. Radiation-scintillator interaction causes the internal temperature to vary and as the temperature increases the light yield decreases. This limits the length of exposure time because cooling the entire scintillator requires a liquid nitrogen bath. There is little that can be done to prevent this from occurring, but tests will be run to demonstrate the length of effective use. The second effect that reduces the light yield is due to the random nature of scattered light. When luminescent photons are generated, they are scattered in every direction. The reflections against the aluminum shield before interaction with the detector occurs causes resolution to decrease. Collimators can be used to decrease these effects by acting as guideposts for light to pass cleanly through.

2.3.c.ii Scintillator Noise

For indirect detection, the dark current for silicon detectors is given as a figure of merit for an equivalent wavelength on all datasheets and will be consulted to achieve the best response for our concerns. To estimate equivalent noise charge, the charge injection test can be performed on the pre-amplifier frond end when the scintillator/photodiode probe is connected. This is due to the induced current having a magnitude in the mA range at the pre-amp input. Otherwise, the equivalent noise charge can be calculated in the same way as shown in section 2.2.c.iii. Additionally, the noise due to the scintillator will have to be considered, but not calculated. This is because the induced photocurrent will much greater than the noise threshold so that device design will not have to be optimized to pull the photocurrent up above the noise threshold as in the case of direct detection. Additional figures or merit related to noise and equivalent noise charge such as NEP and D^* will also be readily available and no calculation will be necessary as the detector will be rated as specified in the datasheet. Spectral resolution will be affected, however, and will be considered next.

2.3.c.iii Resolution (FWHM)

The differentiating factor for indirect versus direct resolution is related to the full width half maximum. It is increased from that of direct detection and therefore worse in terms of resolving. However, because of the range of energies detectable using the scintillator, the payoff is cost effective. The FWHM of typical energies are given on the Lawrence Berkeley National Laboratory scintillator page and has been tabulated below.

Scintillator	Energy Resolution (% FWHM @ 662 keV)
NaI	3.8
NaI(Tl)	5.6
CsI	16.7
CsI(Tl)	5.7
CsI(Na)	7.4
BGO	9.05
Plastic (BC408)	10
LSO	7.9

Table 2.3.c.iii.i: Typical energies at FWHM

The theoretical evaluation of FWHM is given by $\frac{\Delta E}{E} = 2.35\left(\frac{J}{N_{pg}} + \frac{\alpha^2-1}{N_{ph}} + \frac{ENC^2}{N_e}\right)^{1/2}$, where N_{pg} is the number of photogenerated photons, N_{ph} is the number of photons generated by the scintillator, and N_e is the number of electrons at the preamplifier input. The excess noise factor is between $0 < J < 1$, α is the variance due to statistical noise in the scintillator, and the equivalent noise charge. ENC is evaluated in the same way as given in section 2.2.c.

2.4 AMPLIFIERS

2.4.a Preamplifer

At the photodiode front end we require a charge transfer device that will isolate the high impedance from the photodiode from the op amp, thereby allowing instantaneous potential responses from output to input across the feedback network. In addition, we require the output impedance to be low so that it does not load down the proceeding shaping circuitry and degrade the signal. Ultra low noise considerations will have to be optimized against stability to allow optimization of charge collection and thereby resolution. These parameters in many cases will compete, so that the charge preamplifier is simple to conceive, but difficult to design for our concerns. Finally, circuit topology will be considered once noise and stability analysis has been matched, to further reduce any noise contributions.

2.4.a.i Charge Integrating Preamplifiers

Charge integrating preamplifier circuits transfer an input current to a proportional output voltage by isolating the high photodiode impedance from the output and integrating the charge across a feedback capacitance. A large feedback resistor is typically placed in

parallel with the feedback capacitance to effectively discharge the capacitance and the RC network forms the decay constant. This is depicted below in figure 2.4.a.i along with the relevant read-out expressions.

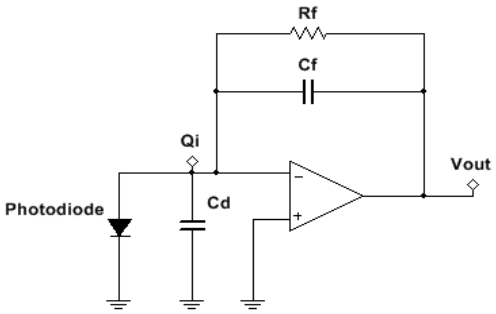

$$V_o(t) = -\frac{Q_i}{C_f}e^{-t/\tau} \text{ and } \tau = R_f C_f$$

Figure 2.4.a.i.i: Typical charge integrating preamplifier

Three device gain parameters are usually shown alongside the output voltage to rate the device: charge gain, sensitivity, and charge collection efficiency. Charge gain is given as the ratio of the output voltage to the input charge and is simply $1/C_f$. The sensitivity of the preamplifier is given as the ratio of the output voltage to MeV of incident radiation and determines the approximate resolution of the read-out signal. Assuming each incident high energy particle produces an EHP that adds to the photocurrent the relationship for the input charge is provided by $Q_i = \frac{qE_{ph}}{\varepsilon_i}$, where ε_i is the ionization energy (Si = 3.6 eV) and E_{ph} is the particle energy in keV. Assuming $t << \tau$, the relationship $V_o = \frac{qE_{ph}}{\varepsilon_i C_f}$ applies so that the μV/keV can be evaluated. This then allows optimization of sensitivity by appropriate choice of feedback capacitance. However, as will become apparent later in this section, the interplay of sensitivity, noise, and stability limits the range of feedback capacitance values when coupled to R_f and complicates optimization so that a balance of several parameters will have to be met. If we assume a 2 pF feedback capacitance, then the sensitivity is roughly 22 μV/keV. For our purposes we will be measuring 0.059 keV particles with direct detection and 0.662 MeV with indirect detection (coupled scintillator/photodiode), which yields an output voltage of 1.3 mV and 14.7 mV respectively. This ensures our read-out will be larger than the sensitivity limit and therefore usable. The charge collection efficiency is the ratio of the input charge to the signal charge and represents the loss of charge due to charge sharing across the detector and equivalent input op amp capacitance. The equivalent input capacitance is found by via the Miller effect as $C_{in} = (1+A_{OL})C_f$. The signal charge at the input is then shared between the parallel combination of the detector capacitance and the equivalent input capacitance as $Q_s = Q_D + Q_i$. Using the parallel voltages relationship, the charge at the input can be related to the signal charge by $Q_i = \frac{Q_s(A_{OL}+1)C_f}{C_D+(A_{OL}+1)C_f}$. The ratio of the input charge to the signal charges give the charge collection efficiency and rates the expected percent charge transferred. So, if the open-loop gain is large, all of the signal charge will be transferred to the output.

Moving forward in the design requires the determination of a stable range of feedback capacitances based on the following equation $C_f = \sqrt{\frac{C_{in}}{2\sqrt{2}\pi f_{GBW} R_f}}$, where C_{in} is the input FET capacitance of the op amp and f_{GBW} is the frequency at which the open-loop is zero. From here, the values of both R_f and C_f will have to be adjusted to achieve a suitable integration time τ. The parallel RC feedback configuration acts as a low pass noise filter and signal shaper. Cutting off too much of the signal will degrade its collection. Leaving too much of the signal in will allow noise to collect. In addition, the speed of incoming pulses is quite high and the integration time needs to be sufficiently quick to avoid charge collection build-up or overlap.

After determination of a suitable RC feedback configuration is made, adjustments related to the intersection of the noise gain and open loop gain will have to be considered. Feedback factor analysis shows that the parallel combination of the input FET and feedback capacitance contributes a zero to the 1/f noise, changing its slope from 0 dB to 20 dB. The intersection of the 1/f curve and open loop gain limits the useful range of operation and is determined by $1 + C_d/C_f$. As the feedback capacitance increases, the zero and pole frequency decrease and the 1/f noise gain contribution correspondingly increases. So the feedback capacitance should be kept low for these purposes. However, considerations of crossover between the noise gain/open-loop gain responses by decreasing feedback capacitance also needs to be kept in mind. This is because the noise-gain will approach infinity if the pole extends beyond $f_c = GBPW/(1 + \frac{C_D}{C_f})$. Competing with these concerns is that the noise gain will flatten out at intersection of the feedback frequency and will extend until it intersects with the open-loop gain -20 dB slope. The problem arises because the noise contribution is evaluated as the integral of the noise density of the bandwidth, which is equivalent to the area under the noise gain plot. Therefore, the larger the flat-band extends until intersection with f_c, the larger the noise contribution.

The analysis of the preamplifier is quite intensive. A complete analysis of the effects of varying feedback capacitance and resistance values will have to be performed, as well as stability analysis. This will have to take account of variations in photodiode capacitance and shunt resistance as well. Note that each variation has a corresponding change in the preamplifier operation. This makes optimum pre amp selection to be of upmost importance for adequate charge collection. Noise analysis will then have to follow after a reasonable range of feedback capacitor and resistor values have been chosen. This evaluation will have to consider both parallel and spectral noise densities without any simplifying assumptions if the matching of photodiode and preamp is to be possible. Unlike the ENC evaluation at the photodiode end, the noise analysis at the output will have to take into account each contribution to noise and optimize the part selection. The details of the analysis will be discussed in each corresponding section. In addition, since evaluation will vary from noise analysis, to stability analysis, to time shaping optimization it will be more effective to deal with each individually rather than correlating them all at once. It will also be imperative to perform in depth experimentation and final adjustments at the design end due to statistical variation and general unreliability of theoretical noise analysis.

2.4.a.ii Noise Analysis

Proper component selection for the charge amplifier involves finding a balance between the desired gain of the amplifier (1/Cf) and equivalent noise charge which is dependent on the voltage noise on the output of the opamp. These parameters must be optimized while ensuring stability of the amplifier, which puts a constraint on the value of the feedback capacitor. The goal is therefore to minimize noise while maximizing the gain. To aid in noise analysis the article "Noise In Photodiode Applications" by Art Kay and Bryan Zhao was utilized. The process involves finding the circuit's output voltage noise density spectrum. This function can be integrated over the circuit's bandwidth, yielding an RMS voltage noise. This value can be determined while varying parameters of interest such as the feedback capacitance using a software package like MATLAB. If these curves are plotted for a variety of low noise opamps we can optimize the selection of the circuit's component values as well as the selection of the opamp.

Figure 2.4.a.ii.i displays the model used in noise analysis of the amplifier. Cd is the photodiode's capacitance, id is the photodiode's shot noise caused by dark current, Rsh is the shunt resistance of the photodiode, Cin is the opamp's input capacitance, Vn is the opamp's voltage noise, and in is the opamp's input current noise.

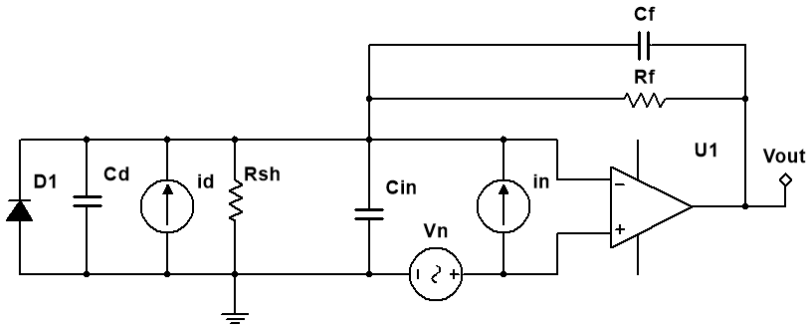

Figure 2.4.a.ii.i: Model used in noise analysis amplifer

There are several sources of noise in this circuit: the photodiode's shot noise and thermal noise (due to shunt resistance), the opamp's voltage noise and current noise, and the thermal noise of the feedback resistor. Cd, Cin, and Cf together with Rsh and Rf will determine the noise gain of the circuit. The noise gain will contain both a zero and a pole due to the effects of the photodiode's capacitance, the opamp's input capacitance, and the feedback capacitance. Combining the opamp's voltage noise density with the noise gain and the opamp's open loop gain enables determination of the total output noise of the circuit. Figure 2.4.a.ii.ii shows the different spectral components that combine to form the output voltage noise density.

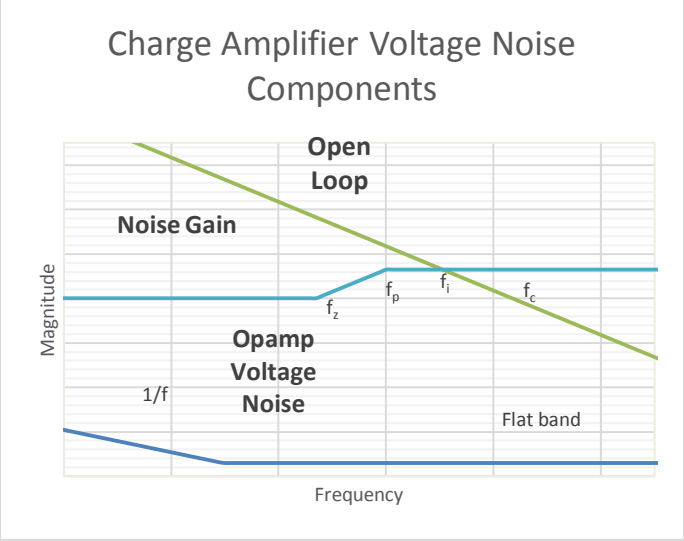

Figure 2.4.a.ii.ii: Components of charge amplifier output voltage noise

The output referred voltage noise due to the opamp's voltage noise is equal to the noise gain multiplied by the opamp's voltage noise density. Note that the opamp's open loop gain will cause the noise density to roll off at the point of intersection of the noise gain and open loop gain. fz is the noise gain zero formed by the input capacitance, fp is the pole formed by the feedback capacitance, fi is the point of intersection of noise gain and open loop gain (the point where they are equal), and fc is the opamp's unity gain bandwidth. These components can be combined to form the output referred voltage noise density from the opamp voltage noise. See figure 2.4.a.ii.iii for an illustration of the output voltage noise density.

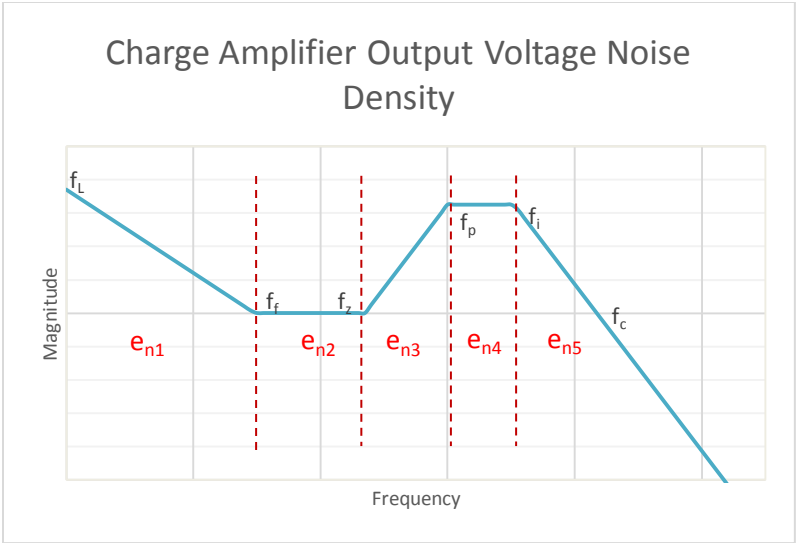

Figure 2.4.a.ii.iii: Output voltage noise density showing different noise voltage regions

The first region is formed by the 1/f noise from the opamp voltage noise combined with the noise gain and levels off at the 1/f corner frequency. The second region is formed by the flat band voltage noise and the noise gain. The slope in the third region is due to the zero in the noise gain from the input and photodiode capacitance. This slope levels off due to a pole caused by the feedback capacitance (region four). Finally the intersection of noise gain and open loop gain causes the noise density to roll off in region five. The equations for the contribution to total voltage noise from these regions are given in. f_f is the 1/f corner frequency, f_L is the starting frequency (0.1Hz usually), and C_i is the input capacitance of the opamp plus the photodiode capacitance. Note that these equations assume that f_z and f_p lie to the right of f_f. The equations must be rewritten if the zero or pole position has moved into a different region (this is possible with certain values of C_i and C_f). Once these noise voltages have been calculated the total output voltage noise due to the opamp voltage noise density is $e_n = \sqrt{e_{n1}^2 + e_{n2}^2 + e_{n3}^2 + e_{n4}^2 + e_{n5}^2}$. Next the feedback resistor thermal noise and the voltage noise due to photodiode current noise must be calculated and added to the opamp voltage noise e_n.

Region	Total Voltage Noise
1	$e_{n1}^2 = e_{nf}^2 f_f \ln\left(\frac{f_f}{f_L}\right)$
2	$e_{n2}^2 = e_{nf}^2 (f_z - f_f)$
3	$e_{n3}^2 = \left(\frac{e_{nf}}{f_z}\right)^2 \left(\frac{f_p^3 - f_z^3}{3}\right)$
4	$e_{n4}^2 = \left(e_{nf}\frac{C_i + C_f}{C_f}\right)^2 (f_i - f_p)$
5	$e_{n5}^2 = \frac{\left(e_{nf} f_c\right)^2}{f_i}$

Table 2.4.a.ii.i: Total voltage noise equations for charge amplifier noise density

The thermal noise of the feedback resistor is given by $e_{nR} = \sqrt{4KTR_f BW}$ where $BW = \frac{\pi}{2}\frac{1}{2\pi R_f C_f}$. The voltage noise contribution due to the photodiode's current noise and opamp's current noise is given by $e_{ni} = i_n R_f \sqrt{BW}$ where the total current noise is $i_n = \sqrt{i_{n\_opa}^2 + i_{nd}^2}$. Current noise density of opamp is given in datasheet, while the diode current noise is given by $i_{nd}^2 = i_{sd}^2 + i_{Rsh}^2 = \frac{4KT}{Rsh} + 2qi_d$ where i_{sd} is the shot noise due to photodiode dark current (i_d) and i_{Rsh} is the current noise of the shunt resistance of the photodiode. Summing all noises we get: $e_{n\_total} = \sqrt{e_n^2 + e_{nR}^2 + e_{ni}^2}$.

2.4.a.iii JFET Buffer Stage

The noise analysis provided above indicates that the current noise contribution across the feedback resistor will dominate for low feedback capacitance values because of its bandwidth dependence. Simply selecting a low current noise density op amp will not work because we will see a correspondingly large voltage noise density as they are inversely related. This will offset the reduced current noise and prevent optimization. This indicates that we must select an op amp with ultra-low voltage noise density and provide a path to ground for the current noise density to travel.

The following diagram represents a method for accomplishing this goal. The inverting terminal adds current noise to the feedback loop by way of $I_{na}R_f$ a traditional configuration. However, in the configuration below, the current noise will add voltage noise in the same way, but across source resistance not across the feedback resistance. Since the source resistance will be kept small the voltage noise contribution across it will be small compared to the voltage noise caused by the feedback resistor.

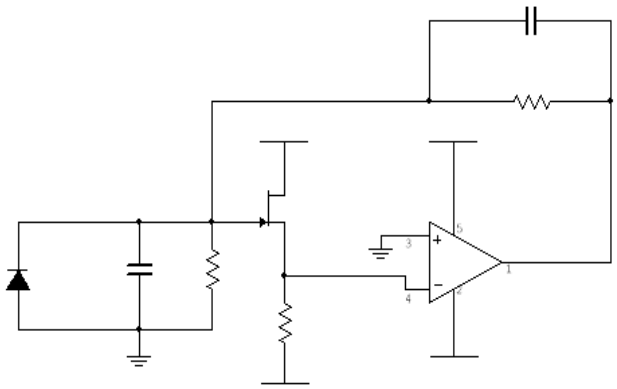

Figure 2.4.a.iii.i: Typical configuration utilizing a JFET buffer stage

The addition of the FET does not change the noise analysis considerably. Rather, in the new configuration the current noise due to the op amp can be neglected and in its place the voltage noise due to the source resistor added along with the FET voltage noise density. This, however, is negligible if the transconductance of the FET is large and the source resistor small. In the first instance, the voltage noise model of the JFET is dominated by Johnson noise, which is inversely proportional to the transconductance so that a large transconductance will reduce the voltage noise effect. This is easiliy accounted for and a common design parameter of JFET devices. The relationship that will be used for noise analysis is provided by $e_n^2 = \frac{8kT}{3g_m}$. The current noise of the FET can be neglected because it is virtually zero. An analysis of the improved noise configuration will be supplied in the design section to compare with traditional charge preamplifier configurations.

2.4.a.iv Stability

While voltage-feedback amplifiers are very versatile and accurate, capacitive circuit effects can have a tendency to make them unstable. Circuit instability is usually defined as some undesired oscillatory effect in the output of the circuit. For our purposes we do not only want the circuit to be stable (as in, no oscillation), but we would also like to design the circuit to have good phase response and a minimal amount of overshoot and ringing. These effects occur before the circuit reaches an oscillatory state. This section will analyze the stability of the charge amplifier as far as it pertains to the project.

Figure 2.4.a.iv.i shows the charge amplifier configuration used in stability analysis. Rf and Cs represent feedback resistance and capacitance, with a total impedance Z_f. Cs and Rs represent the photodiode capacitance and resistance, with a total impedance of Z_i.

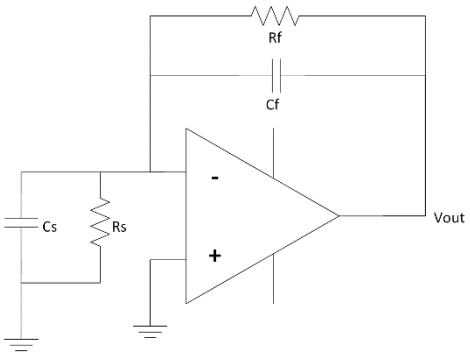

Figure 2.4.a.iv.i: Charge amplifier with Cs and Rs representing photodiode capacitance and shunt resistance, respectively

The fraction of the output voltage fed back to the input of a voltage feedback amplifier is $\beta(f) = \left(\frac{Z_i}{Z_i+Z_f}\right)$. Noise gain is defined as the gain applied to an opamp's voltage noise when it appears at the output. Voltage noise in opamps is modeled at the non-inverting input. For a standard non-inverting or inverting amplifier the noise gain is equal to the non-inverting gain, $1 + \frac{R_f}{R_1}$, or the reciprocal of the feedback fraction β. The noise gain for the charge amplifier is $A_N = \frac{1}{\beta} = \frac{Z_i + Z_f}{Z_i}$.

This noise gain assumes an ideal opamp with infinite open loop gain. In reality the noise gain for an opamp with finite open loop gain is $A_{NT} = A_N(1/(1 + \frac{A_N}{A_0}))$ where A_o is the amplifier's open loop gain.

Operational amplifiers typically have a single dominant pole inserted into the open loop gain to reduce any nonlinearity caused by components inside the opamp. The equation for a single pole open loop response is $A_o(\omega) = \frac{A_o}{1+\frac{j\omega}{\omega_o}}$.

A measure of feedback stability used for opamps is gain margin and phase margin. Gain margin is the difference between unity gain and the gain measured at the point where phase goes to $\pm 180°$ on a bode plot. Phase margin measures how close the phase is to $\pm 180°$ (whichever is closest) at the unity gain point. Gain margin is used as it is important to have a gain of less than unity when the phase causes a sign reversal. A negative feedback system with unity gain and $180°$ phase would cause positive feedback, making the system saturate and become unstable. Phase margin is used as it can measure the amount of overshoot or ringing a system may have. Generally a phase margin of at least $45 - 60°$ is desired.

Instead of using the transfer function of a transimpedance or charge amplifier for stability analysis one can use the noise gain and open loop gain functions. Since feedback into the operational amplifier is equal to the attenuation factor multiplied with the open loop gain ($\beta(j\omega) * A_o(j\omega)$, or $\frac{A_0(j\omega)}{A_N(j\omega)}$), for stability a phase margin of at least $45°$ is desired at the intersection point of the open loop gain and noise gain (unity gain of the feedback transfer function). This is equivalent to a net slope between the two functions of $20dB$ or less at the point of intersection, as a $40dB$ difference would eventually lead to a $180°$ phase shift. Figure 2.4.a.iv.ii illustrates this concept.

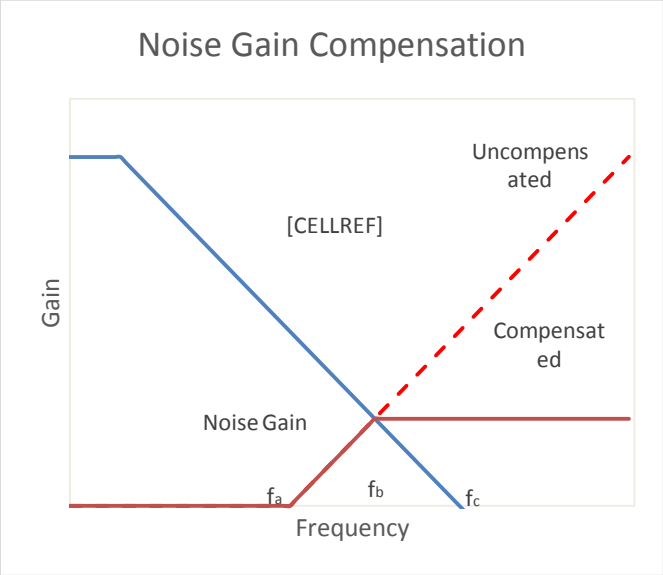

Figure 2.4.a.iv.ii: Noise gain compensation is required in transimpedance (charge) amplifers to meet the 20 dB slope requirement. This involves placing a pole system by adding a feedback capacitor.

Figure 2.4.a.iv.ii shows the general shape of the opamp open loop gain and noise gain on a bode plot. The uncompensated noise gain is the noise gain without feedback capacitor C_f. The compensated noise gain is due to the addition of the feedback capacitor C_f (figure 2.4.a.iv.i). The zero at f_a is due to the capacitance of the photodiode while the pole that levels off the compensated noise gain at f_b is due to the added feedback capacitance. The frequencies are $f_a = \frac{1}{2\pi R_s C_s}$ and $f_b = \frac{1}{2\pi R_f C_f}$. f_c is simply the opamp's unity gain frequency. By calculating C_f so that f_b is the mean of points f_a and f_c we can avoid a

lengthy derivation and take a shortcut to find a proper value of C_f to ensure a phase of $45°$ at the point of intersection. Because the three points form an isosceles triangle and all sides are equal length $f_b = \sqrt{f_a f_c}$. Since we know the equations that define these points we can substitute them to find C_f. Solving for C_f, we find $C_f = \sqrt{\frac{C_s}{2\pi R_f f_c}}$. This value will provide a phase margin of $45°$. A larger capacitance will decrease the circuit's bandwidth and increase the phase margin. Once C_f has been chosen the value can be further optimized experimentally by varying it and observing the impulse response of the circuit. This will account for any side effects such as input capacitance.

One final note to consider is that while it may seem beneficial to increase C_f to ensure circuit stability, this may not be a good choice if high gain is necessary on the preamplifier stage. This is because the gain of the charge amplifier is inversely proportional to the feedback capacitance. In practice this value must be carefully optimized to maximize circuit gain while ensuring stability. On the other hand, circuit bandwidth will also need to be taken into consideration. Noise gain determines the amplification of any noise voltage present on the input of the opamp (hence the name). Therefore if bandwidth is increased the spectral density of the noise gain is increased as well. Even worse, as the noise increases in frequency the amplification increases nonlinearly at a rate of 20dB per decade. It is therefore crucial to find an optimum balance between gain, bandwidth, phase margin, and noise. This will require careful design of the preamplifier circuit configuration and the photodiode itself (due to the device's capacitance).

2.4.b Pulse Shaping

Every signal has its natural spectrum in a frequency domain and a noise spectrum is added to it. Pulse shaper circuits are used to manipulate a signal to achieve a desired output. Essentially, pulse shapers are implemented as filters to improve the signal noise level. For the purpose of this project we will implement a Gaussian filter. A Gaussian filter is a filter whose impulse response is a Gaussian function. Gaussian filters have the properties of having no overshoot to a step function input while minimizing the rise and fall time. This behavior is closely connected to the fact that the Gaussian filter has the minimum possible group delay. Mathematically, a Gaussian filter modifies the input signal by convolution with a Gaussian function. The shaping function of the main amplifier is vital to the production of high-quality spectra. Essentially, the amplified pulses are shaped to optimize the signal-to-noise ratio and to meet the pulse-shape requirements of the pulse-height-analysis electronics. Because single-channel and multichannel analyzers measure the input pulse amplitude with respect to an internal reference voltage, the amplifier output must return quickly to a stable voltage level, usually zero, between gamma-ray pulses. The stability of the baseline fluctuation distorts the measurement of the gamma-ray pulse amplitude and contributes to the broadening of the full energy peak. A narrow pulse shape permits a quick return to the baseline. However, the pulse must be wide enough to allow sufficient time to collect all of the charge liberated by the interaction of the gamma ray detector. The pulse shaper should also provide a signal-to-noise ratio that minimizes the variation in output pulse amplitude for a given quantity of charge quantity deposited by the preamplifier unit.

2.4.b.i Differentiator

Qualitatively, differentiation removes all low frequencies. Differentiation is characterized by a time constant, usually having units of microseconds, that defines the degree of attenuation as a function of frequency. The greater the time constant, the greater the attenuation of low frequencies by the differentiation. When both differentiation and integration are used, the low and high frequency components are strongly suppressed and a relatively narrow band of middle frequencies are passed and amplified. Most spectroscopy amplifiers function best when the differentiation and integration constants are equal. We will adopt this rule and keep out time constants equal to ensure the optimal output and symmetrical pulses. We will mention the integrator more extensively in the next section. Generally, capacitor current moves through the feedback resistor, producing a drop across it, which is the same as the output voltage. A linear, positive rate of input voltage change will result in a steady negative voltage at the output of the op-amp. Conversely, a linear, negative rate of input voltage change will result in a steady positive voltage at the output of the op-amp. This polarity inversion from input to output is due to the fact that the input signal is being sent (essentially) to the inverting input of the op-amp, so it acts like the inverting amplifier mentioned previously. The faster the rate of voltage change at the input (either positive or negative), the greater the voltage at the output.

The input signal to the differentiator is applied to the capacitor. The capacitor blocks any DC content so there is no current flow to the amplifier summing point, at the negative terminal of the operational amplifier, resulting in zero output voltage. The capacitor only allows AC type input voltage changes to pass through and whose frequency is dependent on the rate of change of the input signal. At low frequencies the reactance of the capacitor is "High" resulting in a low gain (R_2/X_c) and low output voltage from the op-amp. At higher frequencies the reactance of the capacitor is much lower resulting in a higher gain and higher output voltage from the differentiator amplifier. However, at high frequencies an op-amp differentiator circuit becomes unstable and will start to oscillate. This is due mainly to the first-order effect, which determines the frequency response of the op-amp circuit causing a second-order response which, at high frequencies gives an output voltage far higher than what would be expected. To avoid this high frequency gain of the circuit needs to be reduced by adding an additional small value capacitor across the feedback resistor R_2. The equation below (equation 1) governs the output voltage of the differentiator. Equation 1: $V_{out} = -R_f(C)*(dV_{IN}/dt)$.

Two major disadvantages of the differentiator op-amp is that it suffers from instability at high frequencies as mentioned above, and the other is that the capacitive input makes it very susceptible to random noise signals and any noise or harmonics present in the source circuit will be amplified more than the signal itself. This is because the output is proportional to the slope of the input voltage so some means of limiting the bandwidth in order to achieve closed-loop stability is required. The first phase of the pulse shaper is the differentiator; the output of the preamplifier is directly being fed into the pulse shaper. This means that there will need to be some shielding between the pulse shaper and the preamplifier to block out the noise or have the two circuits on different boards. Consider the improved op-amp differentiation circuit, if we add a resistor at the input, $R_{in.}$ Adding

the input resistor limits the differentiators increase in gain at a ratio of (R_f/R_{in}). The circuit now acts like a differentiator amplifier at low frequencies and an amplifier at high feedback frequencies giving much better noise rejection. Additional attenuation of higher frequencies is accomplished by connecting a feedback capacitor in parallel with the differentiator feedback resistors, as mentioned above.

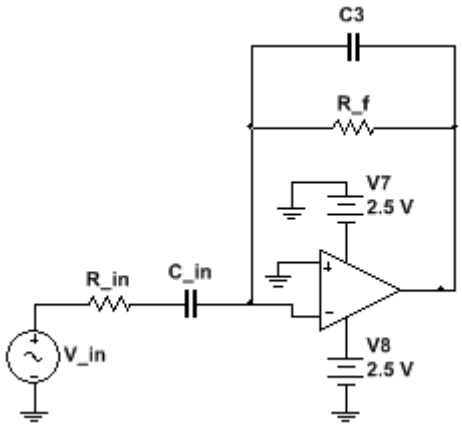

Figure 2.4.b.i.i: Differentiator

2.4.b.ii Integrator

Qualitatively, integration removes all high frequencies. Integration is characterized by a time constant, usually having units of microseconds, that defines the degree of attenuation as a function of frequency. The integrator configuration performs the mathematical operation of integration, which means we can cause the output to respond to changes in the input voltage over time as the op-amp integrator produces an output voltage which is proportional to the integral of the input voltage. In other words the magnitude of the output signal is determined by the length of time a voltage is present at its input as the current through the feedback loop charges or discharges the capacitor as the required negative feedback occurs through the capacitor. As the feedback capacitor C begins to charge up due to the influence of the input voltage, its impedance X_c slowly increase in proportion to its rate of charge.

The capacitor charges up at a rate determined by the RC time constant, (τ) of the series RC network, as mentioned above. Negative feedback forces the op-amp to produce an output voltage that maintains a virtual ground at the op-amp's inverting input. Since the capacitor is connected between the op-amp's inverting input (which is at ground potential) and the op-amp's output (which is negative), the potential voltage, V_c developed across the capacitor slowly increases causing the charging current to decrease as the impedance of the capacitor increases. This results in the ratio of X_c/R_{in} increasing producing a linearly increasing ramp output voltage that continues to increase until the capacitor is fully charged. At this point the capacitor acts as an open circuit, blocking anymore flow of DC current. The ratio of feedback capacitor to input

resistor (X_c/R_{in}) is now infinite resulting in infinite gain. The result of this high gain (similar to the op-amps open-loop gain), is that the output of the amplifier goes into saturation as shown below.

If we changed the square wave input signal to that of a sine wave of varying frequency the op-amp integrator performs less like an integrator and begins to behave more like an active low pass filter, passing low frequency signals while attenuating the high frequencies. This circuit connects a high value resistance in parallel with a continuously charging and discharging capacitor. The addition of this feedback resistor, R_2 across the capacitor, C gives the circuit the characteristics of an inverting amplifier with finite closed-loop gain of R_2/R_1. The result is at very low frequencies the circuit acts as a standard integrator, while at higher frequencies the capacitor shorts out the feedback resistor, R_2 due to the effects of capacitive reactance reducing the amplifiers gain.

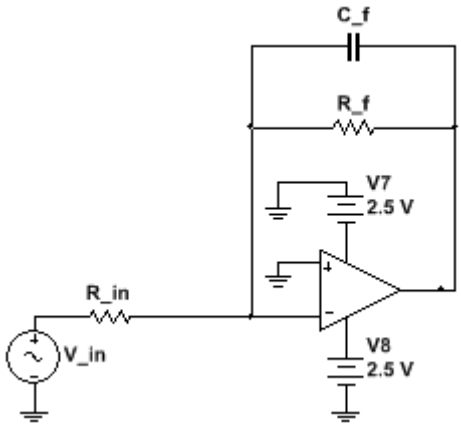

Figure 2.4.b.ii.i: Integrator

2.4.b.iii Circuit Topology

The output of the preamplifier will be the input of the pulse shaper. The output of the preamplifier will be in the microvolts range and will directly be fed into the differentiator, the first configuration of the pulse shaper, as shown in figure 3. The pulse shaper will also be responsible for amplifying the output signal from microvolts to volts. The differentiator amplifier converts DC voltage to a pulse with pole zero cancellation. The integrator amplifiers convert a pulse to gauss pulse instead of cusp pulse and separates it from noise. Cusp pulse is ideal for integrator amplifier. The simplest concept for pulse shaping is the use of a CR high-pass filter followed by an RC low-pass filter. In the amplifier, the preamplifier signal first passes through a CR, high-pass filter. This improves the signal-to-noise ratio by attenuating the low frequencies, which contain a lot of noise and very little signal, as mentioned in the differentiator section. The decay time of the pulse is also shortened by this filter. For that reason, it is often referred to as a CR differentiator. Just before the pulse reaches the output of the amplifier, it passes through an RC low-pass filter. This improves the signal-to-noise ratio by attenuating high frequencies, which contain excessive noise. The rise time of the pulse is lengthened by this filter.

Typically, the differentiation time constant $\tau_D = C_D R_D$ is set equal to the integration time constant $\tau_I = R_I C_I$. In that case, the output pulse rises slowly and reaches its maximum amplitude. The decay back to baseline is controlled primarily by the time constant of the CR differentiator. In this simple circuit there is no compensation for the long decay time of the preamplifier. Consequently, there is a small amplitude undershoot. This undershoot decays back to baseline with the long time constant provided by the preamplifier output pulse. This pulse-shaping technique can be used with scintillation detectors, which was studied for research purposes. For this application, the shaping time constant t should be chosen to be at least three times the decay time constant of the detector to ensure complete integration of the signal.

In our research we explored silicon and germanium detectors. On silicon and germanium detectors, the electronic noise at the preamplifier input makes a noticeable contribution to the energy resolution of the detector. This noise contribution can be minimized by choosing the appropriate amplifier shaping time constant. At short shaping time constants, the series noise component of the preamplifier is dominant. This noise is typically caused by thermal noise in the channel of the field-effect transistor, which is the first amplifying stage in the preamplifier. At long shaping time constants the parallel noise component at the preamplifier input dominates. This component arises from noise sources that are effectively in parallel with the detector at the preamplifier input (e.g., detector leakage current, gate leakage current in the field-effect transistor, and thermal noise in the preamplifier feedback resistor). The total noise at any shaping time constant is the square root of the sum of the squares of the series and parallel noise contributions. Consequently, the total noise has a minimum value at the shaping time constant where the series noise is equal to the parallel noise. This time constant is called the "noise corner time constant." The time constant for minimum noise will depend on the characteristics of the detector, the preamplifier, and the amplifier pulse shaping network. For silicon charged-particle detectors, the minimum noise usually occurs at time constants in the range from 0.5 to 1 µs. Generally, minimum noise for germanium and Si (Li) detectors is achieved at much longer time constants (in the range from 6 to 20 µs). Such long time constants impose a severe restriction on the counting rate capability. Consequently, energy resolution is often compromised by using shorter shaping time constants, in order to accommodate higher counting rates.

Finally, the circuit configuration of the pulse shaper, as shown below, will consist of one differentiator and three integrators. As previously discussed, the differentiator will act as a high pass filter and the integrators will act as low pass filters. The reason we chose three integrators is to ensure that we improve the signal-to-noise ratio by attenuating high frequencies, which contain excessive noise and to lengthen the rise time of the pulse. Final pulse shaper configuration is shown in figure 2.4.b.iii.i on the following page.

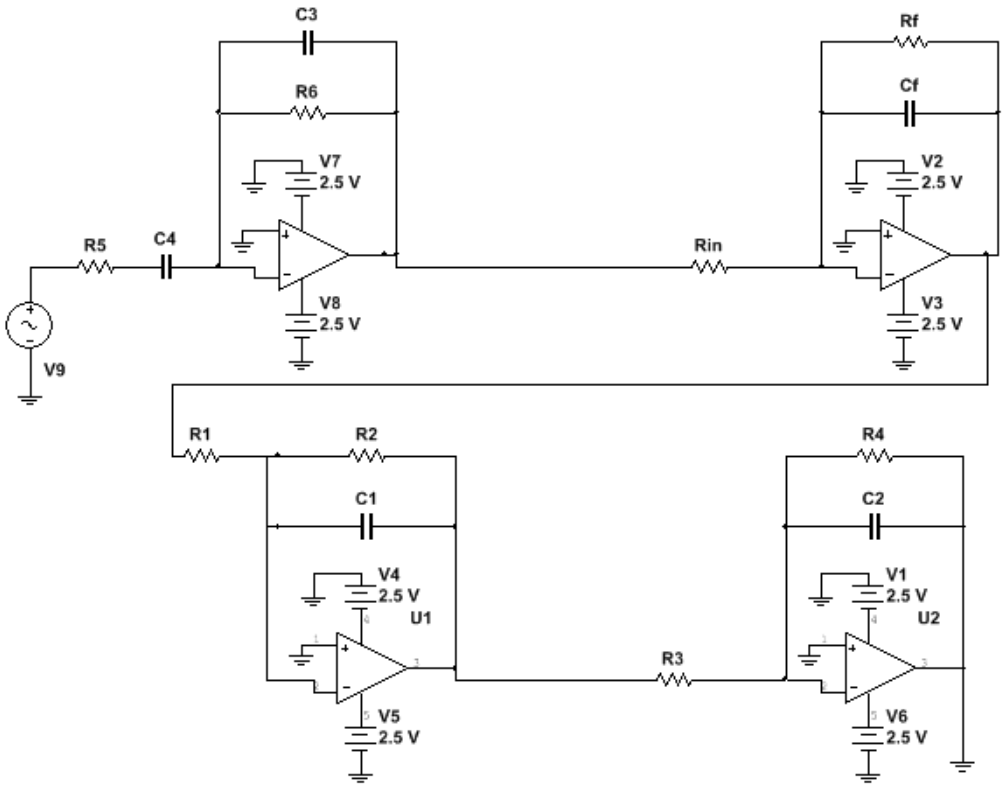

Figure 2.4.b.iii.i: Pulse Shaper

2.4.b.iv Pulse Processing & Equivalent Noise Charge

Two main objectives to consider when processing the pulse are signal-to-noise ratio and to improve pulse pair resolution. These two objectives are somewhat conflicting and a fair balance between the two must be maintained in order to retrieve optimal signal. Improving signal-to-noise ratio increases the pulse width. Typically, the pulse shaper transforms a narrow detector current pulse to a broader pulse, to reduce electronic noise, with a gradually rounded maximum at the peak time. If the shape of the pulse does not change with the signal level, the peak amplitude is also measure of the energy, pulse height measurements or pulse height analysis is used to measure the energy spectrum.

The second objective is improving pulse pair production, by reducing pulse pile-up. Pulse pile-up is when pulses arrive closer in time than the pulse resolution time for a give system. If the pulses are very close in time the system will simply record the two pulses as a single event with combined pulse amplitude, this is known as peak pile-up. If the pulses are spaced further apart the system may simply accept both events and record the incorrect pulse amplitude, this is known as tail pile-up. In both of the aforementioned cases the events will end up in the wrong energy channels and the spectrum will be incorrect. Reducing shaping time will eliminate pile-up. Improving pulse pair production to separate pulses will decrease pulse width. We will have to maintain a decent pulse width and reduce pile-up to obtain correct results. For the pulse shaper circuit, when both time constants (RC) are equal for both configurations, the circuit will exhibit similar

behavior to the one shown below. The integrator will act as a low pass filter allowing lower frequencies to pass and the differentiator will act as a high pass filter allowing higher frequencies to pass. The combined frequency response is shown in the figure below.

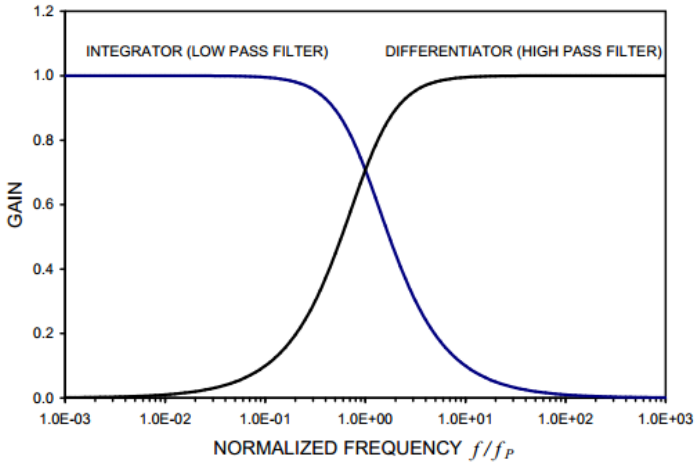

Figure 2.4.b.iv.i: Integrator and Differentiator filtering

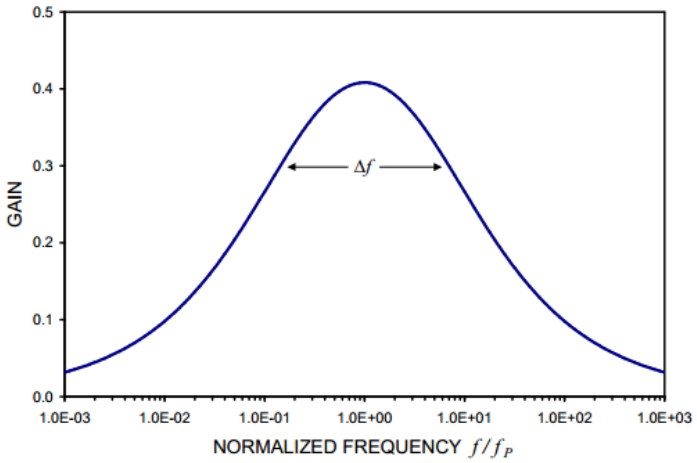

Figure 2.4.b.iv.ii: Combined frequency response of pulse shaping circuit

Equivalent noise charge, is a combination of current noise, voltage noise and source noise which depends on the upper and lower cutoff frequencies. Current noise is independent of detector capacitance, consistent with the notion of counting electrons, using integration. Voltage noise increases with detector capacitance or reduced signal voltage. Source noise charge (1/f) is independent of shaping time. Generally, the total noise of a "1/f" source depends on the ratio of the upper to lower cutoff frequencies, not on the absolute bandwidth. The figure below exhibits the equations that can be used to model equivalent noise charge.

2.5 DIGITAL HARDWARE

This section discusses all research pertaining to digital hardware component selection.

2.5.a Microcontrollers

The microcontroller is an embedded computer which is responsible for interfacing with all of the spectrometer's subsystems and running the digital logic to control the device. Since the microcontroller interfaces with the color LCD screen, touch screen, SD card, USB connection, gamma ray pulse signal, and battery management IC, it is essential that the controller has a large number of GPIO pins available. It is also important that the microcontroller is a low power device intended for battery operation. The microcontroller should have a large amount of flash for program storage (at least 128KB) and a moderate amount of internal RAM (at least 16KB) to enable the development of all auxiliary libraries required to interface with all other IC's / subsystems in C or C++ . Hardware I2C and SPI support is preferred. A higher speed microcontroller is preferred, but there must be a balance between performance and cost.

Table 2.5.a.i displays the microcontrollers under consideration for this project. The STM32F303VCT6 was chosen as most suitable microcontroller due to the number of GPIO available, flash and RAM size, and balance between price and performance. ST's ARM Cortex Mx based STM32 microcontrollers are supported by a variety of compilers, including IAR Embedded Workbench and KEIL. These two compilers are code limited to 32KB for the free versions. Though the STM32F303VCT6 has the highest ADC sample rate of 5Msps, the ADC peripherals of all microcontrollers researched was not higher than 12 bits, which may be fine for general purpose analog signal sampling, but will not be adequate for the precision required in the gamma ray spectrometer. Therefore a dedicated ADC will be used which supports a higher sampling rate and better noise performance. The ST microcontroller can be purchased on the ST32F3DISCOVERY development board for a reasonable price with all 87 GPIO pins available for use on expansion headers.

CPU	Model	Flash (KB)	RAM (KB)	Max Speed (MHz)	GPIOs	ADC Res. (Bits)	ADC Sample Rate (kSPS)	Price	Dev Kit
TI	TM4C123GH6PM	256	32	80	43	12	1000	$11.30	$12.99
TI	TMS320F28027	64	12	60	20	12	200	$7.54	$17.05
PIC	PIC32MX795F512L	512	128	80	85	10	1000	$11.76	$55.00
ST	STM32L152RC	256	32	32	51	12	1000	$6.46	$12.25
ST	STM32F051R8T6	64	8	48	55	12	1000	$3.77	$7.83
ST	STM32F303VCT6	256	48	72	87	12	5000	$9.15	$16.20
ST	STM32F407VGT6	1024	192	168	82	12	2400	$12.78	$14.25

Table 2.5.a.i: Microcontroller comparison showing major specs under consideration

The STM32F303VCT6 is an ARM Cortex M4 device available in a low profile QFP package (LQFP-100). This is a 14x14mm surface mount package with 100 pins and a thickness of 1.4mm. While the size of this package enables a compact footprint on the PCB, the small size and spacing of the leads (0.5mm) makes this a tough IC to solder. Since most of the parts researched had similar surface mount packages, this was not a deciding factor in choosing the right microcontroller for the project.

2.5.b Flash Memory

Some form of non-volatile memory will be used to store the spectrum display of a sample. Flash memory is typically used for applications where data is stored and can be electrically erased and reprogrammed. We will utilize some form of flash memory to store the data of a sample so one can retrieve it via the interface of the device. Typically, for small devices SD (Secure Digital) cards are used due to their size and speed. We will consider the micro and mini SD cards with different capacities, speed and prices mentioned in the following sections.

2.5.b.i Speed

An SD card's speed is measured by how quickly information can be read from, or written to, the card. For our application we will require sustained write throughput. Speed Classes 2, 4, and 6 assert that the card supports the respective number of megabytes per second as a minimum sustained write speed for a card in a fragmented state. Class 10 asserts that the card supports 10 Megabyte/s as a minimum non-fragmented sequential write speed. The speed class rating does not totally characterize card performance. Different cards of the same class may vary considerably while meeting class specifications. In addition, speed may vary markedly between writing a large amount of data to a single and writing a large number of small files, for the purpose of this project speed will be mostly standardized, due to writing smaller files. Class 2 will be sufficient for the type of data we will be writing and reading from the SD card. (See Table 2.5.b.i.i)

Class	Minimum Performance
Class 2	2MByte/sec
Class 4	4MByte/sec
Class 6	6MByte/sec
Class 10	10MByte/sec

Table 2.5.b.i.i: SD card speed classes

2.5.b.ii Capacity

We will consider three different types of SD cards in terms of storage capacity; standard storage (SD), high capacity (SDHC) and extended capacity (SDXC). The following figure (Figure 2.5.b.ii.i), illustrates the different types of SD cards we are considering. We will only consider up to 4 gigabytes of memory storage, this will ensure that we have enough capacity and keep costs low. We will only consider the different options for a mini and micro SD card, due to size constraints of the device.

Manufacturer	Price	Capacity	Size	Speed	Mini	Micro
Kingston	$5.99	4GB	0.9 x 0.1 x 1.2 in	4 MByte/sec	✓	
SanDisk	$7.49	4GB	0.59×0.43×0.039 in	2 MByte/sec		✓
SanDisk	$1.40	4GB	0.59×0.43×0.039 in	2 MByte/sec		✓

Table 2.5.b.ii.i: Various SD cards under consideration

2.5.c LCD Technologies / Interface

An important aspect of the gamma spectrometer is a professional and user friendly interface provided through a color LCD screen capable of displaying fairly high resolution gamma spectrum plots and other useful data. A display that measures at least 3.2" diagonally and has a resolution of at least 320x240 pixels (QVGA) was initially specified as part of our project requirements. This provides a good balance between display size and speed of the microcontroller necessary to update the whole screen at a reasonable rate to provide a smooth user interface. Since the microcontroller provides 87 I/O pins, either a 16-bit or 32-bit RGB color LCD screen with parallel interface can be used. However, for our application the 32-bit screen seems unnecessary, as that level of color precision is not required and it would therefore be a waste of GPIO pins. Though it seems preferable to use a screen with a serial interface to use the GPIO more efficiently, this would provide an unacceptable refresh rate on the screen as at a minimum the screen would require a data rate of 320 x 240 x 16 bits = 1.23 Mbit/s for a single frame per second. For a smooth update rate of 30 frames per second the screen requires a data rate of 36.86Mbit/s. It is easier to interface with these LCD screens through a parallel interface, which reduces the data rate to 2.30Mbit/s for 30 frames per second.

As shown in table 2.5.c.i, a quick search through Digikey leads to LCD screens that quickly exceed our price range, especially when paired with a touch screen for user input.

Part	Part	Price (USD)	Touchscreen	Backlight	Dot Pixels	Interface
Newhaven	NHD-3.5-320240MF	$28.50	No	LED	320 x 240	Digital
Newhaven	NHD-3.5-320240MF	$31.50	Yes	LED	320 x 240	Digital
Newhaven	NHD-4.3-480272EF	$35.00	No	LED	480 x 272	Parallel
Newhaven	NHD-4.3-480272EF	$38.00	Yes	LED	480 x 272	Parallel
Newhaven	NHD-5.0-800480TF	$44.00	No	LED	800 x 480	Parallel
Newhaven	NHD-3.5-320240MF	$44.50	Yes	LED	320 x 240	Digital

Table 2.5.c.i: Sample of LCD screens available from Digikey

A search using the part number of the SSD1289 LCD controller on the screens from Digikey revealed many cheap boards available from different electronics retailers that include an LCD screen, a touch screen and serial touch screen controller (on some), and a SD card slot (on some). These boards are available in the $20 price range, a much better alternative than obtaining all of these parts individually from Digikey. The boards have all necessary pins broken out to headers to interface to the microcontroller (about 40 pins), so they are easy to prototype with and stack on top of a main PCB designed to interface with all system components.

The board chosen for the LCD screen, touch screen, and SD card interface is SKU:20-011-918 “SainSmart 3.2" TFT LCD Display+Touch Panel+PCB adapter SD Slot“ from electronics retailer www.sainsmart.com. This board features a SSD1289 LCD controller, which is a popular LCD controller IC also used in the Digikey parts. The SSD1289 controller communicates through a parallel interface requiring 20 GPIO pins (16 for data, 4 for control). The screen is 3.2” and 320x240 RGB, which meets our project requirements. It uses the TI ADS7843 touch screen controller, which is a popular 12-bit analog to digital converter used to drive 4 wire resistive touch screens. What makes this board attractive as opposed to the other options from Digikey is that the board is cheap ($15.99) and provides a touch screen as well as an SD card slot.

The part has a SPI interface, which is convenient as the SD card can also be interfaced to the microcontroller through SPI. The touch screen controller and SD card slot has a pinout for chip select lines, meaning the SPI control lines can conveniently be tied to the same peripheral interface on the microcontroller.

The SD card slot is mounted on the bottom of the PCB such that the SD card when inserted aligns with the edge of the board. Drawings with board layout and dimensions as well as controller datasheets are all available, making it easy to design our main PCB with dimensions such that the LCD board can be stacked on top. The board will also be mounted on standoff screws onto the main PCB for mechanical support. See figure 2.5.c.i for an image of the LCD board used.

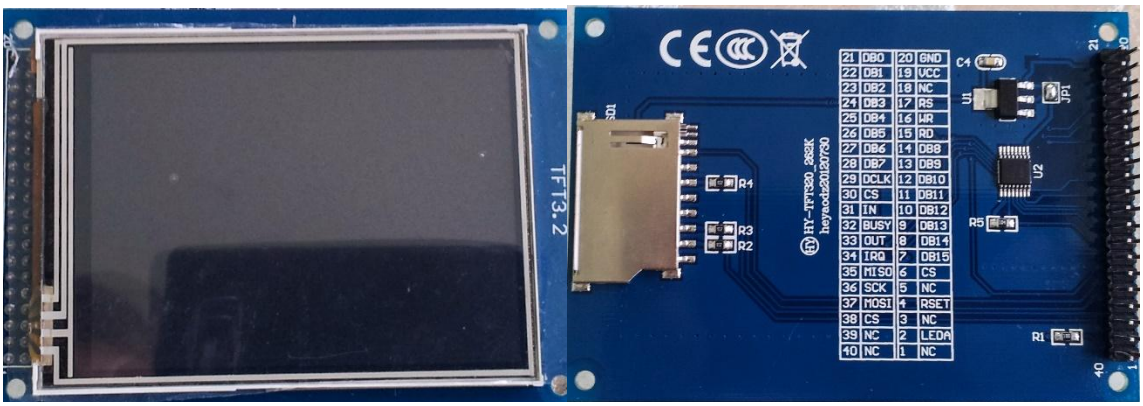

Figure 2.5.c.i: Color LCD display, touch screen, SD card board purchased for the gamma spectrometer

2.5.d Touch Technologies

For the LCD display we will consider only two different touch technologies, resistive and capacitive. Consider the resistive touchscreen; it is the most common type of touchscreen. The resistive touchscreen relies on resistance. In that respect, it's pretty intuitive to understand – the pressure you apply causes the screen to respond. A resistive touchscreen is made out of two thin layers separated by a thin gap. These are not the only layers in the resistive touchscreen, but for the sake of simplicity. These two layers both have a coating on one side, with the coated sides facing each other inside the gap, just like two pieces of bread in a sandwich. When these two layers of coating touch each other, a voltage is passed, which is in turn processed as a touch in that location. So when your finger, stylus, or any other instrument touches a resistive screen, it creates a slight pressure on the top layer, which is then transferred to the adjacent layer, thus starting the cascade of signals. Because of this process, you can use anything you want on a resistive touchscreen to make the touch interface work; a gloved finger, a wooden rod, a fingernail – anything that creates enough pressure on the point of impact will activate the mechanism and the touch will be registered. For this very same reason, resistive touchscreen require slight pressure in order to register the touch, and are not always as quick to respond as capacitive touchscreens. In addition, the resistive touchscreen's multiple layers cause the display to be less sharp, with lower contrast than we might see on capacitive screens. While most resistive screens don't allow for multi-touch gestures such as pinch to zoom, they can register a touch by one finger when another finger is already touching a different location on the screen.

Now we will consider the capacitive touchscreen. As opposed to the resistive touchscreen, which relies on the mechanical pressure made by the finger or stylus, the capacitive touchscreen makes use of the electrical properties of the human body. A capacitive screen is usually made of one insulating layer, such as glass, which is coated by a transparent conductive material on the inside. It is uses the human body because it is conductive; the capacitive screen can use this conductivity as input. When you touch a capacitive touchscreen with your finger, you cause a change in the screen's electrical field. This change is registered, and the location of the touch is determined by a processor. This can be done by several different technologies, but they all rely on the electrical change caused by a light touch of a finger. Since capacitive screens are made of one main layer, the screen will be thinner, which will enhance the portability feature of our device.

Specification	Resistive touchscreen	Capacitive touchscreen
Visibility indoors	Very good	Very Good
Visibility in sunlight	Typically poor, the extra layer reflects too much ambient light.	Typically very good.
Touch Sensitivity	Pressure is needed to make the contact within the screen's layers, can be affected with fingers.	Even the slightest contact of your electron-rich finger with the screen's glass is enough to activate the capacitive sensing system is low.

Table 2.5.d.i: Resistive versus Capacitive touchscreens

Specification	Resistive touchscreen	Capacitive touchscreen
Accuracy	Accurate to at least display pixel resolution, as can be seen when drawing (or writing characters) with a stylus. Useful for handwriting recognition and interfaces with smaller control elements.	Accurate to within a few pixels, in theory, but seriously limited by the physical size of your fingertips, which make it hard to accurately press any control element or select something on screen that's smaller than $1cm^{2.}$
Cost	Cheap to use in a phone design.	Definitely more expensive than resistive screens, by between 10% and 50%, depending on manufacturer.
Robustness	The very nature of resistive screens means that their top layer is soft, soft enough to press down and indent. This makes such a screen vulnerable to scratches and other minor damage. A resistive screen also gradually wears out and requires more frequent calibration.	Glass can be used as the outer layer. Although not invulnerable (and certainly prone to shattering on major impact), glass is more resistant to casual scratches and blemishes.
Environmental concerns	Will work between -15°C and +55°C and at all real world humidity's.	Typical operating temperature is 0° to 35°, requires at least 5% humidity (for capacitive effect to work)

Table 2.5.d.i: Resistive versus Capacitive touchscreens (continued)

There are many different types of capacitive touchscreens, for our device we will consider the TFT (thin film transistor) touchscreen. Fundamentally, the TFT touchscreen is capacitive. Each pixel on a TFT-LCD has its own transistor on the glass itself, which offers more control over the images and colors that it renders. While TFT-LCDs can deliver sharp images, they also tend to offer relatively poor viewing angles, meaning they look best when viewed head-on. If you view a TFT-LCD from the side, it can be difficult to see. TFT-LCDs also consume more power than other types of cell phone displays. In general, TFT-LCDs are used for portable handheld devices, which will be suitable for our purpose. As discussed, in a previous section, the SainSmart 3.2" LCD-TFT + touch panel + PCB adapter SD slot.

2.6 POWER MANAGEMENT

2.6.a Component Power Requirements

The gamma ray spectrometer will require a specific amount of power for each of its components; therefore it is necessary to clarify these values in the following subsections of 2.6.a as to give us a rough idea of which batteries, chargers, controllers, and regulators should be researched with more integrity. This method allows us to filter through power supply component options in a cost-effective manner, reducing the chance of ordering parts that are not functionally compatible with each other. It is also beneficial to have a valid set of requirements so that optimal performance can be calculated and predicted. Figure 2.6.a.i below is a block diagram which illustrates the power system input and output parameters needing investigation. The block diagram is also a possible solution to the task at hand in regards to powering the gamma ray spectrometer effectively.

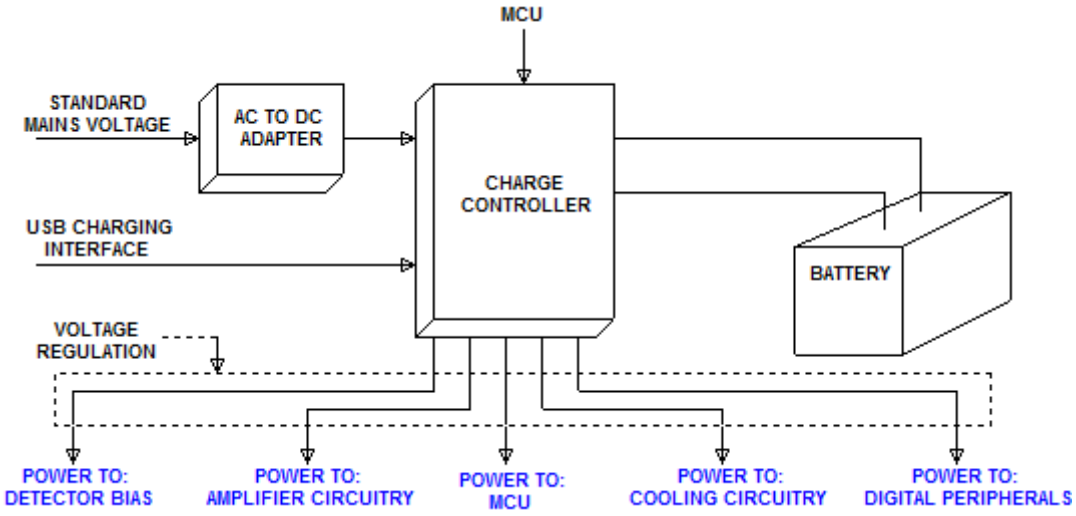

Figure 2.6.a.i: Block Diagram indicating foreseen battery-powered power system solutions

From the block diagram, it is noted that proper voltage regulation (dashed line) is required for each of the power rails that are leading to their respective loads. Voltage regulation may be accomplished by what is shown in the block diagram if an IC can be found that can regulate that many outputs. Otherwise, it might be preferable to take the output at the positive terminal of the battery and configure it such that each line will contain a specific regulator to meet its output requirements. This method may prove to be more stable if the adequate calculations and theoretical assumptions are taken into account.

It's also evident that we have to consider the controlling capabilities over the power management IC. This topic along with many others mentioned or not, will be covered thoroughly in later power management sections. The following 2.6.a subsections will convey operational ratings/requirements for the typical components involved in the accurate production and processing of gamma ray energy spectra.

2.6.a.i Detector Bias

Whether it be a p-n junction or PIN structured photodiode, it will need to be biased such that it operates in its photoconductive mode. This mode of operation will be accomplished by appropriately applying the required reverse biased voltage across the photodiode that is to be used for design. This will be necessary as it will lower junction capacitance to improve responsivity of the photodiode. Figure 2.6.a.i.i displays the effects of applying a reverse bias voltage across the terminals of a typical photodiode and figure 2.6.a.i.ii displays the effects that temperature has over dark current generation. Table 2.6.a.i.i offers optimal baseline reverse-bias and temperature requirements that will be design for in chapter 4.

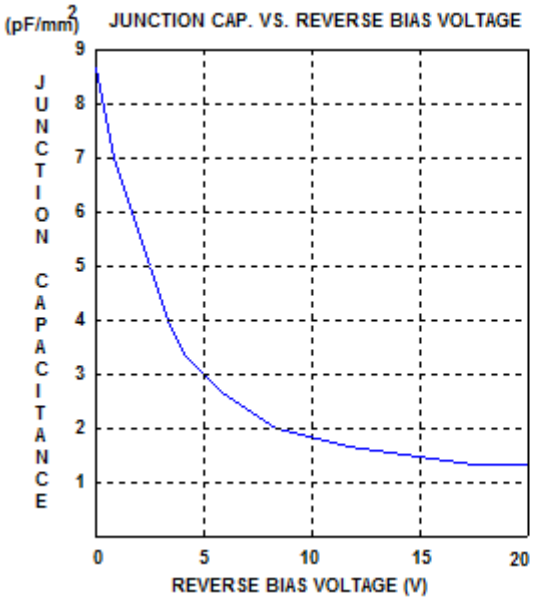

Figure 2.6.a.i.i: Generated plot depicting the effect of increasing reverse bias voltage to reduce junction capacitance

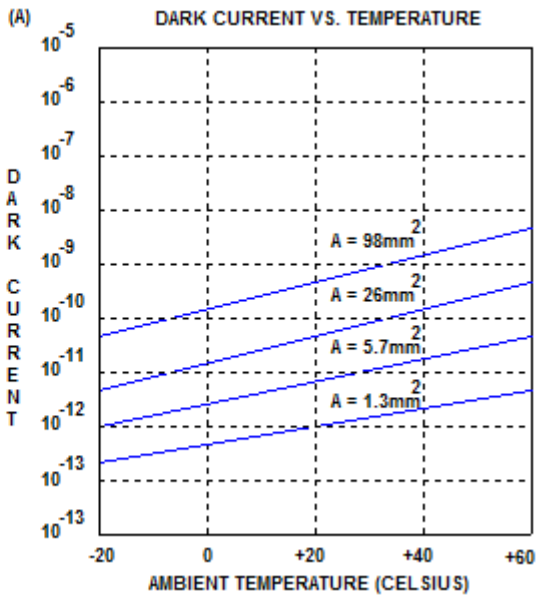

Figure 2.6.a.i.ii: Generated plot depicting the effect of decreasing ambient temperature to reduce dark current generation.

Optimal Performance Ratings/Requirements for Typical Photodiodes	
Reverse-bias Voltage	15V to 30V
Temperature	-30˚C to -15˚C

Table 2.6.a.i.i: Optimal performance ratings/requirements for typical photodiodes

As noticed from figure 2.6.a.i.i, there is quite a large amount of voltage involved in obtaining the smallest junction capacitance. It is therefore going to be the scope of section 2.6.c to demonstrate methods that will both regulate and boost voltages to the typical required bias seen in the MATLAB plot above. Special consideration will also be taken into account for methods that will effectively reduce the temperature of the photodiode as to decrease its sensitivity to light and to decrease the amount of dark current generated from the applied reverse bias voltage. Low temperatures will be obtained with the use of thermoelectric coolers, which will be discussed thoroughly in section 2.6.d.

2.6.a.ii Amplifiers

Operational amplifiers commonly have very similar power requirements in terms of voltages and currents. Although for our purposes of gamma ray spectroscopy, noise injection will be the focal point of our power system design requirements. Since we will be detecting very fast and low amplitude pulses, it will be a must to have little to no noise injected and mixed with the pulses that are received from the detector. Therefore it will be the focus of section 2.6.c to employ methods of voltage regulation with very little noise injection to the power supply pins of the operational amplifiers. Table 2.6.a.ii.i below displays typical requirements for operational amplifiers.

OPERATIONAL AMPLIFER	
Operating Ratings	
Temperature	-40˚C to 125˚C
Supply Voltage ($V_s = V^+ - V^-$)	
$0°C \leq T_A \leq 125°C$	1.8V to 5.5V
$-40°C \leq T_A \leq 125°C$	2.0V to 5.5V
Supply Current (Typical)	1.3 mA
Supply Current (Max)	1.7 mA to 1.9 mA
PSRR (Typical)	96 dB

Table 2.6.a.ii.i: Optimal performance ratings/requirements for typical photodiodes

As we can see from the generated table above, the voltage and current ratings are very common which makes it very simple in choosing a voltage and current specification that we can work with for the course of the design phase. Knowing that the generated information is common to almost all op-amps, we can probably stick with the standard 5 volts and a maximum current draw of 25 mA from the power source. The current specification may be increased if need be, but it's of little concern because op-amps only draw a few milliamps and we plan on using five to six of them. Temperature ratings of operational amplifiers can be neglected for the most part since we our device will not be subject to such temperature limits.

Even so, with a thermoelectric cooler and a heat sink, we should have no problem in regulating low ambient temperatures. As for power supply rejection ratio (PSRR), we will need to factor this in when prototyping step-up converters, boost converters, all-purpose DC-DC converter IC's, and other switching regulator options. This is important because switching regulators have oscillations (noise) superimposed on their DC output. These oscillations will appear at the output of an op-amp if they are large enough to surpass the rated PSRR. PSRR is heavily dependent on frequency; therefore it might be essential to specifically utilize electrolytic capacitors for low frequency decoupling and ceramic capacitors for high frequency decoupling.

2.6.a.iii Microcontroller

The power specifications for most microcontrollers are all relatively similar, usually stating on their datasheets that the external requirements are of 3.3 volts with a maximum current draw of 300 milliamps. The 300 milliamps is not necessarily consumed by the microcontroller, it is just the maximum it can output draw and output to power external digital peripherals. The battery voltage will have to be regulated down to 3.3 volts with either a buck converter or linear regulator. Either regulator type can be used, but it will be most efficient to use a linear LDO regulator since they output the least amount of noise.

Also, it will be most desirable to continuously have the battery power the microcontroller. This will be acceptable because the microcontroller is cable of self-limiting the current that it draws by sitting in an idle state called stop mode. The idle state can limit the current it draws to a just few micro amps and can be resuscitated by an interrupt signal. This feature will result in longer battery life since the battery can be considered as nearly disconnected from its load application when not being used.

2.6.a.iv Thermoelectric Cooler

The thermoelectric cooler which will be identified and thoroughly explained in section 2.6.d will require around 5 to 10 volts and a maximum current draw of 1.5 amps. The current draw specification isn't based off of the available TEC's. It is based off the amount of current that is capable of being delivered from the battery. As will be shown in further detail later, TEC's that are only 200 square millimeters require a massive 4 amperes in order to attain maximum differential temperatures across their ceramic plates. Although, for our purposes the TEC surface area needs to be no more than 100 square millimeters. TEC's at this size normally require a minimum of 1.5 amperes to achieve maximum temperature differentials. 100 square millimeters will be the desired size of the TEC because it will effectively drop the temperature of the photodiode to subzero temperatures.

The thermoelectric cooler will also require a driving circuitry that will allow it consume the voltage and current it needs from the battery so that it to stabilize the differential temperature. This may be accomplished by means of a simple H-bridge circuit configuration or by the use of a driver IC that is specific to cooling modules. The more reliable option is go with the driver IC because it will provide us with the option of control and monitoring. Controlling the temperature is an option that we can afford to neglect because we only desire the lowest temperature the TEC can achieve. On top of that, to make adequate use of the controlling option of the module IC, we would most likely need to incorporate an external PID loop circuit and a pin from the microcontroller that's dedicated to adjust TEC temperature. The monitoring option of the module IC will be applicable because it will provide us with information on the actual temperature the TEC is outputting to the photodiode.

The TEC will also require the use a heat sink so that it can be passively cooled and pushed to the lowest temperature. There will also need to be careful consideration in the size of the heat sink. Implementing a large heat sink requires more space, which may result in a larger casing for the spectrometer. Having too small of a heat sink will create

too much heat. A small heat sink may become so hot that it begins lowering the temperature differential across the TEC by transferring the heat to the cold ceramic plate of the TEC. There is also a possibility that thermal noise may be injected into the detector circuitry causing inaccurate measurement. All of these requirements will be further investigated and possible solutions to them will be shown in section 2.6.d on sensor cooling.

Figure 2.6.a.iv.i is an illustration of a general mounting technique that most sensor manufactures recommend to properly cool a photodiode.

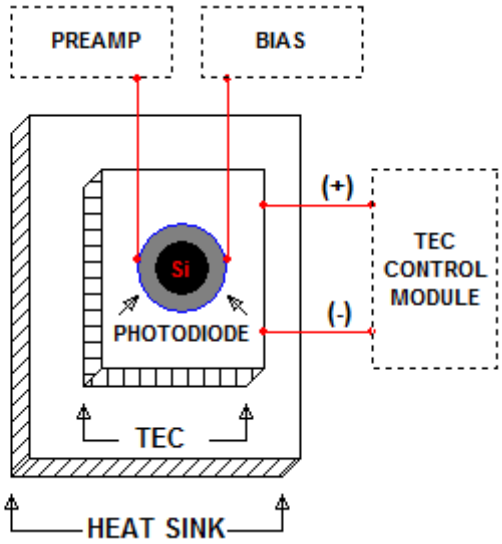

Figure 2.6.a.iv.i: Mounting assortment that will be required to passively and actively cool the photodiode.

2.6.a.v Digital Peripherals

Since all of the digital hardware is monitored entirely by the microcontroller, it is probably accurate to say that direct power distribution from the battery is not required. The microcontroller can receive regulated power from the battery via a 3.3 volt regulator. The power can then be distributed from the microcontroller as it must to all of the digital hardware that requires a supply voltage to operate. As a beneficial requirement, it will be required to implement soft start circuits in between the digital peripherals and the microcontroller. This requirement ensures that power transients are controlled and dampened so that sudden and/or long term damages to components are reduced. The soft start circuits will reduce the amount of inrush current transients that may occur for each start up of the device. Not only will it reduce the current spikes, but it will transition the inrush currents into the loads in a smooth linear manner. The scope of this section was implemented to incorporate all power management requirements, though digital peripheral solutions will not be discussed thoroughly in later power management topics. Accurate solutions to these requirements will be delivered in section 4.4.b.

2.6.b Battery Management

Effective battery management is crucial in portable applications, especially those that involve diverse and complex power requirements for their components. Battery technologies, battery charge controlling, and battery charging interfacing are the foremost attributes of a portable power supply that are considered first for design. Thorough research will be delivered in the following section to ascertain information on batteries and charge controllers that will satisfy the load requirements stated earlier in section 2.5.a. Once an appropriate battery and charge controller are chosen, a charging interface method will need to be included that will be capable of charging the battery and powering the device components simultaneously. The source interface will either be an AC to DC wall outlet interface or USB charge interface or maybe even both. Figure 2.6.b.i below displays a more detailed power source interface system that will be highly desired for implementation into the power system of the spectrometer.

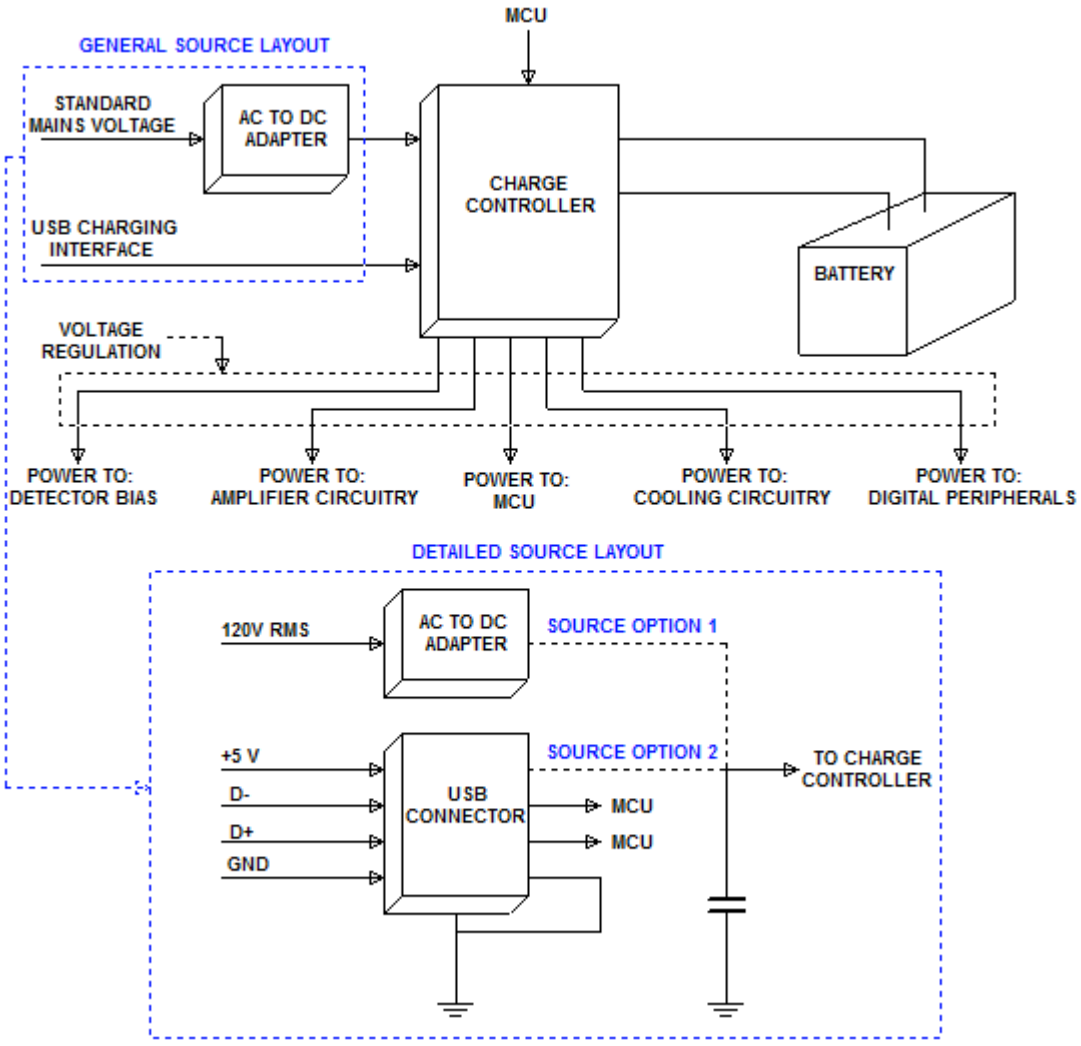

Figure 2.6.b.i: Block Diagram displaying a more detailed power source interface

2.6.b.i Battery Technologies

Electronic portability is the probably one of, or if not the most important aspect of everyday life. In our technologically advanced society, the word portability has no value without the existence of batteries. The industry today offers two types of batteries, primary and secondary cell, better known as non-rechargeable and rechargeable batteries, respectively. These two battery cell technologies are manufactured chemistry specific in either a dry or liquid electrolytic cell. The major distinction between the two batteries is that the secondary cell has reversible electrochemical properties, while the primary cell does not. The reactive elements in a primary cell can only be exhausted once to produce energy and the energy cannot be restored to the cell by electrical means. These cells are known as disposable or non-rechargeable batteries and are commonly manufactured using zinc-carbon and alkaline chemistries. The chemical reactions that occur in a secondary cell can be reversed electrically, allowing the cell to restore its chemical composition. This means that the cell is capable of charging, discharging, and recharging many times over, hence the more common name "rechargeable battery".

Although it may seem that primary cells are obsolete in comparison to secondary cells, that is not the case as they are still widely used in portable devices that are used intermittently such as calculators, flashlights, remote devices, and many electronic outdoor tools. The reason for this is due to the fact that primary cells maintain high energy density with extremely low self-discharging rates. Self-discharging is the discharging process that occurs when a battery is sitting idle with no connection to its terminals. This is really convenient when it comes to the use of say a flashlight that runs on primary cell technology. One might use the flashlight two times out of an entire year and it would still have maintained nearly the same charge in its battery as the first use. On the other hand, a flashlight powered by a secondary cell could completely deplete its charge within a week or possibly a few days of no use. There are also many additional differences between the two battery technologies that are worthy of mentioning such as environmental impact and cost, but it is mainly the low self-discharging of primary cells and electrical reversibility of secondary cells that divides the two technologies. Generally, the rule of thumb is to use primary cell technology with devices that are intended for occasional/less frequent use and to use secondary cell technology with devices that are intended for daily/frequent use. Laptops, cell phones, media players, portable gaming devices, and industrial tools are prime examples of devices that commonly use secondary cell technology. Therefore, if we intend to design the gamma ray spectrometer for daily industrial use, then it would be practical to utilize secondary cell technology.

Battery chemistry is another important aspect that will need to be decided on so that the optimum charging capabilities are upheld if secondary cell technology is to be used. Battery engineers focus on testing different chemistry configurations in hopes to compensate for the standard flaws that are associated with secondary cells. The most common choices of rechargeable battery chemistries are lead-acid (SLA), nickel-metal hydride (Ni-MH), nickel cadmium (Ni-Cd), and lithium-ion (Li-Ion).

Lead-acid batteries are the oldest type of rechargeable battery and were mainly intended to serve as ignition starters for automobiles. They have the lowest specific energy density among all the battery chemistries making them physically large in size. Lead-acid batteries also have practically no self-discharge, which allows them to be stored away for long periods of time and still maintain their original charge.

Ni-Cd batteries were developed not long after the lead-acid battery and were considered quite an advancement in rechargeable battery technology. They were an improvement in terms of specific energy density which made them smaller in size and allowed them to be implemented in many of the first portable industrial tools.

Ni-MH batteries were introduced commercially in the early 1990's and were designed specifically to replace the Ni-Cd batteries. Although they did surpass the Ni-Cd batteries in terms of specific energy density, they lacked in other areas such as overcharging tolerances and self-discharge rates. Most battery manufacturers highly recommend using Ni -MH batteries in applications that call for long duration with low current loading.

Li-Ion batteries are probably the most desirable battery chemistry of today because they offer the highest specific energy density than any other commercially available battery. This density improvement using lithium ion technology allows for the manufacturing of very small package sizes that maintain the batteries internal and terminal characteristics. Li-ion batteries also have very fast-charge time and long cycle life making them even more desirable for consumers. Fast-charge time is the time it takes to fully charge a battery and cycle life is defined by how many times a battery can be fully charged and then fully discharged before the battery life begins to degrade. Due to these features, lithium-ion batteries will probably be the best candidate among the other battery chemistries for powering the components of the gamma ray spectrometer. Table 2.6.b.i.i is tabulated to show the different types of rechargeable battery chemistries and their characteristics.

Specifications	Lead acid	Ni-Cd	Ni-MH	Liquid Li-Ion	Polymer Li Ion
Nominal Voltage (V)	2	1.2	1.2	3.6	3.6
Specific Energy Density (Wh/kg)	35	50	80	125	170
Cycle life (times)	300	500	500	800	1000
Fast-charge time (hours)	8-16	1	2-4	<1	<1
Self-Discharge(%/month)	0	25-30	30-35	6-9	2-5
Overcharge Tolerance	High	Moderate	Low	Low	Low
Circuit Safety Requirements	Thermally stable	Thermally stable, fuse protection common		Protection circuitry mandatory	

Table 2.6.b.i.i: Battery specifications and their typical values

Circuit protection is mandatory for Lithium-Ion batteries therefore it will be beneficial to include the use of either protected lithium ion batteries that have built-in protection or unprotected Lithium-Ion batteries with an external protector. Protected Lithium-Ion batteries have a small built-in circuit that shuts them off in the event of over-charging, over-discharging, overheating, and short circuit faults. The unprotected batteries will need an external IC such as those manufactured by Texas Instrument (BQ series) which offer monitoring and protection of overvoltage for each cell. Another option may be to just use a charge management controller to provide the protection along with the added feature of acting as a smart grid, allowing it to charge the battery, sense and measure battery temperature, and power external components simultaneously. Table 2.6.b.i.ii shows a list of various batteries and their specifications including information on whether it's protected or unprotected.

Supplier	Type/ Shape	Model	Nominal Voltage (V)	Nominal Capacity (mAh)	Weight (g)	Dimensions (mm)	Internal Protection
Tenergy	Li-Ion/ Round	30073-0	3.7	1400	48	65 x 18	No
Tenergy	Li-Ion/ Round	30016	3.7	2600	50	69.5 x 19	Yes
Amazon	Li-Ion/ Round	SDI ICR18650-26F	3.7	2600	45	65 x 18	No
Sparkfun	Li-ion/ Non-round	PRT-10053	9	350	N/A	50 x 28 x 5	Yes
Sparkfun	Li-Ion/ Coin	PRT-10319	3.6	110	6.4	24.5 x 5.2	No
Sparkfun	Li-Po/ JST	PRT-00731	3.7	1000	2.65	50 x 33 x 5.9	Yes

Table 2.6.b.i.ii: Product prices and specifications of various Lithium-Ion batteries

Table 2.6.b.i.ii supplies us with information on which lithium-ion batteries are capable of satisfying the power system requirements stated in section 2.5.a. The voltages displayed in the table do not necessarily meet all of the stated requirements, but they do provide us with enough input voltage that can be stepped-up or down with the proper regulator. It is the current and physical size that will be of greater concern. The current ratings noted for the Sparkfun batteries may be too low to power all of the spectrometers components accurately. This does not imply that a 110 mAh battery is unable to power the spectrometer, it only means that the fully charged battery would heat up and discharge very fast if its operating conditions are exceeded. Also, the current requirement for the microcontroller alone is to be around 300 mA. Although this does not imply that it draws 300 mA all the time, it is still a sizeable amount of current that may need to be delivered if necessary. The common round shaped batteries offered by Tenergy and the flat JST connector battery by Sparkfun would supply more than enough current and for a long period of time, though they would require much more space resulting in less proper cooling. It also might be feasible to go with the coin-shaped lithium-ion battery offered by Sparkfun. Since these batteries are much smaller, it may be possible to put them in series and/or in parallel to meet the power requirements.

2.5.b.ii Charge Controller

Before going into the details of a charge controller, it should mentioned the type of charge controller that is being referred to. The first and more common one is the "stand-alone charge controller". This controller is often sold as its own separate device and is most commonly associated with solar and wind power generation applications. The second one is the "charge controller integrated circuit". This controller is the one that has been referred to in the previous power system sections and will continue to be referred to for all charge controller topics.

Charge controller IC's were introduced to increase power efficiency in portable electronics, particularly cell phones and laptop computers. Charge controllers for the most part are just regular battery chargers. Although they are only specific to microchips/integrated circuits and can involve much more functions than just charging a battery. There are three basic functions that a standard charge controller must accomplish regardless of the battery chemistry.

- Charging the battery of interest
- Charging at a controlled rate
- Terminating the controlled charging process

Charging the battery is the most simple since it's essentially an internal transistor switching action that takes place upon a closed-loop connection. This means that once a power source is connected to the charge controller, it will turn on the transistor via a small voltage drop and allow current to flow into the battery.

Charging at a controlled rate is specific to a batteries chemical composition. The battery can be damaged if the amount of electrical energy being pumped into the battery is too fast for chemical reactions in the battery to take place properly. The chemical reactions associated with any rechargeable battery are not instantaneous upon electrical and chemical interaction. That is why charge controller IC manufactures implement controlled charging rates into the design of the IC to take into the account the specific battery chemistries.

Terminating the controlled charging process ensures that overcharging is eliminated so that heat cannot be generated sporadically. Overcharging occurs when a battery continues to charge beyond its maximum capacity, once it passes this threshold point it begins to convert its electrical energy into thermal energy. If the thermal energy continues to build up, it will result in a permanent reduction in battery life and/or an electrolytic explosion. The battery charging circuit in a charge controller should be able to detect the overcharge cutoff point and terminate the flow of charge to preserve battery life. Also, In the event that the circuit cannot detect the cutoff point, it will need alternative methods to compensate for the failure. One alternative is a temperature sensor that is designed to sense the heat that is generated at the overvoltage occurrence and to initiate a shutdown protocol or to trip a resettable fuse. Another option is a safe timing circuit that considers the battery as fully charged after a time that is predetermined.

In the previous section on battery technologies, it was determined that lithium-ion chemistry would be the most suitable option for our design purposes. Therefore, it will be of greater benefit to continue with focus on charge controller IC's and charging processes that are specific to lithium-ion chemistry. Charge controller IC's that are intended for lithium-ion chemistry must function to carry out the following stages of the lithium-ion charging process in order to accomplish their function of controlled charging:

- Pre-charge
- Constant current charge
- Constant voltage charge
- Charge termination

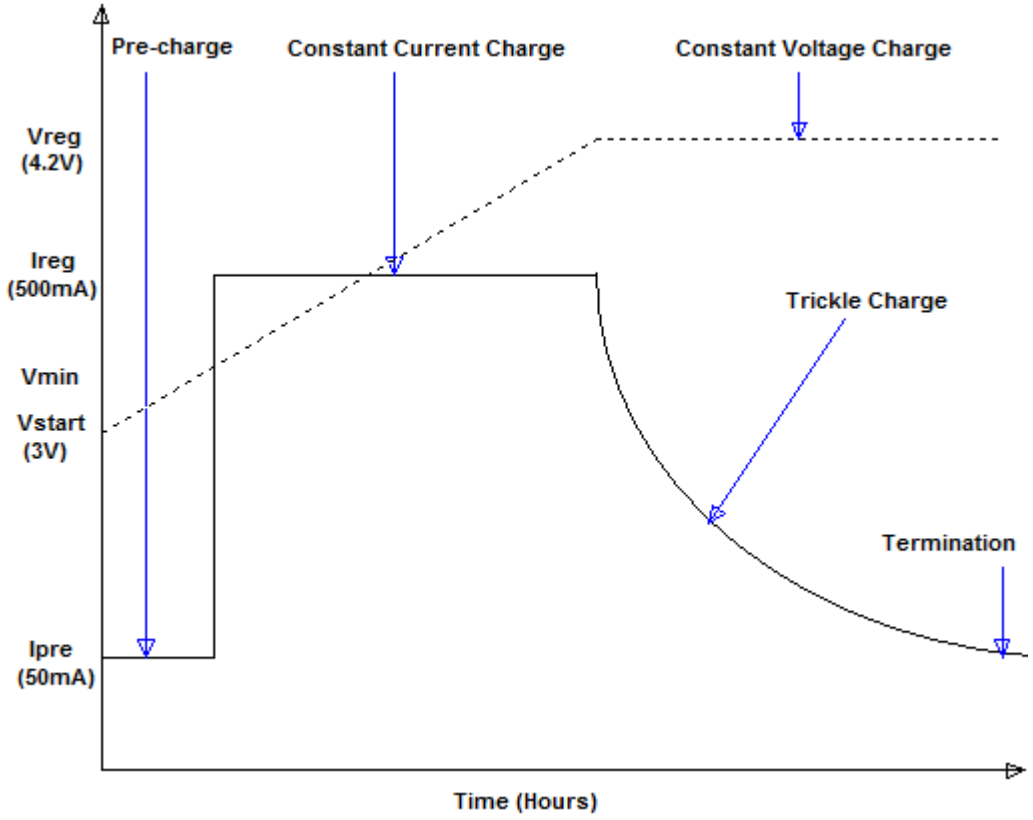

Figure 2.5.b.ii.i: Charge controlled stages associated with lithium-ion batteries

Pre-charge also known as "slow charge" is the first stage that takes place to employ charging to deeply depleted cells. A cell is considered depleted when the cell voltage drops below a particular threshold, generally around 3 volts. When this occurs, a low constant current charge rate of 0.05C to 0.1C is invoked to raise the cell voltage. This stage of charging is to safely recover from possible overcharging of the cell that may have occurred if the associated protection circuitry of the battery or charge controller fails to regulate at the threshold voltage.

Constant current charge also known as "fast charge" is the second stage of charging that occurs after the cell voltage has risen above its threshold. The constant current charge from the previous stage is increased to 1C and continues at this rate until the battery voltage rises to what is called the "float" voltage. The float voltage is the maximum voltage that regulates across the terminals of the battery. In order to preserve the constant current rate, the charging voltage must increase in unison with the cell voltage to avoid any back EMF generated as the cell charges up.

Constant voltage charge also known as "trickle charge" is the third stage of charging that occurs when the float voltage is reached. Once this voltage level is attained, it is maintained while the current rate begins to decrease to a trickle charge until the charging cycle is completed.

Charge termination is a method used to terminate current going into the battery when the charging cycle approaches completion. This is normally accomplished by termination at a minimum charge current or by means of a timer. The minimum charge current approach is used to monitor the charge current during the constant voltage stage and to terminate the charge when it diminishes below a predetermine C rate.

In the analog IC industry, there are two charge controller IC solutions that are offered to accomplish the lithium-ion charging requirements. They are:

- linear charging
- switch-mode charging

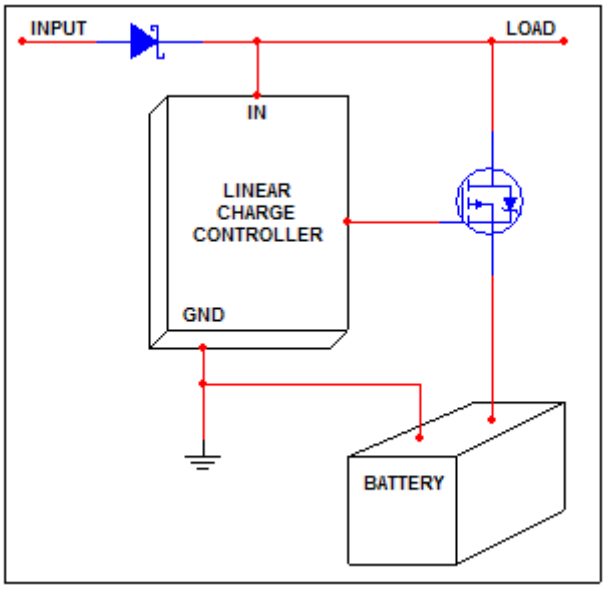

Figure 2.6.b.ii.ii: Simple model of a linear charge controller circuit

Linear charging solutions (figure 2.6.b.ii.ii) are generally used when adequate source regulation is available to the IC. Linear charging IC's, for most applications, are offered in much smaller component sizes and are extremely cheap in comparison to switch-mode charging IC's. The only disadvantage to using a linear IC is their low efficiency due to the excess heat generation from the internal linear regulators and the internal/external pass transistor associated with the IC. The heat is mostly generated during the initial pre-charging to constant current charging stages where maximum power is dissipated through the pass transistor. Thermal efficiency is a direct function of the input voltage, charge current, and thermal impedance between gate pass transistor and ambient air. Therefore, it is essential that thermal design be incorporated if linear charging IC's are to be used.

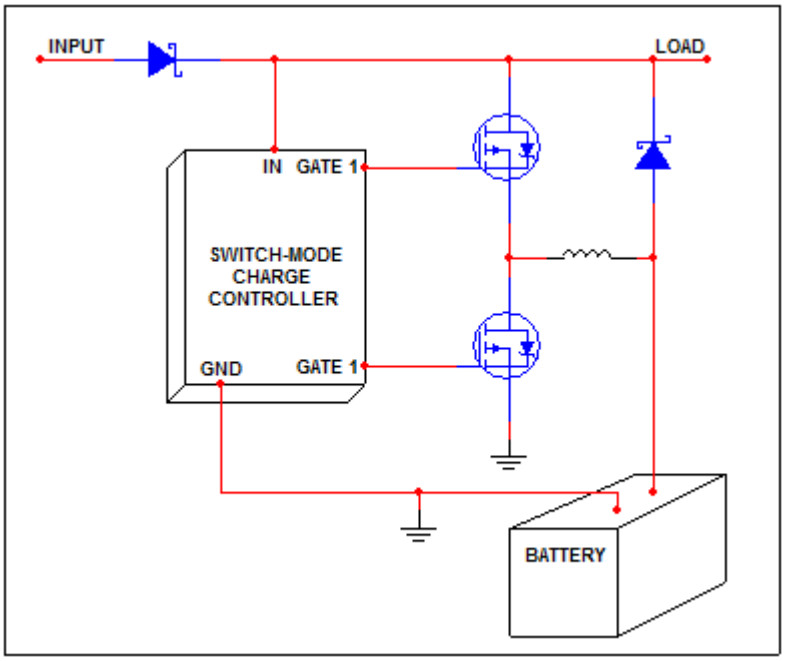

Figure 2.6.b.ii.iii: Simple model of a switch-mode charge controller circuit

Switch-mode charging solutions (figure 2.6.b.ii.iii) are generally used in applications where the input sources vary in a wide ranges. They are also used in instances where the application requires for high input to out voltage differentials. Switch-mode IC's have the benefit of having much high efficiency than the linear IC's. The only downfall to switch-mode IC's are the complex external circuitry, large component sizes, and higher cost. Although, modern switch-mode IC's operate at high switching frequencies which employs the use of much smaller external inductors and ceramic capacitors, making the application circuitry much smaller and relatively simple. Switch-mode IC's have the advantage of utilizing circuit topologies such as buck, boost, buck-boost, flyback, and SEPIC.

2.6.c Voltage Regulators

After choosing the appropriate battery chemistry and charge controller, the next step is going to be deciding on methods of regulated power distribution. Distributing power to multiple circuits/devices requires that voltage regulation be delivered efficiently through each rail to its respective application. This will be done by means of a "voltage regulator". Figure 2.6.c.i below gives a more accurate depiction of the regulation and distribution of power that will be required for the gamma ray spectrometer.

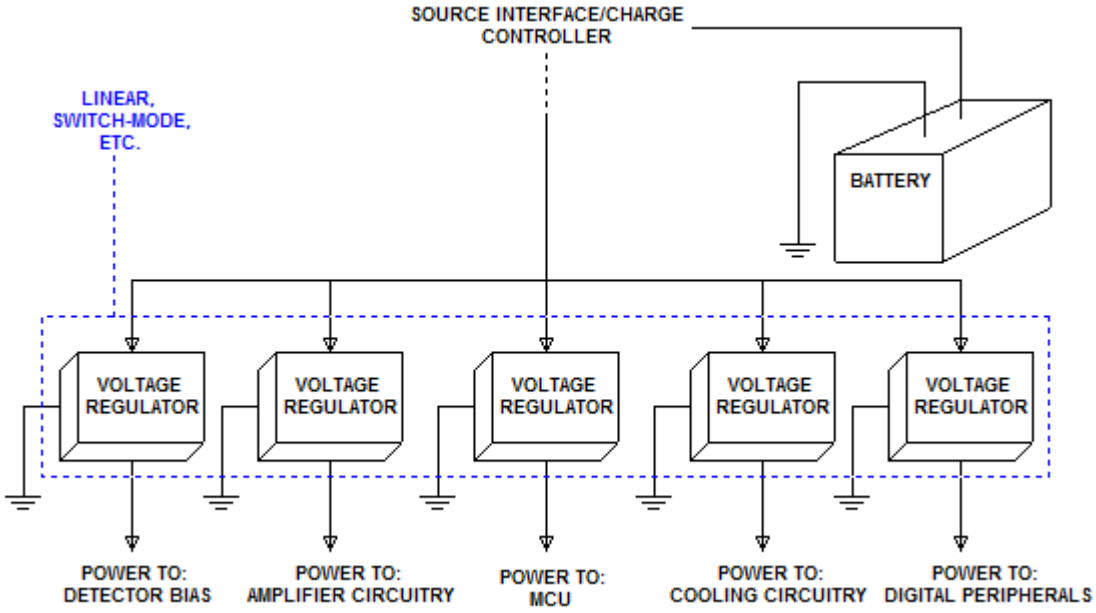

Figure 2.6.c.i: Block Diagram displaying a more detailed regulator scheme

A voltage regulators basic function is to output a stable DC voltage regardless of input voltage fluctuation and load current. The simplest voltage regulators consist of a resistor in series with a diode, specifically a Zener diode that operates in its avalanche breakdown region. This type of voltage regulator configuration is known as the series regulator and is one of the two basic regulator circuits that are governed by “linear” regulation. The other is the shunt regulator, which consists of a resistor in parallel with a Zener diode. As the circuits become more complex, the transition into “switching” regulation may become more desirable if greater efficiency is required.

The two classes of regulators, the linear (dissipative) and the switch-mode (non-dissipative) will be investigated in the following subsections to offer insight on their control and stability of the power that will be distributed. Linear and switch-mode regulators each serve their purpose to a specific application; neither is inherently universal to every application. Though it will be demonstrated that in fact both will be beneficial to any design, especially radioactive detection devices.

2.6.c.i Linear Regulator

Linear Regulators operate by the use of a voltage-controlled current source which creates a fixed voltage across its output terminals with low noise. The internal control/sensing circuitry monitors the output terminal loading so as to adjust and maintain the fixed voltage. The control circuitry of a linear regulator is composed of a feedback loop, which is compensated to assure loop stability. The exact method of output voltage control is dependent upon the topology. In the industry there are three main linear regulator topologies:

- Standard linear regulator
- Low dropout linear regulator
- Quasi low dropout linear regulator

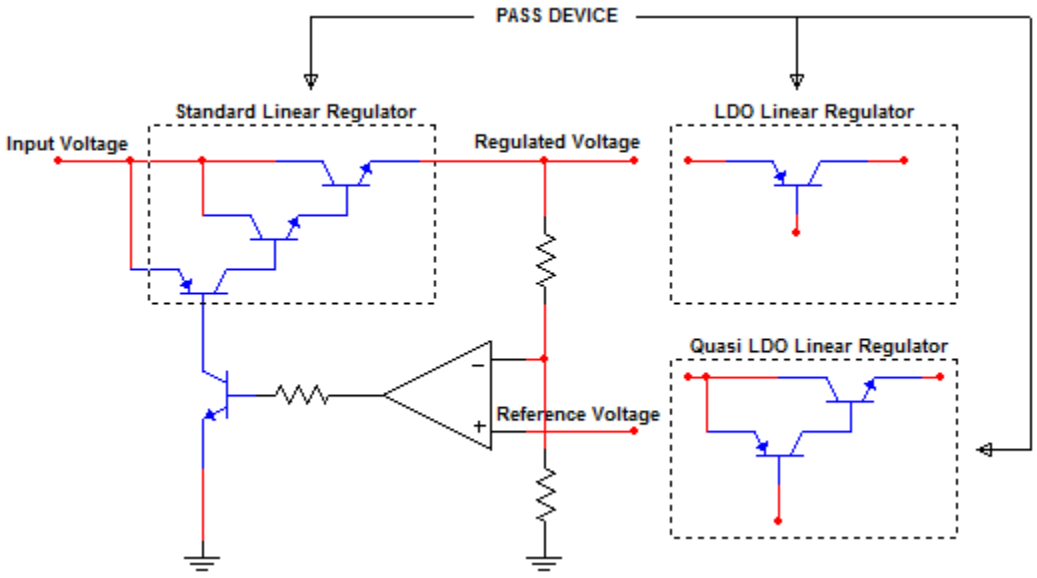

Figure 2.6.c.i.i: Multisim schematic depicting the typical configurations of the three types of linear regulators

Standard linear regulators utilize an NPN Darlington pair configuration driven by a PNP transistor. This transistor network is known as the "pass device", which allows regulation at the output. The pass device requires a minimum voltage ($V_{min} = 2V_{BE} + V_{CE}$) in order to accomplish proper regulation. The minimum voltage is generally between 2.5 to 3 volts for a typical standard linear regulator. The voltage at which the output regulation begins to degrade is known as the "drop out" voltage. The drop out voltage for standard linear regulators is typically 1.5 to 2 volts, which is considered to be the worst among the three types of linear regulators. The one benefit of standard linear regulators is the low ground pin current that is required to drive the base of the pass transistor. The reason for this is that the drive current to the base of the pass transistor is equal to the load current divided by the pass device gain. The pass device gain of standard linear regulators is generally extremely high due the transistor configuration involved. Therefore little current is required to drive the base of the pass transistor, resulting in low ground pin current.

Low dropout linear regulators (LDO's) make use of only one PNP transistor to act as the pass device. This permits the minimum voltage ($V_{min} = V_{CE}$) requirement to be much less than that of the standard linear regulator. The typical drop out voltage for LDO's is between 0.7 to 0.8 volts, though today's LDO's are manufactured with drop outs in the 0.1 volt range. The low drop out voltage from an LDO is optimal for battery-powered applications, since they're capable of utilizing the available input voltage with much higher efficiency. As for the ground pin current, it is highest among the three linear regulators. The ground pin current is equal to the load current divided by the gain of the single PNP transistor, which results in a much higher current draw.

Quasi low drop out linear regulators use a pass device composed of an NPN and PNP transistor. The minimum voltage ($V_{min} = V_{BE} + V_{CE}$) is in between that of the standard and LDO linear regulators, hence the "quasi" term. It's not entirely noted on what the general minimum voltage is, but one could make the fair assumption that is it between the standard and LDO regulator (≈ 1.5 volts). The same goes for the ground pin current, which would probably put the current limit to be less than 10 milliamps.

Now that all three types of linear regulators have been discussed, it seems that it is in our best interest to use an LDO since it is most applicable for battery-powered applications. Though it might not be entirely applicable for all regulated voltage rails, it will still be needed where low noise implementation is required. Therefore, it will be necessary to continue with focus on LDO noise generation and additional properties that will need to be considered for power supply design.

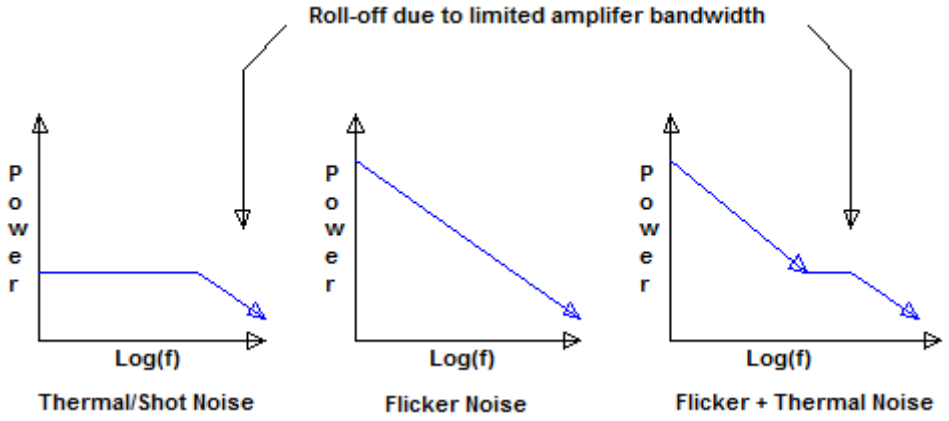

Figure 2.6.c.i.ii: Types of noise introduced in an LDO IC

The types of noise in an LDO consist of thermal, flicker, and shot noise and are generated by transistors and resistors that make up the internal circuitry. Thermal and shot noise is considered to be random in nature, though its power is flat over frequency. The power remains flat up to the bandwidth of the internal amplifier. Flicker noise comes from the trapped charges in metal oxide transistors. As depicted in figure 2.6.c.i.ii, the noise they generate often follows the 1/f roll-off in power versus frequency, hence the noise is higher at low frequencies and will dominate until its magnitude decreases that of the thermal noise.

Noise in an LDO, is shown by two methods. One is the spectral noise density, which is a curve that displays noise ($\mu V/\sqrt{Hz}$) versus frequency. The other is integrated output noise, also known as output noise voltage (μV_{RMS}); it is the spectral noise density integrated over a specific range of frequencies and can therefore be thought of as the total noise in a specified range of frequencies. The noise that is outputted to the load comes from the internal workings of the regulator IC. It consists of the band gap, resistor divider network, and the input stage of the operational amplifier.

It is important to note that the power supply rejection ratio (PSRR) is not associated with the generated internal noise of the regulator IC. PSRR is just a measure of a circuits power supply rejection expressed as a ratio of output noise to noise driven into the power supply input. It provides a measure of how well a circuit rejects the ripple voltage that is superimposed on the regulated DC input over a wide range of frequencies. The PSSR equation is:

$$PSRR = 20Log\left(\frac{Ripple_{IN}}{Ripple_{OUT}}\right)$$

PSRR is equates logarithmically and is expressed in terms of decibels (dB), where $Ripple_{IN}$ denotes the noise ripple of the input signal and $Ripple_{OUT}$ denotes the noise ripple seen on the output signal.

In summary, all linear voltage regulators are excellent for powering devices when there is a small difference between the input and output voltages. As long they remain within a low differential voltage, there will be low losses in energy and noise generation will be minimal. The one major disadvantage to the linear regulator is that the differential voltage will almost never be small enough to be considered negligible. The small difference in voltage is wasted by being dissipated as heat into and through the internal circuitry. In some instances a linear regulator can waste more energy stepping down a voltage than it actually ends up delivering to the load. This makes linear regulators slightly to highly inefficient, especially in high powered applications involving multiple loads that require different input and output voltages. These types of applications would call for the use of not only linear regulators, but also switch-mode regulators. It is now clear that choosing only linear regulators will not accomplish the task at hand of power each and every circuit of the spectrometer. Since there are only two types of regulators, it is evident that the use of a switch-mode regulator will be included in the design. It will be the focus of the following section 2.6.c.ii to illustrate their characteristics and how they can be utilized with linear regulators to obtain optimal performance and efficiency.

2.6.c.ii Switch-Mode Regulators

Switch-mode regulators come in a variety of forms, but all of them regulate voltage by utilizing a series switching element to charge a capacitor/inductor when the voltage/current falls below a predetermined level. A basic switch-mode regulator can be constructed using an inductor or capacitor though both are generally mixed together to form a more effective, efficient, and robust design. Figures 2.6.c.ii.i and 2.6.c.ii.ii display the fundamental circuits that are used as a basis of understand for switch-mode regulation.

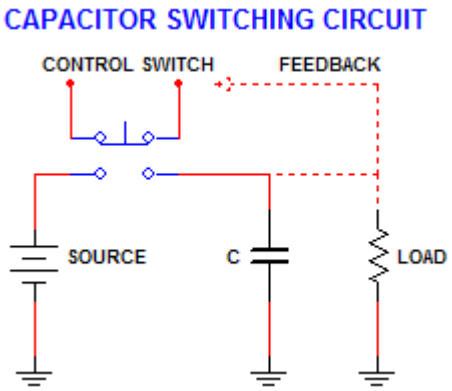

Figure 2.6.c.ii.i: Displays a basic capacitor-switch circuit that is fundamental to switch-mode power supply design.

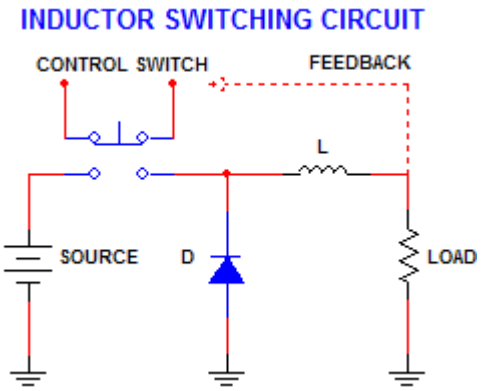

Figure 2.6.c.ii.ii: Displays a basic inductor-switch circuit that is supplementary to creating an efficient switch-mode power supply.

A basic capacitor switching circuit (figure 2.6.c.ii.i) will have a power source, capacitor, and a switch connected in series, along with a load connected in parallel to the capacitor. When the switch is closed, the power source will charge up the capacitor to a predetermined voltage. The switch will then open and the capacitor will feed current into the load. As the voltage across the capacitor begins to decrease below the predetermine voltage, the switch will close and again charge the capacitor. Intuitively, one should realize that the switching speed of the switch will need to be extremely fast in order to switch at the exact time it is needed. Therefore, it will be required that a control circuit be implemented to detect and then control the switching times of the switch. The capacitor switching method is very fundamental, it is not an efficient solution to modern day regulation applications due to the loss of energy associated with the circuit switching. Theoretically a capacitor does not dissipate energy, but the loss of energy only appears during the transition time when the circuit switches. Energy is lost during this transition due to parasitic resistance of the capacitor and arcing of the switching contact. As a result of this, efficient switch-mode regulation cannot be obtained with capacitor techniques alone.

An inductor can used be used in a switch-mode regulator to supply current from a power source via switch and diode. In this circuit (figure 2.6.c.ii.ii) there is a power source connected in series to a reverse-biased diode which are both paralleled to an inductor and load series connection. When the switch is closed, current is fed into the load for device operation. When the switch is open, the built up magnetic field of the inductor collapses

to begin producing a voltage across the load once again. Fast switching time is needed to maintain the voltage and current that the load requires to operate. The diode is necessary to provide a path for the current of the inductor to flow when the switch is open. Otherwise the built up magnetic field across the inductor will collapse in the form of current in the opposite direction and dissipate energy through an arc in the switch.

Both circuit configurations are fundamental to the design of an efficient switch-mode regulator and are combined and manipulated to produce switch-mode regulator topologies that step-up, step-down, and invert currents and voltages. They are subcategorized under switch-mode regulators and are known as converters. In the context of this section, the terms regulator and converter will be used interchangeably. In the analog electronic industry they are by the following:

- Buck converter
- Boost converter
- Buck-Boost converter

The analysis of the following circuits will be explained under the assumption that constant on/off switching has occurred. This will simplify the explanations due to the fact that these circuits have non-linearity's associated internal workings.

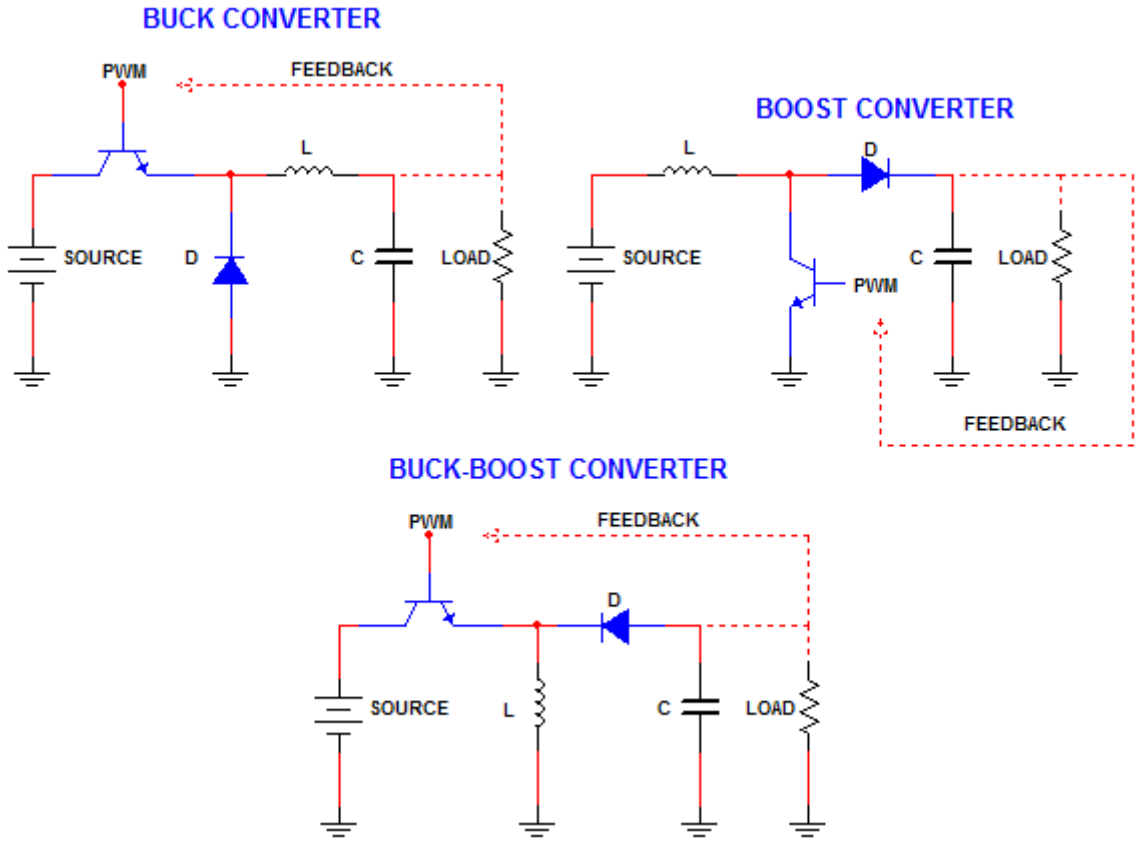

Figure 2.6.c.ii.iii: The three most common topologies of a switch-mode regulator

The buck converter is the most common of the switching converters and is used to down-convert (step down) a DC voltage to a lower DC voltage with the same polarity. This is essentially relevant to systems that need to distribute power to local sub-systems with very little power loss. As stated early, all switching regulators require some form of switching to properly regulate voltage. In the case of the converters, a transistor is used as the switch and is commonly controlled using pulse-width modulation (PWM). When the switch is closed in the buck converter circuit, the source feeds the circuit and the inductor current flows into both the load and the capacitor. Once the switch is open, the magnetic field of the inductor begins to collapse, resulting in a increase in inductor voltage that tries to stabilize the current. The voltage and current bias the diode and once again supply the load. Also, the capacitor discharges simultaneously into the load, contributing to the total current being supplied to the load.

The boost converter takes an input DC voltage and boosts it (steps up) to a higher voltage at the output. When the switch is closed in a boost converter, the inductor current and the capacitor charge builds up. Though, the current in the inductor is shorted by the switch, which allows the current to peak and circulate the source-inductor loop only while the capacitor current flows through the load. When the switch is closed, the current in the inductor decreases linearly, which momentarily biases the diode and spikes the capacitor voltage even higher than the source voltage. This process creates the "boost" in the voltage and is effectively stabilized by employing a high switching frequency at the base of the transistor switch.

One important note of the boost converter is that output load current is not going to be equal to the switch current. The maximum available load current will depend solely on the switch transistor, and will always be less than the current rating that the transistor can support. In summary, since the voltage is higher on the output than the input, it should recognized that the output current must be less than the input current.

The buck-boost converter takes an input DC voltage and inverts it to a voltage of opposite polarity at the output. The inverted output voltage can be of lower or higher magnitude than that of the input voltage and will depend on the application it is intended for. When the switch is closed in a buck-boost converter, a similar process occurs to that of the boost converter. The current from the inductor will circulate through the source-inductor loop while the capacitor current feeds the load. When the switch is open, the current in the inductor decreases linearly and momentarily biases the diode to allow current to flow through both the capacitor and load. Though this time, the current flows in the opposite direction and flips the polarity across the capacitor, resulting in an inversion of polarity at the output.
In summary, the inductor supplies the load with current when the switch is open and the capacitor supplies the load with current when the switch is closed.

In conclusion, it is clear that switch-mode regulators will be required in the design of the power system of the spectrometer. It will be a must to use a boost converter to supply high reverse-bias voltage to the photodiode in order for optimal detection to take place. If a single-cell lithium battery is used, then it will also be necessary to use a boost converter to boost the 4.2 volts to 5 volts so that the amplifiers of the pre-amplifier and pulse shaping circuit may operate correctly.

2.6.d Sensor Cooling

As previously stated in the requirements section, it will be absolutely necessary that temperatures of the detector be dropped to at least -15˚ Celsius. This will be accomplished by investigating the properties and operation of thermoelectric peltier coolers and employing specific solutions to our design. Also, the use of a heat sink will be required to alleviate the excess heat generated from the hot side of the peltier cooler. Driver circuitry will be used to accurately deliver power to the TEC, whether it by means of a designed circuit or a dedicated module IC. Figure 15 displays the sensor cooling scheme that we want to employ to actively and passively cool the photodiode detector

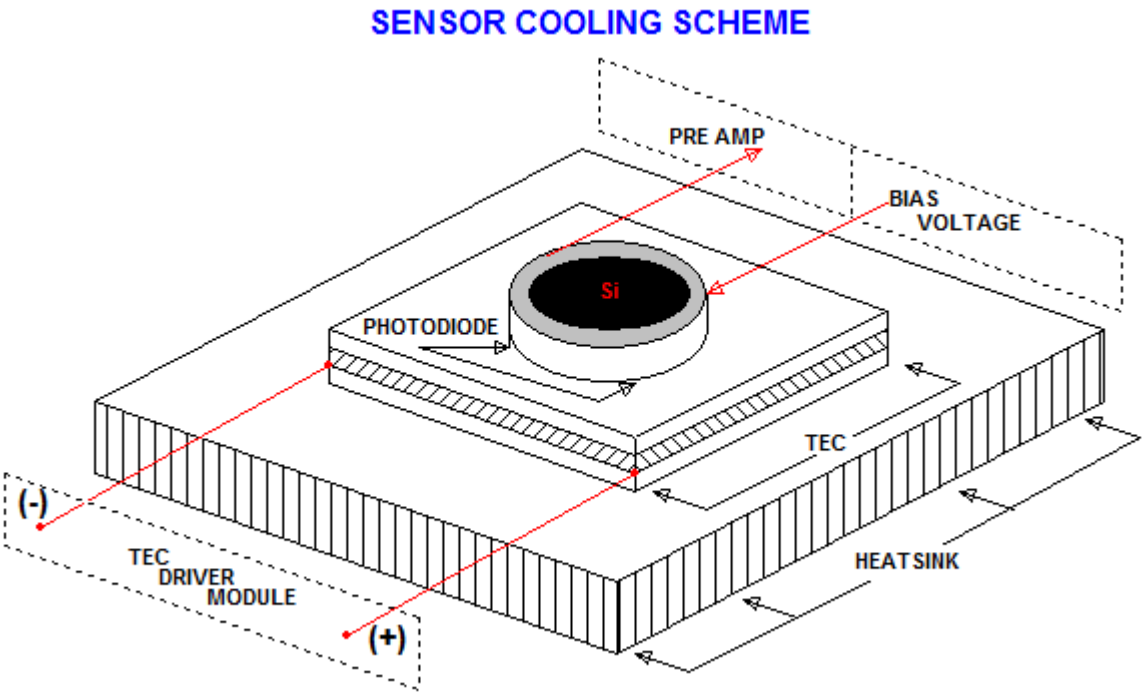

Figure 2.6.d.i: Necessary cooling scheme for cooling a semiconductor detector

Temperature control is not a requirement, but if it can be achieved with little design effort then it will be implemented into our design. The following sensor cooling subsections will be dedicated to provide all of the insight for semiconductor detector cooling methods and basic theory of operation.

2.6.d.i Thermoelectric Cooler

The Thermoelectric cooling effect which was coined by Jean Peltier in 1845 demonstrates that if a DC current passes through the contacts of two dissimilar conductors in a circuit, a temperature differential appears between them. This implies that heat is being pumped from one side (plate) to the other, making one side hot, and the other cold. This process is very similar to the reverse Carnot cycle, which is the basis for refrigeration. This effect will prove to be quite useful when trying to bring the temperature of the photodiode into the negative Celsius range to obtain optimal detection.

When a DC current is applied to the n-type thermoelectric element, electrons pass from the P to the N-type thermoelectric element and the cold side temperature decreases as heat is extracted (absorbed). The heat is then transferred to the hot side of the cooler, where it is dissipated into the heat sink and the surrounding environment. The heat absorption is proportional to the current and the number of thermoelectric couples in the TEC. This process is depicted in figure 2.6.d.i.i.

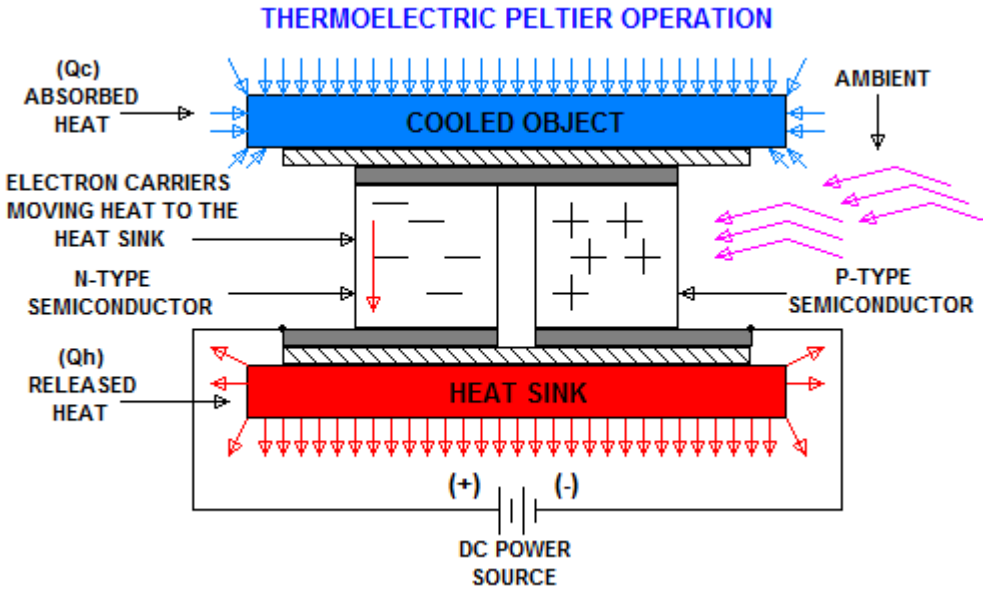

Figure 2.6.d.i.i: Theory of operation for a thermoelectric Peltier cooler.

Before choosing a TEC or heat sink, it is necessary to determine the amount of heat that needs to be pumped away from the cold side of the TEC. Minimizing the heat load allows a TEC to achieve colder temperatures or reduces the power required to reach the predetermined cooling temperature. The following few paragraphs will be dedicated to illustrate common techniques that are used to estimate active and passive steady-state heat loads.

First off, a heat load can consist of two types; active or passive, or a combination of both. An active load is the heat dissipated by the device that is being cooled. In almost all cases, the heat dissipated by the device equals the input power that is fed into it. Passive heat loads are parasitic and are considered oddities. They may consist of radiation,

convection, or conduction. An active heat load's dissipation can be described by the equation:

$$Q_{active} = \frac{V^2}{R} = I^2R$$

Where Q_{active} is the active heat load dissipation, V is the voltage applied across the device being cooled, R is the internal resistance of the device, and I is the current circulating through the device.

Radiation loading occurs when heat is exchanged by two objects that are at different temperatures and close in proximity. This is permitted since electromagnetic radiation is emitted from one object and absorbed by another, hence the exchange of heat. The equation for radiation loading is described by:

$$Q_{rad} = FesA(T_{amb}^4 - T_c^4)$$

Where Q_{rad} is radiation heat load dissipation, F is shape factor, e is emissivity, A is the cooled surface area, T_{amb} is the ambient temperature, and T_c is the TEC cold side temperature.

Convection loading occurs when the temperature of a fluid flowing over, around, or into a device differs in temperature from that device. The amount of heat transfer varies depending on the rate at which the fluid is flowing relative to the device. Convective loading is a function of the exposed area and the difference in temperature between the area and the surrounding fluid. The equation for convection loading is described by:

$$Q_{conv} = hA(T_{air} - T_c)$$

Where Q_{conv} is convection heat load dissipation, h is the convective heat transfer coefficient, A is the cooled surface area, T_{air} is the surrounding temperature of the air, and T_c is the TEC cold side temperature.

Conduction loading occurs when energy exchange takes place by direct impact of molecules traveling from a high temperature gradient to a low temperature gradient. This implies that heat exchange is done within the same material or by an external material that is adjacently touching. The equation for conduction loading is described by:

$$Q_{cond} = \frac{kA\Delta T}{L}$$

Where Q_{cond} is conduction heat load dissipation, k is thermal conductivity, A is the cross section area of the material/device, ΔT is the total diffence in temperature of the entire path, and L is the length of the path.

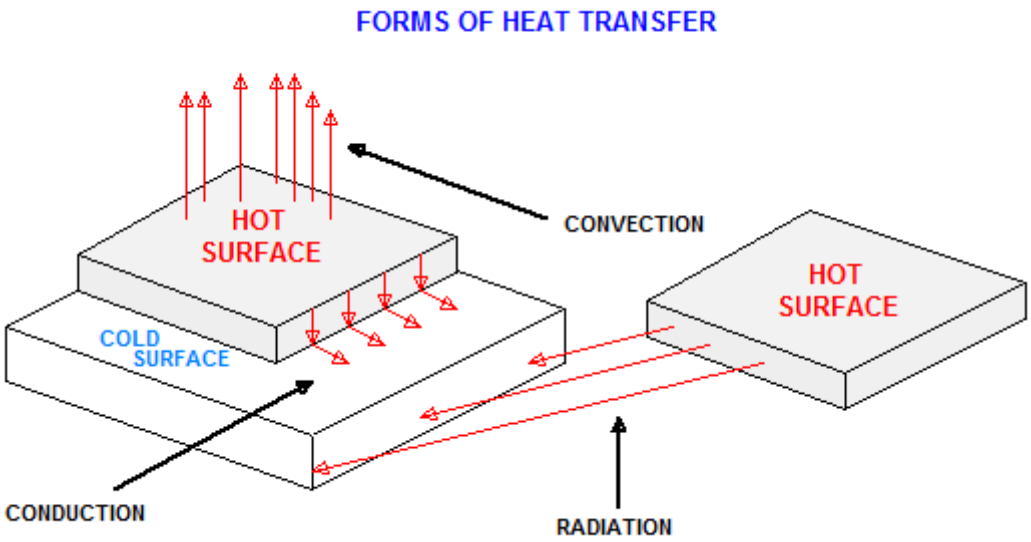

Figure 2.6.d.i.ii: Different forms of heat transfer

Now that all the external heat loads have been discussed, it will be the focus of the following to discuss the properties and equations that govern the internal heat transfer of the thermoelectric coolers

Thermoelectric applications depend almost entirely on three parameters. These parameters are the cold surface temperature (T_c), the hot surface temperature (T_h), and the heat of the load that needs to be absorbed by the cold surface (Q_c). The hot side of the thermoelectric module is the side where heat is released when DC power is applied. This is the side where the heat sink is applied and convection takes place, either natural or forced. The applied heat sink gives rise to the following set of equations:

$$T_h = T_{ambient} + R_{therm} Q_h$$
$$Q_h = Q_c + P_{input}$$

Where $T_{ambient}$ is the ambient surrounding temperature, R_{therm} is the thermal resistance of the heat sink, and P_{in} is the input power to the TEC. The thermal resistance of the heat sink will cause temperatures to increase above the ambient if the resistance is high. Thermal resistance is inversely proportional to the surface area of the heat sink. Therefore it must be noted that the smaller the heat sink, the more heat will be dissipated when power is applied to the TEC. Also, the equation that achieves higher differential temperatures is given by:

$$\Delta T = T_h - T_c$$

Where ΔT is the differential temperature across the two ceramics plates. As can be seen from this equation, the differential temperature will only increase if the difference between T_h and T_c is increased. The more heat that is being transferred by the TEC, the less efficient it becomes, because the TEC must dissipate both the heat being transferred, as well as the heat it generates from its own power consumption. The amount of heat that can be absorbed by the TEC is proportional to the current and time:

$$W = PIt$$

Where P is the Peltier coefficiant, I is the current, and t is the time. The Peltier coefficient is dependent on the temperature and the material of the TEC.

For the purposes of the average TEC consumer, it is not necessary to use the previously stated equations unless intensive background is required for extremely sensitive applications. In the industry, operation of TEC's are given at a specific value of T_h and is rated for I_{max}, Q_{max}, V_{max}, and ΔT_{max}. The following figures 2.6.d.i.iii and 2.6.d.i.iv illustrate these ratings for a typical 200 square millimeter TEC.

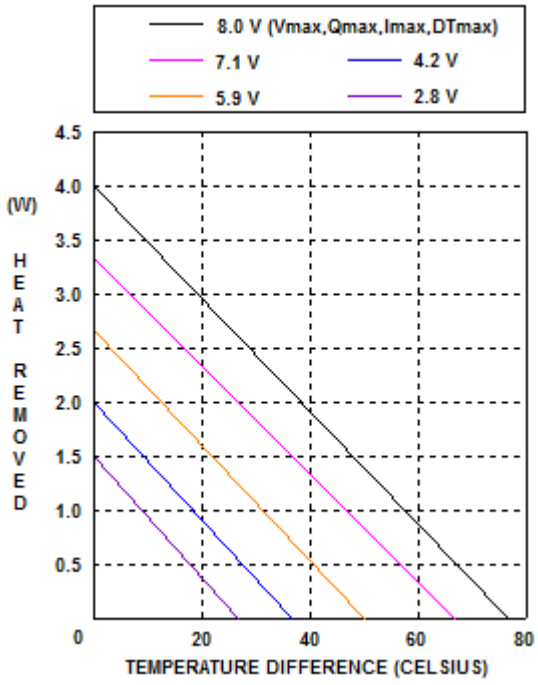

Figure 2.6.d.i.iii: Generated plot showing the performance ratings required to remove heat from the cold side of the TEC.

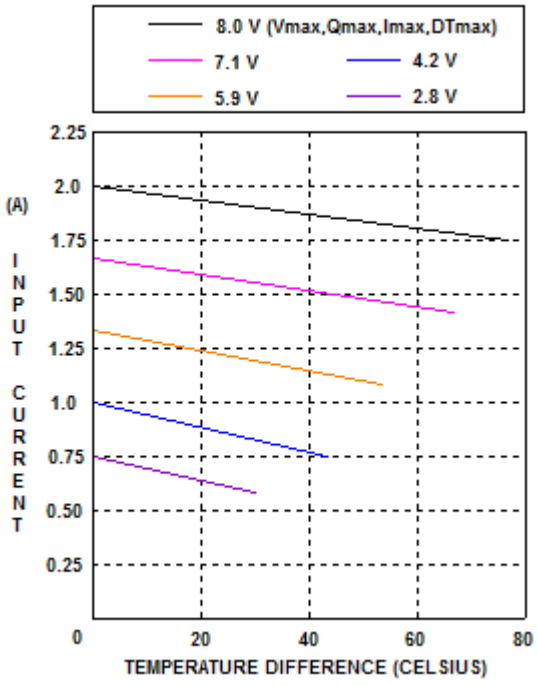

Figure 2.6.d.i.iv: Generated plot showing the input current required to create a temperature differential across the two plates.

In the industry, TEC's come in various shapes and sizes and can be manufactured to suit consumer needs for specific applications. The most common models consist of thermoelectric couples (P and N-type semiconductor pellets) that are connected electrically in series, in parallel thermally, fixed by soldering, and sandwiched between two square ceramic plates. The semiconductor pellets are typically composed of bismuth telluride (BiTe) and are the key component in generating thermal differentials. The hot and cold ceramic plates are shaped from materials such as aluminum oxide (Al2O3), aluminum nitride (AlN), and beryllium oxide (BeO). Aluminum nitride and beryllium oxide will not be of much interest as they are both much more expensive and beryllium oxide is known to be poisonous. Figure 2.6.d.i.v displays the general construction of single and stage TEC's.

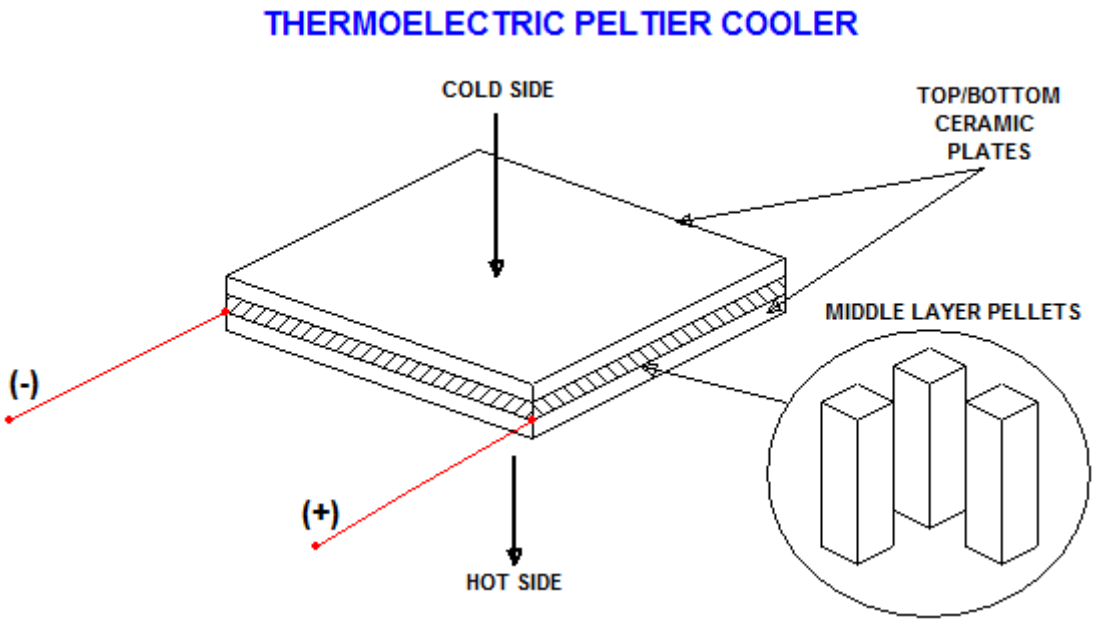

Figure 2.6.d.i.v: General construction of a single stage TEC.

There is also the method of stacking TEC's (multi-staging). This is done for special applications that require much greater temperature differentials. The theory behind it is just the same as for a single TEC. If the cold side of one TEC is applied to the to the hot side of the another TEC, it acts like a heat sink although with greatly enhanced absorption capabilities. This method along with addition of a fan actively cooling the heat sink would greatly improve the temperature gradient between the two ceramic plates.

In summary, it will be required that special care be taken in choosing the right TEC. A TEC must be chosen that can achieve 85+ C° temperature differentials with low maximum current draw. In this case, it be may necessary to go with a multi-stage TEC for the high temperature differential capabilities. Also, proper heat sink size and material will be required. It is most desirable to choose a heat sink that is small for portability but also made of a material with high thermal conductivity so as to compensate for the internal thermal resistance.

2.6.d.ii Driver Circuitry

Driver circuits are used to control and regulate power of another circuit and/or component. The driver circuit for our purposes will drive the thermoelectric cooler into the lowest cold side temperature possible. Simplistically, a basic regulated source would do just fine in powering the TEC just as long as it is operated within its specifications. Though it will probably be most efficient and robust to make use of H-bridge circuitry with power MOSFETS.

The most commonly available drivers utilize a PWM based power stage using either full H-bridge or half H-bridge power MOSFET switches. A full H-bridge is used for both heating and cooling a TEC, while a half H-bridge is used for only one of the two. An H-bridge is a circuit that enables voltage and/or current to be applied across a load in either direction. This circuit technique is most often used for applications that involve motor control, since forward and reverse actuation is a must. That is why it is also applicable to TEC's, because reversible polarity capabilities allow either heating or cooling to take place. For our purposes, it is only necessary to use the half H-bridge topology since cooling is all that is required of our design. Figure 2.6.d.ii.i demonstrates the usage of H-bridges for a TEC.

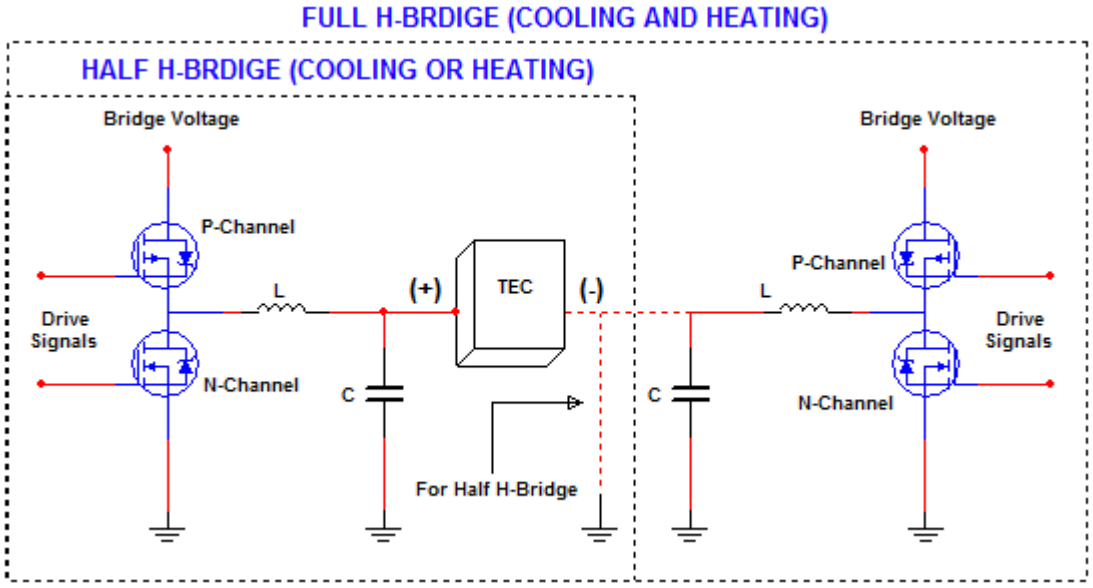

Figure 2.6.d.ii.i: Full and half H-bridge circuits used to regulator power to a TEC

H-bridge configurations either half or full, are necessary because they prevent thermal shock and thermo-mechanical due to rapid or sudden on/off commands. The LC filtering further facilities this circuit and provides the TEC with minimal slew rates to maintain constant current.

In summary, it will be necessary to either incorporate the design of a discrete driver circuit as previously suggest or to once again use a dedicated IC that is already supplied with the PWM bridging mechanism. The module IC's also contain additional monitoring and temperature control circuits that may be of use.

3.0 PROOF OF CONCEPT

Due to the high cost of application specific Si gamma ray detectors, the use of low cost conventional visible light photodiodes for the purpose of gamma ray detection was investigated. A quick search for photodiode gamma detectors reveals several amateur projects that indicate that regular photodiodes are sensitive to high energy gamma radiation. Unfortunately the use of low cost conventional photodiodes does have its price: there is no data available in the datasheets on quantum efficiency for x-ray or gamma ray wavelengths. In fact, most datasheets show the responsivity rapidly declining in the UV range. This means that if we decide to use a low cost part not designed for gamma ray detection we would need to experimentally determine the performance of the diode and perform calibration. Nevertheless, because one of our design goals is to produce a low cost device it is worth pursuing visible light photodiodes. The use of sampled low noise opamps from several manufacturers enabled us to produce a proof of concept circuit to test the response of conventional photodiodes at no cost.

3.1 PROTOTYPE TEST GOALS

The main goal of the proof of concept design is to experimentally investigate the x-ray and gamma ray absorption of low cost photodiodes designed for visible light detection. Specifically, this design will enable us to verify our theoretical knowledge obtained from research. It is known that gamma ray interaction with semiconductor devices occurs in the forms of the photoelectric effect, Compton scattering, and pair production. Will we be able to identify and distinguish these interactions from the photodiode response? What range of energies will we be able to absorb and measure using these photodiodes? Additionally, our experimental data may suggest which circuit parameters are essential for optimizing our signal to noise ratio. These parameters include effects that cannot easily be modeled by simulation, such as signal leakage due to PCB layout.

An important consideration for a silicon gamma detector is device geometry. It would be ideal to have a very large surface area photodiode as this increases the probability of interactions with gamma rays. However, a larger junction increases a device's charge capacity. This increased capacitance reduces the sensor's bandwidth and reduces the amount of charge transferred from detector to the charge amplifier. By testing multiple photodiodes in parallel we can experimentally verify the effect of increased photodiode capacitance and determine whether the reduced bandwidth and signal attenuation vs increased active area is a fair tradeoff.

Equivalent noise charge is an important figure of merit for photodiode amplifiers, as this indicates the lowest amount of charge discernible from background noise. The POC circuit will be designed with low noise in mind, and will be fully shielded in a metal enclosure. Low noise is critical in a silicon detector, and as part of our initial prototype we will investigate the charge injection test used to measure the charge to voltage amplification and equivalent noise charge. An ideal gamma spectrometer should have a high gain and responsivity but as low as possible ENC.

Current noise in photodiodes contributes to a higher ENC, so coupling a conventional photodiode with a low noise amplifier so that the current noise is dominant should give us a rough idea of the ENC achievable with low cost diodes.

3.2 DESIGN

The prototype was designed with two amplifier sections: the preamplifier and pulse shaper. Though the preamplifier provides a very high level of amplification, it is not sufficient for obtaining a high resolution signal for analysis. Additionally, the output of the preamplifier will appear as a step signal that then decays as the amplifier's feedback capacitor discharges the accumulated charge through a feedback resistor. This signal must be shaped into a Gaussian pulse with a time constant chosen to minimize noise and maximize signal amplification. A second amplifier section composed of multiple integrators and differentiators is used to accomplish this pulse shaping. Figure 3.2.i illustrates a high level overview of the prototype setup.

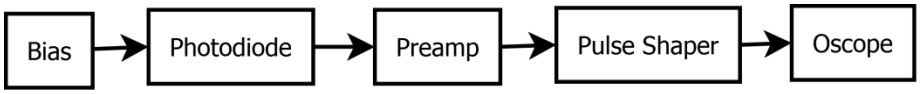

Figure 3.2.i: Proof of concept high level overview

The following components were used in the prototype design:

Component	Manuf	Part	Input Capacitance (pF)	Offset Voltage (mV)	Bias Current (pA)	Voltage Noise (nV/rtHz)	Current Noise (fA/rtHz)
Preamp	TI	OPA322	4	0.5	0.2	8.5	0.6
Pulse Shaper	TI	LMP7721	?	0.026	0.003	6.5	0.01
Component	**Manuf**	**Part**	**Active Area (mm^2)**	**Reverse Breakdown (V)**	**Dark Current (nA)**	**Capacitance (pF)**	**Rise Time (nS)**
Detector	Vishay	BPW34	7.5	60	2	70	100

Table 3.2.i: Specifications of components used in prototype design

3.2.a Preamplifier Design

The charge integrating preamplifier design is based on a standard charge amplifier (see figure 3.2.a.i below). The charge gain of this circuit is $G_c = \frac{V_{out}}{Q_i} = \frac{1}{C_f}$. The feedback resistor is necessary to provide the opamp with DC stability, provide a path to discharge the feedback capacitance, and implement a low frequency cutoff. While it may seem tempting to use the smallest capacitor possible, this may lead to circuit instability. The proof of concept circuit was therefore not designed to maximize gain and minimize noise, but it was designed with only one important parameter in mind: circuit stability.

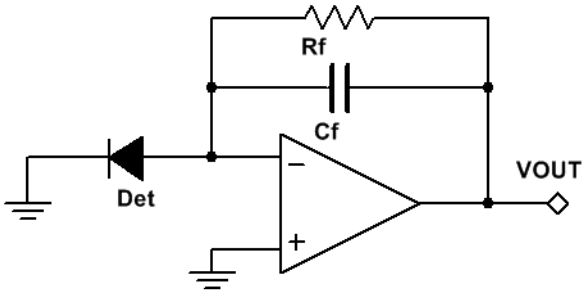

Figure 3.2.a.i: Basic transimpedance amplifier configuration

A charge amplifier's stability is determined by the amplifier's noise gain. That is, the reciprocal of the amplifier's feedback transfer function. Specifically, to ensure stability, the difference in slope between noise gain and the opamp's open loop gain at the point where they cross must be less than 40dB/dec. The feedback capacitor creates a pole in the frequency response that levels off the noise gain to 0 dB/dec. This must occur before the two gains cross. See the opamp stability section in the research chapter for details. To ensure stability of the LPM7721 opamp the following equation can be used to calculate the required feedback capacitance: $C_F = \frac{1}{4\pi R_F f_{GBWP}}(1 + \sqrt{1 + 8\pi R_F C_i f_{GBWP}})$. For our preamplifier circuit a value of $R_F = 10M$ was chosen, our test photodiode (Vishay BPW34) capacitance is $C_i = 18pF$ at a bias voltage of 5V, and the amplifier's gain bandwidth product is 15MHz. Derating this gain bandwidth product by 60% to account for process variability in manufacturing, we obtain a feedback capacitance of $C_F = 0.36pF$. To ensure stability we selected a value of 1pF for the feedback capacitor.

Since our amplifier's charge gain is $\frac{Q_i}{C_f}$ some preliminary estimates can be made about the amplifier output for known energy emission peaks of test sources. For instance, Cs-137 emits gamma rays in a single peak of 661.6 keV. Since this is one of the test sources used in this experiment, suppose that the full energy of an incident gamma ray is captured by the detector. To produce one electron-hole pair in silicon a photon 3.65 eV of energy is required. Assuming ideal absorption of all energy in the gamma ray this results in $\frac{661.6\ keV}{3.65\ eV} = 181.26k$ electrons. The total charge deposited is therefore $181.26k * 1.6\ x\ 10^{-19} = 29.16\ fC$. Using the gain of the charge amplifier, the output pulse

produced from the preamplifier should be $\frac{29.16fC}{1\ x\ 10^{-12}} = 29.16mV$. Since most interactions will occur through Compton scattering at ~600 keV we should expect to mainly see lower amplitude pulses due to incomplete energy absorption. It is reasonable to assume we would see some pulses in the ~10mV range. These pulses will be hard to resolve with an oscilloscope so a pulse shaping circuit with additional gain is necessary to analyze the output.

The photodiode was reverse biased and AC coupled to the opamp input. Because a single supply was used to power the opamp (0V-5V) the output was biased to the midpoint of the supply voltage via the noninverting feedback pin. See figure 3.2.a.ii for the schematic of the preamplifier section of the circuit.

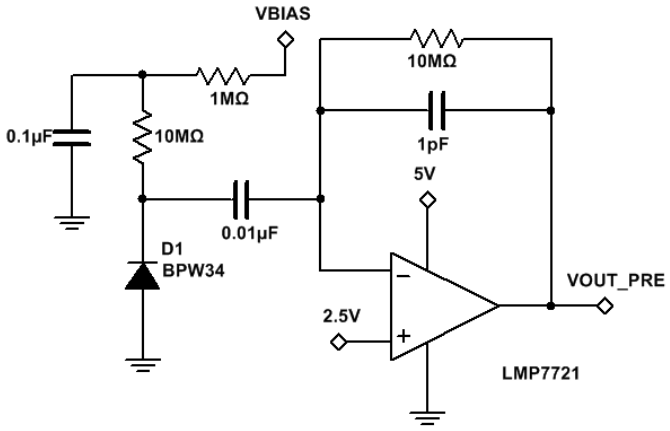

Figure 3.2.a.ii: Preamplifier section of POC circuit

3.2.b Pulse Shaper Design

The pulse shaper circuit consists of a differentiator stage and three integrator stages all using the same time constant. This forms a band pass filter which helps to shape the pulse into a Gaussian pulse and filters high frequency flat band noise as well as low frequency 1/f noise. Because both types of noise sources exist in the amplifier, the time constant can be optimized to find the minimum equivalent noise charge (ENC). Again, since our only goal in this prototype was to investigate feasibility and performance of different photodiodes, we did not attempt to optimize ENC and used a time constant of 10uS for the pulse shaper. Based on other works researched this value seems to provide good filtering of 1/f noise and flatband noise. For the final design of the project an extensive noise analysis of the entire amplifier circuit will be performed to determine the optimal value.

For the pulse shaper circuit the TI OPA4322 quad operational amplifier was chosen. This IC has a fairly low voltage noise density of 8.5nV/rtHz and a low current noise density of 0.6fA/rtHz. In comparison the LMP7721 has a current noise density of 10fA/rtHz, quite high for such a low bias current amplifier. For the pulse shaping time constant a value of 10uS was chosen for both differentiator and integrator opamp circuits.

Figure 3.2.b.i is the pulse shaper circuit designed for the prototype. The first stage is a differentiator used to convert the preamp output into a pulse. The last three stages are integrator stages. The component values (22k resistor and 470pF capacitor) were chosen to form a time constant of roughly 10us. DC gain of each stage is set by $\frac{22k}{1.8k} = 12.2$. This gain will not be the actual gain seen across each stage for the pulses as it will be determined by the frequency dependant impedance of the reactive elements.

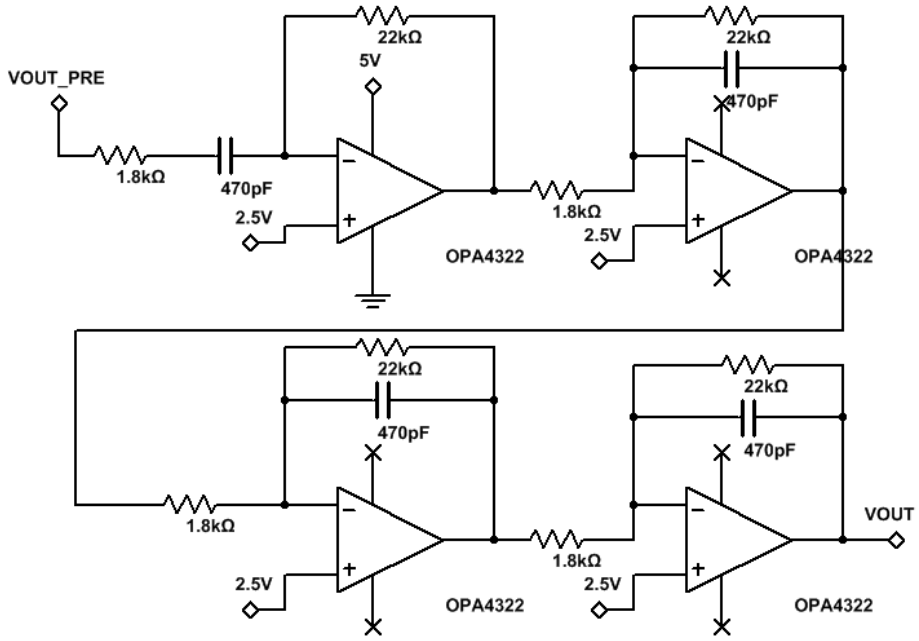

Figure 3.2.b.i: Pulse shaper section of POC design

Figure 3.2.b.ii shows the prototype design in Eagle, as well as the final board and test enclosure. Provisions were made to mount multiple BPW34 photodiodes to determine the effects of the increased (parallel) capacitance vs the increase in sensitivity from larger surface area of using an array of photodiodes. However, once the photodiode geometry was tested an enclosure was modified to mount power and signal jacks as well as a photodiode holder (tube). This made testing much faster as it was no longer required to wrap the circuit with aluminum foil for shielding. Since the OPA4322 comes in a 14TSSOP package and the LMP7721 in a SOIC-8 package, surface mount 0805 resistors and capacitors were used in order to minimize usage of board space and to be able to group all components tightly together for the smallest signal path. A single 5V power supply was used for both opamp IC's. This power supply was decoupled at both IC's by a 1uF capacitor. Because the output pulse of a transimpedance amplifier is negative, the output of all stages was biased at 2.5V by a resistor divider with filter capacitor connected to the noninverting input of all opamp stages. This allows the output to swing "negative" between 0V and 2.5V. Test points were included for the preamplifier output and all pulse shaper stages for troubleshooting and testing. The prototype PCB was manufactured at home using the laser toner transfer method on a copper clad board.

The masked copper board was then etched and populated with parts. A copper fill was used for a ground plane to reduce noise and allow for mounting of a metal shield when testing the circuit. The final circuit was mounted inside a metal enclosure with the ground plane of the circuit connected to the enclosure for proper shielding. All components were hand soldered. Final board was washed in ultrasonic cleaner with warm isopropyl alcohol solution to dissolve all traces of flux. This helps minimize leakage current from the sensitive preamp section.

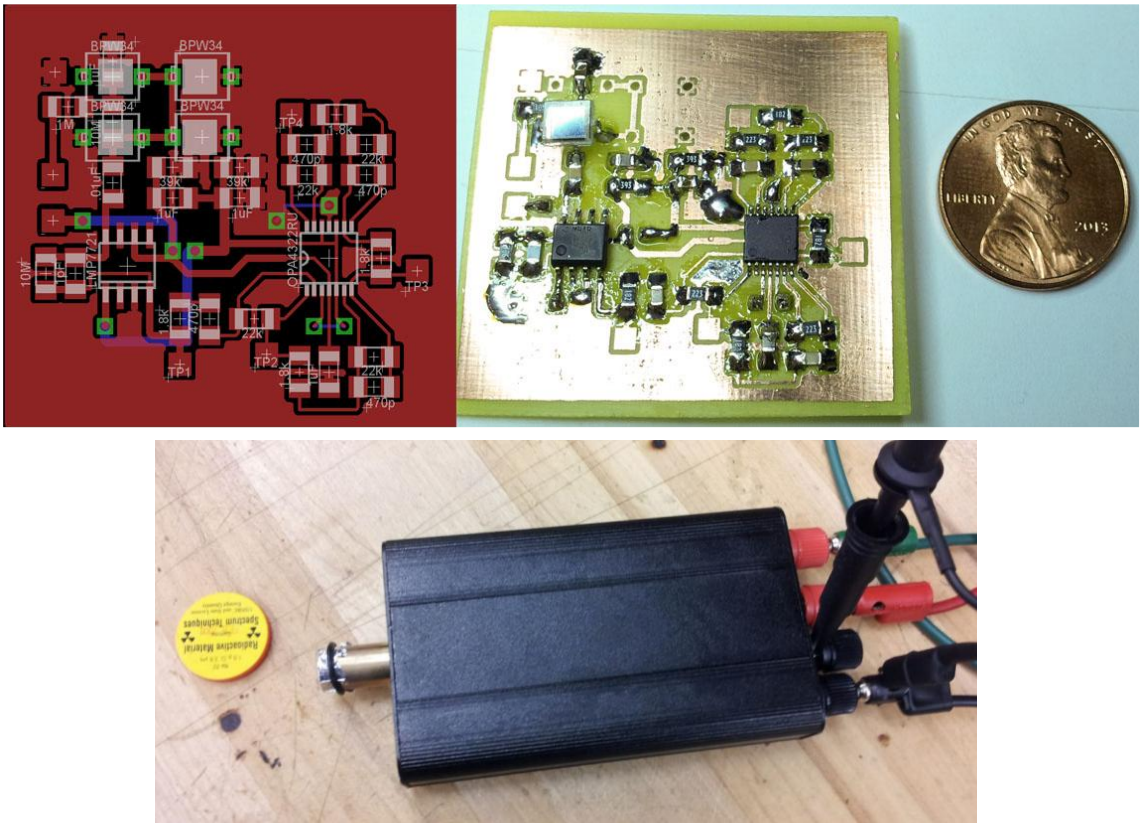

Figure 3.2.b.ii: Prototype board Eagle design, final board and enclosure

During initial testing it was discovered that a DC bias current flowing between the final pulse shaper opamp stage and the third pulse shaper stage resulted in a final stage output offset of 3.69V instead of the 2.5V offset it was designed with. The solution to this problem was to AC couple all opamp stages. To avoid having to design, etch, and populate a new board the coupling capacitors were placed in series with existing 1.8k resistors between stages. The parts were sandwiched in a inverted V shape over the original resistor traces. The board was initially tested with a single BPW34 photodiode.

3.3 SIMULATION / EXPERIMENT RESULTS

The table below lists all radioactive test sources used in testing of the prototype. With the exception of the Na-22 source (2008), the samples are from the year 2000. Except for Cs-137 they have all undergone significant decay. However, since we are only interested in the gamma emission peaks they were still usable.

Isotope	Activity	Half-life	Peaks of Interest (MeV)
Ba-133	1uCi	10.8 y	0.081, 0.276, 0.303, 0.356, 0.384
Cs-137	1uCi	30.2 y	0.662
Co-60	1uCi	5.27 y	1.172, 1.333
Na-22	1uCi	2.6 y	0.511, 1.275

Table 3.3.i: Radioactive test sources used in testing of prototype

3.3.a General Device Response

All of the following results were recorded with a Tektronix DPO 4034B oscilloscope using the scope's persist feature unless otherwise noted. This provides an overview of the pulse height distribution observed with each source. A reverse bias voltage of 12V was used with the source positioned as close to the detector photodiode as possible. Each division on the oscilloscope screenshots represents 750mV.

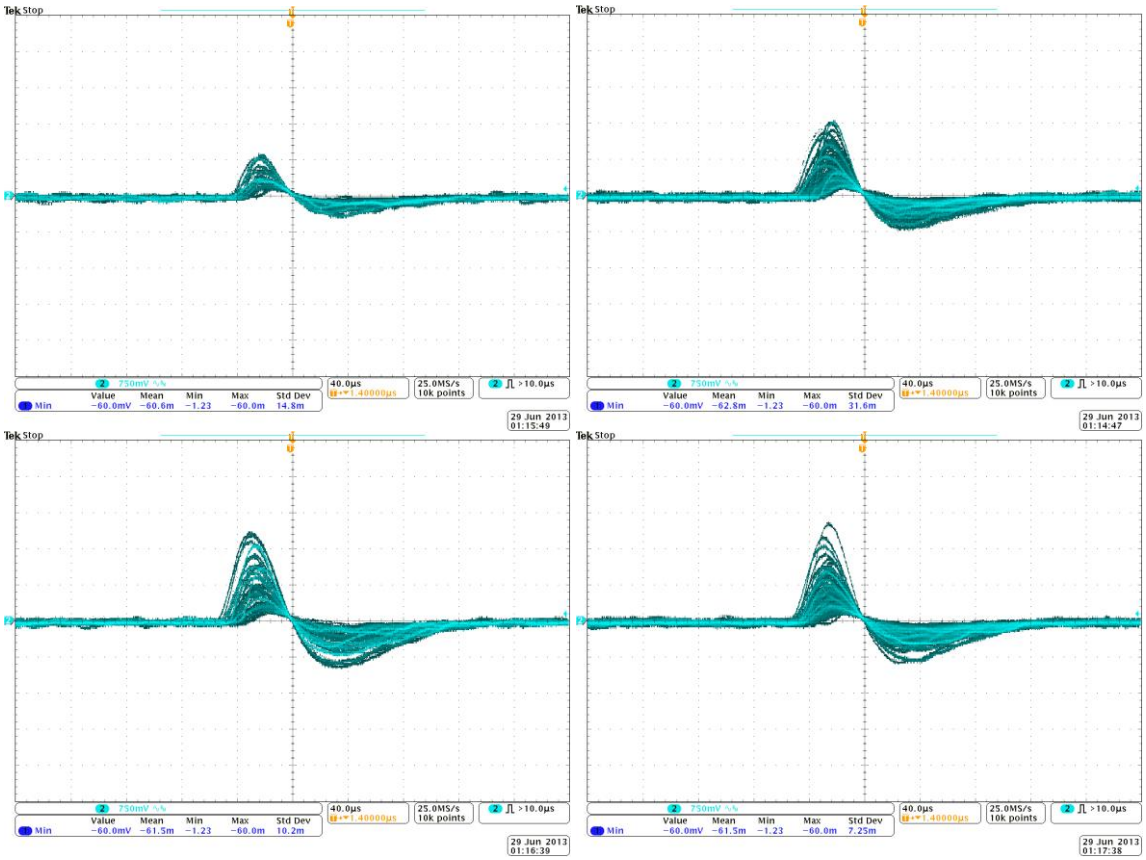

Figure 3.3.a.i Pulse height distribution of Ba-133 (top left), Cs-137 (top right), Co-60 (bottom left), and Na-22 (bottom right)

One immediate observation is that there does seem to be a correlation between pulse height and the energy of gamma rays, indicating spectroscopy is possible with the BPW34 photodiode and our amplifier configuration. Ba-133 emits the lowest energy gammas out of all gamma emitters tested (average energy 0.266 MeV). The lower energy gammas result in a lower proportional pulse height, as seen in the top left of figure 3.3.a.i. While Cs-137 emits gammas at a single energy level (0.662 MeV), the primary method of interaction at this energy level is Compton scattering. Compton scattering will result in a wide distribution of different energy levels as the incident gamma rays can scatter at any angle when they collide with an electron. We would therefore expect to see a wide distribution of pulses. Co-60 and Na-22 both follow the same trend, and while the last three spectrums look very similar, what they don't tell us is the count rate for each energy level. At this point we have not developed the code or circuitry yet to utilize the STM32F303's AD converter to sample and process the peaks into a spectrum for comparison. One final note on these results is that the Ba-133 sample seems to approach the lower limit of resolution achievable with the BPW34 diode. The BPW34's glass encapsulation (0.7mm thick) places a lower limit on the resolution obtainable. For optimal low energy response a windowless photodiode is a must.

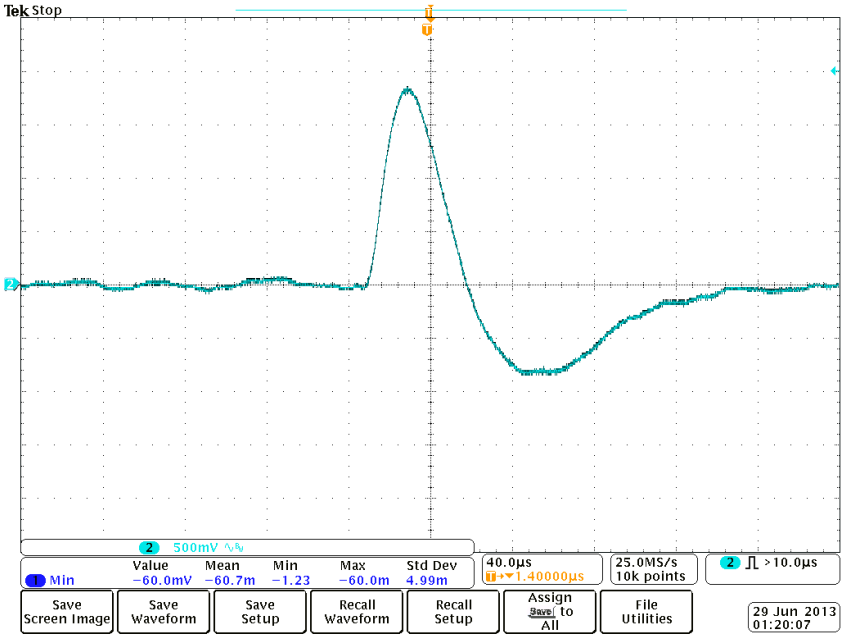

Figure 3.3.a.ii Sample pulse output from Na-22 sample

Figure 3.3.a.ii depicts a sample pulse recorded from an incident Na-22 gamma ray. A characteristic Gaussian pulse can be observed from the pulse shaper output. The pulse width is about 50us, and pulses appear very clean with low background noise present. We observed a count rate of about 130CPM from the 1uCi Na-22 source, which is quite impressive for the small 7.5mm^2 active area of the BPW34. Circuit noise was measured to be 33.3mV RMS, 197mV peak-to-peak.

3.3.b Device Geometry

While initial results appear promising, a small diode active area means it may take a long time to collect a sufficient number of samples for gamma spectrum analysis. It is easy to increase the active detector area by placing multiple photodiodes in parallel in an array. To mitigate reduced signal bandwidth resulting from increased detector capacitance the array could be divided and grouped to different preamplifier circuits. The resulting signals can then be summed and treated as one. The problem with an array implementation is that it increases cost (opamps and photodiodes) and complexity. It will be much more difficult to cool a collection of photodiodes and preamplifier opamps with a peltier cooler than if a single large device is used with a single stage preamp. A pulse distribution was collected on the oscilloscope using the persist function for both a single BPW34 photodiode and 4 BPW34 photodiodes in parallel. All photodiodes shared the same preamp input. See figure 3.3.b.i for experiment results.

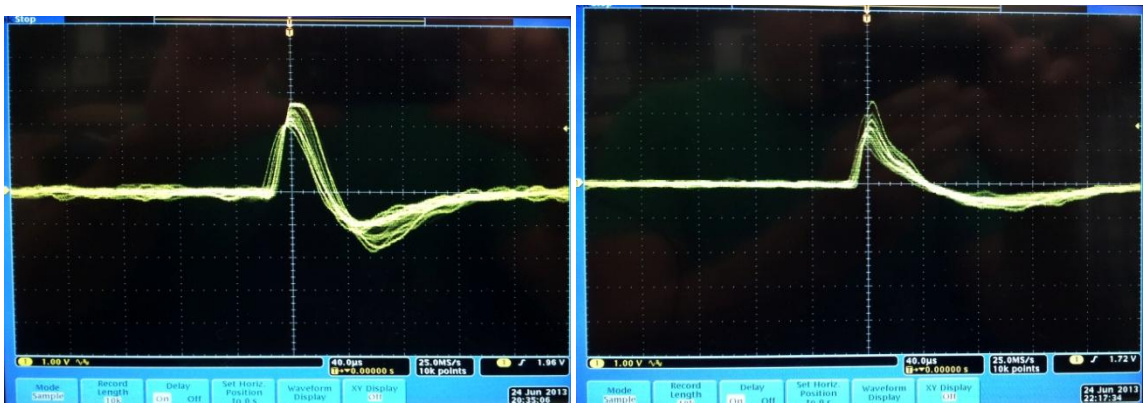

Figure 3.3.b.i Difference in pulses observed from (left) single BPW34 and (right) four BPW34 photodiodes in parallel

There is a definite attenuation of pulse amplitude and change in bandwidth noticeable due to increased detector amplitude in the results of the parallel BPW34 test. While there was not a significant change in pulse width between the two, there is a large difference in pulse width of the overshoot. This increased overshoot results in increased detector dead time.The parallel photodiode response also appears distorted, with a small second peak appearing in the positive part of the pulse. While the distortion may not be significant (we cannot obtain an accurate gamma spectrum at this point to verify this), count rate did increase significantly, so the tradeoff may be worth it.

3.3.c Charge Injection Test

By connecting a pulse generator to the preamplifier input through a coupling capacitor of known value, one can inject a specific amount of charge to test the operation of the amplifier. This follows directly from $q = CV$. Since capacitance and voltage of the pulse is known, we can select the appropriate combination to inject a specific amount of charge into the circuit. Since capacitors block DC current the charge transfer will only occur during the rising edge or falling edge of the pulse. Application note AN250-3 by Amptek describes a test procedure for their charge preamplifiers. It describes simulating a 1 MeV particle in their solid state detector by injecting its equivalent charge of 0.044pC. Their

amplifier outputs 500mV per picocoulomb of charge so they suggest a 2pF capacitor and a pulse of 22mV. Since these characteristics are all amplifier and detector dependent we started with the lowest output possible from the Tektronix AFG3022B function generator. Initially a voltage pulse of 10mV and a capacitance of 2pF was used. Note that the rise time of the signal must be fast (<= 20ns) when using such a small capacitance for full charge transfer to the amplifier. The AFG3022B has a rise time of 18ns which meets this criteria. The charge injection test will enable us to determine the amplifier's voltage to charge gain. In addition, it will enable us to measure the amplifier's equivalent noise charge (ENC), which is an important noise figure in gamma spectrometry. The charge injection test was carried out in a Multisim simulation and experimentally, and the results were compared. Figure 3.3.c.i and 3.3.c.ii display simulation and experimental results.

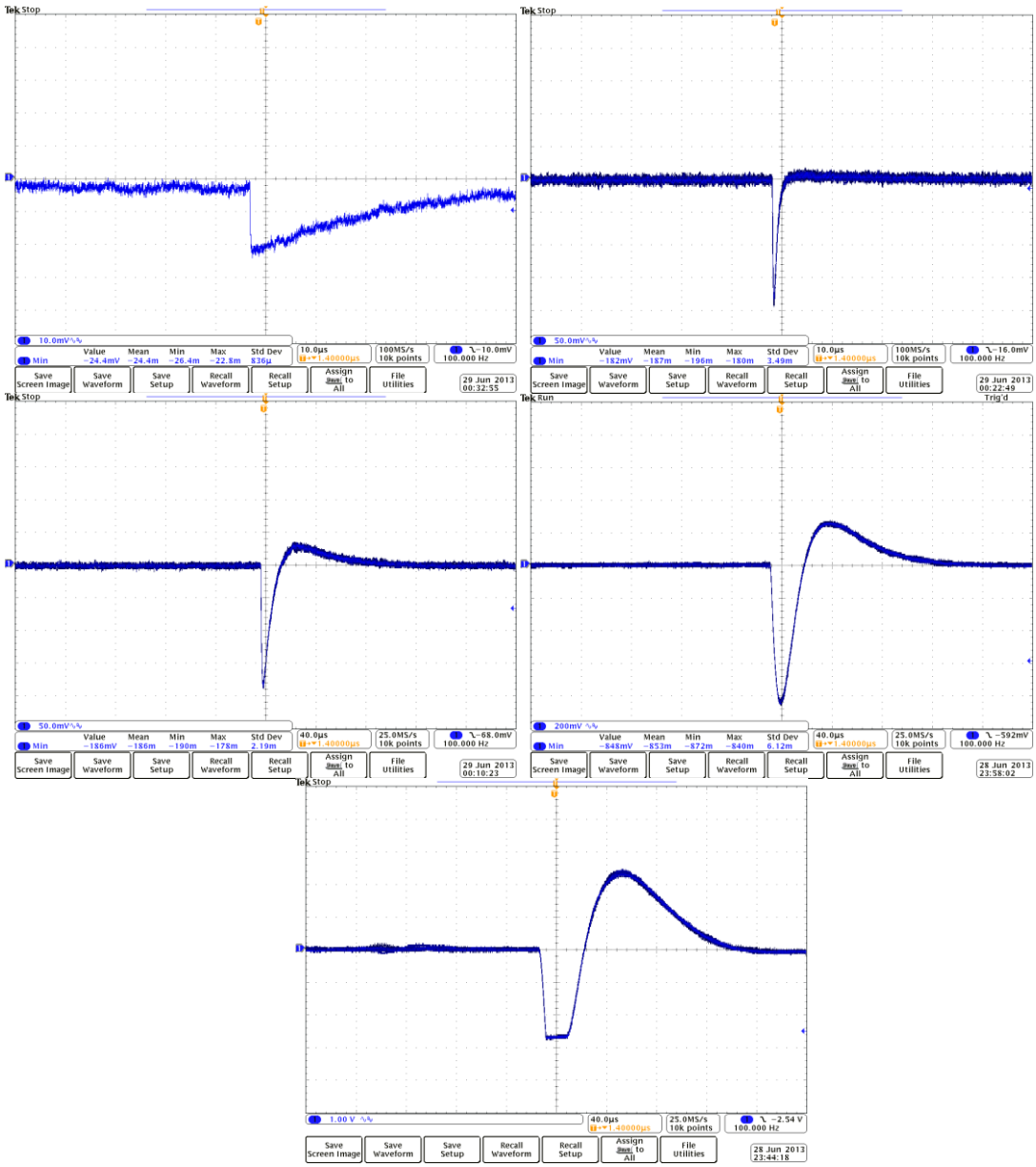

Figure 3.3.c.i Charge injection output (10mV pulse, 2pF capacitor) as measured at all circuit test points. From left to right, top to bottom is the preamp output and all four pulse shaping stage outputs

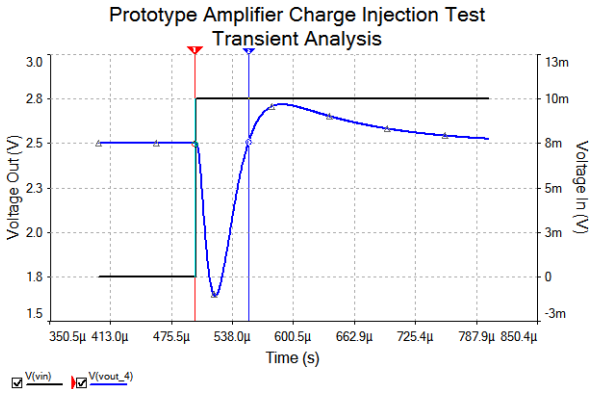

Figure 3.3.c.ii MULTISIM charge injection simulation

The injected charge collects on the feedback capacitor of the preamplifier, which is then amplified and appears on the output terminal of the preamp as shown in 3.3.c.i. The differentiator's purpose is to filter the low frequency capacitor discharge (as determined by the preamp RC time constant) from the output signal and amplify the high frequency step response from the charge injection. This yields a sharp impulse signal which is then integrated by the three integrator stages for the purpose of reshaping it into a gaussian pulse and to filter out high frequency noise to improve the signal to noise ratio. Note that since all amplifiers are inverting the pulses should be inverted in the 1st and 3rd stages but because the oscilloscope was triggered on the falling edge and a square wave was used to test the circuit the waveforms captured are all of the same polarity.

Unfortunately we were not able to obtain a signal from the final stage of the pulse shaper which was not saturated, even with the lowest possible function generator output of 10mV. In addition, While the pulse shape of our circuit output very closely follows the Multisim simulation (the pulse widths on both results are very close, ~40us), the Multisim output pulse did not saturate the amplifier. We suspect that these differences are a result of differences in device modeling of our selected opamps in Multisim and actual device characteristics. We can still get an approximation of circuit gain. Assuming complete charge transfer, a 10mV pulse through a 2pF capacitor should inject $Q = CV = 2x10^{-12} * 0.01 = 20fC$ of charge. This is equivalent to $\frac{20x10^{-15}}{1.609x10^{-19}} = 124.30k$ electrons. Since our final output pulse was greater than 2.5V, the gain is greater than $\frac{124{,}300e}{2500mV} \approx 50\frac{electrons}{mV}$, or equivalently the actual charge gain is greater than $0.008\frac{fC}{mV}$. The true gain is probably closer to $20\frac{electrons}{mV}$, but we can't be certain until we have some test equipment to perform smaller charge injection tests.

Noise measurement on our system using an oscilloscope showed RMS noise of 35.7mV. Using the figure of $50\frac{electrons}{mV}$, we can estimate that our ENC is less than $35.7 * 50 = 1785$ electrons RMS. While this is not a particularly impressive figure, our goal of this prototype was not to optimize the ENC. By adjusting the time constants on the differentiator and integrators we can adjust the pass band of 1/f and flat band noise. The ENC must be individually optimized depending on choice of detector and opamps (different spectral noise figures).

3.4 DISCUSSION

Results using the BPW34 photodiode are very promising. Output pulses generally look very clean and there is relatively little noise considering that there was no work done to minimize noise in the circuit design. The BPW34 seems to have a wide sensitivity, capturing energy from photons of several hundred keV to several MeV. The glass encapsulation does appear to put a lower limit on the resolution achievable with the device. Therefore low cost windowless visible light photodiodes should be investigated as an option for the detector. ENC will be optimized in the final design through extensive noise analysis of opamps and feedback circuitry. A numerical solution can be obtained if a system is obtained where total circuit noise (1/f and flatband) is modeled as a function of the pulse shaper RC time constant. The spectral current and voltage noise data can be obtained from opamp and (some) photodiode datasheets. A smaller time constant is preferred as this reduces the detector dead time (the overshoot of the pulse). Noise can also be reduced by actively cooling the detector and preamplifier stage, as these are the largest contributors of noise in the circuit. This will reduce both thermal noise effects and semiconductor noise sources. For simplicity a single preamplifier and photodiode is preferred if using a peltier cooler system.

It is impressive that we were able to observe a count rate of ~130CPM from the 1uCi Na-22 sample, considering the small active area and the fact that the quantum efficiency of silicon in the MeV range is below 1%. However, since there are typically 20,000-30,000 counts required for an accurate gamma spectrum the active area should be larger to allow for fast spectroscopy results. While we still don't have many parameters available from the datasheets of visible light rated photodiodes that can be directly applied to the design of a spectrometer we now have a better idea of device response obtainable with these low cost diodes.

The next step is to optimize the preamplifier design by doing a complete noise analysis of all stages of the amplifier starting at the photodiode, and choosing the best combination of sensor, opamps, and feedback components that will minimize the current, voltage, shot, and thermal noise. The most difficult part of this process will be finding the most appropriate photodiode to use as sensor. The BPW34 is a general purpose photodiode with no information available on its sensitivity to x-rays and gamma radiation. Most low cost photodiodes are general purpose photodiodes which are not optimized for detecting x-rays or gamma radiation. Therefore more sampling and testing of different detectors will be necessary before a final design is completed.

4.0 DESIGN

4.1 DETECTOR DESIGN

4.1.a Direct Detector Performance Characteristics

The quantum efficiency and responsivity plots for silicon over a depth of 350 µm at 59 keV and 1 µCi for Am-241 gamma decay are given below. They will remain similar among Si diode configurations and will have to be used due to lack of laboratory equipment to experimentally determine.

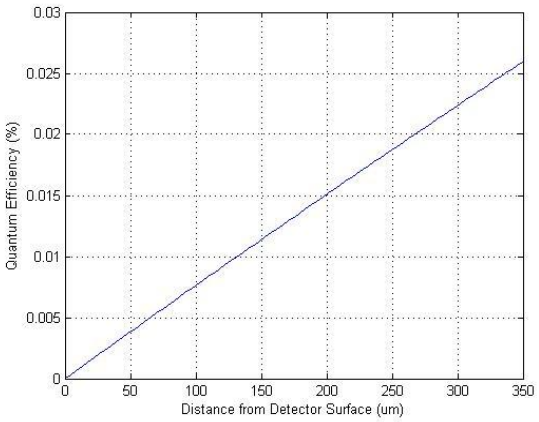

Figure 4.1.a.i: Quantum Efficiency versus Distance from Detector Surface

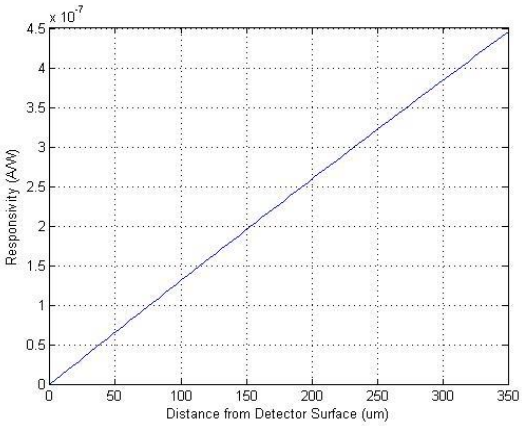

Figure 4.1.a.ii:Responsivity versus Distance from Detector Surface

We were limited in our choice for photodiode detectors primarily by our budget. A high-end detector rated for high energy detection can cost as much as $1,700.00. The largest active area p-i-n diode within our budget is First Sensor's X100-7 SMD, which can be purchased for $84.46 from Mouser Electronics. The table below gives the detector characteristics.

First Sensor: X100-7 SMD						
Symbol	**Characteristic**	**Test Condition**	**Min**	**Typ**	**Max**	**Unit**
A	active area		100	mm^2		
T	operating temperature		-20		70	℃
V_{max}	maximum reverse voltage			50		V
I_D	dark current	V_R = 12 V		5		nA
$T(I_D)$	Temperature coefficient; percent change of dark current	V_R = 12V		13		%/K

Table 4.1.a.i: X100-7 SMD detector characteristics

First Sensor: X100-7 SMD						
Symbol	**Characteristic**	**Test Condition**	**Min**	**Typ**	**Max**	**Unit**
C_J	junction capacitance	V_R = 0 V; f = 10 kHz		500		pF
		V_R = 12 V; f = 10 kHz		80		
t_r	rise time	V_R = 12 V; E = 10 keV; R_L = 50 Ω			500	ns
R_{sh}	Shunt resistance	V_R = 10 mV		40		MΩ
I_n	Noise current	V_R = 12 V		61		fA/√Hz
V_{BR}	Breakdown voltage	I_R = 2 µA	50	80		V

Table 4.1.a.i: X100-7 SMD detector characteristics (continued)

Using the tabulated quantities in table 4.1.a.i, the relevant theory provided in the research section, and the decay scheme of Am-241 (E_γ = 59 keV) at 1 µCi we can expect to obtain the following readout.

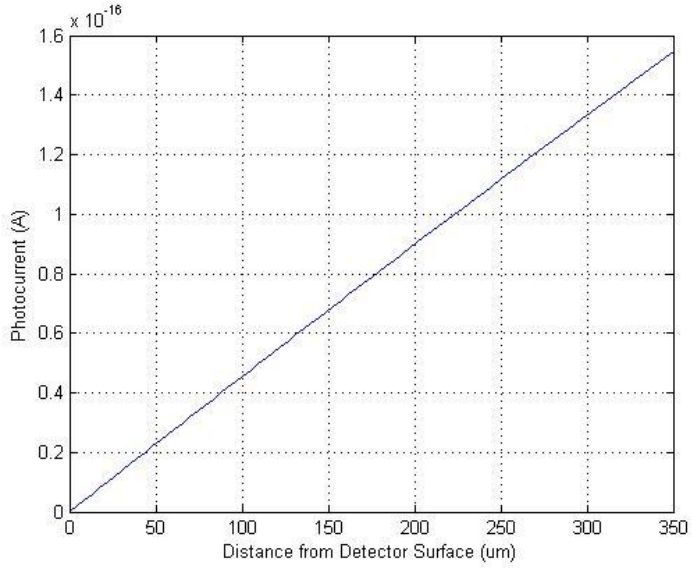

Figure 4.1.a.iii: Expected readout of photocurrent

Noise analysis at the preamplifier output was conducted and a feedback resistance R_f = 30 MΩ and feedback capacitance C_f = 5 pF and Analog Devices AD743 op amp was chosen for optimization. Using these values the estimated photocurrent, dark current and noise current can be evaluated and results in the following detector rating given in table 4.1.a.ii.

First Sensor: X100-7 SMD Am-241 @ 59 keV and 1 μC activity Performance Characteristics	
Parameter	**Calculated Value**
incident optical power (P_o)	3.482×10^{-10} W/cm^2
number of generated EHPs (N_{ehp})	1.638×10^4
generation rate (G_{op})	2.868×10^4 /cm^{3}s
initial charge collected (Q_i)	2.614 fC
linear attenuation (μ)	0.7721 cm^{-1}
FWHM	*k(128.016) eV*
resolution	1.835 %
dark current (I_D) @ T = -20° C and V_R = -20V	1.2204×10^{-12} A
current noise (I_n)	7.29×10^{-16} A/√Hz
photo current (I_{ph}) @ peak	1.6×10^{-15} A
e$^-$ RMS	122
Responsivity	0.45 μA/W
SNR	64.5 dB
NEP	1.62×10^{-9} W/√Hz
D*	6.18×10^8 cm√Hz/W

Table 4.1.a.ii: Performance characteristics of X100-7 SMD

As is apparent from the computed performance characteristics of the X100-7 SMD photodiode, the generated photocurrent is near the noise threshold, so that it might be masked by it. However, the dark current is only an approximation because an empirical relationship was used for its determination. With that in mind, the probability of effective collection above the noise threshold seems precarious. The computed photocurrent assumed ideal interaction and complete energy transfer, which will not always occur. The design parameters that affect either the generated photocurrent or the noise current are the detector active area and operational temperature, respectively. The generated photocurrent is tied to the magnitude of the incident optical power where *P α activity,* which signifies that a smaller active area will yield a larger incident optical power and therefore generation rate. Increased optical generation can improve photocurrent yield when optimization is key. The payoff for this, however, will be reduced gamma interaction. The reduced interaction will not affect any other intrinsic optical parameter, such as quantum efficiency, or responsivity because these assume interaction has occurred. The limiting operational temperature of the X100-7 is -20° C, but the dark current is too high for effective current collection. It was previously shown that the dark current will drop rapidly as a function of decreasing temperature, and cooling the detector to -40 C will drop the dark current by orders of magnitude.

The total photodiode current at the input to the op amp feedback network will be due to the noise current and photogenerated current entirely because the dark current will be blocked by an AC coupled capacitor. As a result, the total current at the op amp front end will be $\approx I_{ph}$, which is precisely what we wanted. The charge there can be estimated by evaluating the voltage drop due to I_s across the shunt resistance using Ohm's law and applying $Q_{in} = C_{total}V$, which yielded 4.72 pF. The ideal charge collection is given by $qE_{ph}/\varepsilon_i = 2.64$ fC for $E_{ph} = 59$ keV. This produces a 79% error from the ideal according to the developed theory.

The estimation of use of the x100-7 was ultimately determined by an ENC evaluation, where the photodiode capacitance was varied in order to estimate its effect on resolution and noise. What we achieved was that the diode capacitance can be used at 80 pF and only increase the RMS e^- by roughly two times. This is sufficient for our purposes and solidifies the dominance of the photocurrent over the noise threshold since the ENC is a measure of the signal currents fluctuation from the mean. Displayed in the figure below, for different op amps, the trend in ENC increase matches expectations, but can be optimized at the op amp end. This is because of the input FET spectral noise components vary for each op amp. The ENC is quite low, which additionally matches the FWHM analysis for solid state detector and silicon in particular.

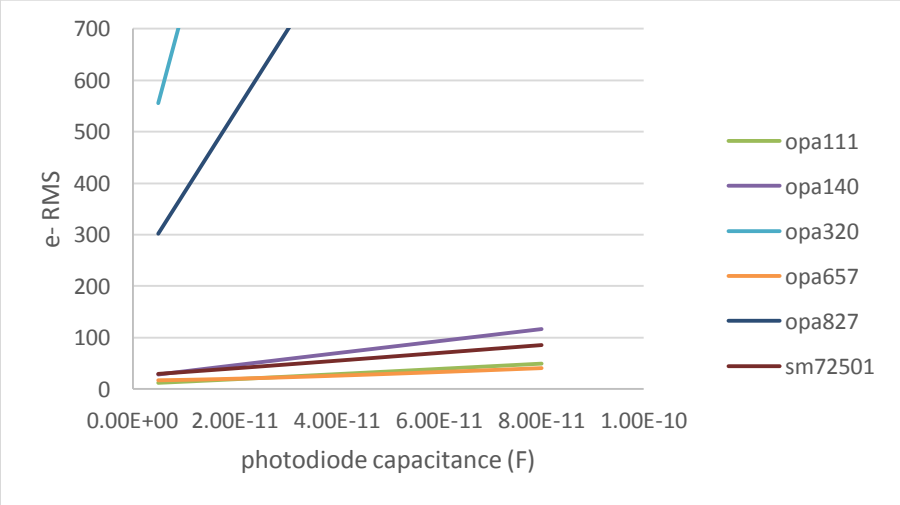

Figure 4.1.a.iii: Expected readout of photocurrent

For these reasons we will be using the large active area of the x100-7, despite increases in generation rates for smaller active area detectors.

4.1.b Direct Detector Package

The detector schematic is shown below in figure 4.1.b.i. It is a surface mount device that is encapsulated in black epoxy and housed in a ceramic package. There are 10 surface mount pins each 1.00 x 1.80 mm with anode at pin 8 and cathode at pin 3. The detector/epoxy encapsulant occupies 1.38 mm , with the epoxy having 0.48 mm depth and detector 0.90 mm depth. The total active area is 100 mm^2 and is housed in a 16.5 mm x 16.50 mm package. The ceramic packaging is ideal because it prevents any fluorescence from occurring when radiation bombards the walls. The SMD configuration allows thermoelectric coolers to be placed directly up against the detector for efficient cooling. In addition, the black epoxy completely shields the detector from visible light and weak to medium UV interaction, so that we can be confident signal generation is due entirely to gamma interaction.

4.1.c Direct Detector Shielding

The shielding of our photodiode will have to prevent both light and charged particle interaction. Metal is the ideal choice because it achieves both goals. A display of the types of interacting particles is given below. Alpha particles are weakly penetrating and can be stopped by material as thin as paper. Beta particles are also weakly penetrating and are absorbed easily by aluminum. However, they may penetrate the foil if they are high energy and cause bremsstrahlung interactions. Charge beta particles also emit gamma energies due to electron-positron annihilation. Neutron radiation is highly penetrating and causes secondary gamma radiation due to nuclei absorption.

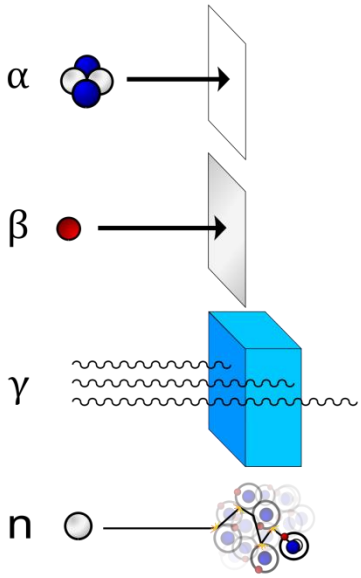

Figure 4.1.c.i: Types of radiation interaction with matter showing penetration capability (Image license under Creative Commons Attribution Share Alike v. 2.5).

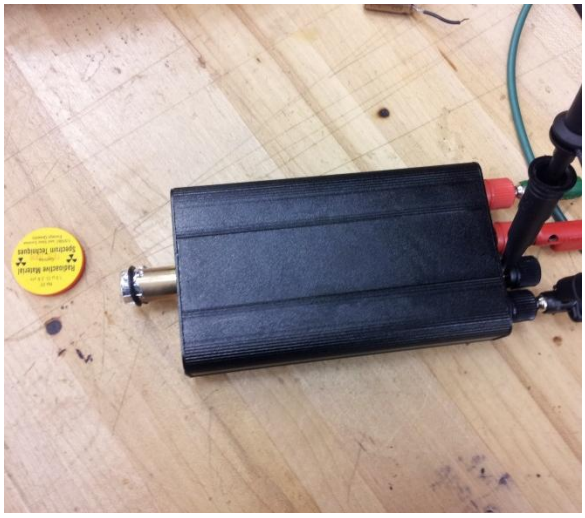

Figure 4.1.c.ii: Electronics housing and probable probe shielding and casing

Wrapping the photodiode in aluminum or Mylar will be the probable solution to blocking necessary irradiation because both materials are widely available. Multiple layers can be used to be careful to block all incidental interaction. If geometry allows, a short laser casing can be hollowed and the circuitry inserted. The length of the probe is pertinent because any increased distance from the photodiode/preamp frontend and pulse shaping circuitry increases the noise. An alternative is to mount the detector in an opening dead-bug style on the circuitry. The final design decision will rest on housing availability and final PCB size. The casing used in section 'proof of concept' will be the housing used to mount the probe and is shown in the figure 4.1.c.ii.

4.1.d Scintillator Performance Characteristics

Due to its availability and low cost, the plastic scintillator BC-408 was chosen for high energy gamma ray detection. The scintillator material is made of polyvinytouene that has a density of 1.032 g/cc and refractive index of 1.58. The material is soluble in aromatic solvents, chlorine, and acetone and insoluble in water, dilute acids, lower alcohols, silicone fluids, and grease. It is best suited for detection of gamma rays in the energy range of 100 keV to 5 MeV, but can also be used for charged particle detection as well as cosmic ray detection. For that reason, shielding and mounting the device properly will be essential to ensure the photogenerated current is due only to gamma rays. Section 4.1.f will discuss the procedure. The general datasheet characteristics are given in table 4.1.d.i below.

BC408 (polyvinyltoluene) Premium Plastic Scintillator	
Light Output (% Anthracene)	64
Rise Time (ns)	0.9
Decay Time (ns)	2.1
Pulse Width (ns)	~2.5
Light Attenuation Length (cm)	210
Wavelength of Max Emission (nm)	425
No. of Electrons per cm^3 (x 10^{23})	1.104
Photons/MeV	10,000

Table 4.1.d.i: Datasheet characteristics for BC408

Its dimensions are 100mm x 32mm x 32mm and weight approximately 120 g. The range of relative light output extends from roughly 360 nm to 520 nm. This spectral range provides a rubric for detector choice.

4.1.e Indirect Detector Performance Characteristics

The detector we chose to couple to the scintillator is the PS100-6b THD. It has an active area of 100 mm^2, which, unlike the photodiode for direct detection, is needed because pulling the current signal out of the noise regime will not be an issue. Instead we need to optimize light/detector interaction. The scintillator output area is much larger than the photodiodes, but high energy secondary interactions are not an issue in the visible regime. The detector characteristics are displayed in table 4.1.e.i below.

First Sensor: PS100-6b THD @ 23°C						
Symbol	**Characteristic**	**Test Condition**	**Min**	**Typ**	**Max**	**Unit**
A	active area			100		mm^2
T	operating temperature		-20		60	℃
V_{max}	max reverse voltage			50		V
I_D	dark current	V_R = 5 V		1		nA
C_J	junction capacitance	V_R = 0 V		720		pF
		V_R = 12 V		275		
t_r	rise time	V_R = 12 V; Λ = 410 nm R_L = 50 Ω		200		ns
R_{sh}	Shunt resistance	V_R = 10 mV		50		MΩ
I_n	Noise current	V_R = 5 V; Λ = 410 nm		80		pW/√Hz
V_{BR}	Breakdown voltage	I_R = 2 μA	50			V

Table 4.1.e.i: Characteristics of the indirect detector PS100-6b THD

The quantum efficiency and responsivity plots are given as datasheet materials and, since we will be operating our detector within the rated range, we can use them to approximate the read-out. They are given in appendix II.

As an example, Cs-137 with 1 μCi activity emits gammas at 0.662 MeV so that the light output in photons/Mev will be 4,965 photons at roughly 425 nm. The scintillator power at the output is related to the input power by the light output % anthracene and is given as the absolute efficiency. For anthracence the absolute efficiency is 0.4, which yields η_{bco} = .026. Therefore, using $P_{out} = \eta_{bco} P_{in} \approx 0.1$ nW. At 425 nm, the responsivity is given as ~0.28 A/W and the quantum efficiency 80%. Therefore, to a good approximation, the generated photocurrent will be ~0.28 pA. The expected FWHM at 662 keV is 66.2 keV. The current noise and dark current are as specified in the datasheet and will be negligible when cooled compared to the photocurrent as before.

4.1.f Indirect Detector Package

The package for the detector to be used with the scintillator is shown below in figure 4.1.f.i. It is housed in a ceramic package and is windowless. The active area is 100 mm^2 and is housed in a package 16.5 mm x 15.00 mm with a viewing angle of 120°. The detector sits 0.60 mm from the surface for optional glass encasement. There are two pins for anode (pin 1) and cathode (pin2) with a notch indicating anode. The leads are separated by 12.50 mm and will be used to fit TEC on backside. The mounting and shielding procedure will be discussed in the next section.

4.1.g Scintillator Mounting/Indirect Detector Shielding

Before mounting the scintillator to the photodiode, it should be carefully polished with room temperature water and isopropyl alcohol using fine grained sandpaper in order to achieve optimum transparency and then dried with cloth; the majority of smoothing should be at the photodiode coupled window. Gloves should always be worn while handling the scintillator to prevent any oil from being deposited on the surface. There are several commercially available options for wrapping the scintillator to shield it from light such as Teflon, Mylar and aluminum foil, which ensures the detected light at the photodiode end results solely from the scintillator. For our purposes heavy duty aluminum foil will be used because it is easily purchased in bulk. The procedure for wrapping is as follows:

- Cut a sheet of foil that is approximately four times the width and one and a half times the length of the scintillator so that when the top and bottom surfaces, and both ends can be covered twice.
- Lay out the sheet of foil on a flat, smooth surface and place the scintillator centered at the foils edge.
- Fold the foil snuggly around the scintillator leaving enough room for reflective interaction on the foils interior and taking care not to tear the corners.
- Use masking tape to tightly seal the foil at the top, bottom and entrance windows only.
- Cut off any remaining excess foil starting at the exit window. If the scintillator area is larger than the detector area, use the detector as a guide to trace out a window.
- Wrap the scintillator with electrical tape so that the foil is completely covered. Leave the previously cut window uncovered.
- Apply a minimal amount of optical grease/cement to cover the detector face.
- Press the detector face to the open window of the scintillator applying pressure such that the grease will spread out past the scintillator edges.
- There should be no air bubbles and from here on out the detector and scintillator should remain attached.
- Mount the scintillator to the detector by applying vertical strips of electrical tape.
- Starting from the detector, wrap electrical tape completely around the coupled device up to the top of the scintillator. Pay careful attention to the scintillator/detector interface – this section can be wrapped several times to avoid light leakage.
- After completing wrapping, the coupled scintillator/detector can be placed in its housing.

4.2 CHARGE AMPLIFIER

This section discusses the design of one of the most crucial components of the spectrometer: the charge amplifier. This amplifier design requires special consideration as it must be ultra-low noise but still have a high gain. To minimize the equivalent noise charge, and therefore improve signal to noise ratio (SNR), an extensive analysis was performed to determine the optimum component selection.

4.2.a Schematic

The layout of the charge amplifier follows the standard design of a charge amplifier. Since we are operating all opamps with a bipolar ($\pm 5V$) power supply, the noninverting terminal of the opamp is grounded, turning the inverting terminal into a 'virtual ground'. This will cause the output to swing positive or negative with respect to ground. The power supply bias connection to the opamp is filtered with RC network R1*C1, using a low cutoff frequency (R1 ~ 1M, C1 ~ 0.1uF). Current is then limited to the photodiode by R2 (~10M). To avoid having to deal with a DC voltage offset caused by the photodiode's dark current, the photodiode is AC coupled to the preamplifier. Additionally, since DC offsets resulting from opamp bias current will result in large voltage offsets on the output of each stage, the amplifier stages were AC coupled to remove the offset. Selecting a large value for the AC coupling capacitor ensures that the reactive effects of this component can be ignored in circuit analysis. See Figure 4.2.a.i for a schematic of the charge amplifier.

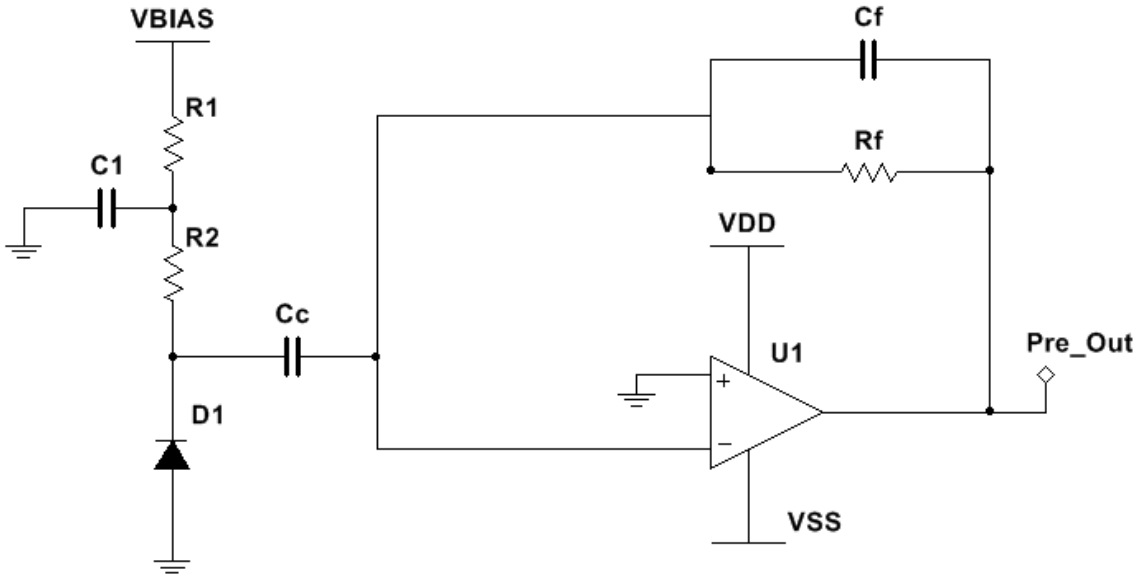

Figure 4.2.a.i: Charge preamplifier layout. D1 represents the photodiode

The analysis provided in section 2.3.a.ii was used to determine the total output noise of the charge amplifier circuit for different low noise opamps with varying capacitance for the feedback capacitor and photodiode. MATLAB was used to generate the data for the plots. Routines were written to determine the location of the noise gain zero and pole and adjust the voltage noise density equations for different regions accordingly. The results are shown in figure 4.2.b.i, figure 4.2.b.ii, and figure 4.2.b.iii. Circuit values used in the C_d plot are $R_f = 10M$, $C_f = 5pF$, $R_{sh} = 40M$, $i_D = 5nA$. Circuit values used in the C_f plot are $R_f = 10M$, $C_d = 80pF$, $R_{sh} = 40M$, $i_D = 5nA$. Values used in the R_f plot are $C_f = 5pF$, $C_d = 80pF$, $R_{sh} = 40M$, $i_D = 5nA$. Other values were obtained from the respective opamp's datasheet. It is evident that voltage noise dominates in the region of increasing noise gain. The opamps that seem to fare best are the ones with the lowest bandwidth. Therefore the best way to limit noise in this type of amplifier is to simply limit the circuit bandwidth. This can be achieved by selecting a lower bandwidth opamp and limiting bandwidth by adjusting the feedback capacitance of the circuit. The R_f plot shows that overall noise goes up as the resistance increases, even though opamp voltage noise and bandwidth decreases as R_f increases. This is due to the diode's shot noise (due to dark current) causing a voltage drop across the feedback resistor. Increasing the size of the resistor causes an increase in the voltage drop across R_f.

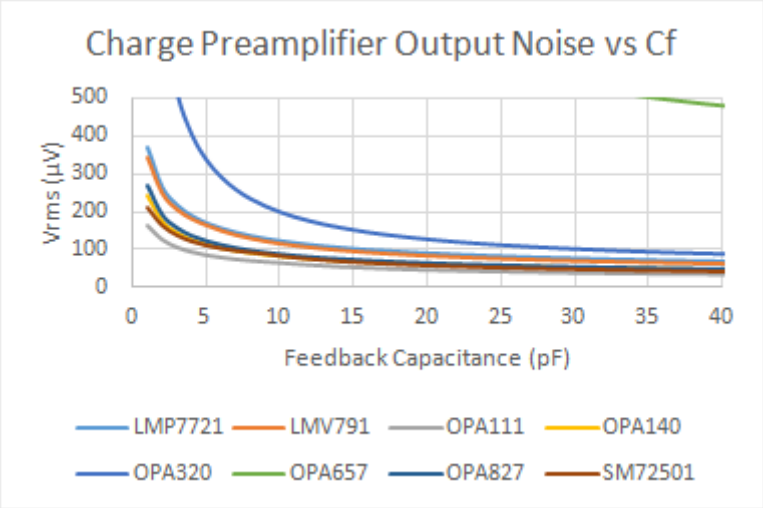

Figure 4.2.b.i: Charge preamplifier total noise with varying feedback capacitance

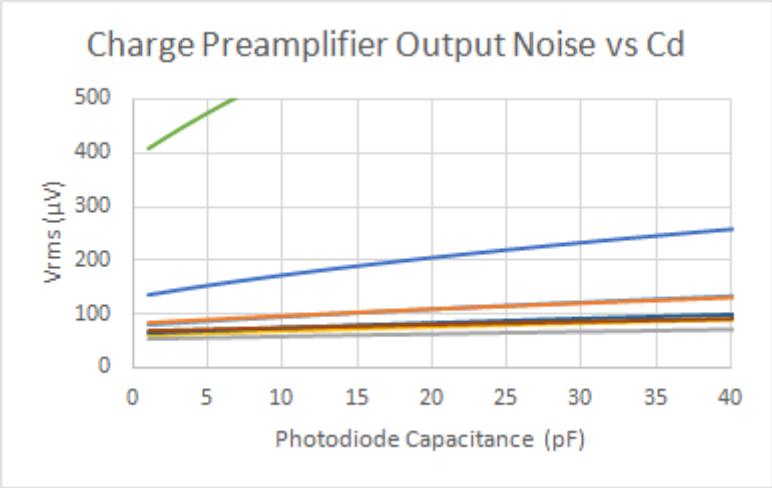

Figure 4.2.b.ii: Charge preamplifier total noise with varying photodiode capacitance

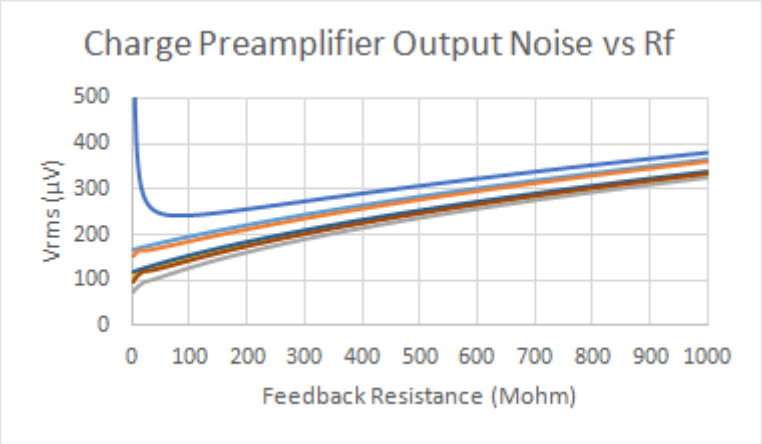

Figure 4.2.b.iii: Charge preamplifier total noise with varying feedback resistance

As previously discussed a balance needs to be found between circuit gain and noise while maintaining stability. While output noise has dropped off to a nearly flat level at a capacitance of around 20pF (figure 4.2.b.i), this greatly reduces the circuit gain when a low as possible capacitance is desired (such as 1pF). A good compromise would be to choose a value such as 5pF. Charge amplifier circuits researched typically use 1pF as the lower limit of the feedback capacitance (due to stability issues) so the difference in gain of 5 can easily be made up for in the gain of the pulse shaper stage. At 5pF the stray capacitance of a resistor would also be less of a concern as it would not have a large impact on the total parallel capacitance. Feedback resistance must be large enough so that the circuit operates like a charge integrating amplifier instead of a transimpedance (current to voltage converter) amplifier. Overall output noise increases as feedback resistance increases. This is due to the increasingly dominant effect of the photodiode's shot noise current causing a voltage drop across the feedback resistor which is reflected to the circuit output. Since bandwidth is a concern (high enough bandwidth desired to

minimize overlap of signals, yet small enough to limit noise appropriately) a value of 30M was chosen for the feedback resistor. As shown in the figures, the TI SM72501 has the best noise performance.

4.2.b JFET Buffered Implementation

In addition to the op amp optimization and selection above, a similar analysis was performed using the FET configuration in order to compare the produced output voltage noise. NXP semiconductor BF862 N-channel JFET was chosen due to its use in several app notes we looked over. It has a capacitance of C = 1.9 pF, and a voltage noise density of 0.8 nV/√Hz. The matlab code was changed accordingly and added the voltage noise due the JFET, the JFETs 1/f noise and the voltage noise due to the op amps current noise density across a 1 kΩ source resistance. The current contribution across the feedback capacitance is now strictly due to the photodiode current noise and will be reduced due to the op amp current noise bypass. This is because the dark current contribution will be considerably lower than the op amp contribution, where the op amp current contribution dominated in the traditional configuration. A plot of the results showing the SM72501 read-out with traditional and FET configurations is shown below.

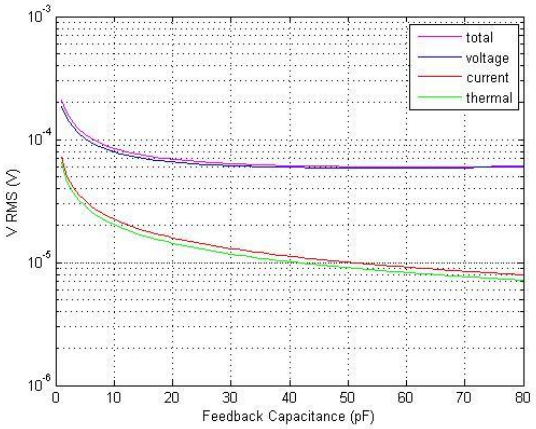

Figure 4.2.b.iv: SM72501 performance versus feedback capacitance

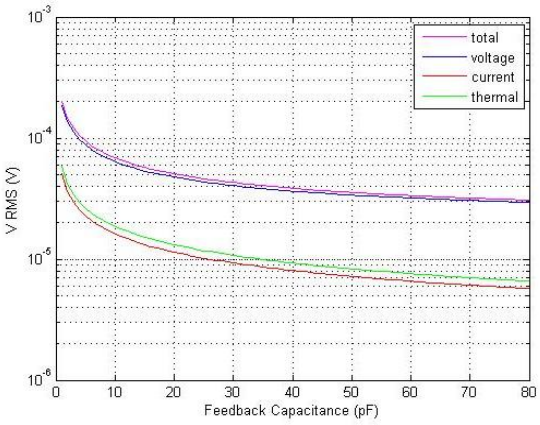

Figure 4.2.b.v: JFET performance versus feedback capacitance

On the left the traditional configuration is shown for the SM72501 performance versus feedback capacitance, and the right figure depicts the JFET configuration. It is quite obvious that the noise contribution has improved, both for current and voltage dominance regimes. In the regime < 10 pF, the current contribution has dropped below the thermal contribution and the voltage contribution shows a steeper drop off below 5 pF. This allows a wider selection of feedback capacitance values to be selected from the traditional configuration. Previously, the 5 pF limit reached a minimum and limited selection there, but now the noise decreases across 60 pF and then saturates. Beyond this threshold improvement is difficult because the noise becomes thermally limited.

Due to the considerations previously stated, we continued searching for an op amp with the new parameter considerations of low voltage noise and a minimum GBWP. In each case, noise analysis was applied for optimization. The AD743 from analog devices was ultimately selected. Using the JFET configuration, the noise was decreased the RMS voltage by half compared to the SM72501. This reduction is depicted below. As can be seen, the drop off is drastically improved and noise reduces to 40 µV RMS by 10 pF. Compare this to the nearly 70 µV RMS using the SM72501 at 10 pF. The current noise is similarly reduced, but it is the reduced voltage noise of the AD743 at 2.9 nV/√Hz with bandwidth of 4.5 MHz that shows the largest improvement. Reduction in noise is slim beyond what we have evaluated because the voltage noise is approaching the thermal noise limit. We configured the analysis using a feedback capacitance of 5 pF, and using the output at that value is roughly 50 nV/√Hz. From here we can determine the RMS e^- using the output voltage relationship of Q_i/C_f, which yields 1563 RMS e^-. The pulse shaping stages of our design will act to cut off this number successively.

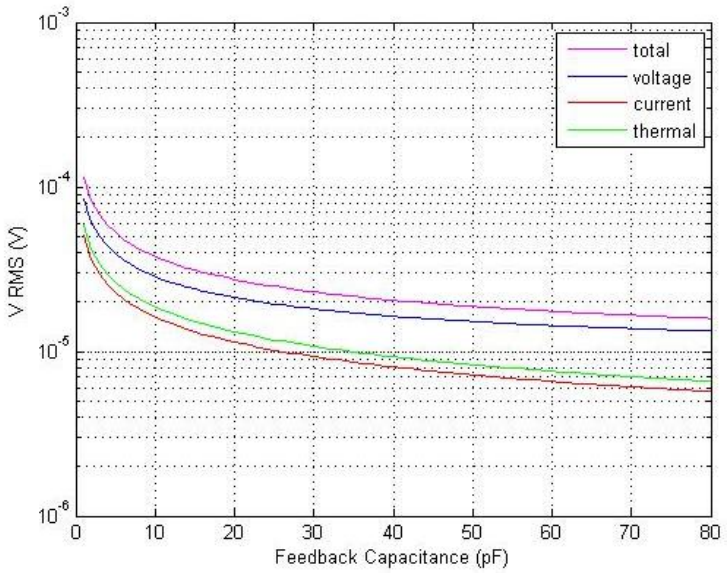

Figure 4.2.b.vi: Optimized noise curves utilizing various opamps with a JFET buffer

The schematic of the finalized configuration is depicted below in figure 4.2.b.vii using the same shaping time feedback components as in the original configurations. Further optimization and adjustments will proceed experimentally if necessary.

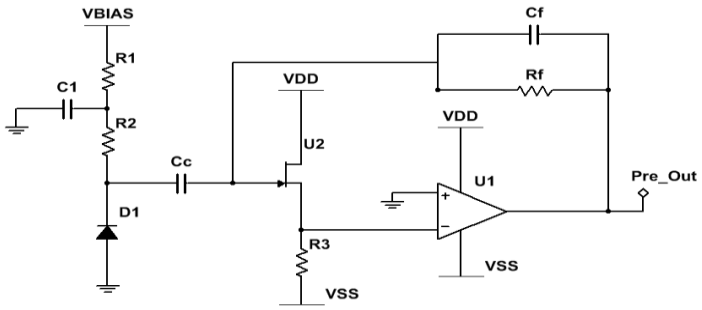

Figure 4.2.b.vii: Final charge amplifier configuration

4.3 PULSE SHAPING

ENC reduction and pole-zero cancellation were the driving concerns for pulse shaper design optimization.

Analysis provided in the research section demonstrated that in order to achieve an optimum ENC, the noise contribution from the voltage and current had to crossover, and when they did the sum of the two plots would yield an optimum shaping time. Because the voltage noise is inversely proportional to the shaping time it will decrease with increasing τ. Similarly, because the current noise is directly proportional to τ it will increase as τ increases. This can be correlated with the analysis provided in both the stability and noise considerations for the pre-amp, where the same methods of evaluation apply. As the value of the feedback capacitance increases, it shifts the pole to the left of the spectral noise plot until it reaches flat bland and its 20 dB contribution is negligible. Analyzed in the time domain, for equal shaping time for the CR-RC filters, the output voltage is given as $V_o(t) = \frac{V_o}{\tau} te^{-t/\tau}$. Therefore, as τ increases the exponential term increases and will approach unity and the inverse relationship will dominate pushing the voltage noise towards zero. As the voltage noise drops below the current noise, its effects begin to become apparent. The increase in current noise, however, occurs because of the increase in parallel noise contributions at the input. Because of the JFET preamplifier configuration, this will be nullified at the front end.

Weighting Function	Series White A_1	Parallel White A_3	Series 1/f $A_{2(approx.)}$
Triangle	2	0.667	0.87
Semi-Gaussian	2.04	0.90	1.01
CR-RC	1.85	1.85	1.39
CR-RC^4	0.45	1.02	1.39
CR-RC^7	0.34	1.27	1.39
Trapezoidal	2	1.67	1.37

Table 4.3.i: Pulse shaping network configuration characteristics

A range of shaping times extending from 1 µs to 500 µs was applied for several different shaping configurations. These included triangular, semi-Gaussian, Gaussian, and trapezoidal shaping schemes. The varying configurations resulted in different weighting constants and shaping geometry along with differing noise responses. A table is provided in section 2.2.c.ii outlining the shape and weighting constant values, but is shown above for convenience. A detector capacitance of 80 pF and shunt resistance of 40 MΩ was used for the X100-7 SMD photodiode. A large value was assumed to obtain the worst case. The NXP BF862 JFET with worst case capacitance of C_{gd} + C_{gs} was used and yields C_{in} = 15.7 pF. The stray capacitance was assumed to be roughly 1 pF. The flicker coefficient of the JFET is is 8.75e-17 VAs. The operating temperature was set to 250 K (≈ -20˚ C) which gives a dark current contribution of 1.22 pA. The table below displays the obtained results.

Shape	Optimum shaping time (us)	e RMS
Triangle	123	60
semi-Gausssian	185	51
CR-RC	123	60
CR-RC4	81	37.5
CR-RC7	63	37
trapezoidal	135	59.6

Table 4.3.ii: Optimized shaping time through various configurations

We initially assumed that the CR-RC4 pulse shaping network would yield the best results for our purposes. The CR network acts to cut-off any low frequency flicker noise effects and the cascaded RC network shapes the tail of the step response. In so doing we are able to reduce the preamplifier RMS e^- contribution from ≈ 1500 e^- RMS to ≈ 37.5 e^- RMS. The analysis also illustrates the negligible affect additional integration stages will have on the noise response, which is only a difference of 0.5 e^- RMS from RC^4 to RC^7. Because we were limited by the photodiode active area, capacitance at the detector end could not be reduced. Ideally, matching the JFET capacitance to the photodiode capacitance would produce the best results. The limit would imposed by our budget and the X100-7 limiting capacitance is 50 pF at 40 V bias. Any optimization beyond this point will therefore occur during the experimental phase of our design. With that said, the ENC plot showing the variance in noise response at increasing shaping times is shown below in figure 4.3.i and will be used to fit the resistor and capacitance values.

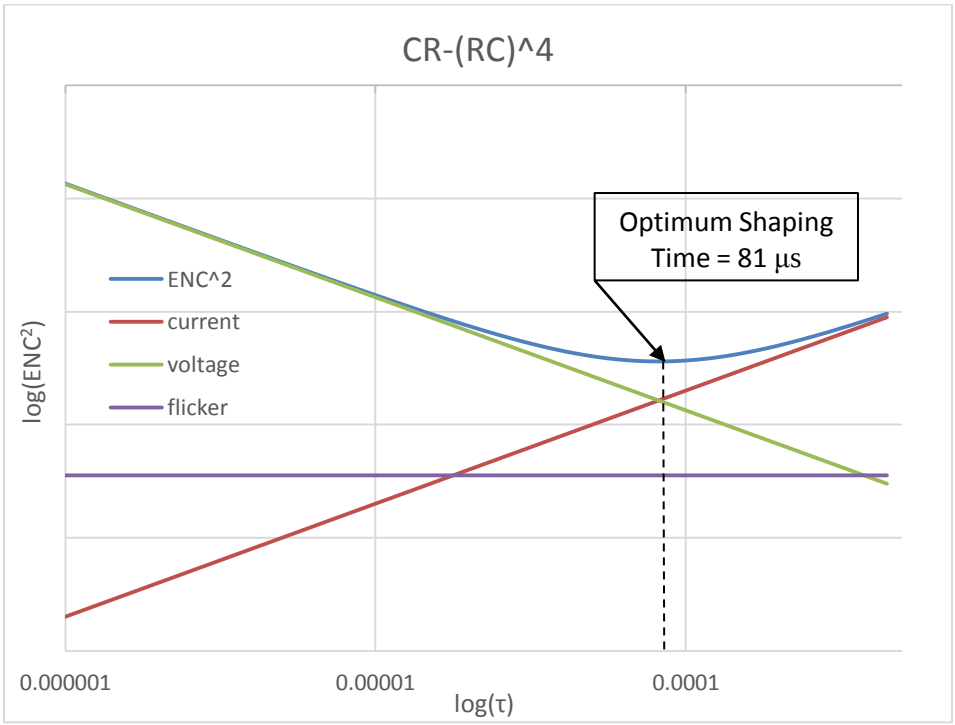

Figure 4.3.i: ENC plot depicting the point at which optimal noise characteristics occur

The next task was to perform pole zero cancellation on the differentiator stage of the pulse shaper. The cancellation occurs via $\tau_{pz} = CR_{pz}$, where τ_{pz} is the integration time at the preamplifier stage given by 150 µs. The filter capacitance was set to 12 nF and using an 81 µs shaping time gives R = 6.75 kΩ. From here R_{pz} can be found as 12.5 kΩ.

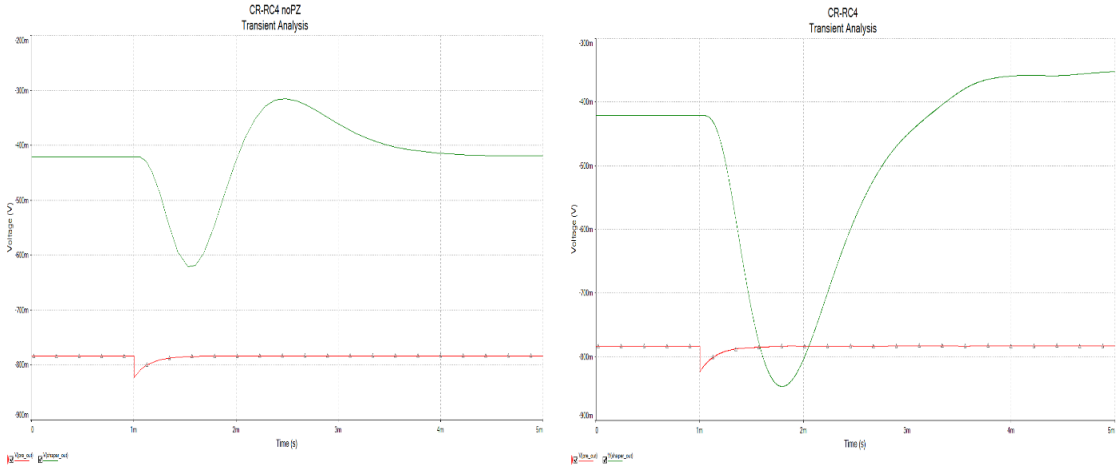

Figure 4.3.ii: Effects of pole-zero cancellation

The cancellation is important because the pulse rate will fast and build up will necessarily occur. Overlapping of pulses degrades the resolution and reduces effective spectrum identification because the resolution will be worsened. In addition, peak height identification will be degraded, as is apparent. If a high resolution spectrum is to be attained, then differentiation between Compton and photo-peak output will be necessary. The overshoot actively reduces the peak response and thereby makes distinction between gamma events difficult. The tail characteristically decays in a similar fashion for pole displayed responses, despite the amplitude increase. The decay is difficult to reduce beyond this point because signal cutoff may occur. As has been the case throughout design, comprising between competing concerns is necessary and in this case a slower decaying tail pays off due to optimum signal capture.

The design of the CR-RC^4 shaper is outlined below. The first stage shows the preamplifier for completeness. The CR network is next and is AC coupled to block the DC bias at the preamp output. The CR-RC shaping times are all set to equal 81 µs. This yields C = 12 nF and R = 6.75 kΩ. The pole-zero cancellation resistor is R_{pz} = 12.5 kΩ. The passive differentiator is set at the non-inverting of TI's SM72501, which has a low offset voltage and displayed excellent noise characteristics. Gain is added to boost the signal and will be adjusted to fit our concerns. For the 4 integrator stages, the same shaping time will be used and a gain will be added as a feedback resistor that will be experimentally adjusted. These adjustments are necessary because resistors display thermal noise and will add to the total ENC. Linear Technologies LT6204 quad op amp

will be used to reduce noise and limit the space constraints for PCB design. It is specified at 1.9 nV/√Hz and 1.1 pA/√Hz, which are both ideal for the overriding noise concerns. In addition to this, the LT6202 was used along with JFET at the input to cancel noise in the preamplifier stage so that it has been utilized for low noise operations.

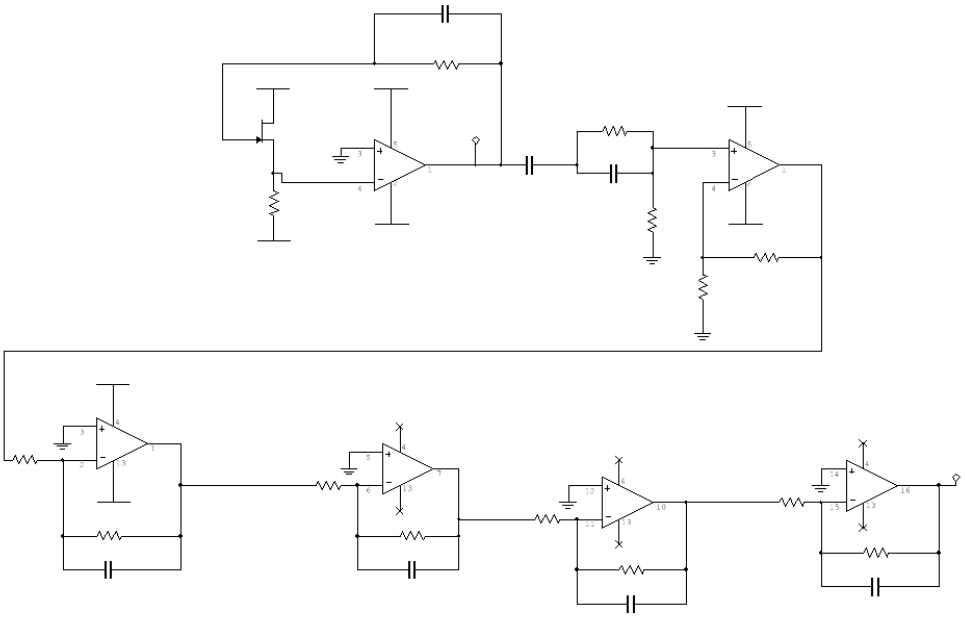

Figure 4.3.iii: Circuit schematic overview

4.4 DIGITAL HARDWARE

The digital hardware design of this project focuses on interfacing the analog and power peripherals (spectrometer pulse signal, battery charge level, power regulation / control, charge control, etc) as well as digital peripherals (USB data, SD card flash storage) to a microcontroller. The microcontroller will integrate all of these peripherals and enable a robust user experience through the use of a color LCD touch screen. The spectrometer will be able to record data and plot it on a gamma spectrum, save or load the data to / from an SD card, and transfer data to a computer via USB. In order to implement these features it is important to utilize a fast microcontroller with many digital and analog peripherals and a sound architecture such as the 32-bit ARM architecture. This section will provide an overview of the design methodology of all of the device's digital subsystems and their interconnections to the analog and power subsystems. Detailed schematics are provided for all digital hardware components.

4.4.a MCU

The ARM Cortex M4 based STMicro STM32F303VCT6 microcontroller was chosen for this project to meet several important requirements:

- High speed (72MHz), large flash (256K), and large RAM (48K)
- Integrated hardware floating point unit (FPU)
- High speed ADC peripheral (up to 5MSPS)
- Large number of GPIO pins (87, 42 of these 5V tolerant)
- UART, SPI, I2C, USB peripherals
- Cheap dev board available (STM Discovery F3 @ $16.20)

A high speed microcontroller was required mainly to provide the user with a relatively smooth refresh rate of the LCD (320x240x16 bit). The high GPIO pin requirement was to satisfy the number of pins needed to interface the parallel LCD screen as well as all other peripherals. This part comes in a LQFP-100 package, which is a very small surface mount package with a lead spacing of 0.5mm. See figure 4.4.a.i for a schematic showing connections to the microcontroller. Since this part has a very high pin count (100 pins) table 4.4.a.i has been provided as a summary of port connections to peripherals in addition to the detailed schematic.

STM32F303VCT6 Port Mapping	
Port	**Peripheral**
PA	LCD_DATA, USB, UART, SWD
PB	PWR_CTRL, SD CARD, TOUCH PANEL
PC	LCD_CTRL,CLOCK CRYSTAL
PD	ADC, SD CARD, TOUCH PANEL
PE	USR_BTN
PF	PLL CRYSTAL, TOUCH PANEL

Table 4.4.a.i: Port mapping of microcontroller to system peripheral

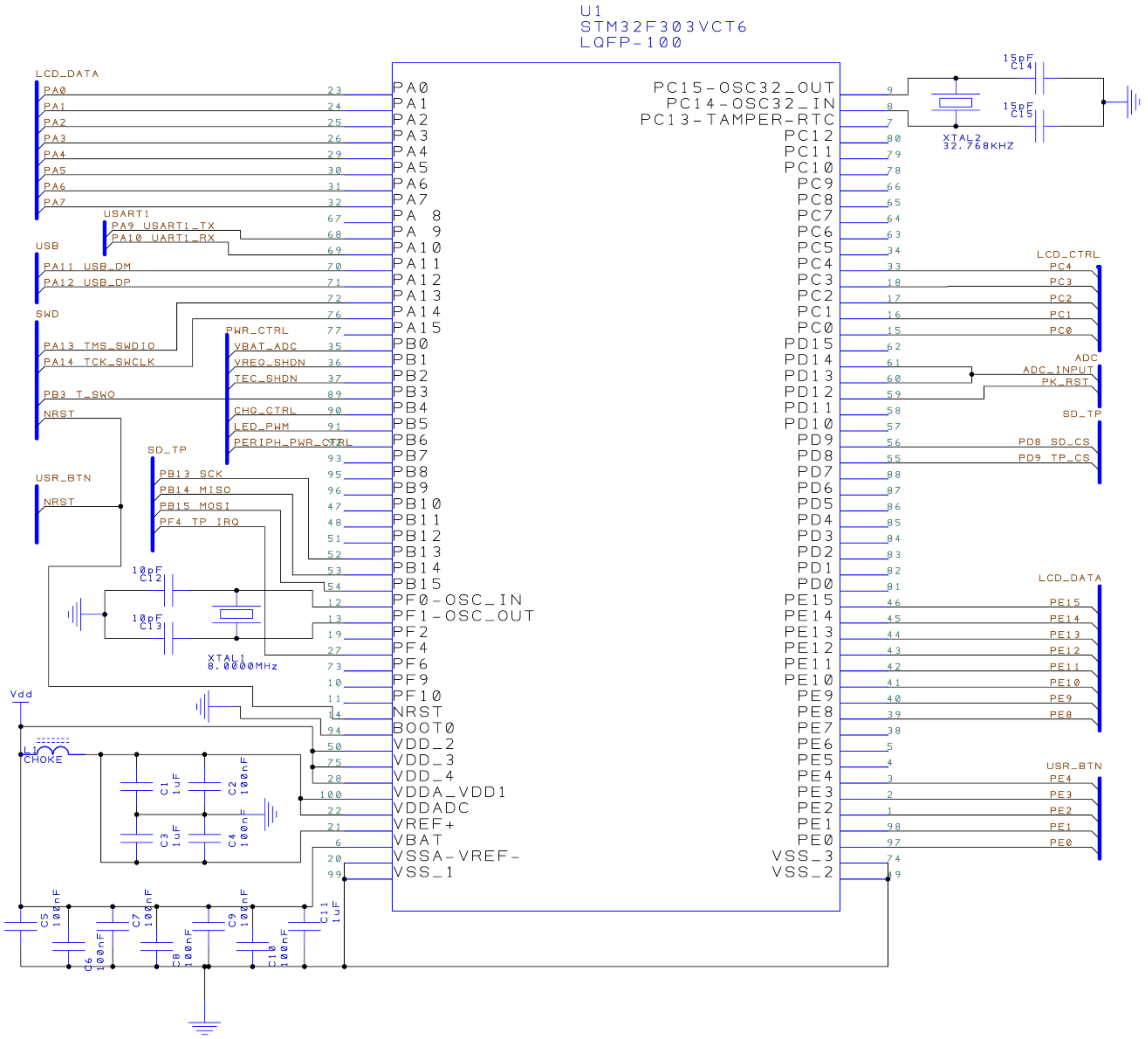

Figure 4.4.a.i: STM32F303VCT6 microcontroller schematic showing crystals, power supply filtering, and connections to other systems (buses)

The microcontroller has a total of 8 pins distributed throughout the part connecting it to the supply voltage and ground. Therefore a large network of filtering capacitors will be implemented around the controller to help with filtering of analog and digital sections of the IC. The analog supply voltage and analog reference will be connected through a choke to filter high frequency switching noise as well as additional filtering capacitors. The schematics from the Discovery F3 development board were very helpful in determining proper power supply decoupling and layout around the microcontroller. A 8 MHz crystal was selected to drive the phase locked loop (PLL) which generates the 72 MHz system clock. To drive the system real time clock (RTC) a 32.768 kHz watch crystal was selected. STMicro's application note AN2687 'Oscillator Design Guide' was used as a reference to determine the appropriate load capacitors for both crystals to guarantee oscillator startup and stability.

4.4.b Power Control

We have chosen to continuously power the microcontroller from the battery through a 3.3V linear regulator. This is necessary because USB current draw must be limited to 500uA when the USB host requests it (so called USB suspend). Therefore the microcontroller must actively monitor the USB data lines for these requests so that it can switch power to the charge controller when required. Because the microcontroller is always powered on, special care must be taken to run the controller in a low power mode while actively powering down all unnecessary peripherals to limit quiescent current draw from the battery. The STM32F303 microcontroller can achieve a low current draw of 10uA when running in low-power 'stop' mode. In this mode the microcontroller can still be woken by an external interrupt (such as from a button or USB event). At the same time the 5V linear regulator (opamp supply and TEC supply) and sensor bias voltage regulator can be shutdown using dedicated shutdown pins. 3.3V power supply to the signal conditioning opamp and LCD screen will also be shut down by the microcontroller during low-power mode.

To enable power control microcontroller pins PB1 (VREG_SHDN), PB2 (TEC_SHDN), PB4 (CHG_CTRL), PB5 (LED_PWM), and PB6 (PERIPH_PWR_CTRL) are used. VREG_SHDN and TEC_SHDN pins connect directly to the voltage regulators and TEC driver's shutdown pins and do not require any special driver circuitry. CHG_CTRL connects to a PMOS soft switch which switches 5V USB power to the charger IC. The soft switch has been designed to limit inrush current to 100mA assuming a max capacitive load of 100uF on the charging circuit. This is required so that the host's USB port is not overloaded when the charger is first switched on. Motorola application note AN1542 'Active Inrush Current Limiting Using MOSFETs' was used to aid in the design of the soft switch. A similar switch was designed for the 3.3V peripheral power control (PERIPH_PWR_CTRL), which power to the LCD screen and part of the signal conditioning circuit so that these can be disabled when the device is powered down. figure 4.4.b.i displays the 3.3V and 5V switching circuits. figure 4.4.b.ii shows the Multisim circuit simulation output.

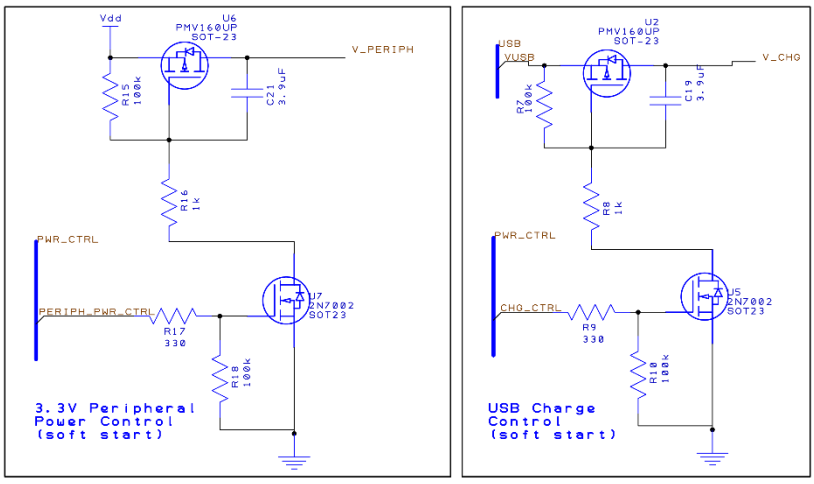

Figure 4.4.bi: Soft switch circuits for 3.3V peripheral power and USB charging

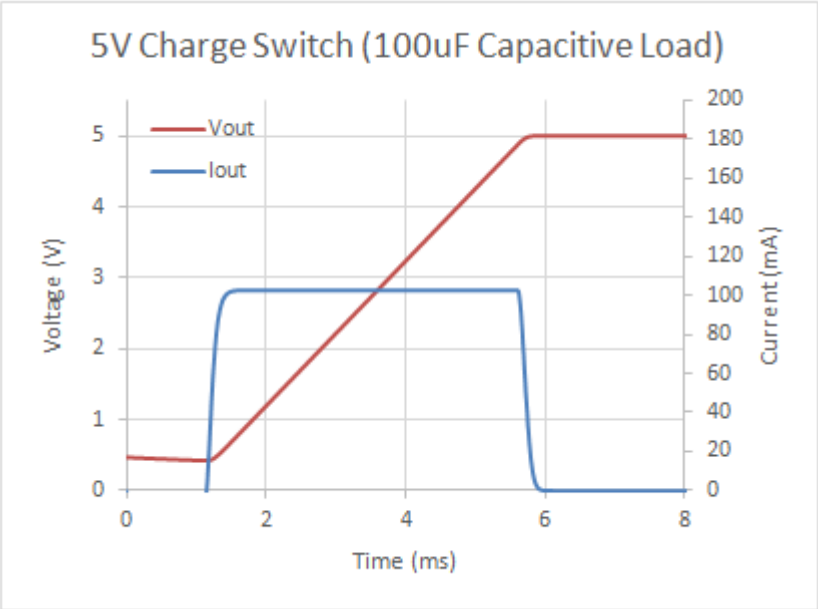

Figure 4.4.b.ii: 5V charging switch waveforms from Multisim circuit simulation

As shown by the charging waveforms, current is limited to 100mA when charging the capacitive load on the USB power switch. This is important as the USB 2.0 specification specifies a maximum device current of 500mA, and a sudden capacitive load could draw several amps of current from the USB supply. This would be detected by a USB host and power would be cut to the device by the host. Since the current limit is dependent on load capacitance, a higher load capacitance will result in a higher inrush current. It is therefore important to ensure that the capacitive load of the charging circuit does not exceed 100uF. Capacitance on the 3.3V peripheral power line will be much lower than 100uF, which means a lower inrush current but roughly the same turn on time (~5ms).

To limit current draw and extend battery life a simple NMOS switch was designed to dim the LED backlight on the LCD screen. For this circuit a NMOS and PMOS combination was used again for high side load switching. The NMOS transistor will be driven by a PWM signal from the microcontroller at 10 kHz. When the transistors are turned on the LED backlight will draw a max current of ~90mA. When the transistors turn off the LED backlight will turn off. By varying the duty cycle on the PWM signal the average current through the LED can be controlled, effectively dimming the light and conserving power. A fast switching speed will ensure that any flickering will be too fast for humans to notice. Since this circuit will switch at a much higher frequency than the other power control circuits a lower value resistor must be selected to bias the P channel MOSFET's gate-source. This ensures that the PMOS transistor will turn off fast enough during the 0V portion of the PWM signal to cut off current to the LEDs. Figure 4.4.b.iii shows the PWM dimming circuit as well as output waveforms for PWM signal, output current, and average output current using a diode dummy load current limited to a max of 30 mA with a resistor. Since the LED backlight on the LCD screen will draw more current a 10uF filtering capacitor will be placed by the PMOS transistor to help filter switching transients.

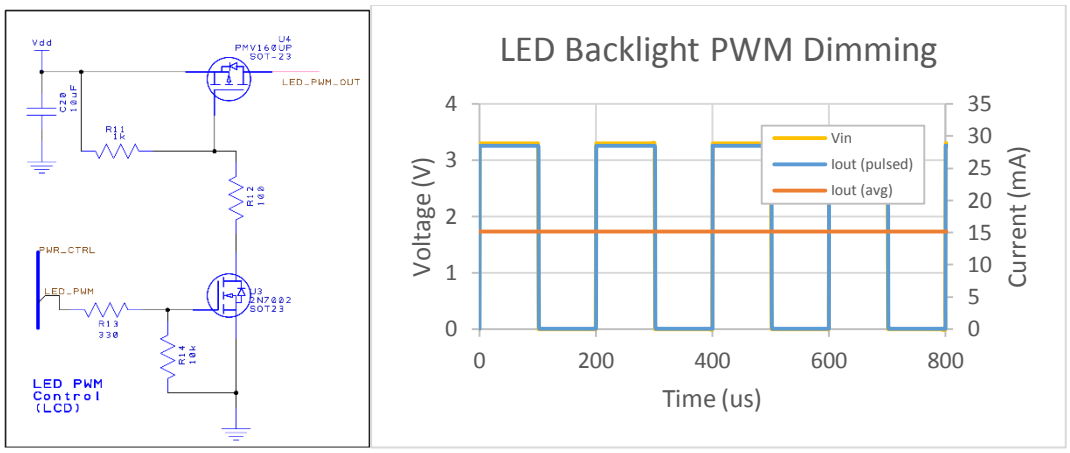

Figure 4.4.b.iii: PWM backlight dimming circuit and simulation showing max pulsed and average current for a 50% duty cycle PWM signal

4.4.c Peripheral Connections

The LCD controller used in this design (SSD1289) has a 20 bit parallel interface comprising 16 data lines and 4 control lines. It would be ideal to route all data lines so that they are connected to a single port (since all ports on the STM32F303 are 16 bit). However, as the schematic shows the pin assignment of all 16 bits on all ports is not continuous. The lower and upper half of both PA and PE are placed on opposite sides of the device. To avoid a manual signal routing nightmare it is therefore more beneficial to wire these data lines so that they occupy a continuous pin assignment around the device. This can be best accomplished by wiring D0-D7 on the LCD to PA0-PA7, and D8-D15 to PE8-PE15. While this will require one more write cycle on the microcontroller to write data to the LCD, it may be worth saving the hassle of routing pins across the entire device. Ultimately the data and control lines will all run to a single 20x2 header which the LCD screen will plug into (in addition to being mechanically secured to the device enclosure). LCD_CTRL lines and SD_TP lines (SPI interface to SD card and touch screen) will also be routed to the LCD screen header, so these were wired to pins which were relatively close to the LCD data pins on the MCU.

Table 4.4.c.i displays the signal connections from microcontroller to the LCD board. Not shown are power connections and backlight connection. Figure 4.4.c.i shows a schematic view of the 20x2 header power and signal connections. Filtering capacitors will be placed close to the power terminals to reduce digital switching noise. Labels below the connector indicate names of pins on the LCD board while labels above indicate microcontroller connections.

LCD Board Pin Mapping												
Type	**LCD Data**		**LCD Control**					**SD/Touch (SPI)**				
LCD	DB0-DB7	DB8-DB15	RS	WR	RD	CS	RSET	DCLK, SCK	IN, MOSI	OUT, MISO	CS (SD) CS (TP)	IRQ (TP)
MCU	PA0-PA7	PE8-PE15	PC0	PC1	PC2	PC3	PC4	PB13	PB15	PB14	PD8,PD9	PF4

Figure 4.4.c.i: LCD to MCU pin mapping

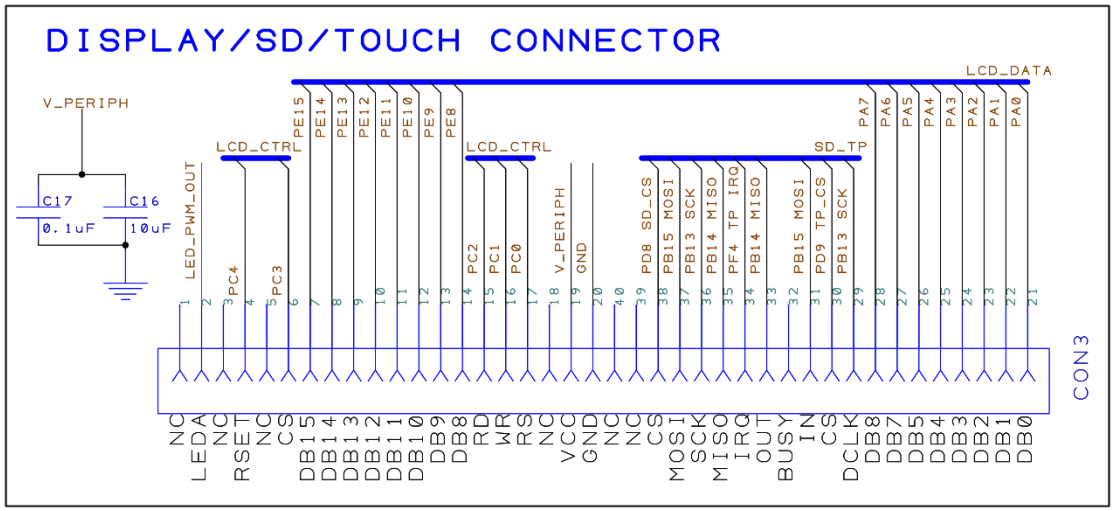

Figure 4.4.c.ii: Power and signal connections from microcontroller to 20x2 LCD header

In addition to the LCD header the SWD (programming / debugging interface), USB, and UART connections will also be broken out to headers and connectors. The embedded STLink programmer on the STM32 Discovery F3 development board can be utilized to program other STM32 microcontroller as well. This requires a total of five connections (ground and four signal connections). The Discovery F3 board has 22 ohm resistors installed on all STLink programming lines in order to dampen any ringing that may occur when long wires are used to connect them to a different board. Therefore no additional components will be required on the programming signal lines on the spectrometer. The 5V power line from the USB connector is wired to a low voltage drop Schottky diode to the charging switch in order to protect the device from reverse polarity voltage (however unlikely it may be if a standard connector is used). A 1.5K pullup resistor is connected to the D+ line on the USB connector to signal to the USB host that our device is a full speed USB device. D- and D+ on the USB connector are connected to PA11 and PA12, respectively, through 22 ohm resistors. This dampens any ringing that may occur from signal switching due to a long USB cable. Pin 4 (ID) on the micro USB connector is left floating as this device has no on the go (OTG) requirement. UART pins are broken out to a 3 pin header which allows for debugging using printf statements.

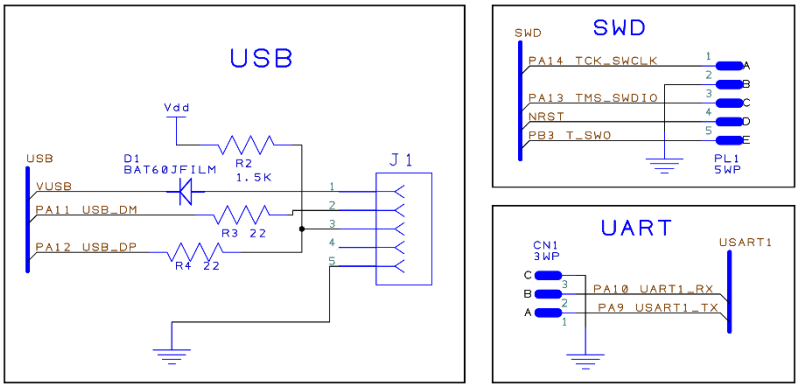

Figure 4.4.c.iii: USB, SWD, and UART connectors/headers

In addition to the touch screen there will also be five tactile buttons available for user input. This is because the touchscreen is a resistive screen, and because resistive screens can be noisy and inaccurate we thought it would be a good alternative to provide a traditional button input as well. These buttons are wired to PE0-PE4. A button is also wired to the NRST pin on the microcontroller to allow resetting of the microcontroller. This button will most likely only be available as a small surface mount button on the circuit board for debugging.

4.4.d Signal Conditioning

The microcontroller will sample two analog signals that will require some conditioning before being interfaced with the ADC: the detector pulse signal and the battery voltage. The pulse shaper signal needs to have the offset due to opamp bias current removed and needs to be half wave rectified as we are only interested in the positive voltage of the pulse (not the negative overshoot). A peak detector circuit will then continuously track the peak voltage until it is sampled and reset. It then needs to be scaled to 3.3V to match the ADC reference voltage in order to maximize resolution. The battery measurement voltage also needs to be scaled down to a maximum voltage of 3.3V (the maximum battery voltage for a 2 cell lipo is 8.4V) so that it can safely be sampled by the microcontroller's analog to digital converter. See figure 4.4.d.i for a schematic diagram of the peak detector.

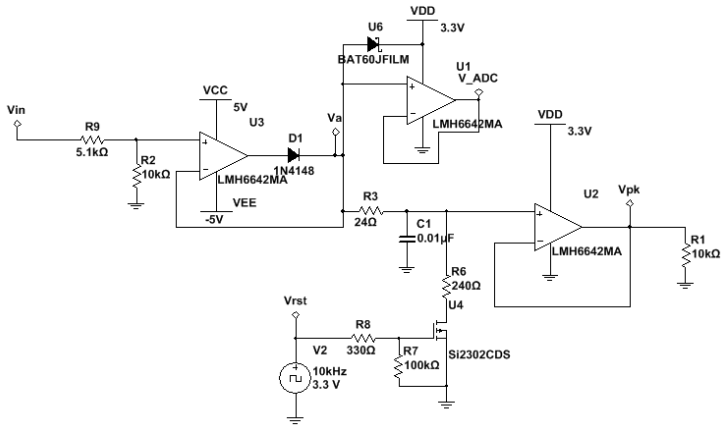

Figure 4.4.d.i: Peak detector circuit. The peak voltage of the input signal is tracked and scaled to 3.3V

The signal from the pulse shaper is AC coupled to the rectifier stage and divided to 3.3V max with the resistor divider formed by the 5.1k and 10k resistors (pulse shaper signal is 5V peak). After rectification capacitor C1 is charged up and tracks the peak voltage. The N-channel FET U4 is used to reset the charge on the capacitor by shorting it to ground when Vrst is pulled high. This allows microcontroller reset of peak after sampling. The peak and rectified pulse voltages are buffered and sampled by the microcontroller at V_ADC and Vpk. Note that since in this configuration opamp U3 is driven to the rail when the input goes negative a high speed opamp is required. See figure 4.4.d.ii for the

peak hold output and reset waveforms. The capacitor and resistor value was chosen so that the capacitor charges quickly while limiting opamp output current. A low leakage FET was chosen to ensure that leakage current would not cause the capacitor to discharge before sampling.

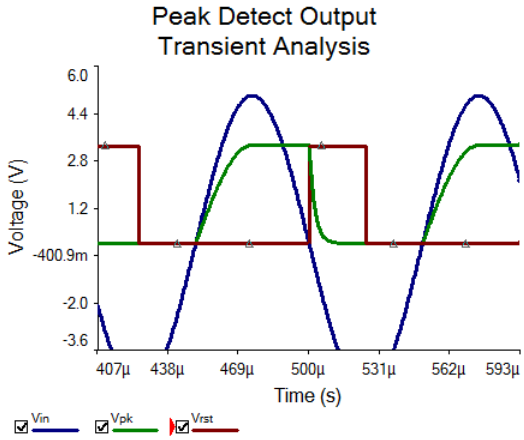

Figure 4.4.d.ii: Peak detector capacitor output and scaled 3.3V output.

For the battery voltage measurement circuit a low cost, low power, and low speed opamp was chosen, as speed is not crucial in this application. This circuit consists of a simple buffer amplifier driven by a voltage divider. The divider scales a max voltage of 9V (should never be reached with 2S lithium ion battery) to $9 * \frac{R1}{R1+R2} = 9 * \frac{300}{510+300} = 3.33V$. Figure 4.4.d.iii shows the schematic for this circuit.

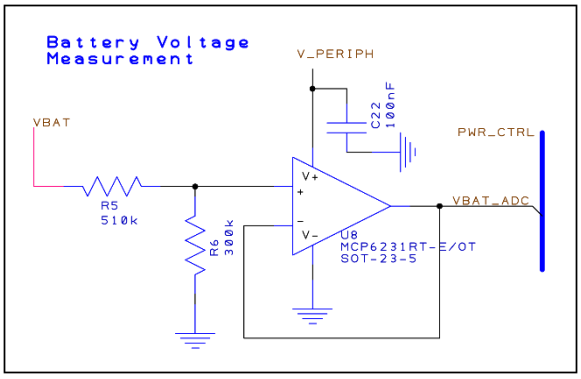

Figure 4.4.d.iii: Battery measurement signal conditioning. 9V max voltage is scaled to 3.3V

SECTION 4.5 POWER MANAGEMENT

The design for power management will be laid out systematically such that the battery, charge controller, regulator, and thermoelectric cooler selections are stated first, then followed by necessary calculations and integration schemes. The end results are tabulated below in table 4.5.i and will be referenced in later sections.

MAXIMUM POWER CONSUMPTION OF SPECTOMETER SUBSYSTEMS			
Circuit/Module/IC	**Equations**	**Specifications**	**Resulting Power**
Pre-amp and Pulse-shaping Amplifiers	$P_{max} = \sum[I_s(\max) * \mathrm{V_s}(\max)]$	$I_s(max) = 1.75\ mA$ $V_s(max) = 5\ V$	P_{max}: 52.5 mW
Detector Bias	$P_{max} = I_{bias}(\max) * \mathrm{V_{bias}}(\max)$	$I_{bias}(\max) = 25\mathrm{mA}$ $\mathrm{V_{bias}}(\max) = 16\mathrm{V}$	P_{max} 16μW
Microcontroller/Digital Peripherals (STM32F303VCT6)	$P_{max}(\mu C) = I_{DD}(\mu\mathrm{C}) * \mathrm{V_{DD}}(\mu\mathrm{C})$ $P_{max\ (perf)} \approx \sum[I_{DD}(\mathrm{perf}) * \mathrm{V_{DD}}(\mathrm{perf})]$ $P_{max}(tot) = P_{max\ (perf)} + P_{max}(\mu C)$ $I_{tot}(\max) = \mathrm{I_{DD}}(\max) + \mathrm{I_{DD}}(\mathrm{perf})$ $V_{DD}(\max) = \mathrm{V_{DD}}(\mu\mathrm{C}) = \mathrm{V_{DD}}(\mathrm{perf})$	$I_{tot}(\max) = 300\ \mathrm{mA}$ $V_{DD}(\max) = 3.3\mathrm{V}$	$P_{max}(tot)$: 990mW
Thermoelectric Cooler (TE-2-31-12-1.0)	$P_{max} = I_{TEC}(\max) * \mathrm{V_{TEC}}(\max)$	$I_{TEC}(\max) = 1400\mathrm{mA}$ $\mathrm{V_{TEC}}(\max) = 4.1\mathrm{V}$	P_{max}: 5.74W
TOTAL POWER REQUIRED FOR SUBSYSTEM TO FUNCTION ACCURATELY →			**6.78W**
POWER CONSUMPTION OF CHARGE CONTROL/REGULATION/DRIVER IC'S (TAILORED FOR CURRENT DRAW OF SUBSYSTEMS)			
Charge Controller (LT1513)	$I_{IN} = 4mA + \frac{V_{BAT} I_{chg} * 0.024}{V_{usb}}$ $P_{SW} = \frac{I_{chg}^2 R_{SW}(V_{BAT} + V_{usb}) V_{Bat}}{V_{usb}^2}$ $P_{LT1513} = I_{IN} V_{usb} + P_{SW}$	$I_{chg} = 800mA$ $V_{BAT}(min) = 7.4V$ $V_{BAT}(max) = 8.2V$ $V_{usb} = 5V$ Result(min,max): $I_{IN} = 28mA$,34.5mA $P_{SW} = 704mW, 830mW$	P_{LT1513}: Min: 840mW Max: 1W
5V Regulator (LT1761)	$P_{Diff} = I_s(max) * (V_{BAT} - V_s(max))$ $P_{GND} = I_{GND} V_{BAT}$ $P_{LT1761} = P_{Diff} + P_{GND}$	$I_{GND} = 0.25mA$ Result(min,max): $P_{Diff} = 4.2mW, 5.6mW$ $P_{GND} = 1.85mW, 2mW$	P_{LT1761}: Min: 6.05mW Max: 7.6mW
3.3V Regulator (LT1762)	$P_{Diff} = I_{tot}(\max) * (V_{BAT} - V_{DD}(\max))$ $P_{GND} = I_{GND} V_{BAT}$ $P_{LT1762} = P_{Diff} + P_{GND}$	$I_{GND} = 5.25mA$ Result(min,max): $P_{Diff} = 1.23W, 1.47W$ $P_{GND} = 39mW, 43mW$	P_{LT1762}: Min: 1.26W Max: 1.51W
Boost Converter (3494A)	*Multiple derivations* $P_{3494A} = I_{IN} V_{BAT} + P_{SW}$	$I_{IN} = 24.7mA$ $V_{BAT} = 7.4V, 8.2V$ Result(min,max): $P_{SW} = 220mW, 284mW$	P_{3494A}: Min: 403mW Max: 487mW
TEC Driver (MAX8520)	*Multiple derivations* $P_{MAX8520} = I_{IN} V_{REG}$	$I_{IN} = 21mA$ $V_{REG} = 5V$	$P_{MAX8520}$: 105mW

Table 4.5.i: Table of power specifications

POWER CONSUMPTION OF CHARGE CONTROL/REGULATION/DRIVER IC'S (TAILORED FOR CURRENT DRAW OF SUBSYSTEMS CONTINUED)			
Circuit/Module/IC	**Equations**	**Specifications**	**Resulting Power**
5V/1.5 A Regulator (LT1086)	$P_{LT1086} = (V_{BAT} - V_{REG})I_{TEC}(max)$	$V_{BAT}(min) = 7.4V$ $V_{BAT}(max) = 8.2V$ $V_{REG} = 5V$	P_{LT1086}: Min: $3.36W$ Max: $4.48W$
TOTAL POWER REQUIRED FOR IC'S TO FUNCTION ACCURATELY →			$\mathbf{7.6W}$

Table 4.5.i: Table of power specifications

4.5.a Battery

The battery chosen for this project will be a rechargeable 18650 lithium-ion battery. We will use two of these batteries, each rated for 3.7 - 4.2 volts and a minimum C-rate of 1800 milliamp hours (mAh). They will be connected in series by the use of an 18650 2-cell Li-ion holder to obtain the necessary 7.4 nominal volts. The Li-ion holder is PCB through hole compatible and will be mounted on the end result power PCB.

A battery voltage of at least 7.4 - 8.2 volts was required so that we could avoid the use of a boost converter on the supply rails of the analog preamp and pulse-shaping amplifiers. Boost converters typically have much higher output noise compared to other regulator types, so we deciding to go with a higher input battery voltage so that we can use a low-noise LDO regulator to regulate power to the analog circuit.

A minimum of 1800 mAh was required so that all components could be powered for an hour of use. This was verified by totaling up the maximum current draw of each subsystem and then taking the C-rate of the battery (1800 mAh) and dividing it by the maximum current draw:

$$I_{total}(max) = 6 * I_s(\max) + \mathrm{I}_{\mathrm{tot}_{\mu C+\mathrm{dig}}}(\max) + \mathrm{I}_{\mathrm{bias}}(\max) + \mathrm{I}_{\mathrm{TEC}}(\max) + \mathrm{I}_{\mathrm{PS}}(max)$$

$$I_{total}(max) = 10.5mA + 300\,mA + 16mA + 1400mA + 60mA = 1786.5mA$$

$$Time = \frac{C - rate}{I_{total}(max)} = \frac{1800\,mAh}{1786.5\,mA} \approx 1.01\,Hours$$

This implies that the device can be used for approximately 1.01 Hours if all components within the device are working at full capacity. Though this is not necessarily accurate because it cannot be expected that we use every function of the spectrometer at all times at maximum settings. Therefore the end user can expect to use the device for well over an hour if needed.

Lastly, the batteries/battery holder will be directly connected to a charge controller (for charging) and will also be connected to regulation IC's via a discrete soft-start circuit composed of power MOSFETS (outputs SS_BAT).

4.5.b Charge Control

In order to properly charge the 2-cell Li-ions, we needed to decide on a charge controller IC that would be capable of taking the low 5 volts from the USB and boosting it to a higher 7.4-8.2 float voltage range. Therefore, we decided on using Linear Technologies LT1513 SEPIC charge controller IC. The charge controller is capable of delivering a maximum charge current of 800 mA at a steady 5 volts input. The controller also offers pre-charging, constant current charge, constant voltage charging, and charge termination which is essential for Li-ion charging.

Figure 4.5.b.i below is the generated schematic of the charge controller circuit that we plan to implement into our design. The 5 volt input from the USB will first be activated by the USB protocol through communication with the microcontroller. When the signal from the microcontroller turns on the USB, the soft-start switches will turn on and gradually deliver full power to the VIN pin so that charging can take place. The float voltage for the battery will be set to 8.2 volts which will be accomplished by adjusting the divider network of R16 and R17 to the values 228 kΩ and 41.2 kΩ respectively. The current charging limit will be set for 800 mA, since that is the maximum charge current that the LT1513 allows for a 5 volt input. This is done by adjusting the resistor R15 to 61.9 kΩ in addition to changing the divider network of R18 and R19 to 39Ω and 0.08Ω respectively. Two 22 µF capacitors will be placed at the terminals of the battery so as to capture any unwanted switching noise that may flow into the battery during charging.

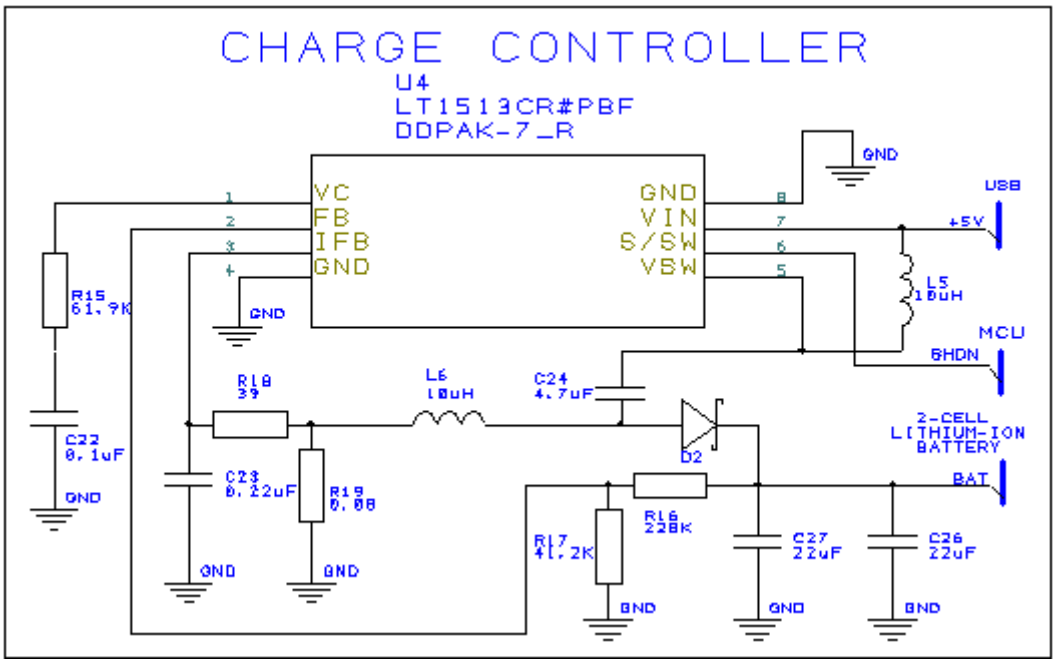

Figure 4.5.b.i: Designed application circuit using the LT1513 charge controller

When charging reaches its constant voltage stage, trickle charging will kick in and decay down to the termination phase. Once this happens, the microcontroller will be notified and an active low shutdown command will be employed on pin S/SW so that charging is stopped. To prevent the battery from delivering power back to the charge controller, the schottky diode will be present with the cathode facing the positive terminal of the battery. This will block almost all current from re-entering the charge controller, whether the battery is being charged or at full capacity. Theoretically, if the inrush limiter (soft-start) charge transition time is negligible and the battery is charged at maximum current, then the time it takes to charge the battery to full capacity is estimated to be:

$$t_{charge} = \frac{C - rate_{bat}}{I_{charge}(max)} = \frac{1800\,mAH}{800\,mA} = 4.5\,Hours$$

4.5.c Regulation

The following regulation IC's were chosen to adhere to the specifications set for the pre-amplifier and pulse-shaping op-amps, microcontroller, and photodiode detector, and TEC driver IC. In the following paragraphs it should be noticed that all the regulators that we choose have shutdown pins (SHDN). The shutdown pins perform in the same manner as the LT1513 charge controller that we chose; shutting down on active-low commands from the microcontroller. Also, as previously stated in section 4.5.a, both the regulator and driver IC's input voltage pins will be tied directly to the output of the soft-start switching circuit. This will limit the stress caused by inrush current when sudden transients are present at on/off switching.

The first set of regulation specifications were for the pre-amplifier and pulse-shaping amplifiers, which required 5 volts, 10.5 mA, and ideally less than 30 µV of noise voltage injection. These specifications led us to choose the LT1761ES5 low noise LDO regulator. We chose this regulator because it's capable of outputting 5 volts, 100 mA, and 20 µV of voltage noise with a minimum input voltage of 6 volts, which put us well within spec. We chose this regulator because it turned out to be one of the few that could put out 5 volts with noise levels that could be easily rejected by the PSRR ratings of the op-amps of the pre-amp and pulse-shaping circuits. Figure 4.5.c.i shows the schematic design we intend to fabricate for our design.

This regulator will take in 7.4 - 8.2 volts from the battery and regulate 5 volts and 20 µVrms of superimposed ripple to the output capacitor and load (op-amps). The low noise level is attained by bypassing the LT1761 regulators reference voltage through the OUT and BYP pins with a 0.01 µF capacitor.

We will also include another regulator, the LTC 1174HV-5, which will be used in an inverter topology so that – 5 volts can be supplied to the negative supply pins of the opamps. We chose LTC 1174HV-5 because it was capable of being configured such that it can take in a 4V to 12V voltage range, and output – 5 volts at with a maximum of 45 mA.

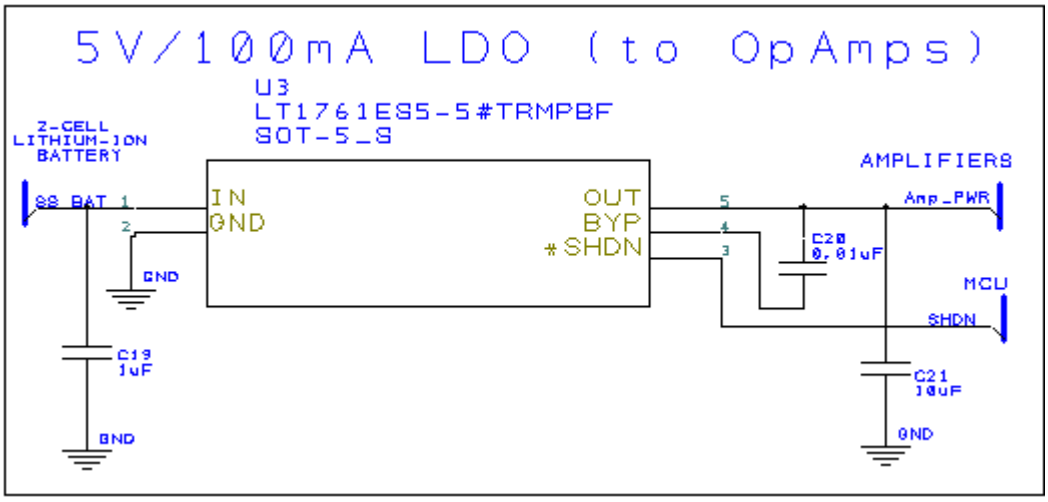

Figure 4.5.c.i: Designed application circuit using the LT1761 (for Op-Amp power)

The second set of specifications were for the STM32F303VCT6 microcontroller and the associated digital sub systems, which required 3.3 volts and 300 mA. The regulator we chose was the LT1962 low noise LDO, which was almost identical to the LT1961 model stated previously, except this regulator is specced perfectly at 3.3 volts and 300 mA with a minimum input voltage of 3.8 volts. Once power is regulated and delivered to the MCU, it will be the MCU's responsibility to distribute power to the peripherals. Figure 4.5.c.ii displays the designed LTC1962 regulator circuit.

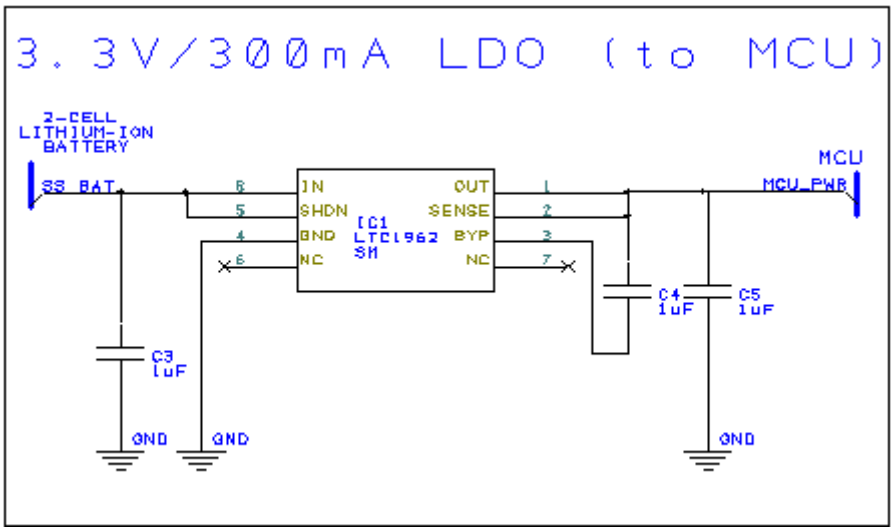

Figure 4.5.c.ii: Designed application circuit using the LT1762 (for MCU power)

The third set of specifications were for detector biasing, which required that at least 15 volts be utilized to reverse-bias the detector so that optimal detection is achieved. We decided to go with the LT3494 Boost converter to accomplish this. The LT3494A was chosen because it offered the capability of taking in a 2-cell battery voltage and up-

converting it to 16V. Figure 4.5.c.iii displays the schematic layout to be used for the LT3494A boost converter.

The external to this regulator require that R7 be 2.21$M\Omega$. This value was approximated based on the available SMT resistor and was predicted by the equation given in the datasheet:

$$R7 = 182 * \left(\frac{V_{out}(MAX)}{1.225} - 1\right) k\Omega$$

Where $V_{out}(MAX)$ is the max voltage output needed for the load. The 182 value comes from the internal resistor (182 kΩ), which is tied to the FB pin and ground. The inductor L1 was chosen to be 5 µH and output current to the bias was limited to 25 mA. The inductor and output current were calculated by lengthy steps and equations given from the LT3494A datasheet.

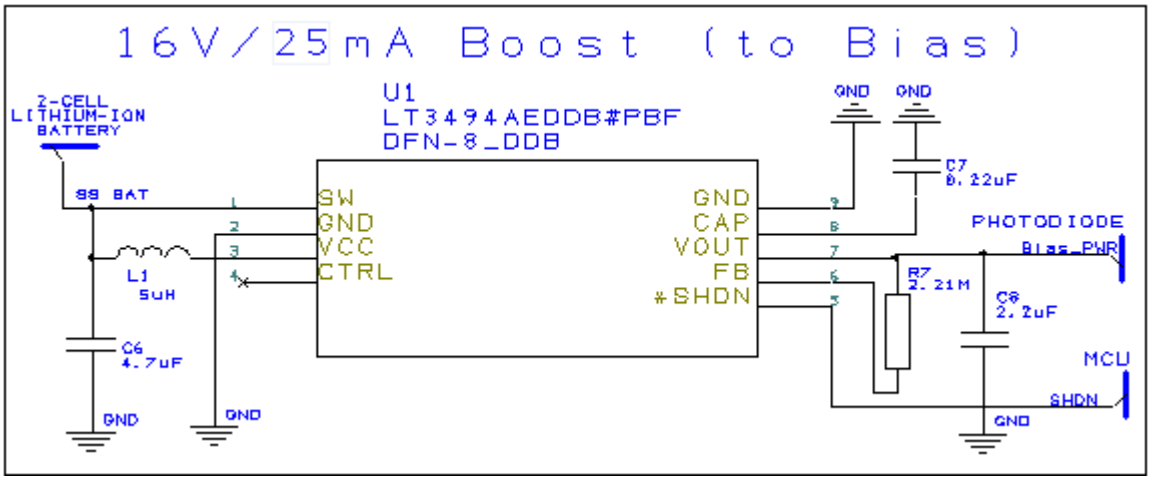

Figure 4.5.c.iii: Designed application circuit using the LT3494A (for bias voltage)

The last set of specifications were for the TEC driver circuit, which required 5 volts input and 1.4 amps. For this specification we decided to utilize the LT1086 LDO regulator. The LT1086 5 volt model regulates 5 volts and 1.5 amps which suited the driver requirements perfectly. Initially, we didn't want to use a regulator on the TEC rail because we knew there would be large losses in power due to the high current and differential voltage that's blocked and wasted in the regulator. Therefore, we had to succumb to fact and choose the appropriate regulator that would have the least amount of power losses. Figure 4.5.c.iv displays the circuit we used to utilize the LT1086 regulator. In this circuit the output electrolytic capacitor value of 150 µF was chosen to optimize on the output ripple and the resistor values for the divider were chosen based on a application circuit in the LT1086 datasheet that was similar to our application. Instead of using the 150 µF, we could have went with the other 22µF ceramic capacitor, which was also highly suggested by the LT1086 datasheet.

The resistor network divider was verified with the following equation given in the datasheet:

$$V_{out} = V_{REF}\left(1 + \frac{R_{21}}{R_{20}}\right) + I_{ADJ}R_{21}, where\ I_{ADJ} = 50\mu A$$

Also, the ADJ pin of the regulator had to be bypassed to ground with a 10 µF capacitor to help aid the output capacitor with ripple rejection. If the bypass capacitor wasn't implemented, then ripple rejection would become independent of ADJ and become a function of output voltage. The ripple at the output would increase directly as the ratio of the of V_{OUT}/V_{REF} increases. Special considerations had to be taken for ripple rejection specs, since any slight increase in ripple for high current regulators decrease system power efficiency.

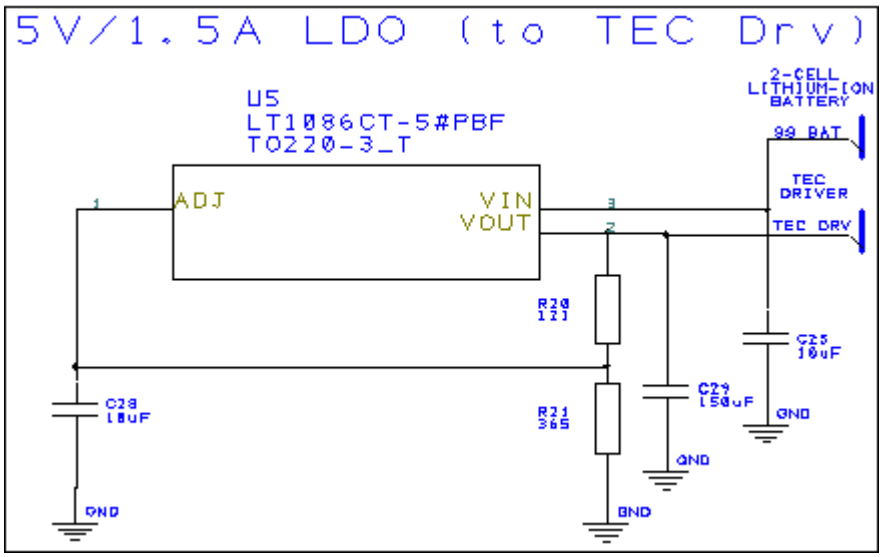

Figure 4.5.c.iv: Designed application circuit using the LT1086 (for TEC Driver IC)

4.5.d Sensor Cooling

In order to get the best results out of the spectrometer, we needed a way to drop the temperature of the photodiode detector. The temperatures specifications for the diode were to be at least -15 C˚. For this we decided to investigate the use of a thermoelectric cooler (TEC or Peltier module), which eventually led us to choose the TE-2-31-12-1.0 multi-stage TEC. The cooler is capable of creating a differential temperature of 103 C˚ across its ceramic plates. The cold side the TEC can extract up to 1.8 watts, which translates to a cold side temperature of -20 C˚. The TEC will be mounted directly onto a heat sink so that heat can be extracted from the cold side. The heat extracted from the cold side will be smoothly transitioned over the hot plate and into the heat sink (proper dissipation).

The TEC we chose has a relatively large amount of current (1.4 amps), so we had to investigate then decide on the use of either a discrete driver circuit or a driver IC. In the end it was determined best to go with the driver IC, specifically the MAX8520. The MAX8520 utilizes a half H-bridge circuit for current stability, two network divider circuits for MAX pins, and power ground pins that are used to reduce ground loop mixing between communication and power signals. The first resistive network divider that's used on the MAXV pin, serves the purpose of setting the max voltage for the TE-2-31-12-1.0. Also, a second network divider was used on pins MAXIP and MAXIN so that the max current limit could be set to match that of the TE-2-31-12-1.0.

As shown in figure 4.5.d, the TEC driver IC will receive power from the battery without the use of a regulator. The TEC driver IC will then be connected to the cooler via pins OS1 and OS2. The current draw going into the TEC will be stabilized with the use of inductors (chokes) coming from pins LX1 and LX2.

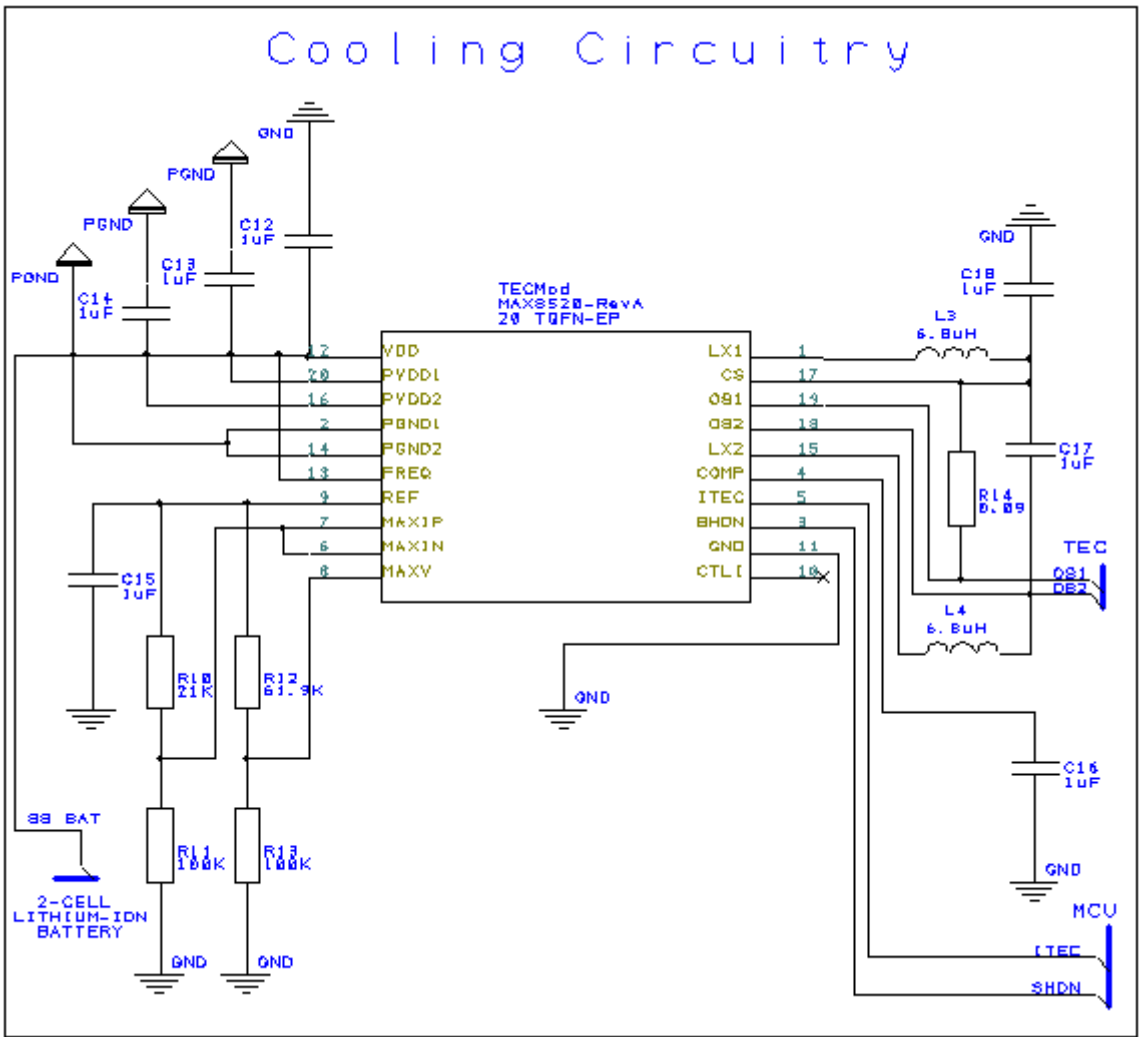

Figure 4.5.d.i: Designed application circuit using the MAX8520 driver (for TEC control)

4.6 SOFTWARE

This section will outline the design of the software portion of the project. While a low noise high performance analog front-end is crucial in the success of this project, the microcontroller will be responsible for processing amplifier output and providing the user with an easy to use interface. It must also provide all data storage and transfer functions via SD card storage and USB interface. IAR Workbench was chosen to write the software for the STM32 microcontroller as this is a widely used and supported software package in the industry. ST Micro provides a software peripheral library which enables quick setup of the microcontroller's peripherals. In addition to the microcontroller's datasheet and the vendor's application notes, ST Micro also provides a nearly 1000 page reference manual (RM0316) specifically for the STM32F303xx ARM Cortex MCU with detailed information on the configuration and use of all device peripherals. Having such a widely supported and powerful microcontroller definitely aids the design process.

4.6.a Program Overview

The diagram below shows a high level overview of the microcontroller program. The microcontroller will run through a software loop with an idle task of updating the LCD screen with the latest spectrum data. The loop will check the status of several flags which can be triggered by the device's subsystems. Specifically, interrupt routines will trigger when a pulse is detected (through comparator peripheral), upon user input request and upon USB communication request. Since CPU time is valuable and interrupts will interrupt any other software functionality, CPU cycles will only be allocated to these routines to set flags. The main routine checks these flags and if set will handle appropriate CPU response.

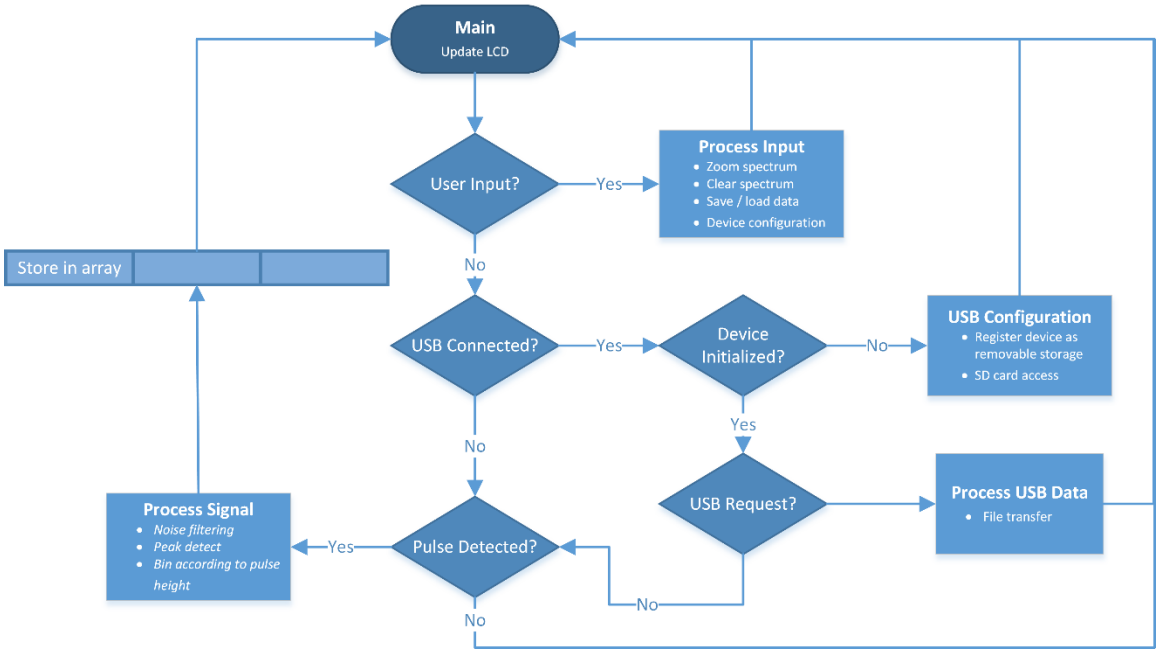

Figure 4.6.a.i: High level overview of device software functionality

For user input the device will have a touch screen and five buttons in a D-pad configuration (up, down, left, right, center). These buttons will be connected to one of the microcontroller's ports and will have an edge triggered interrupt configured. This interrupt will alert the main routine of user input by setting a flag. The touch screen has a IRQ (interrupt request) data line which will also be connected to a pin configured with an edge triggered interrupt. By wiring this pin to a different port we can differentiate from touch screen and button input. This is important because touch screen input will require some different noise reduction processing than the button debouncing required with tactile buttons.

The gamma spectrometer interface will have several menus for data processing, spectrum manipulation / isotope identification, and device configuration. Since the device will operate with two different probes the user will specify the probe in use (low energy detector or scintillator) so that the device can load the appropriate calibration profile. This profile will be unique to the probe as each probe will operate in a different energy range and will operate through different modes of interaction with incident gamma radiation. In addition, the low energy detector will utilize a thermoelectric cooler to cool the sensor and preamplifier down to -20C to reduce noise and extend the detector's usable range. The user will be able to turn the thermoelectric cooler on or off, with the tradeoff being increased measurement range and decreased noise vs decreased battery life.

The detector pulse will be shaped to enable full range measurement in either mode of operation (5-100 keV or 100 keV to 5 MeV). The device will be calibrated so that a pulse with the highest energy of interest will result in a sampled pulse of 3.3V, the highest voltage the ADC can record. After pulse shaping the pulse will pass through a peak detector circuit which will hold the peak until it is sampled. The pulse signal will be routed a comparator input while the peak signal will be routed to the ADC. By using the microcontroller's comparator peripherals a precise software selectable reference voltage can be set for the pulse trigger, much like an oscilloscope's trigger controls. While this trigger shouldn't drift under optimal device operation (the TEC has cooled the device down to -20C), this will enable quick initial calibration of the trigger level. The microcontroller will set a flag when the comparator interrupt fires, and will begin sampling the peak signal after a specified delay. This peak value will be used as detected pulse height. The microcontroller will then "bin" this value in a histogram array it maintains of every possible ADC value (12 bits / 4096). Finally the microcontroller issues a "reset" pulse to the peak hold circuit to reset the peak back to zero. This process repeats for every pulse detected.

In order to communicate with all digital systems used in the device, device drivers will need to be written for the LCD screen, touch screen, SD card, and USB peripheral. Touch screen and SD card communication will be fairly trivial as these devices can both communicate using the SPI protocol. The LCD screen uses a parallel communication protocol which is outlined in the controller's datasheet. The SSD1289 LCD controller is a widely used controller which has been supported on many different microcontrollers. It should therefore not be difficult to write a library with graphics functions to support this display. The USB driver will be challenging as none of us have any experience with the

USB communication protocol. There is however some example code available for the STM32 controller utilizing its USB peripheral. The goal is to essentially bridge the SD card interface to the USB peripheral to enable file management through a PC.

4.6.b Classes and Methods

When designing a project which involves the use of many different peripherals it is essential to organize and distribute the code between different classes. Each peripheral and set of device functions will have their own class of functions and data structures, linked and accessed by the main program loop. Figure 4.6.b.i below illustrates the different program classes and methods designed for the gamma spectrometer.

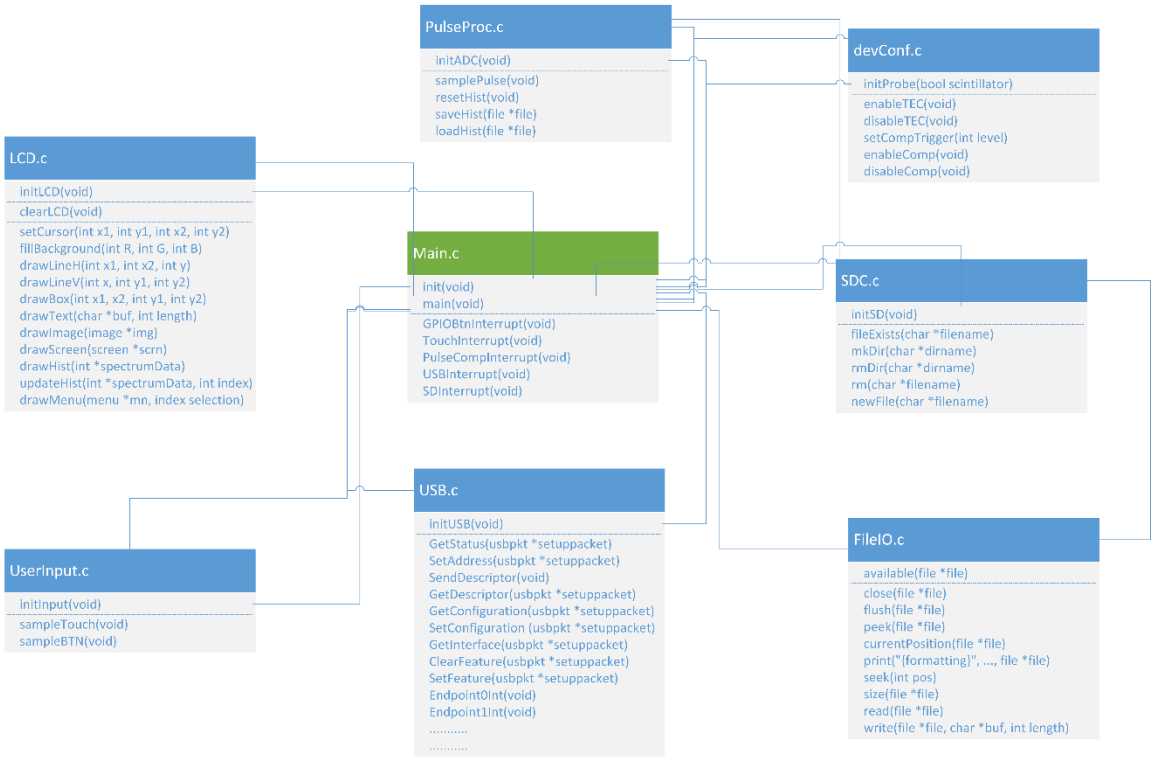

Figure 4.6.b.i: Software class structure showing some of the class interconnections

Note that this diagram is far from comprehensive, as it would not be practical to attempt to list every single function used in the program and show all code interconnections. Furthermore, we expect to implement more auxiliary functions to achieve a fully functioning gamma spectrometer. The sampling of functions in the diagram are intended to provide an insight as to the design of the different subsystems in the project. The design of the program is intended to be scalable so that device hardware (such as the probe) can be easily upgraded in the future without any major software change.

LCD.c

This class provides the interface between the microcontroller and LCD screen. It contains both the low level code necessary to communicate with the SSD1289 LCD controller as well as the high level graphics functions for drawing the device's GUI. First the device is initialized through the initLCD function. This function will reset the LCD controller and initialize the device's configuration registers (portrait / landscape mode, screen size, 15 bit / 16 bit colors, etc). The device registers are all listed in the controller datasheet, and will be placed in the header file of this class for easy reference. The high level functions are for drawing basic shapes such as pixels, lines, boxes, and solid rectangles. In addition, there will be functionality to draw images to the screen that have been preloaded to the device's flash. This enables us to design different screens for our device on a PC and take care of a lot of the drawing by simply loading the relevant screen and filling in the pixels that represent dynamic data on top of the image file screen buffer. Figure 4.6.b.ii displays a conceptual drawing of the user interface as it would be drawn on the 3.2" color LCD used in the project.

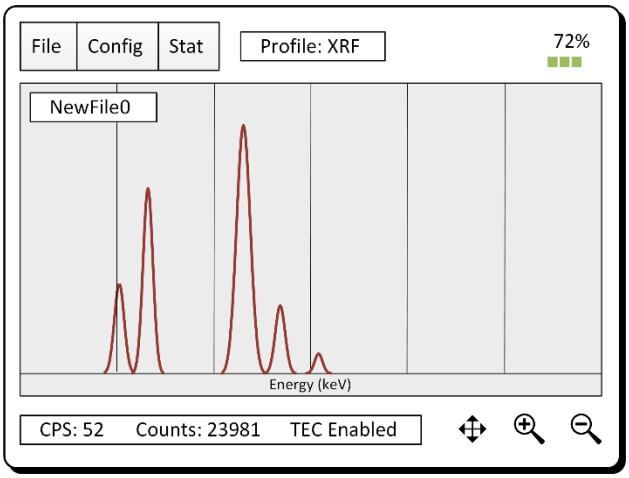

Figure 4.6.b.ii: Concept drawing of user interface

The menu at the top left of the screen enables the user to save and load spectrum data, as well as perform some basic file management functions (create folders, delete files / folders). It also provides access to a configuration menu where various settings such as TEC functionality and probe type (calibration profile) can be changed. Finally, a statistics menu will provide the user with dosimetry data which can be used to assess environmental and user safety. The percentage and battery icon at the top right of the screen is used to indicate battery charge level and indicate charging or discharging status. When charging, the device will flash the battery bars incrementally. When discharging, the number of solid bars will indicate charge level (from 1-4). The current profile in use is displayed across the top of the screen. XRF stands of x-ray fluorescence, which will be used to indicate that the low energy probe is in use, as x-ray fluorescence is the primary use of this probe. When this probe is in use the user can enable or disable the probe's TEC, which is not present in the high energy scintillator probe. The gamma ray spectrum is displayed in the plot in the middle of the screen. This plot is updated as new data is sampled by the controller. Additionally, some statistics are displayed at the bottom of the

screen, such as counts per second and total counts recorded. The user can use the icons in the bottom right corner to zoom in / out of the data, and to move the viewing area of the plot to a specified region of interest.

UserInput.c
The UserInput class will provide functions for reading the x,y value of the resistive touch screen (digitally filtered) as well as reading all five tactile buttons (debounced). These functions will be triggered from the main routine when an interrupt services an edge triggered GPIO interrupt either from the touch screen IRQ line or the button GPIO lines.

PulseProc.c
This class will provide functionality for processing and maintaining the current sampled gamma spectrum (histogram). It will first initialize the ADC when initADC() is called. The ADC will take full advantage of its 5MSPS sample rate and may use some oversampling techniques for noise reduction. When a rising edge on the amplifier's pulse signal output triggers an interrupt the samplePulse() routine will be called. This routine will sample the pulse height from the peak hold circuit after a specified delay (to allow enough time for the peak hold circuit to capture the full pulse height) and send a reset signal to the peak hold circuit to reset the peak value. The pulse height will then be binned in the histogram. Histogram data storage is accomplished by setting up an array of 4096 integers and initializing these to zero. Because the STM32F303VCT6 has a 12 bit ADC, we will read in values between 0 and 4095. The value read in will be used as an index to the array. The value at the specified index will then be incremented by one for every pulse read with that value. It is then up to the routines in the LCD class to display this array in the plotting area with the appropriate scaling factor (dependent on zoom). This array can also be directly stored on the SD card in a comma-separated values (CSV) format for further processing in Excel or Matlab. This class will also contain procedures for processing the spectrum (such as smoothing) and resetting, storing, and loading the spectrum.

devConf.c
Due to the nature of the device there will be a lot of user defined settings stored in flash. The spectrometer will use two different probes for the different energy ranges measured. Since these probes have a different method of interaction and a different response to gamma rays, they will each use their own calibration data. Additionally, the low energy Si detector will require a thermoelectric cooler (TEC) to function properly (lower noise). While the detector will still function without the cooler, measurement range will be greatly reduced (due to the increased noise floor). However, to enable a compromise between sensitivity and battery life, functionality is included to enable or disable the TEC module in the probe. ADC capture trigger level will also be defined here, and can be adjusted by the user during runtime. This will be especially useful during initial testing and calibration.

SDC.c / FileIO.c

These classes will be responsible for all file management in the gamma spectrometer. SD card communication will use the SPI protocol. This will be initialized in the initSD() function. To simplify file management, the FAT32 file system was chosen for our project. This is a popular file system that is supported by virtually every operating system (unlike the more recent NTFS filesystem). It is also fairly simply to implement. The code to implement FAT32 will be written in the SDC class. The SDC class will have basic file manipulation functions such as checking whether a file or folder exists on the card, creating new folders and files, and deleting folders and files. The FileIO class will implement the raw data write / read functionality to enable saving and loading of spectrum data. Fortunately there are already standard C library functions that can accomplish this task, and our data manipulation functions can simply reference these, which will greatly simplify implementation of this functionality. In addition to interfacing with the microcontroller for the purpose of storing and loading spectrum data, these classes will also interface with the USB peripheral to enable remote file management from a computer. This will allow the user to copy, delete, or move files by using the SD card as if it were removable storage directly attached to the computer. The device will most likely also have functionality that allows editing the device configuration through a file stored on the SD card.

USB.c

The USB peripheral on the STM32F303VCT6 is USB 2.0 compliant (full-speed) and provides up to 8 endpoints to the user. The microcontroller's hardware takes care of transaction formatting (token packets, data transmission / reception, handshake packets), including CRC generation and checking. To comply with USB specifications, the device will not draw power from the USB bus when in suspend. This means the microcontroller will control power to the charge controller and disable this through a FET when the USB controlled signals a suspend on the bus. The USB peripheral in the microcontroller utilizes a series of buffers known as endpoints. Each endpoint consists of an input and output buffer (register). When the USB host sends a packet assigned to a specific endpoint the hardware processes the packet and assigns it to the endpoint. The endpoint then raises an interrupt at which point the packet can be processed. Because the USB protocol is host centric (that is, the USB device cannot send data until it is requested by the host), whenever data is ready the device must place it into the endpoint in buffer until the host is ready to receive it. The host will signal a request for endpoint data at which point the USB peripheral will send the buffer's contents. Figure 4.6.b.iii shows the interconnections between device USB peripheral and software. While only two endpoints are shown for compactness, up to 8 endpoints can be utilized as buffers in the device.

The USB standard supports four different endpoint types: control transfers, interrupt transfers, isochronous transfers, and bulk transfers. Control transfers are mandatory in any device as these are used in command and status operations. Interrupt transfers are used when the microcontroller requires the host's attention.

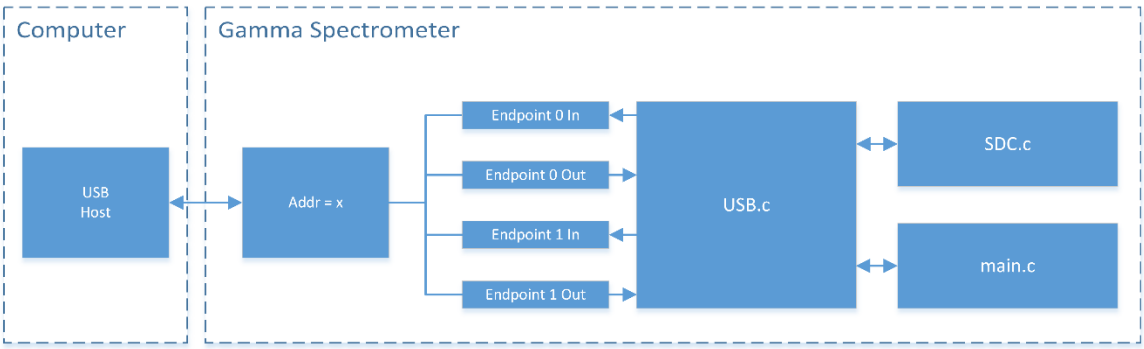

Figure 4.6.b.iii: High level USB communication diagram showing hardware and software interconnections

The microcontroller can queue an interrupt request in an endpoint until the host polls the device for interrupts, at which point a data packet is transferred. Since our mass storage device does not require any data transfer unless the PC requests it, interrupt transfer endpoints are not important and will not be used. The vast majority of USB mass storage devices will utilize a bulk-only transport (BOT) protocol defined by the USB mass-storage class specification.

There are eight standard device requests in the USB protocol: get_status, clear_feature, set_feature, set_address, get_descriptor, set_descriptor, get_configuration, and set_configuration. Standard interface requests are get_status, clear_feature, set_feature, get_interface, and set_interface. Standard endpoint requests are get_status, clear_feature, set_feature, and synch_frame. These requests will all be handled in functions written in USB.c to identify the device as a USB mass storage device and enable the PC to transfer files to and from the SD card. The device will be enumerated to the PC through a process in which a device descriptor is transferred to the computer which identifies the device's USB revision, product and vendor IDs, and complete endpoint configuration. This device descriptor will be stored in USB.c. Figure 4.6.b.iv displays the USB device descriptor hierarchy.

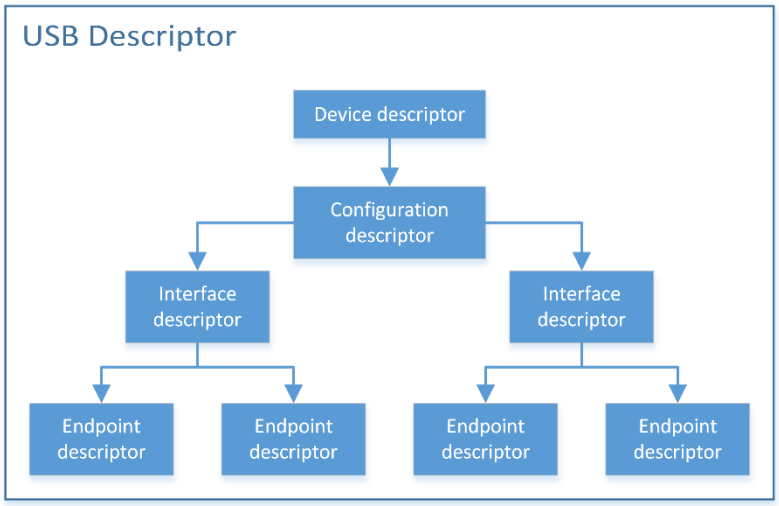

Figure 4.6.b.iv: USB device descriptor hierarchy

4.6.c Multi-channel Analyzer

Traditional gamma-ray spectroscopy uses an analog amplifier to process the pulses from the preamplifier in order to remove noise, reject pile-up signals, and shape the signals into some desirable forms before sending them to the analog-to-digital converter (ADC) to be digitized. Unlike the case in analog spectroscopy, digital signal processing (DSP) systems directly digitize the pulses from the preamplifier and then filter and optimize the digitized signals using digital processing algorithms. There are several advantages of digital signal processing over analog signal processing. The first one we will discuss is energy resolution, electrical signals are digitized earlier, therefore less analog components are used which should improve noise due to less having less hardware and better temperature stability giving potentially better resolution. Digital filter design techniques provide a high degree of freedom, which may result in better noise suppression and better resolution. Usually the pulses from the detector are not coming uniform in time and the time of arrival cannot be predicted. In the case of high counting rates, two or more pulses can overlap with high probability (pile-up). Using analog circuits, it is very difficult to separate them, and one or more pulses should be rejected which decreases number of processed events, that is, system throughput. In order to keep the throughput high, one can decrease pulse width, but it will compromise energy resolution since pulse shape will be far more from optimal. Since digital pileup rejection is more efficient, it will result in a higher throughput; this will be further discussed in this section. Higher density and lower supply voltage integrated circuits reduce size and improves portability of nuclear spectrometry systems; this is an important factor for our device because it will be handheld. Multifunction operation, the in-circuit reprogramming enables digital systems to be reconfigured and adapted for new applications or be updated. For example, a digital spectrometer may feature a multichannel analyzer, multichannel scaling and oscilloscope simultaneously. The ability to implement adaptive and scalable shaping is important for improving the pulse processing aspect of the device. The shaping time constant, that is, the time-length of the filter, may depend on the time between successive pulses. Thus, for a pulse that is closely followed by a successive pulse, a very short shaping constant can be used, whereas for a pulse that is essentially isolated, a much longer shaping constant is used. This results in a system that suffers much less pileup than conventional systems, allowing higher throughput. The other possibility is to adapt the filter shape and its coefficients to the shape of the pulse in order to correct the pulse and allow better resolution.

A multichannel analyzer operation is based on the principle of counting the pulse amplitude of an analog signal and providing an equivalent digital number. The MCA consists of an ADC, memory and a display. In this case, the preamplifier and the ADC are on two different units. The output of the pulse shaper will become the input to the ADC. The ADC is an internal ADC, which is already fixed into the microcontroller. Once this conversion has been completed the spectrum will be stored in flash memory for display. So the analog to digital converter (ADC) is a key element of MCA, which converts each pulse amplitude (or energy) into an equivalent digital number. Each energy pulse seen on the display corresponds to the energy pulse that is radiating from the test source. The MCA will enable us to store the pulse of the entire spectrum for further analysis. In this way the output of the ADC is stored in a computer type memory, which

has many addressable locations as the maximum number of channels into which the recorded spectra can be divided. The number of memory locations is determined by the ADC, in our case we will use a 12 bit ADC, which will give us 4096 memory locations (or bins). Each pulse will be stored in its own bin. The maximum content of any one memory location is typically 10^5 or 10^6 counts. The more number of memory bins, the greater the potential resolution of the instrument. Typically, the clock frequency is 50MHZ to 100 MHZ to ensure a high sampling rate. So the basic function of the MCA involves the ADC memory and display. In this way the entire histogram plot of count versus pulse height can be recorded almost simultaneously and displayed on the screen as a spectrum. The performance of the ADC is a key feature in getting good results in terms of resolution and throughput. Both resolution and throughput improve with faster sampling rates (higher frequency of ADC) and more channels in the ADC.

After the signal has been digitized, stream from the ADCs is sent to a real time processing unit at the full ADC sampling rate. This real time processing via microprocessor capability is made possible using a pipelined architecture. Pipelining is a technique used in digital processing where the microprocessor executes instructions concurrently or the memory can transfer multiple data segments simultaneously. This unit performs digital filtering for the incoming stream of data. The key difference from analogical signal filtering is in the type of filter used. Digital circuits are more suited for the implementation of finite impulse response filters, and in our case a trapezoidal filter.

It takes a finite amount of time to measure a pulse; the MCA must close off its entrance to further pulses to prevent degradation by mixing two consecutive signals, this can lead to pile-up. When the MCA closes off its entrance this is called “dead time”, when no signal is being displayed, due to the delay in processing. When the signal is being displayed after processing, this is referred to as “live time”. The faster the clock frequency of the MCA, the lower the dead time. We want to ensure a high sampling rate to avoid having a lot of dead time. The pulse shaping circuit on the analog board will handle removing very high frequency components, using the low pass filter; this can also be done programmatically using gain stage and offset control.

4.6.c.i Digital Filtering

With our current analog pulse processing systems the preamp signal from the detector is shaped, filtered and amplified by a shaping amplifier, and then digitized by a peak sensing ADC at the very end of the analog signal processing chain. The digitized signal pulse is then shaped digitally and the pulse height is extracted. The digital processor is the key element doing this operation. After extraction of the pulse height, one count is added to the memory address corresponding to the pulse height as in analog pulse processing.

Digital filtering works with signals that have been digitized, consisting of a string of discrete values, separated in time by a constant interval. Given a certain pulse, the obvious approach to determine the peak value would be to take some sort of average over the points before the step and subtract it from the value of the average over the points after the step, this known as the moving averages algorithm. We will consider some

filters/ digital signal processing algorithms later in this section. Digital pulse processing allows implementation of signal filtering functions that are not possible through traditional analog signal processing. Digital filter algorithms require considerably less overall processing time, so that the resolution remains fairly constant over a large range of count rates whereas the resolution of analog systems typically degrades rather rapidly as the counting rate increases. As a result, digital signal processing will provide a much higher throughput without significant resolution degradation. Improved system stability is another potential benefit of DPP techniques. The detector signal is digitized much earlier in the signal processing chain, which minimizes the drift and instability associated with analog signal processing.

The simplest digital filter would be the moving average filter. Since this filter takes an average value for a data length, the high frequency noise component is filtered out and the output is much smoother than the original data. Implementing this algorithm will be considered for pulse processing, however, research shows that the trapezoidal is better for detector applications.

The trapezoidal filter, the following steps will be followed:

1. Compute the average value for the next L data points.
2. The interval is the time interval corresponding to the data length L. Make a separation gap G data points and compute another average for the data length L.
3. The interval t_G is the time interval corresponding to the data length G. The output signal V corresponding to the input point $V_{in.}$

When we apply the above operation to all input data point, the output pulse shape becomes trapezoidal. The output pulse has a peaking time equal to t_l, a flat top equal to t_G, and a symmetrical fall time equal to t_l. The total width of the output pulse is defined by $2\ t_l + t_{G.}$

To ensure good energy resolution and peak position stability at high counting rates, the amplifiers of in the analog circuit are entirely dc-coupled. As a consequence, the dc offsets of the earliest stages of the amplifier are magnified by the amplification gain to cause a large and unstable dc offset at the amplifier output. We will implement a baseline restorer in the software to remove this dc offset, and to ensure that the amplifier output pulse rides on a baseline that is tied to ground potential. When two incident particles arrive at the detector within the width of the shaping amplifier output pulse, their respective amplifier pulses pile up to form an output pulse of distorted height. Depending on the time difference between two pulses, the pile-up pattern is significantly altered. When the second pulse comes relatively late and rides on the falling tail of the first pulse, the rising edge and the height of the first pulse are not distorted, so that the first event can be processed without problem. In contrast, when the second pulse arrives relatively early (2 μs shift case) and rides on the rising edge of the first pulse, the two pulses form a single pulse with a slower rising edge. In this case, both detection events are discarded. A pile-up rejecter will be implemented in software to prevent further processing of these distorted pulses.

The trigger pulse and its quality are of primary importance and have a dominating influence on the energy resolution of the measurements. Good trigger should be characterized by a low detection level, high noise immunity, a low dead time and a very low dispersion. The trigger generation algorithm that we will implement consists of the two following distinct phases. The first phase is called the timing filter phase. The responsibility of timing filter phase is to convert the input wave into a form suitable for extraction for a precise, well determined time reference of incoming discrete pulse. The result of this phase, performed by a timing filter, is smoothed bipolar pulse; this also called a RC-CR2. We can further break this filter down into three elements. The first element is smoothing. This procedure (moving average) is very important, because high frequency noises in the input signal may cause false triggers and instability of the front edge detection. The second element is called first differentiation, this removes from the input wave all low frequency components, i.e. baseline and discharge exponent. This procedure is realized by digital differentiation node where time of differentiation is usually equivalent to the leading edge of the signal from the preamplifier. The third element is called the second differentiation; this produces a bipolar wave, whose zero crossing point is independent of the input signal amplitude. The second phase of the trigger generation is called the zero crossing detection phase. Zero crossing detection operation is rather straightforward, but in our case it should be supported with an isolation mechanism, which can distinguish proper one from many other false trigger occurrences caused mainly by noise. This phase can further be divided into three elements. The first element is called the leading edge recognition. Leading edge recognition, in the moment, when value of the signal from timing filter exceeds a certain threshold level the sense window is started. Because of the noises, the leading edge detection should be verified, the edge detection is assumed valid when the value of signal from the timing filter is above the threshold during n consecutive cycles. The second element of this phase is called rigger generation. Detection of zero crossing (generation of trigger pulse) occurs when the signal from the timing filter crosses zero level. The effective trigger is generated only, when the signal from zero crossing detectors occurs during the time duration of sense window. The third element of this phase is called veto window. At the moment of trigger generation, the second, veto window of time is started. During the course of this window all further triggers are inhibited. This prevents appearance of the false triggers originating in the timing filter and leading edge detector.

Event acceptance, there are three important time reference points having a significant effect on the quality of the measurement. First reference is the “interception point, which is the time when the calculated energy value is temporarily saved. This time is established backward to the end of the trapezoid top. The second important reference point is where the pile-ups are inspected. This is located after the top of the trapezoid, where detection is observed. And the last reference point is the time which establishes time zone when the spectrometer channel is busy. This time is used for the baseline reconstruction disabling. The event is considered valid when the three following conditions are met. Firstly, external gating condition, in the moment of the trigger generation external gating signal should be high in coincidence mode or low in veto mode. Secondly, energy condition, in the moment of interception the calculated energy value should be higher than the preset energy low threshold and lower than the energy

high threshold. Thirdly, lack of pile-ups condition, up to the point of the pile-up inspection no pile-up or input signal over-range is detected. If any of the above condition is not met the event should be rejected. Valid event data is transferred to flash memory for storage and then to the display for viewing. Figure 4.6.c.i sums up the processes involved in processing a gamma pulse.

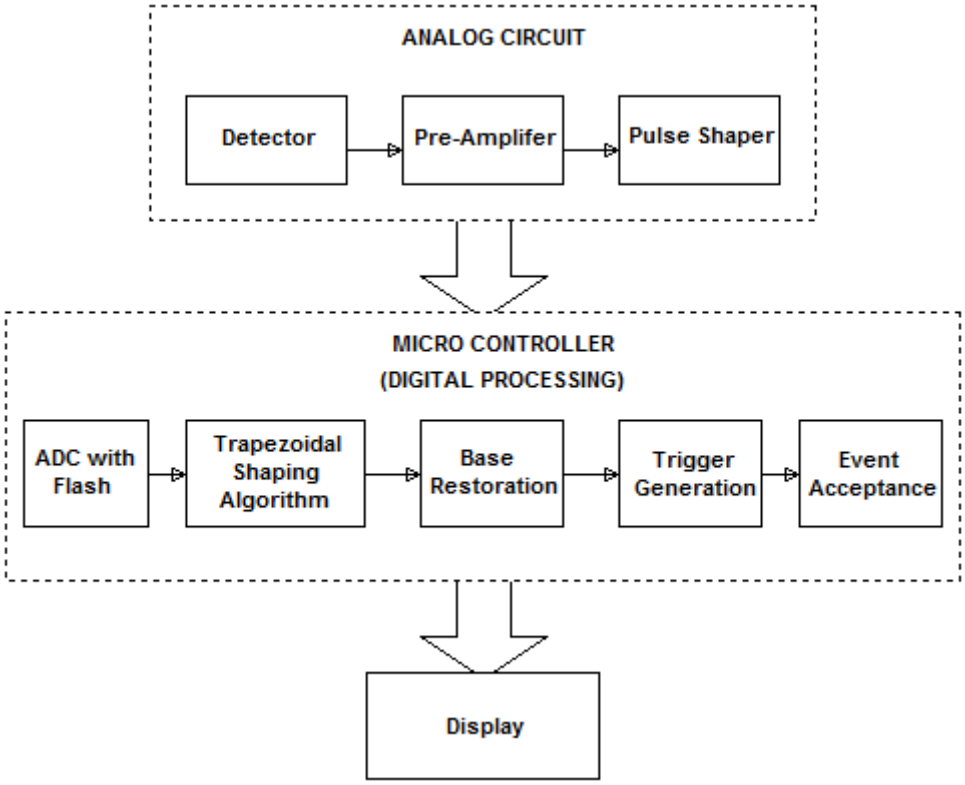

Figure 4.6.c.i.i: Overview of analog to digital processing to a digital display

4.7 PARTS AQUISITION/BOM

We have composed a small list of materials and components what we will use to build the gamma spectrometer. This list may change slightly during our design phase, however will remain mostly the same. PCB assembly will be done in house; therefore, no cost has been accounted for apart from the raw materials.

Description	Part Number	Supplier	Qty	Price
Peak Detector				
MLCC X7R 10V 5%	VJ0805Y103JXQCW 1BC	Vishay	1	$0.06
SMD 0805 1% Tol	ERJ-6ENF2400V	Panasonic	1	$0.08
SMD 0805 1% Tol	ERJ-6ENF1003V	Panasonic	1	$0.08
SMD 0805 1% Tol	ERJ-6ENF3300V	Panasonic	1	$0.08
SMD 0805 1% Tol	ERJ-6ENF24R0V	Panasonic	1	$0.08
SMD 0805 1% Tol	ERJ-6ENF1002V	Panasonic	1	$0.08
SMD 0805 1% Tol	ERJ-6ENF5101V	Panasonic	1	$0.08
Diode Schottky 10V 3A SOD-323	BAT60JFILM	Infineon	1	$0.54
MOSFET 20V 2.9A	SI2302CDS-T1-E3	Vishay	1	$0.15
Diodes - General Purpose 100V Io/150mA	LS4148-GS08	Vishay	1	$0.05
Op Amps Lo Pwr 130MHz 75mA RR	LMH6642MAX	TI	3	$4.35
Detector/Pulse Shaper				
Photodiode 100mm^2	X100-7SMD	Mouser	1	$77.94
Photodiodes Low Dark Current 10x10mm	PS100-6-SM	Mouser	1	$59.57
Scintillator	BC408	Bicron	1	$19
Precision Amplifiers LOW NOISE BIFET IC	AD743JRZ-16	First Sensor	1	$20.66
JFET N-CH 20V 10MA	BF862,215	First Sensor	1	$0.98
SMD 1210 5% Tolerance	ERJ-14YJ106U	Bicron	1	$0.48
SMD 1210 5% Tolerance	ERJ-14YJ105U	Analog Devices	2	$0.48
MLCC X7R 50V 20%	08055C104MAT2A	NXP	2	$0.12
Mica Capacitors 5pF 100Volts .5pF	MC08CA050D-F	Panasonic	2	$2.26
Thick Film Resistors - SMD 1watt 5%	756-HVC2512-30MJT18	Panasonic	2	$1.56
SMD 0805 1% Tol	ERJ-6ENF5001V	AVX	2	$0.16
Quad Low-Noise Rail-To-Rail	TLC2274	Cornell	2	$2.09
Low-Noise Rail-To-Rail	TLC2201	Welwyn	2	$10.64
MLCC - SMD/SMT 16volts 20% X7R	0805YC123MAT2A	Panasonic	2	$0.40
SMD 0805 1% Tol	ERJ-6ENF1202V	TI	1	$0.40
SMD 0805 1% Tol	ERJ-6ENF1202V	TI	2	$0.08
MLCC X7R 50V 20%	08055C104MAT2A	AVX	5	$0.60
Power Board				
Charge Controller	LT1513	Linear Technology	1	$5.45
5V Regulator	LT1761	Linear Technology	1	$1.10
3.3V Regulator	LT1762	Linear Technology	1	$1.30

Figure 4.7.i: Bill of Materials

Power Board (continued)				
Boost Converter	3494A	Linear Technology	1	$1.71
TEC Driver	MAX8520	Maxim Integrated	1	$20.63
5V/1.5A Regulator	LT1086	Linear Technology	1	$2.65
-5V/45Ma Regulator (Inverter)	LTC1174HV-5	Linear Technology	1	$8.34
Peltier TEC	TE-2-(31-12)1.0	TE Technology	1	$48.90
Digital/MCU Board				
MOSFET N-CHANNEL 60V 115mA	2N7002	Fairchild Semiconductor	3	$0.66
3 way Pin Header	22-28-5030	Molex	1	$0.13
40 way 2row vertical through hole header	4-1634688-0	Tyco Electronics Amp	1	$2.50
5 way Pin Header	22-28-6010	Molex	1	$0.08
Micro USB Receptacle type B	1981568-1	Tyco Electronics Amp	1	$1.8
Diode Schottky 10V 3A SOD-323	BAT60JFILM	Infineon	1	$0.54
MLCC X7R 10V 10%	VJ0805Y105KXQTW 1BC	Vishay	3	$0.15
MLCC X5R 10V 10%	C0805C395K8PACT U	Kemet	2	$1.02
MLCC 50V C0G 2%	VJ0805A100GXAPW 1BC	Vishay	2	$0.12
Crystal	MA-505 8.0000M	Epson Toyocom	1	$0.83
Crystal	MC-405 32.7680K	Epson Toyocom	1	$1.01
OP Amp Single GP R-R I/O 6V	MCP6231RT-E/OT	Microchip	1	$0.32
MOSFET PCH	PMV160UP	Fairchild	3	$0.21
SMD 0805 1% Tol	ERJ-6ENF1001V	Panasonic	3	$0.24
SMD 0805 1% Tol	ERJ-6ENF1501V	Panasonic	1	$0.08
SMD 0805 1% Tol	ERJ-6ENF1002V	Panasonic	1	$0.08
SMD 0805 1% Tol	ERJ-6ENF1000V	Panasonic	1	$0.08
SMD 0805 1% Tol	ERJ-6ENF1003V	Panasonic	5	$0.40
SMD 0805 1% Tol	ERJ-6ENF3003V	Panasonic	1	$0.08
SMD 0805 1% Tol	ERJ-6ENF3300V	Panasonic	3	$0.24
SMD 0805 1% Tol	ERJ-6ENF5103V	Panasonic	1	$0.08
SMD 0805 1% Tol	ERJ-6ENF22R0V	Panasonic	2	$0.16
MCU 32-Bit ARM	STM32F303VCT6	STMicroelectronics	1	$9.15
Total				$304.05

Figure 4.7.i: Bill of Materials (continued)

5.0 TEST PLAN

5.1 POWER MANAGEMENT

The test method for this portion of the test plan will be laid out such that each power supply circuit will be tested for full functionality of its intended design. The battery, charge controller, TEC driver IC, and regulators will be tested for voltage verification and continuity tests.

Voltage verification will be done on each power component IC and/or external component if necessary. Calculated voltages from the design and relative research sections will be used to verify our results. The system will first need to be powered up properly (at least as expected) and all design schematic and datasheets should be present. To verify, a multimeter will be employed to probe each contact point with the respect to its common ground. The first pin contacts to probe will be the IN and OUT (or equal value) pins. To do this, the multimeter will need to be configured such that the probes are in the VΩ and COM ports and the dial or switch be set for DC voltage measurements (usually looks $\overline{V}$). Once everything is set up, view the power system schematic and begin measuring voltages, starting at the source and working towards the load respective loads. Table 5.1.i will be used to carry out this portion procedure.

VOLTAGE VERIFCATION			
LOCATION			
USB SOURCE	**PROBE:**	**WITH RESPECT TO:**	**VERIFY:**
	+5V PIN	GND	5V
CHARGE CONTROLLER (LT1513)	**PROBE:**	**WITH RESPECT TO:**	**VERIFY:**
	IN	GND	5V
	+ C26	GND	7.4-8.2V
REGULATOR (LT1761)	**PROBE:**	**WITH RESPECT TO:**	**VERIFY:**
	IN	GND	7.4-8.2V
	OUT	GND	5V
REGULATOR (LT1762)	**PROBE:**	**WITH RESPECT TO:**	**VERIFY:**
	IN	GND	5V
	OUT/SENSE	GND	3.3V
BOOST CONVERTER (LT3494A)	**PROBE:**	**WITH RESPECT TO:**	**VERIFY:**
	SW	GND	7.4-8.2V
	VOUT	GND	16V
TEC DRIVER IC (MAX8520)	**PROBE:**	**WITH RESPECT TO:**	**VERIFY:**
	VDD	GND	5V
	REF	GND	1.5V
	MAXV	GND	4.2V
	0S1	0S2	4.2V

Table 5.1.i: Generated table for testing pin voltage

Continuity tests will be done to ensure that all pins are properly connected as they should be. This is mainly intended for debugging purposes, especially if voltages do not appear at their designated terminal. Testing for these defects is often accomplish by probing the local area of the target pin that has malfunctioned and checking for shorts and open circuits. It will be up to the tester, to either intuitively test common fault points or to test connections with reference to the schematic and necessary datasheets.

5.2 DETECTOR

The test plan for the direct detection and indirect detection of gamma rays will consist of four sections: C-V data collection and doping/geometry parameter extraction, charge injection test, noise measurements, and resolution/FWHM data.

By measuring the change in the junction capacitance over varying applied reverse bias a C-V curve can be plotted. From that curve, the extraction of the doping profile in the base can be extracted via $N_{eff}(d) = \frac{2}{A^2 \epsilon_r \epsilon_o}\left(\frac{d\left(1/C^2\right)}{dV_R}\right)^{-1}$, where A is the active area of the device and d is the width of the space charge region related to the junction capacitance by $C(V) = \frac{A\epsilon_r\epsilon_o}{d(V)}$. Once the space charge region width is known, the corresponding quasi-neutral region doping profile and geometry can be determined analytically. We can then determine accurately the reverse saturation current and noise current as well as the ENC.

The charge injection at the output of the preamplifier stage is given as $V_o = \frac{Q_i}{C_f}$ where Q_i is the injected charge and C_f is the feedback capacitance. If the detector is linear, then $Q_i = \frac{qE_{ph}}{\varepsilon_i}$ and $V_o = \frac{qE_{ph}}{\varepsilon_i C_f}$. If a test capacitor is put at the input to the preamplifier, then $V_i = \frac{Q_i}{C_T}$, where the same relationship for Q_i holds. Measurement of the output voltage yields Q_i, which can then be used to find V_i. Then the known gamma energy can be calculated as $E_{ph} = \frac{\varepsilon_i C_f V_i}{q}$. Plotting the output voltage versus E_{ph} will show the linearity of our device.

Noise measurements will include testing the detector/preamplifier in a low light environment and FWHM analysis at the MCA. In the first case, the detector/preamplifier noise should be tested in a low light environment such as in a box, or in a dark room. At the applied operational bias, the RMS voltage can be measured on the oscilloscope at the output of the preamplifier. This RMS noise voltage will be the superposition of the dark current, current noise and op amp noise. After taking this measurement the equivalent noise charge can be found from the ratio of the output voltage noise to the charge gain as $ENC = V_{n,rms}C_f$.

After taking spectral readings, we will apply the following to determine the resolution as $FWHM = \frac{B-A}{E_{ph}} \times 100\%$ where B and A are half height energies corresponding to channel number. For instance, if half height peaks occur at channels m and n (where m>n) and there are N channels, then the FWHM = (m-n)/N. The corresponding energies are given by $E_m = \frac{mE_{ph}}{N}$ and $E_n = \frac{nE_{ph}}{N}$.

5.3 PULSE SHAPER

Evaluation of the PCB design is a crucial step in evaluating, testing, proving circuit concepts and simulations done. From a testing perspective, a robust test plan adds redundancy to the PCB prototype and enables us to extract the signal from the system without dismantling the system. This is why it is necessary to carefully plan what and when a part of the device is tested. The main purpose of this section is to strategically plan testing so it can be executed simply, practically and conveniently. To avoid error the first step would be to test each circuit component individually. For the pulse shaper we will use a combination of operational amplifiers, resistors and capacitors. Before soldering the printed circuit board we will test the circuit components individually to ensure that they work alone, this will reduce error earlier on in this process. If one component is not operating properly it will be replaced. After the PCB has been soldered and all connections have been made, we will check for visible flaws, such as broken connections, corrosion or burn marks, this will affect the function and operation of the design. If any disjoint connections are seen we will connect these components together to mitigate further error. Then we will test each component once soldered, starting with the largest components on the PCB. We will put the test probes on each end of the component to test the resistance level; if the level is too high then most likely the component is not working. We will mark the components that are not working with fluorescent tape. Once all failing components are identified with multimeter we will begin removing by unsoldering them and replacing them with new ones. For the resistors in the circuit we will try to isolate the resistor so that the readings are accurate for the specific component. We will use a digital multimeter because the results are more accurate than analog. We will connect the multimeter leads to a specific resistor and run a test. The result should be approximately the same as the marked resistor value. For the capacitors in the PCB one end of the capacitor will be removed from the circuit. The DC voltage range will match the range of the particular capacitor so we do not overload the device. When we apply the voltage a few outcomes are possible, if the capacitor has shorted the meter will simply reflect the output voltage of the power supply; if the capacitor is leaking the meter reading will jump high and then drop low, but not to zero; lastly if the meter registers no jump at all the capacitor is either open or capacitance is too low to register. Similarly, for the opamp, we will isolate each individual opamp as much as possible for an accurate reading and test with the multimeter leads for voltage that should match the given datasheet; this is the simplest test for an opamp. If either of these components gives the aforementioned results they will be replaced.

5.4 DIGITAL HARDWARE

Hardware functionality will be tested by splitting up modules into their own subsystems and testing these individually with known inputs to verify the expected output. Essentially we are testing the expected transfer function of each block.

5.4.a MCU

While most testing of the microcontroller falls under software testing, some basic tests can be performed to ensure that the microcontroller is being correctly powered and is responsive to the programmer. Before any of this testing is performed the power supply must be thoroughly tested to ensure that it is working to spec and won't damage the IC. Once the power supply has been tested the IC can be mounted on the PCB and all essential power supply connections can be tested for continuity with a multimeter.

Following is the test procedure for MCU powerup and programming:

1. Verify continuity on all essential power connections on the PCB using a multimeter. Ensure that critical connections are not shorted together (such as 3.3V to ground).

2. Apply power to the 3.3V bus. Before connecting the power supply ensure that it is outputting 3.3V current limited to 100mA. This will limit short circuit current in case of a wiring problem. Verify that the microcontroller is not drawing more than ~50mA (this is within limits when running on a 72MHz clock). If the microcontroller is drawing excessive current immediately disconnect the power supply and troubleshoot connections.

3. Disconnect power and connect programmer to SWD programming header. Ensure both device grounds are connected together. Reconnect 3.3V power to MCU. Verify that the controller is not drawing excessive current.

4. Use the STLink programmer to load a test program onto the microcontroller that configures all required peripherals (RTC crystal, PLL clock, ADC, etc). Step through the code with the debugger to verify proper operation.

The microcontroller should not draw excessive current (50mA max with all peripherals enabled) and should be programmable by the STLink programmer. Debugging functionality should allow for stepping through the code as it runs on the microcontroller.

5.4.b Power Control

Proper operation of microcontroller controlled power switches is essential before connecting a load to these switches. Use the following procedure to test the USB 5V charging switch, 3.3V peripheral power switch, and LED PWM dimming circuit:

1. Connect the power supply to the VUSB terminal (5V, 600mA limit). Connect a 10uF load capacitor to the V_CHG terminal and GND.

2. Turn on the power supply output. Verify that no current is flowing to the circuit. Turn off the power supply output.

3. Connect CHG_CTRL to the power supply (3.3V, 20mA limit). Make sure you connect it to 3.3V or you may damage the microcontroller!

4. Connect the oscilloscope probe to the positive terminal of the load capacitor. Set the trigger and power on the power supply. You should see a waveform that has a constant slope indicating that the capacitor is charging at a constant current. Make sure that the maximum charging current does not exceed 100mA.
5. Attach a load of 500mA to the V_CHG output and make sure the circuit is operating correctly and that the MOSFET transistors are not dissipating an excessive amount of power.

6. Repeat steps 1-5 for the 3.3V peripheral switch. Make sure this circuit is powered from 3.3V only on the power supply.

7. Attach a load resistance of 33 ohms to the LED_PWM_OUT on the LED PWM control circuit (LCD board is disconnected at this point). Connect power supply to the circuit with 3.3V 150mA current limit. Connect the function generator to the LED_PWM pin. Configure a 10kHz 50% duty cycle square wave with 3.3V amplitude. Turn on the output of the power supply and the function generator. Measure the output current as you vary the duty cycle of the square wave. This current should vary linearly with duty cycle between 0mA and 100mA. Verify that the MOSFET transistors are not dissipating an excessive amount of power.

5.4.c LCD / SD Card / Touch Screen

The LCD board that houses hardware for the screen, backlight, SD card interface, and touch screen will plug into the header on the main PCB. A crucial part of testing is to initially ensure that there is no hardware fault resulting in a short circuit of the power supply. Additionally basic communication functionality with these peripherals should be verified, including initialization and control of the LCD, SD card, and touchscreen peripherals. The following instructions assume that appropriate drivers and test code has been written to enable communication and control of these peripherals.

For the LCD board the following procedure should be followed:

1. Connect the power supply pins on the LCD board to 3.3V and GND. Current limit the power supply to 100mA. Verify that the LCD screen does not draw excessive current.

2. Program the microcontroller with a program that tests backlight dimming functionality, power control to the board, drawing to the screen, reading from the SD card, and reading from the touch screen. Power off the board.

3. Plug the LCD board into the main board using the 20x2 pin header.

4. Connect a power supply to the 3.3V bus of the main board with a current limit of 100mA. Turn on the output of the power supply and verify that all peripherals on the LCD board work properly by visually inspecting the screen and using the UART and debugging peripheral to analyze SD card and touch screen data output.

5.4.d Signal Conditioning and Acquisition

The peak detector circuit is responsible for removing the DC offset on the pulse shaping output signal, half wave rectifying this signal, and holding the peak value of the signal until it is sampled and reset by the microcontroller. The battery measurement circuit is responsible for buffering and scaling the battery voltage down to a safe input that can be sampled by the microcontroller.

To test the peak detector circuit:

1. Connect the function generator to PK_DETECT_IN. Configure a 10kHz sine wave with amplitude of 2.5V and an offset of 2.5V. Connect a second channel on the function generator to PK_RST. Configure a square wave on this channel with 10% duty cycle and 3.3V amplitude. Connect the power supply to the opamp rails (Note: refer to the schematic and pay attention to proper supply voltages of 3V and 5V). Connect oscilloscope probes to the function generator output and ADC_INPUT.

2. Turn on the outputs of the power supply and function generator. Verify that the circuit is not drawing excessive current. Vary the phase of the sine wave with respect to the square wave so that the positive portion of the square wave occurs during the negative portion of the sine wave.

3. Verify that the circuit is holding the peak of the sine wave and that reset of the peak is working properly. Vary the amplitude of the sine wave and make sure that the peak voltage tracks the sine wave peak properly (Note: peak output should be 1.3 * sine amplitude). Compare the oscilloscope waveforms to those from the peak detector simulation in the design chapter.

To test the battery measurement circuit:

1. Connect the power supply to the opamp rails with a 3.3V 10mA output.

2. Connect the power supply to VBAT with a variable voltage between 6V and 8.4V. Since this terminal connects to the regulators on the main board select a current limit of 200mA.

3. Turn on the power supply output and measure the voltage on VBAT_ADC. This voltage should be about 3.11V when the input is at 8.4V.

5.5 SENSOR COOLING

Testing the operation and effectiveness of the TE-2-31-12-1.0 multi-stage TEC can be accomplished in many different ways. The first and most obvious method is by touch. Putting your hand close to or if not on the cold side of the TEC will give you an idea if the device is on or not. Also, touching the heat sink to feel if it is warming up (dissipating heat) gives insight on whether or not the TEC is operating.

Another method of testing is by sight will only work if the TEC is operating at one-hundred percent. If the TE-2-31-12-1.0 were operating at full capacity then it would clearly show signs of ice crystals forming on the surface of the cold ceramic plate. Sight can also be used to check for obtrusions or obstructions that could accidently load (passive or active) the cold side of the TEC. Any extra loading on the TEC would drive the internal hot heat to try and balance with the cool (extracted) heat.

Again, another method of testing would be to measure all of the associated circuit elements and IC pin values with the use of a multimeter. If any of the components are out of spec or if there is short circuit faults, that would give a clue as to why/how the TEC is operating the way it is.

Lastly, use a temperature measuring device such as a thermometer or thermocouple to measure the plate temperatures. The measured values can then be used in the equations stated in section 2.6.D.i to determine theoretical values beings seen and then comparing them to those that we designed for initially. If the measured temperatures evaluate to something different than $V_{TEC} = 4.1\,V$ and $I_{TEC} = 1.4\,A$, then it can be said that adjustments to the circuit must be incorporated.

The overall functionality should probably best be tested in the manner just discussed. Any discrepancies with the TE-2-31-12-1.0 or MAX 8520 IC need to be documented, adjusted, and then incorporated to compensate for the initial design flaws.

5.6 SOFTWARE

The microcontroller program ties all systems together and combines them to form a complete, functional gamma spectrometer. As the program design is subject to change during development and the GUI has not been completed yet this section will provide a general overview of expected functionality and appropriate test procedure for each function, instead of a step by step test procedure. It is assumed that all hardware functionality has been tested and verified before beginning software test. Software testing should be performed when all hardware is fully assembled and connected. At this point the device is tested with lithium ion battery instead of a lab power supply.

As soon as the lithium ion battery is connected the microcontroller should power on into a low power mode and disable power to all nonessential peripherals. Upon pressing the center tactile button on the keypad the microcontroller will wake up and turn on power to all systems except the thermoelectric cooler power supply. The microcontroller will then initialize the LCD screen and touch screen and check to see if an SD card is present on the SPI bus. If so the SD card will also be initialized at this point. The main screen will

then load displaying a dropdown menu on the top left of the screen, a gamma spectrum plot in the center, measurement statistics and plot navigation tools in the bottom, and a battery bar and charge percentage in the top right of the screen. A popup box will ask the user which probe they would like to use (XRF or scintillator). This is required because the two probes measure different energy ranges and the XRF probe also includes a thermoelectric cooler to reduce noise and increase resolution. After selecting the probe the dialog box will disappear and the device is ready for use.

To start a new measurement the user navigates to the 'File' menu in the top left corner and selects 'New Measurement' from the menu choices. If the current plot has not been saved yet this should prompt the user to save the data to the SD card. The current plot will then be cleared. Next the user goes to the 'File' menu and selects 'Start'. This should turn on the comparator interrupt which is connected to the peak hold circuit output. The peak hold circuit is reset by a pulse to the PK_RST pin and any pending interrupt is cleared. When a gamma ray is detected it should now trigger a comparator interrupt at which point the microcontroller delays for 50uS-100uS (to ensure that the pulse has completely passed and the peak level has been captured by the peak detector circuit) and records the current ADC voltage. It should then trigger a reset pulse to the peak detector to reset the level. Proper operation of the reset circuit can be verified with an oscilloscope. This ADC measurement process will continue until the user issues a 'Stop' command through the 'File' menu. A gamma spectrum can be saved at any time by navigating to the 'File' menu and selecting the 'Save' option. The spectrometer should then prompt for a file name and location to store the file on the SD card. An error message should be displayed if no SD card was detected. In addition to saving plots the device should also enable loading of plots stored on the SD card for viewing on the screen. When the user selects the 'Load' option under the 'File' menu the spectrometer should prompt for a file to load. When a file is selected it should load and be displayed on the plotting area. The user can at any point use the navigation tools in the bottom right of the screen to move the active drawing area in the plot or zoom in or out. To zoom the '+' icon should be pressed on the bottom right corner of the screen. The spectrometer should then redraw a zoomed version of the plot centered around wherever the user pressed on the drawing area. Likewise when the '-' icon is pressed and the plot is pressed afterward a zoomed out view of the plot data should be displayed centered about the desired point. The move icon enables the user to drag and drop the viewing area to manipulate the limits of the drawing area. When this icon is selected the viewing area should be redrawn while the user drags and pans the view.

At any point in time the configuration menu can be accessed by pressing the 'Config' button in the top of the window. This should display a dialog box with several configuration options, such as the current probe used (so the user can swap probes and start a new measurement) and if the XRF probe is being used an option to enable the TEC. The device should also display a configurable auto sleep mode which put the device to sleep after a certain amount of inactivity (1 minute, 2 minutes, 5 minutes, 10 minutes, etc). This auto sleep feature is only enabled while the device is not recording a spectrum. Additionally, under the 'File' menu there should be a 'Power Off' button which puts the microcontroller in low power mode and disables power to all peripherals.

If the device is connected to a computer with a USB cable while it is in low power mode the device should wake up and instantiate itself to the USB host as a removable mass storage device. This is accomplished through the use of a USB interrupt which can be triggered while the device is in low power mode. As far as the USB host is concerned the device should operate exactly as a removable storage device and enable the user to browse the file system and transfer or remove files from the device. Whether the device is in low power mode or not, the microcontroller should turn power to the battery charging circuit as soon as it has been instantiated to the USB host. If the device is powered on the static battery icon in the top right of the screen should change to a different icon to indicate that the device is charging. If powered off the device should not turn on when it starts charging. This gives the user the option of charging the battery at a higher rate since no peripherals will be drawing any significant amount of power when the device is in low power mode. The USB protocol mandates that if the USB host requests for a device to suspend the device should not draw more than 500uA of current from the host. When the host requests device suspend the device should turn off power to the charging circuit in order to accomplish this condition. As soon as the device recognizes a request to pull the device out of suspend charging will automatically resume.

Failure of any portion of the above specified requirements could indicate either a problem with program code or an underlying problem with device hardware. Therefore as much thorough testing as possible should be performed with lab equipment (multimeter, power supply, function generator, oscilloscope, etc) on device hardware to rule this out as a problem before debugging device software.

5.7 FULL ASSEMBLY

The full assembly will consist of integrating all of the components of the project together. The primary goal of the project was to achieve x-ray and gamma ray detection using a low cost photodiode rated for visible light. However, different technologies are designed for certain energy ranges. In order to optimize the device's output it would behoove us to use two different probes, one for x-ray energies which consists of a lower range of energies and the other probe for gamma rays which consist of a higher range of energies. For the x-ray test sources we will use a scintillator connected to the x-ray probe and for gamma ray sources we will use a photodiode connected to the gamma ray probe, to test each source with the appropriate input. For the x-ray test source we will use an isotope of americium, americium-241 which exhibits gamma energy of 60 keV. For more lower energy test sources we are also considering using a x-ray fluorescence tube that is optimized for x-ray spectrometry, this will be more cost effective than purchasing individual sources. This will provide more optionality and flexibility in our testing by providing a wider range of sources to test. Table 5.7.i below displays these test sources.

Isotope	Activity	Half-life	Peaks of Interest (MeV)	Energy Range Design Goal
Am-241	1uCi	436.2 y	0.060	X-ray
Ba-133	1uCi	10.8 y	0.081, 0.276, 0.303, 0.356, 0.384	Gamma ray
Cs-137	1uCi	30.2 y	0.662	Gamma ray
Co-60	1uCi	5.27 y	1.172, 1.333	Gamma ray
Na-22	1uCi	2.6 y	0.511, 1.275	Gamma ray

Table 5.7.i: Sources that will be used in x-ray/gamma ray spectroscopy

6.0 ADMINISTRATIVE

6.1 MILESTONE DISCUSSION

The Gantt chart, shown in figure 6.1.i, will help us keep track of our milestones throughout senior design 2. Initially, we will need to finazlie our design based on reasearch and our findings in this report. Due to our thorough research our design has changed since that initial prototype, we will need to discuss the changes as a team to make a final decision. We oredered circuit components in senior design 1 for initial prototyping and did further analysis to see which components would optimize the device characteristics. After our prototype we learned that some components work better than others for our device. We will need to order these components before building. It is important that we each have deliverables throughout senior design 2, to ensure to ensure parallel devlopment so we can complete it in a timely manner. The printed circuit boards will be developed in parallel, as they are not dependent on each other. The pulse shaper and the pre-amp will be on to separate boards to ensure that the pre-amp signal is not negatively effected by noise from other circuitry. The power management board will also be on a separate board. Digital hardware can only be implemented once the PCBs have been developed and software will be implemented after hardware. We will begin testing in early October, there are individual test plans for each part of the device and a system level test plan that will be performed towards the end of the testing phase. Much of the time as been reserved for system optimization, we will need time to optimize the signal to ensure that we are getting the right output pulses for certain energy ranges that it will be calibrated for. There will be two separate probes for input, to account for low and high energy ranges, this will require that we optimize each signal for each input. Towards the end of the semester we will prepare for the presentation, we will present the project to a panel and to the public. We will need to go through the procedure in the same environment several times to ensure that we are able to perform effectively.

Although, these milestones might change along the design process, they will serve as a good initial rubric to follow. To ensure that the milestones are being met in a timely manner we will all complete an individual progress report and share it at the end of each week. The progress report and the milestones in this discussion will be reflective of each other. Any impromptu changes made in the progress report will be updated in the Gantt chart to ensure we timely completion of the project.

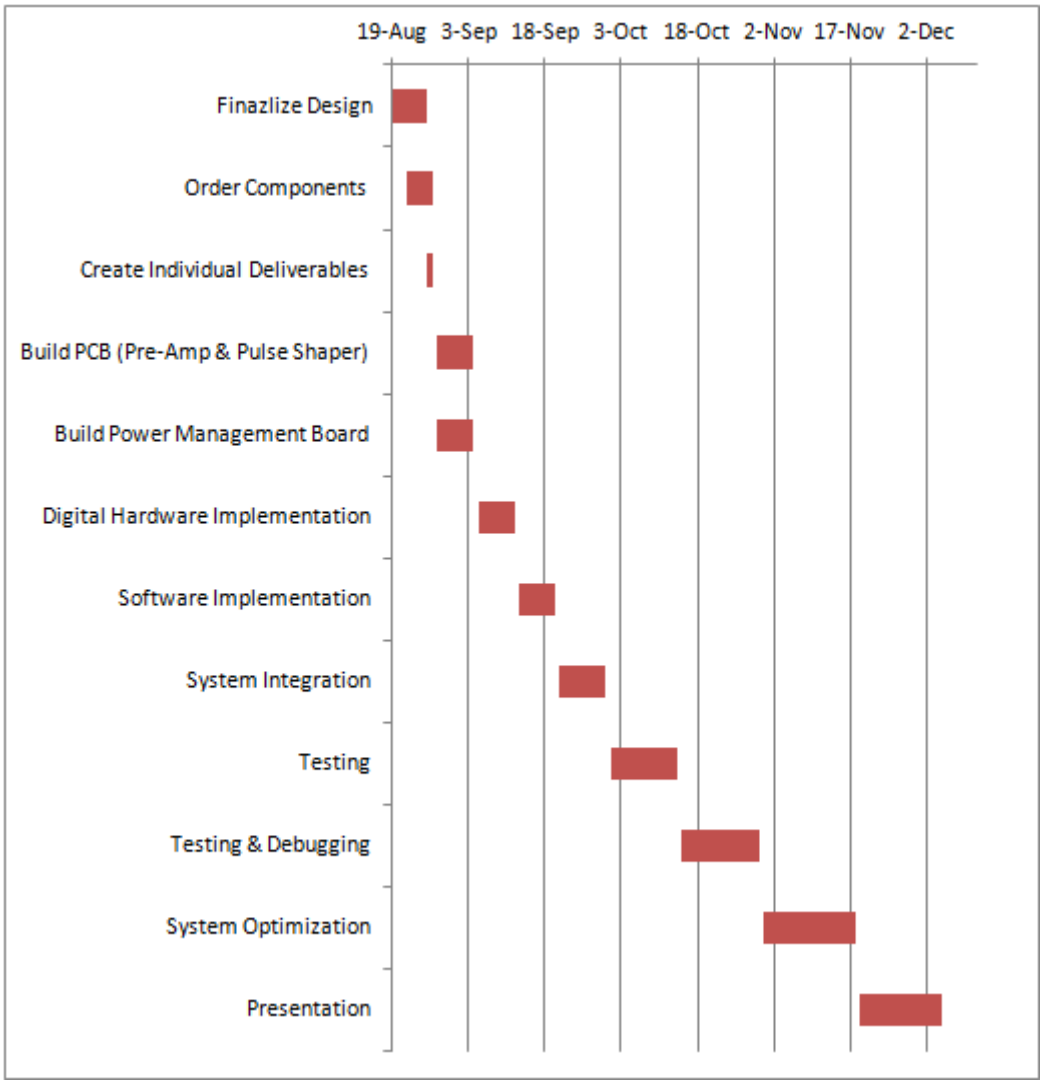

Figure 6.1.i: Gantt chart of projected senior design milestones

6.2 BUDGET & FINANCE

The projected budget for this project was approximately $300 at the beginning of the semester. The goal was to keep a tight budget as possible without sacrificing too much functionality of the product. Our initial estimate was accurate, as shown in the table below. We will be self-financing this project among the four of our group members. There are some unaccounted for costs in the bill of materials due to unpredictable miscellaneous costs. However, they have been accounted for in table 6.2.i.

	Activity	**Credit**
BOM	$304.50	
Miscellaneous Expense	$50	
Funding		$354.05
Total	**$354.05**	**$354.05**

Table 6.2.i: Brief tabulation of projected expenses

APPENDIX

I. REFERENCES

A. Pullia, G. Bertuccio, "Room Temperature X-Ray Spectroscopy with a Silicon Diode Detector and Ultra Low Noise Preamplifier," IEEE Trans. Nucl. Sci. 41(4), 1704-1709 (1994).

F. Ravotii, F. Saigne, M. Glaser, M. Moll, "BPW34 Commercial p-i-n Diodes for High Level 1-MeV Neutron Equivalent Fluence Monitoring," IEEE Trans. Nucl. Sci. 55(4), 2133-2140 (2008).

P. Rehak, "Silicon Radiation Detectors," IEEE Trans. Nucl. Sci. 51(5), 2492-2497 (2004).

K. Park, J. Park, Y. Yoon, et al., "Effects of the Resistivity and Crystal Orientation of the Silicon PIN Detector on the Dark Current and Radiation Response Characteristics," Proc. IEEE Nuclear Science Symp. Conf. Rec., 1068-1072 (2006).

A. Pullia, G. Bertuccio, "Resolution Limits of Silicon Detectors and Electronics for Soft X-Ray Spectroscopy at Non-Cryongenci Temperatures," Nucl. Instruments and Methods in Physics Research A(380), 1-5 (1996).

C.P. Allier, H. Valk, J. Huizenga, et al., "Comparative Study of Silicon Detectors," IEEE Proc. IEEE Nuclear Science Symp. Conf. Rec., 799-803 (1998).

J. Keister, "Silicon Photodiodes for Absolute Soft X-Ray Radiometry," SPIE Solar Physics and Space Weather Inst. II, vol. 6689, 1-11 (2007).

E. Rosencher, B. Vinter. 2004. *Optoelectronics*. Cambridge: Cambridge University Press.

H. Zulliger, D. Aitken, "Fano Factor Fact and Fallacy," IEEE Trans. Nucl. Sci. 17(3), 187-195 (1970).

B. Saleh. 1991. *Fundamentals of Photonics*. Hoboken: John Wiley & Sons, Inc.

G. Rieke. 2002. *Detection of Light: From UV to Submillimeter*. Cambridge: Cambridge University Press.

B. Zeghbroeck. 2011. *Principles of Semiconductor Devices.* http://ecee.colorado.edu/~bart/book/.
G. Lutz. 2007. *Semiconductor Radiation Detectors*. Heidelberg. Springer (Berlin).

B. Henke, E. Gullikson, J. Davis, "X-Ray Interactions: Photoabsorption, Scattering, Transmission, and Reflection at E=50-30000 eV, Z = 1-92," Atomic Data and Nucl. Data Tables, vol. 54, 181-342 (1993).

H. Spieler, *Silicon Detectors: Basic Concepts I* [PDF]. http://www.group.slac.stanford.edu/sluo/lectures/detector_lecture_files/detectorlectures_6.pdf

H. Spieler, *Silicon Detectors: Basic Concepts II* [PDF]. http://www.group.slac.stanford.edu/sluo/lectures/detector_lecture_files/detectorlectures_7.pdf

S. Tavernier. 2010. Experimental Techniques in Nuclear and Particle Physics. Heidelberg: Springer (Berlin).

F. Goulding, D. Landis, "Signal Processing for Semiconductor Detectors," IEEE Trans. Nucl. Sci. 59(3), 1125-1141 (1982).

G. Knoll. 2000. *Radiation Detection and Meausurement*. Hoboken: John Wiley & Sons Inc.

R. Redus, J. Pantazis, A. Huber, et al., "Improved Sensitivity X-Ray Detectors for Field Applications," IEEE Trans. Nucl. Sci. 46(6), 3247-3252 (2002).

R. Redus, A. Huber, J. Pantazis. "Improved Thermoelectrically Cooled X/γ-ray Detectors and Electronics," Nucl. Instruments and Methods in Physics Research A(458), 214-219 (2001).

R. Mao, L. Zhang, R. Zhu, "Optical and Scintillation Properties of Inorganic Scintillators in High Energy Physics," IEEE Trans. Nucl. Sci. 55(4), 2425-2431 (2008).

W. Leach Jr., "Fundamentals of Low-Noise Analog Circuit Design," Proc. IEEE 82(10), 1515-1538 (1994).

F. Ramirez-Jimenez, "P-i-N Diode Detectors," AIP Conf. Proc. 1026, 213-226 (2008).

G. Bertuccio, L. Fasoli, C. Fiorini, et al., "Spectroscopy Charge Amplifier for Detectors with Integrated Front-End FET," IEEE Trans. Nucl. Sci. 42(40), 1399-1405 (1995).

G. P. Westphal, K. Jöstl, P. Schröder, and W. Winkelbauer, "Adaptive Digital Filter for High-Rate High-Resolution Gamma Spectrometry" Nucl Sci. Vol. 48, No.3 (2001)

Zbigniew Guzik, Tomasz Krakowski , "Algorithms for digital γ-ray spectroscopy" NUKLEONIKA 2013;58(2):333-338

Adrian Dumitrescu, "Comparison of Digital And an Analogical Gamma Spectrometer at Low count Rates" U.P.B. Sci. Bull., Series A, Vol. 73, Iss. 4, 2011

Bingham, R. D., Keyser, R. M., Twomey, T. R. "Performance of a portable, Digital-Signal-Processing MCA with Safeguards Germanium Detectors" ORTEC, PerkinElmer Instruments, Inc

Helmuth Spieler "Radiation Detection and Measurement- Pulse Processing and Analysis" Physics Division Lawrence Berkeley National Laboratory

Helmuth Spieler, "Introduction to Radiation Detectors and Electronics", V.3. Semiconductor Detectors - Resolution and Signal-to-Noise Ratio LBNL, Physics Division Lawrence Berkeley National Laboratory (1999)

Lathi, B.P. (1998). "Modern Digital and Analog Communication Systems" (3rd edition). Oxford University Press.

P.W. Nicholson, "Nuclear Electronics", John Wiley & Sons, London, 1973.

W. Blum, W. Riegler, L. Rolandi, "Particle Detection with Drift Chambers" – 2nd edition (Chapter 6),Springer, 2008.

G.F. Knoll, "Radiation Detection and Measurement" - 3rd edition (Chapters 16 to 18), John Wiley & Sons, 1999.

CAMAC ADCs, "Memories and Associated Software" ORTEC, URL: http://www.ortec-online.com/.

"Performance of digital signal processors for gamma spectrometry", Application Note, Canberra Industries, URL: http://www.canberra.com/.

"SDXC memory cards promise 2 TB of storage, 300 MBps transfer". Engadget. 2009-01-07. Retrieved 2010-08-22.

"microSD & microSDHC Cards**",** Memory Solutions, Toshiba

Texas Instruments, Appl. Note SBOA055A, "Compensate Transimpedance Amplifiers Intuitively" [PDF]. http://www.ti.com/lit/an/sboa055a/sboa055a.pdf

Analog Devices, Appl. Note MT-044, "Op Amp Open Loop Gain and Open Loop Gain Nonlinearity" [PDF]. http://www.analog.com/static/imported-files/tutorials/MT-044.pdf

Maxim Integrated, Appl. Note 2236, "Gamma-Photon Radiation Detector" [PDF]. http://pdfserv.maximintegrated.com/en/an/AN2236.pdf

Maxim Integrated, Appl. Note 5129, "Stabilize Your Transimpedance Amplifier" [PDF]. http://pdfserv.maximintegrated.com/en/an/TUT5129.pdf

Amptek, Appl. Note AN250-2 [HTML]. http://www.amptek.com/a250ap.html

Hamamatsu, Appl. Note SD-37, “Characteristics and use of charge amplifier” [PDF]. http://www.hamamatsu.com/resources/pdf/ssd/charge_amp_techinfo_e.pdf

A. Kay, B. Zhao, *Noise in Photodiode Applications* [PPT]. ftp://ftp.ti.com/pub/linear_apps/noise%20power%20point/Noise%20In%20Photodiode%20applicaitons.ppt

STMicro, Technical Document UM1570, “STM32F3DISCOVERY Discovery kit for STM32F303xx microcontrollers” [PDF]. http://www.st.com/st-web-ui/static/active/jp/resource/technical/document/user_manual/DM00063382.pdf

STMicro, Technical Document RM0316, “Reference Manual STM32F302xx, STM32F303xx and STM32F313xx advanced ARM-based 32-bit MCUs” [PDF]. http://www.st.com/web/en/resource/technical/document/reference_manual/DM00043574.pdf

STMicro, Appl. Note AN2867, “Oscillator design guide for STM8S, STM8A and STM32F1 microcontrollers” [PDF]. http://www.st.com/st-web-ui/static/active/cn/resource/technical/document/application_note/CD00221665.pdf

Texas Instruments, Appl. Note SLVA156, “Monotonic, Inrush Current Limited Start-Up for Linear Regulators” [PDF]. http://www.ti.com/lit/an/slva156/slva156.pdf

Analog Devices, Appl. Note EE-289, “Implementing FAT32 File Systems on ADSP-BF533 Blackfin® Processors” [PDF]. http://www.analog.com/static/imported-files/application_notes/EE289.ADSP.BF533.Rev1.Feb.2006.pdf

Cypress Semiconductor, Appl. Note AN57294, “USB 101: An Introduction to Universal Serial Bus 2.0” [PDF]. http://www.cypress.com/?docID=33237

Texas Instruments, Appl. Note SLVA043B, “Noise Analysis in Operational Amplifier Circuits” [PDF]. http://www.ti.com/lit/an/slva043b/slva043b.pdf

Maximintegrated, Appl. Note AN1014, "Designing a Power Supply for a Portable, Wireless Contact Manager" [PDF]. http://pdfserv.maximintegrated.com/en/an/AN1014.pdf

Texas Instruments, Appl. Note slva166a, "Battery Charger Termination Issues With System Load Applied Across Battery While Charging" [PDF]. http://www.ti.com/lit/an/slva166a/slva166a.pdf

TETechnology, Multi-stage Modules http://www.tetech.com/Peltier-Thermoelectric-Cooler-Modules/Multi-Stage.html

II. PERMISSIONS

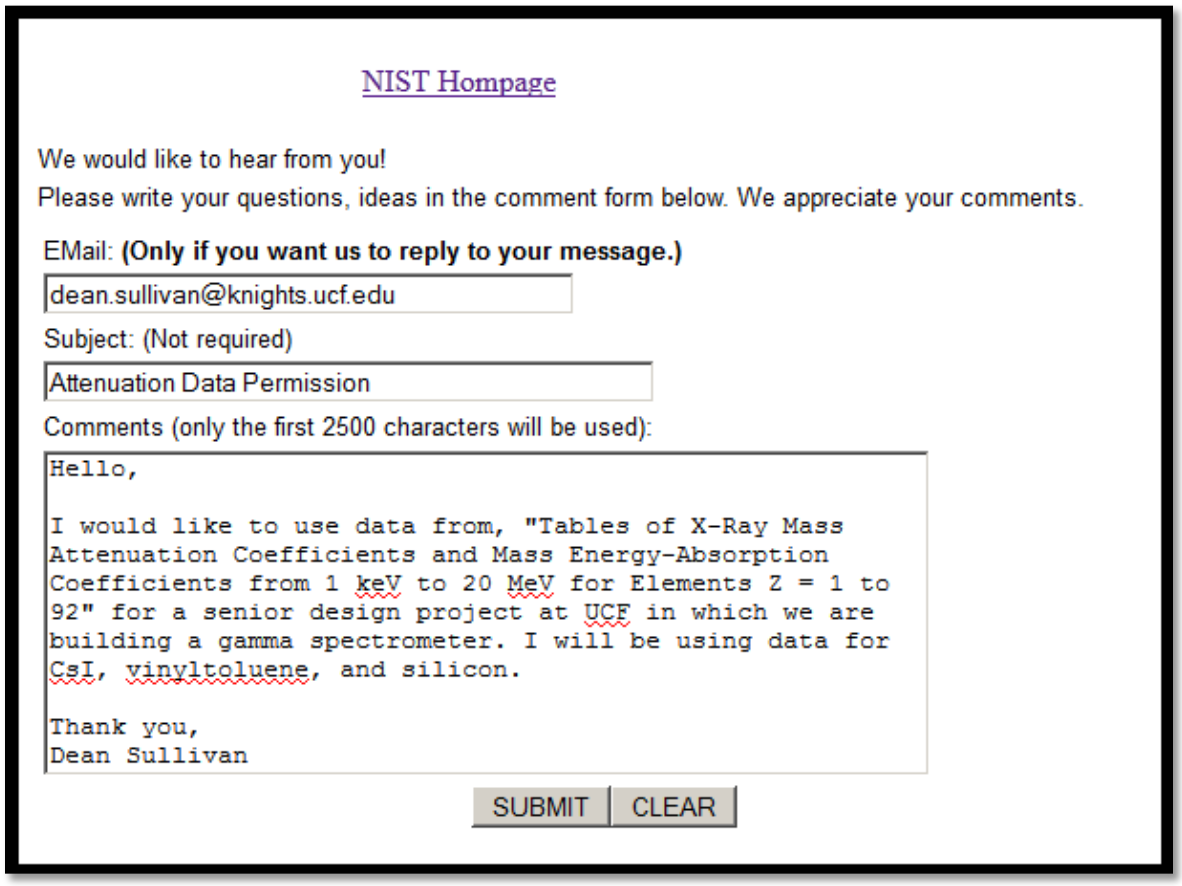
NIST Hompage

We would like to hear from you!
Please write your questions, ideas in the comment form below. We appreciate your comments.

EMail: **(Only if you want us to reply to your message.)**

dean.sullivan@knights.ucf.edu

Subject: (Not required)

Attenuation Data Permission

Comments (only the first 2500 characters will be used):

```
Hello,

I would like to use data from, "Tables of X-Ray Mass
Attenuation Coefficients and Mass Energy-Absorption
Coefficients from 1 keV to 20 MeV for Elements Z = 1 to
92" for a senior design project at UCF in which we are
building a gamma spectrometer. I will be using data for
CsI, vinyltoluene, and silicon.

Thank you,
Dean Sullivan
```

SUBMIT CLEAR

Figure II.I: Permission request